MINISTRY OF EDUCATION AND RESEARCH

THE ANNALS OF "DUNAREA DE JOS" UNIVERSITY OF GALATI

Fascicle IX
METALLURGY AND MATERIALS SCIENCE

YEAR XXVI (XXXI),
May 2008, no. 1

ISSN 1453-083X

2008
GALATI UNIVERSITY PRESS

Fascicle IX

METALLURGY AND MATERIALS SCIENCE

THE ANNALS OF "DUNAREA DE JOS" UNIVERSITY OF GALATI.
FASCICLE IX. METALLURGY AND MATERIALS SCIENCE
N^0. 1 – 2008, ISSN 1453 – 083X

Table of Contents

THE ANNALS OF "DUNAREA DE JOS" UNIVERSITY OF GALATI.
FASCICLE IX. METALLURGY AND MATERIALS SCIENCE
N^0. 1 – 2008, ISSN 1453 – 083X

FATIGUE DEGRADATION OF MATERIALS AS A TOOL FOR DAMAGE ASSESSMENT

Filipe SILVA
Department of Mechanical Engineering, Minho University,
Azurém, 4800-056 Guimarães, PORTUGAL

ABSTRACT

Damage assessment of components or systems is strongly related to the way components fail. Thus, an appropriate understanding of failure degradation of components is necessary. Furthermore, most of the failures are related to fatigue cracks that develop on components under service. This paper is concerned with the fatigue degradation of metallic components. Its emphasis is on the different ways in which the fatigue damaging mechanisms occur, being the main responsible for the failure of components.

This paper has two main sections: one section deals with the fatigue mechanisms and their definition; the second section focuses on the failure analysis of components affected by those mechanisms.

KEYWORDS: damage assessment; failure mechanisms; fatigue; case studies

1. Introduction

Damage prognosis is the prediction in near-real-time of the remaining life of a system given the measurement and assessment of its current damage. A key element in damage prognosis is obviously that of determining the existence and location of damage. The understanding of the basic damaging mechanisms is important in order to determine the possible existence and location of damage, to prevent future occurrence, and/or to improve the performance of the device, component or structure. There are several different categories of physical failures, depending on the classification system. The Failure Analysis and Prevention ASM handbook [1] suggests a convenient way to descriptively categorize and discuss failures. They suggest four categories of failures: distortion and undesired deformation; corrosion; wear; fracture. The first failure category is related to geometry changes (bending, buckling, swelling or shrinkage). The common causes to distortion failures include temperature-induced phase changes or thermal expansion in metals, fluid absorption of non-metallic, and curing shrinkage such as it may occur in grouts and adhesives. The other three categories of failure, associated with degradation of materials are: corrosion; wear; fracture. Corrosion can be essentially considered as the loss of material due to chemical or electrochemical action [1]. Wear is removal or displacement of surface material due to a relative motion between solid, liquid, or gas [1]. Fracture is generally defined when there is separation of material. There are many causes of fracture. These include brittle fracture, ductile fracture, and fatigue. Though distortion, wear, corrosion, and some kinds of fracture are also of great importance, this paper will consider only part of the fracture failures, namely the fatigue failures.

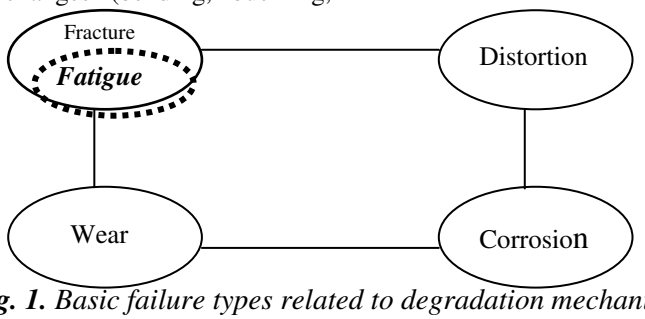

Fig. 1. *Basic failure types related to degradation mechanisms [1]*

Although fatigue is only a sub-group of the fracture failures, there are several different fatigue failure modes. Some fatigue mechanisms, such as mechanical fatigue or thermal fatigue, are well known. However there are also some failure mechanisms that are traditionally attributed to corrosion or wear but that are mainly related to fatigue mechanisms. In this group is for example cavitation fatigue. It is frequently confused with corrosion fatigue because it happens when a component or at least part of the component is in contact with a liquid. It is assumed that pitting observed in the component is always related to corrosion mechanism. Sometimes cavitation is also confused with wear or abrasion.

Another important aspect to highlight is that it is very frequent that different failure mechanisms act together. Sometimes corrosion precedes fatigue or corrosion acts together with fatigue increasing crack propagation rates. In other cases, such as fretting fatigue, both wear and fatigue act together to nucleate fatigue cracks. Therefore, although in their nature they are different in most fatigue failures it is not possible to isolate one failure type.

The emphasis of this paper is to do a survey of some different fatigue degradation mechanisms and its occurrence on damaged components. Although not all of the mechanisms may be addressed on this paper it is also a purpose to do a classification and categorization of the fatigue failure mechanisms assessed.

The paper is divided in two main sections: the first section intends to give a short definition of each fatigue mechanism. The second section is a description of examples of damaged components with the presented fatigue mechanisms.

2. Fatigue Mechanisms

Basic definitions

The basic feature that underlies all the specific fatigue failure mechanisms is the *existence of repeated or cyclic stresses* at some point of the component [2]. This could be considered the basic definition of fatigue. The cyclic stresses or strains give origin to damage accumulation until it develops into a crack that finally leads to failure of the component.

Keeping in mind the basic assumption for a fatigue failure, different definitions will be provided for the specific fatigue failure mechanisms. The different fatigue failure mechanisms are essentially related to the way those cyclic stresses arise in a specific point of the component, or to the cause of the stresses. Sometimes they are also related to the existence of other concurrent or synergistic damaging mechanisms such as wear or corrosion.

The fatigue failure mechanisms, in this paper, are divided into two classes: the primary mechanisms and the secondary mechanisms, according to the following definition:

Primary mechanisms: mechanisms that are able by themselves to initiate and propagate fatigue cracks;

Secondary mechanisms: mechanisms that are not able by themselves to promote fatigue fracture but may either initiate cracks or help on crack propagation of pre-existing cracks.

A definition for the different fatigue mechanisms, either primary or secondary mechanisms, will be subsequently given. Some schemes of the mechanisms are shown on the damaged components section.

Primary mechanisms

Mechanical fatigue - Mechanical fatigue is the widest definition and is traditionally related to components where external loads are applied for example on the connections/supports. In this definition cyclic stresses flow through the component and concentrate in critical points of the component due to loads/restraints that are applied in other points. If mechanical fatigue occurs at high temperature, another mechanism, of creep, is often active.

Thermal fatigue - Thermal fatigue exists under two different situations: the first is in a singular component due to different temperatures (cyclic) in different areas of the same component; the second situation is, for a component with two dissimilar materials, for a certain temperature (cyclic) in both materials at the same time. In the first situation stresses arise due to the difference in temperature; in the second situation stresses arise through different dilatation coefficients of the same component (with at least two different materials). Due to high temperatures involved in the process and depending on the thermal cycle, shape creep may also be active.

Thermal/mechanical fatigue - Thermal/mechanical fatigue exists when both mechanical and thermal fatigue act at the same time. It is common to have superposed thermal and fatigue cycles. Due to high temperature involved creep is sometimes active in thermal/fatigue situations.

Contact fatigue - Contact fatigue exists when two free bodies are in contact but they are not attached one to another. It occurs mainly when there is a rolling contact. The contact forces are the responsible for the Hertzian stresses and strains in the components. On the contact surface between the free bodies and due to the contact deformation there may exist a very small relative displacement between the bodies. Thus sometimes, another mechanism, the fretting one, may be considered as associated with rolling contact fatigue.

Impact fatigue - Impact fatigue is characterized by the existence of an impact contact. Thus there is a load between the two bodies plus the impact energy due to the prior movement of at least one of the bodies.

Cavitation fatigue - Cavitation fatigue exists when bubbles are created inside a liquid in an under-pressure region and, when those bubbles reach higher pressure zones they implode and the wave pressure that is born from the implosion impacts a solid surface. These waves are responsible for the stresses and strains at the solid bodies.

Creep fatigue - Creep fatigue is a superposition of mechanical fatigue and creep (deformation at high temperature at a constant load). According to the high temperature level and load fatigue cycle, waveform creep may be more or less active but it is almost always present.

Secondary mechanisms

Wear-fatigue - Wear fatigue exists when two bodies are not attached one to another but there is contact and a relative displacement between both components. There are the normal contact forces plus the tangential forces due to the sliding movement between both bodies.

Fretting fatigue - Fretting fatigue is similar to wear fatigue because there is wear between the two bodies due to a relative displacement. The main difference is that the two bodies are commonly connected or attached one to the other for example with screws, and the relative displacement between both components is very small (traditionally between 1 to 100 μm)

Abrasion fatigue - Abrasion fatigue exists when two solid bodies are not in direct contact one to the other but a third body (for example dust) promotes the contact and load transmission between the initial two bodies. The third body (for example dust) may be involved in oil or water. Initially they cause pitting or spalling like on contact fatigue but in cases where a pre-existing crack exists, they may promote crack propagation.

Corrosion fatigue - corrosion fatigue exists when structural metals operate in deleterious environments. This detrimental environment accelerates fatigue crack growth. Even materials immune to SCC - Stress Corrosion Cracking are susceptible to CC – Corrosion Cracking (or corrosion fatigue cracking).

Hydrodynamic fatigue – (trapped water/oil fatigue) - There are at least two different ways in which hydrodynamic fatigue is present. One is when there is load transmission between two rigid bodies by means of a liquid (for example oil) and there is a pre-existing crack. The liquid enters the crack and promotes crack propagation by exerting opening loads on the crack surfaces. The other situation is when two solid bodies are in direct contact, for example under rolling contact, and there is a pre-existing crack with liquid inside. When one body contacts the other body on the crack position, the crack closes and the liquid is trapped inside the crack. The pressure on the trapped liquid promotes crack propagation.

3. Damaged Components

In this section, examples of most of the fatigue failure mechanisms presented above are shown. Most of them are from failure analysis carried out at Minho University and the components can be seen in the mechanical engineering department. Some schematic representations of the mechanisms are also shown, for their better understanding.

Primary mechanisms

Mechanical fatigue

This is probably the most common fatigue failure and many damaged components can be found, such as the following crankshaft (fig.2). The fatigue failure occurred in a stress concentration on the radius of curvature. This stress concentration is located between where the loads are applied (journals) and the restraints. The stress concentration occurred along the crankshaft due to geometrical constraints. This type of fatigue is what can be defined as mechanical fatigue failures. Different mechanical fatigue failures can be found in literature such as a crankshaft [3] or tooth gears broken by bending [4].

Fig. 2. *Crankshaft and engine piston broken by mechanical fatigue [Minho Univ.].*

Thermal fatigue

The first situation of thermal fatigue is when, in the same component of the same material, there are different temperatures (cyclic) in different areas of the same component [5]. The brake disk in fig. 3 is an example of thermal fatigue due to different temperatures in a same component. Thermal fatigue cracks develop along the heating front, e.g., parallel to the thermal gradient.

The second situation of thermal fatigue is when a component consists of two dissimilar materials and a certain temperature (cyclic) acting on both materials at the same time. The whole component can be under the same temperature. In this second situation stresses arise through different dilatation coefficients of the same component (with different materials). The material with higher dilatation coefficient tends to be under compression while the material with lower dilatation coefficient will be under tensile stresses. Examples of this second thermal fatigue situation are found, for example, in solder joints [6].

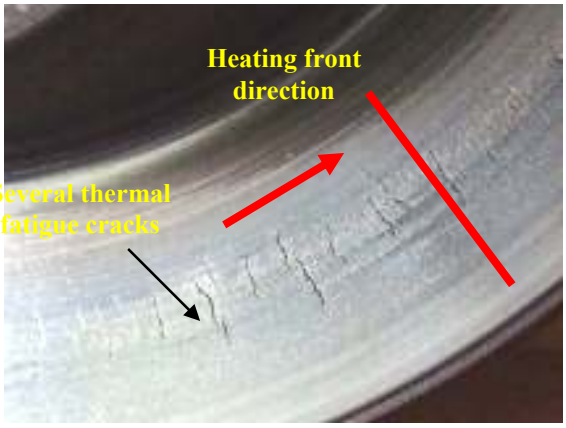

Fig. 3. *Brake disk damaged by thermal fatigue [Minho Univ.].*

If operating temperatures are high, there may exist creep along with thermal fatigue. Fig. 4 shows a train engine piston with several radial cracks along the piston head. In this case thermal fatigue is related to the stresses in the material induced by thermal gradients in the component. The thermal stresses are due to the 'vertical' distribution of the temperature along the piston – high temperatures at the top and lower temperatures at the bottom.

There is a homogeneous and regular gradient of temperature on the radial direction along the head of the component. The bowl rim area is the area where temperatures are higher [7]. Thermal deformations under the operating bowl rim temperature are constrained by the surrounding material. This causes large compressive stresses on the total bowl rim circumference that often exceed the yield strength of the material. These compressive stresses at high temperature cause creep at the bowl rim area. After creep relaxation of the high compressive stresses and when the piston gets cold, creep effect gives rise to tensile residual stresses on the bowl rim. These cyclic tensile stresses trigger cracks distributed all around the rim area, as observed in fig. 4.

Thermal/mechanical fatigue

Thermal/mechanical fatigue is a superposition of both mechanical and thermal fatigue. Examples of this situation are, for example, what happens with turbine disks [8-9]. Sometimes, if operating temperatures are high, creep is also active and very complex thermal mechanical fatigue situations exist. Almost all engine components are under thermal cycles (start-up, steady state, and shut down) and mechanical cycles. Therefore, thermal mechanical fatigue arises. An example is another engine piston [7], on fig. 5. On this picture only one crack prevailed and propagated. This is a symptom that mechanical fatigue was the most important mechanism. However thermal fatigue was also active, as the thermal cycles also existed. If thermal fatigue were the most important mechanism, instead of mechanical fatigue, it would be observed several fatigue cracks, as happened with the train engine piston, shown in fig. 4.

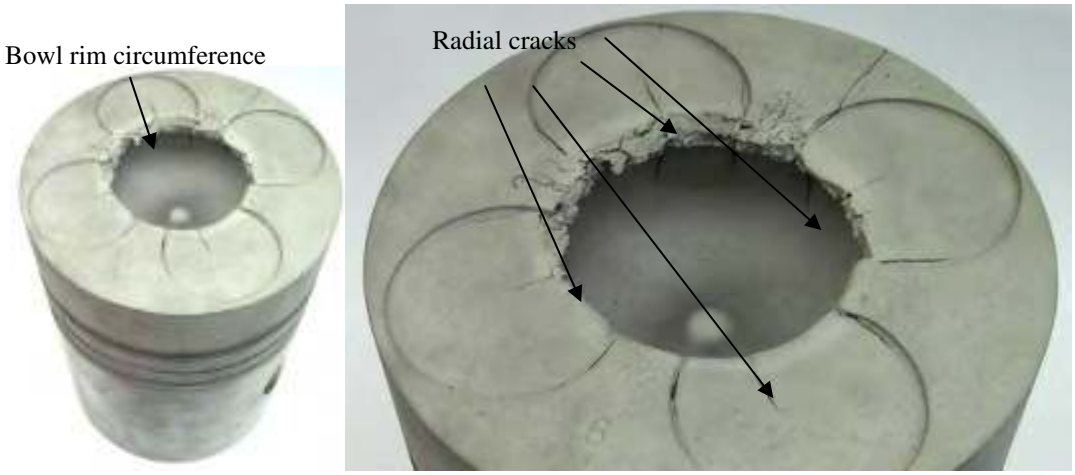

Fig. 4. *Train engine piston – piston damaged by thermal fatigue with creep [7, Minho Univ.].*

Fig. 5. *Engine piston – piston damaged by thermal-mechanical fatigue [10, Minho Univ.].*

Contact fatigue

When two free bodies are in contact but not attached one to another, there may exist contact fatigue. Examples are rolling bearings, gears [10], train wheels on railways, etc. On fig. 6 there is a cylinder arm that was in direct contact with the bearing cylinders.

That cyclic rolling contact promoted 'pitting' or 'spalling' of small regions on the cylinder arm.

In fig. 6 can be clearly seen that the area that suffered pitting is the one where the loads were high during the engine cycle. Sometimes fretting is also associated with rolling contact fatigue. As a fact when two free bodies are in contact and there is deformation between them, it is probable that there is also a small relative displacement between the surfaces (this depends on the geometry of the contacting bodies).

Thus, although the fatigue mechanism is known as 'contact fatigue', it is important to consider that most of the times fretting may also play a role on the degradation evolution.

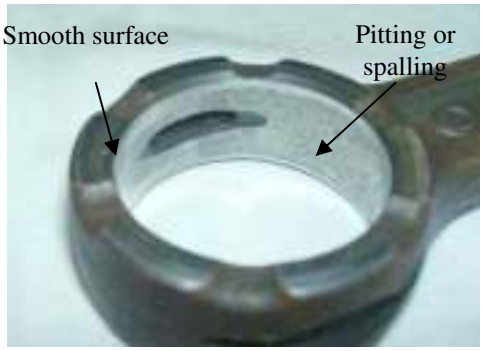

Fig. 6. *Cylinder arm damaged by contact fatigue [Minho Univ.].*

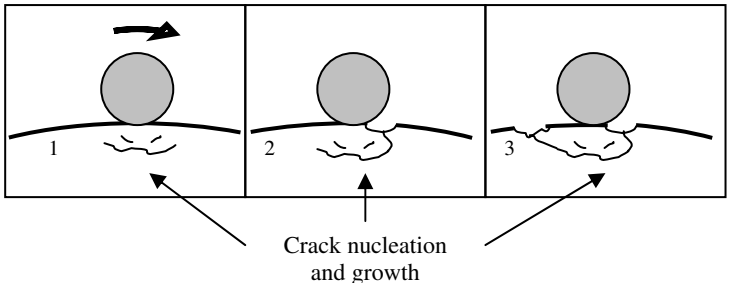

Fig. 7. *Schematic damage evolution under contact fatigue.*

Impact fatigue - Impact fatigue is characterized by the existence of a contact load between two bodies plus the impact energy due to the movement of at least one of the bodies.

According to [11] it is important to take into account the behaviour of the stress waves due to the impact energy in order to predict the fracture strength of the components.

Traditionally impact fatigue exists in components under the form of vibration but in some cases, such as the one shown on fig. 8, there is impact due to the fact that the valve spring was not strong enough and the valve top component used to lose contact with the cam in one part of the cycle (there was an impact in every cycle).

Therefore, besides the contacting load between the cam and the valve top component there was an impact between both components.

The consequence in terms of fracture morphology is that there are many growing surface cracks. This is due to the impact energy that flows from the contact point through the whole body, as a stress wave, promoting the growth of all existing cracks. Although there are not many studies including impact fatigue, this stress wave effect was observed on small crack growth, by Zhang [12].

In Zhang's study, it is clear that impact fatigue and non impact fatigue have very different crack initiation mechanisms.

a) b)

Fig. 8. *a) Valve top component damaged by impact fatigue [Minho Univ.];*
b) Working positioning of valve top component.

Cavitation fatigue - Cavitation fatigue exists due to the wave pressure impacts on solid surface. These waves are responsible for the cyclic deformation of the solid bodies. Basically, the bubbles form in low pressure areas and when they reach higher pressure areas, they implode and pressure waves form. These pressure waves flow through the liquid and impact the solid surfaces. Although this mechanism, also called cavitation erosion, as been a matter of controversy, cavitation fatigue is being understood as a fatigue phenomenon essentially related to cyclic stresses/strains and therefore as a mechanical fatigue phenomenon.

The mechanism is essentially the same as contact fatigue (fig. 7), as described in fig. 9b. It is frequent in diesel cylinder walls due to the vibration of the walls (see fig. 9a), but it is also common in ship propellers, water pumps, injector nozzles [13], and other components that are in contact with liquids.

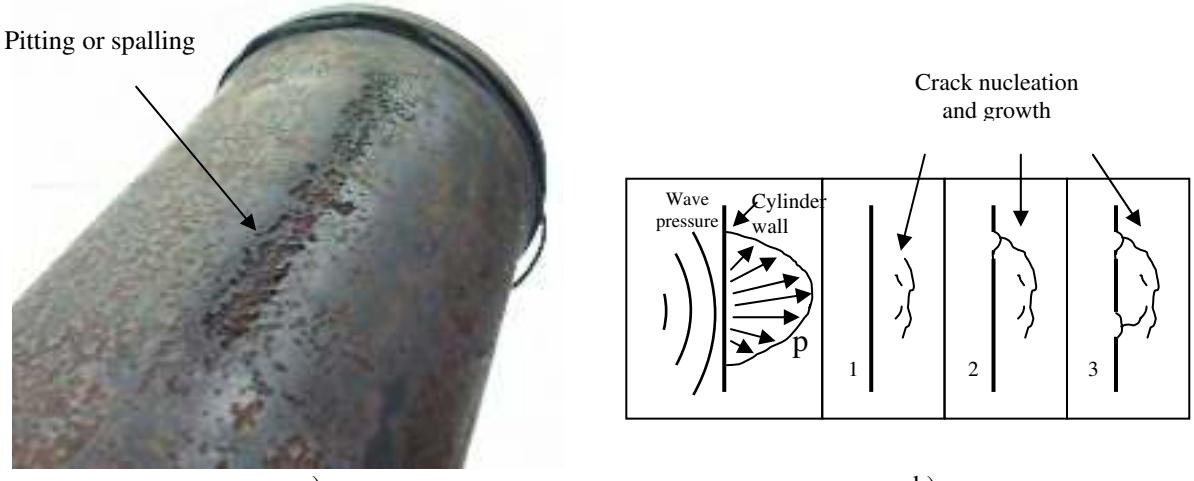

a) b)

Fig. 9. *a) Engine cylinder wall component damaged by cavitation fatigue [Minho Univ.];*
b) Schematic representation of wave pressure damage mechanism
(ex: wave pressure against a cylinder wall).

Sometimes cavitation fatigue occurs in situations where there are also thermal cycles and mechanical cycles, such as that of the cylinder walls (fig. 9a). Thus cavitation fatigue is also, sometimes, superposed to thermal-mechanical fatigue [14].

Creep fatigue - Creep fatigue exists when mechanical fatigue operates in a metal component at high temperature (in plastics there may exist creep fatigue even at room temperature).

Sometimes, when there are thermal cycles with creep, it is also called creep fatigue. Creep fatigue is basically a superposition of mechanical fatigue and high temperature creep [15].

Creep fatigue is common, for example, in power plants or fusion reactors [16].

Due to high temperatures, involved with long hold periods at high temperatures creep is active and promotes crack growth. Due to mechanical cycles, mechanical fatigue is also active promoting also crack growth.

Secondary mechanisms

Wear-fatigue

Wear fatigue exists when there are normal contact forces plus the tangential forces due to the sliding movement between both bodies.

The following crankshaft shows an example [17] of a journal that was in contact with the plain bearing. Besides the normal contact it is clear in the damaged surface (scratched areas) that a sliding contact promoting wear existed between the surfaces. Although the wear was not enough to initiate cracks it is not difficult to admit that, if there were a pre-existing crack, the wear between journal and bearings would help on crack propagation. This is what happened in the crankshaft journal in fig. 10 and the mechanism is schematically described in fig. 11

a) **b)**

Fig. 10. *Crankshaft journal under fatigue wear fatigue [17 - Minho Univ.]. a) pre-existing cracks; b) after crack propagation.*

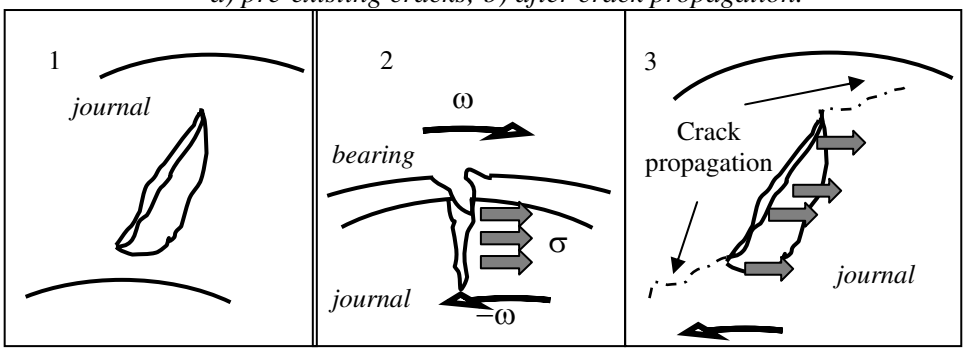

Fig. 11. *Schematic damage mechanism under wear fatigue after a pre-existing crack.*

Wear fatigue is also considered in situations where the load is transmitted from one body to the other under wear conditions. This is what happens, for example, on cutting tools. The cyclic loads come from the alternating slip and stick of the chips, the vibrations of the machines, and the heavily interrupted cutting process itself. However the cracks grow in places where there is no wear. Thus it is mainly a mechanical fatigue process. Most of the times, during the cutting process, it involves cyclic temperatures. Therefore thermal fatigue may also be active [18].

Fretting fatigue

Fretting fatigue is common in situations where two components are connected or attached one to the other for example with screws, and a small relative displacement (traditionally between 1 to 100 μm) exists between both components. Fig. 12 shows a suspension component where fretting fatigue accelerated the fatigue damaging in the contact region between the formed component and the screw head. A small relative displacement between both components was responsible for the fretting process. In this case, the failure region was not the most stressed area of the component. Thus it would not be expected that the contact region between the bolt and the component would fail. However, the relative displacement deteriorated that region causing a premature fatigue crack and consequent failure of the component.

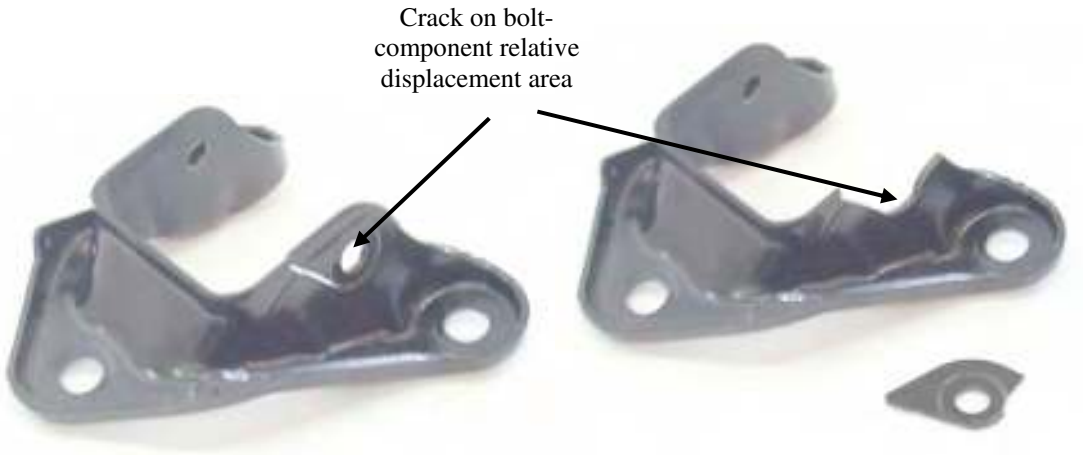

Fig. 12. *Suspension component damaged by fretting fatigue [Minho Univ.].*

Since structures are composed by individual components that are attached one to the others fretting fatigue failures are very common and occur in many components such as propellers hub-flange assemblies, turbines disc/shaft connections, etc [19].

Abrasion fatigue

Abrasion fatigue is common when load transmission between two solid bodies is made by a third body (for example dust).

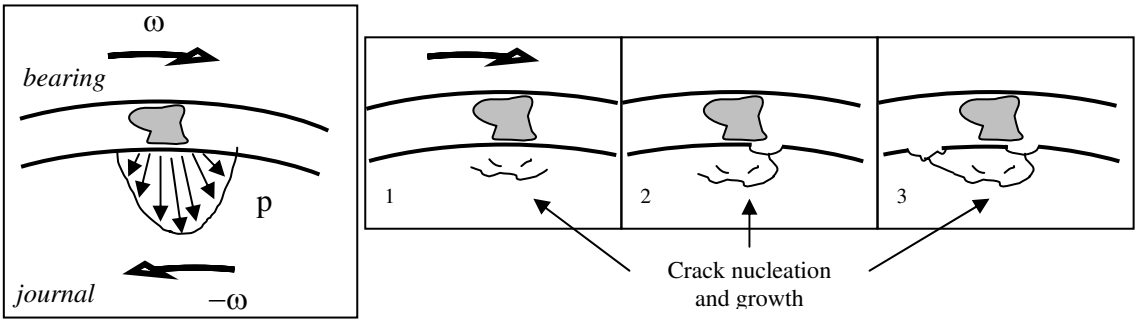

Fig. 13. *Schematic damage mechanism under abrasion fatigue.*

Fig. 14. *Journal bearing damaged by abrasion fatigue [Minho Univ.].*

This third body (for example dust) may be involved in oil or water.

This is very common in bearings such as the one on fig. 14. The mechanism is schematically shown in fig. 13. The third body causes pitting or spalling. If by any reason there is a pre-existing crack the dust particles enter the crack and help in crack propagation. This is schematically exemplified on fig 15. An example of this fatigue mechanism is shown in fig. 10 on the journal crankshaft.

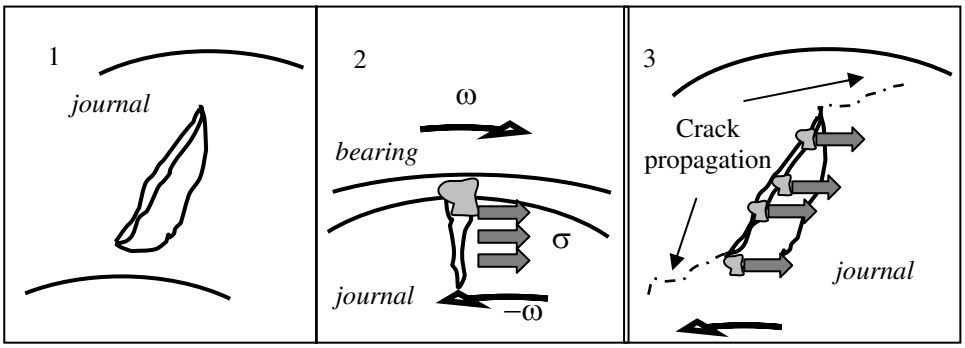

Fig. 15. *Schematic damage mechanism under abrasion fatigue after a pre-existing crack.*

Corrosion fatigue

Although nowadays it is accepted that the normal environment is very detrimental for fatigue (tests under vacuum put this in evidence) corrosion fatigue is commonly considered a fatigue process under very deleterious environments. Corrosion fatigue is a mechanical fatigue process where the detrimental environment accelerates fatigue crack growth. Corrosion fatigue is not the same as SCC - Stress Corrosion Cracking. SCC occurs even when the tensile stress level is constant. Corrosion fatigue occurs under fluctuating loads plus a detrimental environment.

Fig. 8 shows connecting rods broken by corrosion fatigue. The effect of the deleterious environment is clearly observed on the fracture morphology. A microscopic analysis shows that in most cases, due to the deleterious environment, crack propagation is mainly intergranular, as it is peculiar in corrosion fatigue [20].

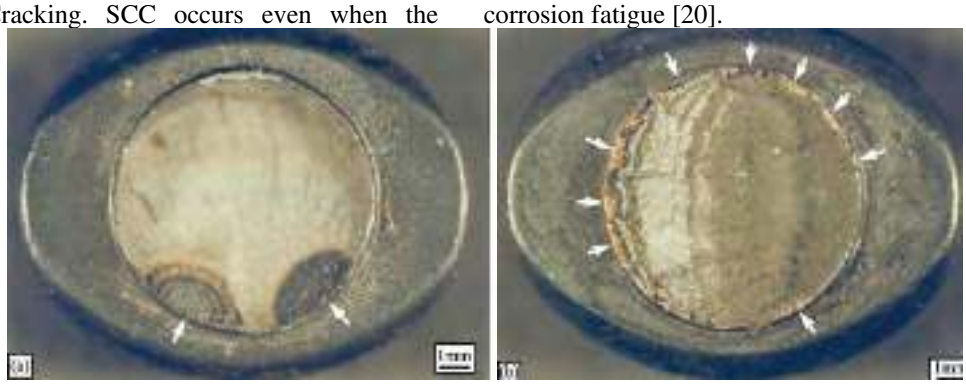

Fig. 16. *Connecting rod bolts damaged by corrosion fatigue [21]*

Hydrodynamic fatigue (liquid pressure and trapped water/oil fatigue)

The first situation where hydrodynamic fatigue may occur is when two rigid bodies exert load by means of a liquid (for example oil) and there is a pre-existing crack. The liquid inside the crack exerts opening loads on the crack surfaces promoting crack propagation. This situation is schematically presented in fig. 17.

This situation may occur, for example, in journals such as that one in fig. 10a), where some cracks induced by the grinding finishing process exist in the journal.

The oil pressure inside the crack during the normal working process of the plain bearing, promotes crack propagation.

The other situation is common under rolling contact. The crack, originated by contact fatigue, retains some liquid. When one body exerts load on one crack side the crack closes and the liquid is trapped inside the crack.

The pressure on the trapped liquid promotes crack propagation. This may happen, for example, on railway axes.

The train wheels close the cracks on the railway axes accelerating its propagation rate [22].

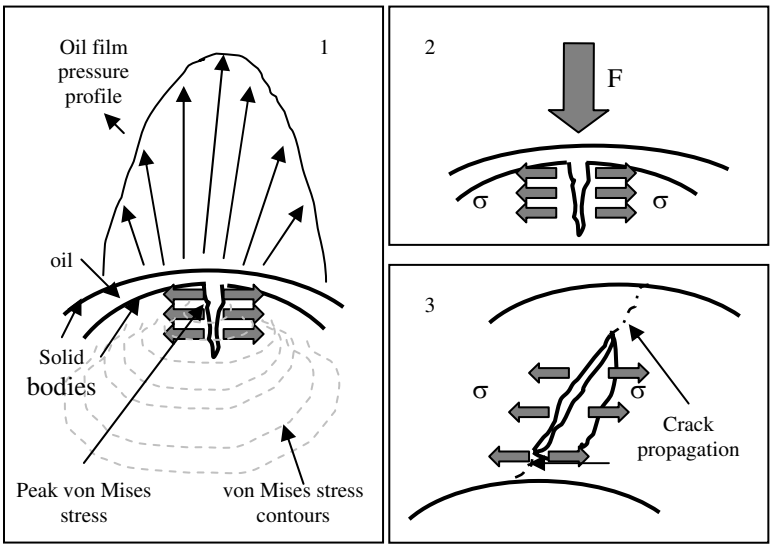

Fig. 17. *Schematic damage mechanism under hydrodynamic fatigue.*

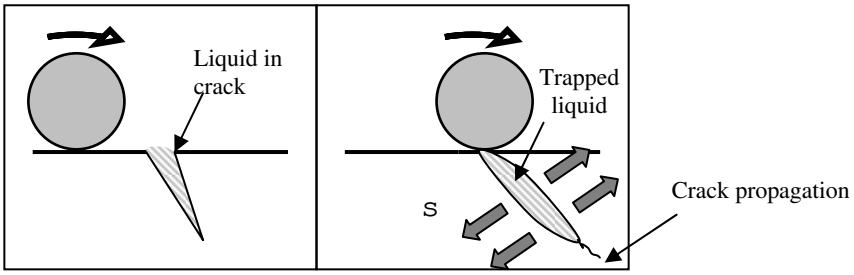

Fig. 18. *Schematic damage mechanism under trapped oil/water fatigue.*

4. Conclusions

Some different damaging mechanisms were presented in this paper.

All of them may be considered fatigue-damaging mechanisms because all of them are related to cyclic stresses or strains occurring in components that lead to initiation and growth of cracks, causing components failure. Some of the damaged components such as engine cylinder walls, propellers, etc, are sometimes not considered damaged by fatigue because the mechanisms are eventually not well understood.

The reason of this paper is to bring a deeper understanding of the basic fatigue damaging mechanisms in order to better determin the possible existence and location of damage, to prevent future occurrences, and to improve the performance of the component or structure.

The main conclusion of this work is that a better understanding of failure mechanisms may be a tool for damage assessment of structures or components.

References

[1]. ASM Handbook, 2002, "*Failure Analysis and Prevention"*, Vol. 11, ASM. Int.

[2]. Fuchs, H. O., Stephens, R. I. 1980, *"Metal fatigue in engineering"* John Wiley & Sons, pp. 2

[3]. Heyes, A. M.-1998, "*Automotive Component Failures",* Engineering Failure Analysis, Vol. 4, No 1, pp. 129-141

[4]. Fernandes, P. J. L. 1996**,** *"Tooth Bending Fatigue Failures in Gears"*, Engineering Failure Analysis*,* Vol. 3, No. 3, pp. 219-225

[5]. **Mackin, T.J., et al**, 2002, "*-Thermal Cracking in Disk Brakes*", Engineering Failure Analysis, Vol. 9, pp. 63-76

[6]. Liu X.W., Plumbridge, W.J., 2003, "*Thermomechanical fatigue of Sn–37 wt.% Pb model solder joints"*, Materials Science and Engineering A362, pp. 309–321

[7]. Silva, F.S, 2006, "*Fatigue on engine pistons – A compendium of case studies"* V.13, pp. 480-492

[8]. Klaus R., Tilmann B., Detlef L., 2003, *"Isothermal, thermal_/mechanical and complex thermal_/mechanical fatigue tests on AISI 316 L steel*/a critical evaluation"*, Materials Science and Engineering, A345, pp. 309-318

[9]. Liu F. , Ai S.H., Wang Y.C., Zhang H., Wang Z.G., 2002**,** *"Thermal-mechanical fatigue behavior of a cast K417 nickel-based superalloy"*, International Journal of Fatigue, 24, pp. 841–846

[10]. Luo J., Dong H., Bell T., 2006, *"Model-based contact fatigue design of surface engineered titanium gears",* Computational Materials Science 35, pp.447–457

[11]. Maekawa, I., 2005, "*The influence of stress wave on the impact fracture strength of cracked member*", International Journal of Impact Engineering 32, pp. 351–357

[12]. Zhang M., Yang P., Tana Y., Liu Y., Gong S., 1999, *"An observation of crack initiation and early crack growth under impact fatigue loading"*, Materials Science and Engineering A271, pp. 390–394

[13]. Osman, A., 2006, "*Failure of a diesel engine injector nozzle by cavitation damage"*, Engineering Failure Analysis, 13, 7, pp. 1126-1133

[14]. Zhang Y., Wang, Z., Cui, Y., 2000, "*The cavitation behavior of a metastable Cr–Mn–Ni Steel"*, Wear 240, pp. 231–234

[15]. Webster, G.A., Ainworth, R.A., 1994, "High Temperature Component Life Assessment", *Chapman & Hall*

[16]. Aktaa, J., Schmitt, R., 2006, *"High temperature deformation and damage behavior of RAFM steels under low cycle fatigue loading: Experiments and modelling"* Fusion Engineering and Design, in press

[17]. Silva, F.S., 2003, *"Analysis of a vehicle crankshaft failure*", Engineering Failure Analysis, Pergamon, V.10, N5, October pp. 605-616

[18]. Llanes, L., Torres, Y., Anglada, M., 2002, *"On the fatigue crack growth behavior of WC–Co cemented carbides: kinetics description, microstructural effects and fatigue sensitivity*" Acta Materialia 50, pp. 2381–2393

[19]. Hoeppner D. W., 2006, "*Fretting fatigue case studies of engineering components"* Tribology International, in press

[20]. Xuan S., Yaowu S., 2003, "*Corrosion fatigue cracking of tube coils in an actifier column catalytic cracker*", Engineering Failure Analysis 10, pp. 297–306

[21]. Lynch, S.P., 2003, "*Failures of Engineering Components Due to Environmentally Assisted Cracking*", ASM International, 5, pp 33-42

[22]. Mota, V.M.M.B., Moreira, P.M.G.P., Ferreira, L.A.A., 2006, "*Stress Intensity Factor Calculation for Inclined Surface-Breaking Cracks Initiated in an Artificial Indentation Under Rolling Contact Fatigue Using the Edge Green Functions*", 10thPortuguese Conf. on Fracture

THE ANNALS OF "DUNAREA DE JOS" UNIVERSITY OF GALATI.
FASCICLE IX. METALLURGY AND MATERIALS SCIENCE
N^0. 1 – 2008, ISSN 1453 – 083X

DECORATIVE COMPOSITE LAYERS

Olga MITOŞERIU, Florentina POTECAŞU,
Elena DRUGESCU, Maria VLAD
"Dunărea de Jos" University of Galaţi
e-mail: mihaela_potecasu@yahoo.com

ABSTRACT

Part of the materials used in the chemical industry, metallurgical, machine construction, can be coated, as with time it occurs either a decrease of its properties, or even a process of advanced faulting, because of the stresses suffered.

The paper presents the structure of some composite coatings with the nickel matrix also pointing out their decorative aspect. The layer is obtained through electrochemical methods, using as a complementary phase carbure and oxide particles (Al_2O_3, ZrO_2, B_4C, SiC) with contents of cca. 4-6%. The maintaining times in electrolyte ranged from 10 to 60 minutes.

The macro and microstructural analysis had as objectives: the exterior aspect at composite depositions; the adherence of the film deposited at the support; the width of the deposition; the film compactity; the size, shape and orientation of the grains in the deposited layer; the distribution of the disperse phase in the metallic matrix.

The microstructures of the composite films Ni+Al_2O_3 and Ni + SiC, performed in cross and longitudinal sections, reveal a dispersion relatively uniform of the aluminum oxide particles and respectively, silicon carbure in the Nickel matrix, a uniform deposition, lack of pores, a good compactity, a very good adherence at the metallic frame

KEYWORDS: exterior aspect, composite coatings, nickel matrix, electrochemical methods, complementary phase carbur and oxyde particles.

1. Introduction

The composite coatings are bi- or policomponent materials made of a matrix and a supplementary phase, and have characteristics that the initial components taken separately do not have. The composite is formed from a basic substance, an alloy or a chemical combination of a matrix and of complementary phases uniformly distributed in the matrix, as a result of a process of heterocoagulation of the phase particles on a support that needs to be protected, in the same time with their coating with the laid material that form the matrix of the composite coating. For these cases though, the bond between the coating layer and the base material has to be very stable and to correspond to some requirements. In between the layer and the base material, an interface zone is being formed, whose size can be adjusted by choosing the parameters of thermal treatment, when the processes of diffusion in contra-current are activated between the layer and the electrodeposited coating. This, besides the wished for properties, can influence the general properties of the material that was started from (e.g.: fatigue resistance).

The difference among different types of materials and composite coating lies in the hardening action on the matrix and in the loading part, taken by the component parts. A highly practical interest arises from the *composite coatings resistant to wearness and corrosion*, as a perspective for enhancing the lifetime of the parts.

Up to now, there are settlements against the interdependence structure – properties, which justifies the research done in the field.

From the analysis of the experimental data, it comes out that a considerable strengthening of the wear resistance of the metals is obtained by the co deposition of some particles formed of oxides, borurs, carburs, nitrurs (that have themselves a high wear resistance, contraction stability, maximum resistance at plastic deformation) in a metallic matrix. The particles take over the friction load and distribute it uniformly in the matrix, ease the creation of a relief that ensures an even better storage of the lubricant film and reduces the deformation and the contraction

of the metallic base. The matrix retains the disperse phase particles in the composite and, having a high plasticity and tenacity, it creates a maximum resistance at friction. The matrix has to have enough stability and hardness to present the maximum wear resistance and it has to present itself under the shape of a continuous mass, in order to protect the particles from being comminuted.

2. Experiment

Remarks on the mechanism of incorporating the particles. The complementary phases present in the coatings are incorporated during the formation of these protective layers and by the quantity and the distribution mode, can influence decisively their physico-mechanical properties.

The material interactions and the structure of the composite materials obtained for certain conditions, by the synergetic effects can realize the wished for properties.

Among the base metallic matrix (Ni, for the present case) and the complementary phases (oxides, carburs) there are quite a few combining opportunities, out of which only some of them can be taken into account, as noticed from the research done.

The mechanism of incorporating the particles during the electrochemical deposition is not yet clarified. The transportation of the particles towards the surface can be done by convection and/or diffusion, depending on the hydrodynamic conditions and on the particles' size.

The electro migration can also be important depending on the load of the particles. Particles incorporation in the coating mass can imply a physical absorption or a chemoabsortion of the particles, or electrochemical reactions of the absorbed species at film's surface. Different models have been proposed in order to take into consideration these processes [3].

As an example, Gugliemi regards the deposition process as a succession of two stages: a slow, electrochemical, absorption stage and a chemical strong one.

The physical sense of the two stages has not yet received a clear explanation, and as for the model, problems related to agitation of the electrolyte are not considered [4].

According to other authors, in the formation process of the composite films, appear the following important stages:

- the transportation of the disperse phase in the space near the electrode;
- holding these at catelectrode:
- heterocoagulation of the disperse phase particles at catelecrode;
- covering the particles with metal.

Celis and his team workers propose another mechanism of incorporating the particles that allows for the calculation of the included particles in the metallic matrix [5]. This model is described in the following lines as being valid for the codeposition of the alumina from the sulphat acid solution.

The co deposition rate of the ceramic particles in the metallic mass depends on the deposition speed of the metallic matrix and on the particles' flux existent towards the surface of the coating. The particle transportation towards the surface, which rises, is controlled mainly by convective diffusion in the case of nanometrical particles and under the cumulative effect of some convection and gravitational forces in the case of micrometric particles.

As a conclusion, the probability that the particles be retained during increasing the electrodeposited coating is dependent on its rising speed and from here on the density of the deposition current.

Depositions were obtained on a special installation with continuous agitation that ensured the maintaining of the disperse phase homogeneity in the electrolyte. For a good adherence between the support and the composite film, an intermediary layer (Nickel) was deposited on the metallic frame that ensured favorable conditions of electro crystallization for the composite film (Nickel + disperse phase).

The current density for obtaining the adherence layer was of 10-15 A/dm^2, for a period of time of 1-5 minutes.

2.1 Macro structural analysis

From the comparative analysis of the composite depositions obtained under the same conditions (figure 1), the following conclusions have been reached:

- the pure nickel layer electrodeposited on steel or copper frame presents a good compactity, a relatively fine and uniform granulation (fig. 1a);
- the composite films Ni + Al_2O_3, Ni + ZrO_2, Ni + SiC are characterized by a uniform granulation, relatively fine, a good compactity – compared to the deposition of Ni (fig 1b, 1c, 1d);
- the composite films Ni + B_4C present a coarse granulation, dendritic, with a low compactity, with large open pores (fig. 1.e.).

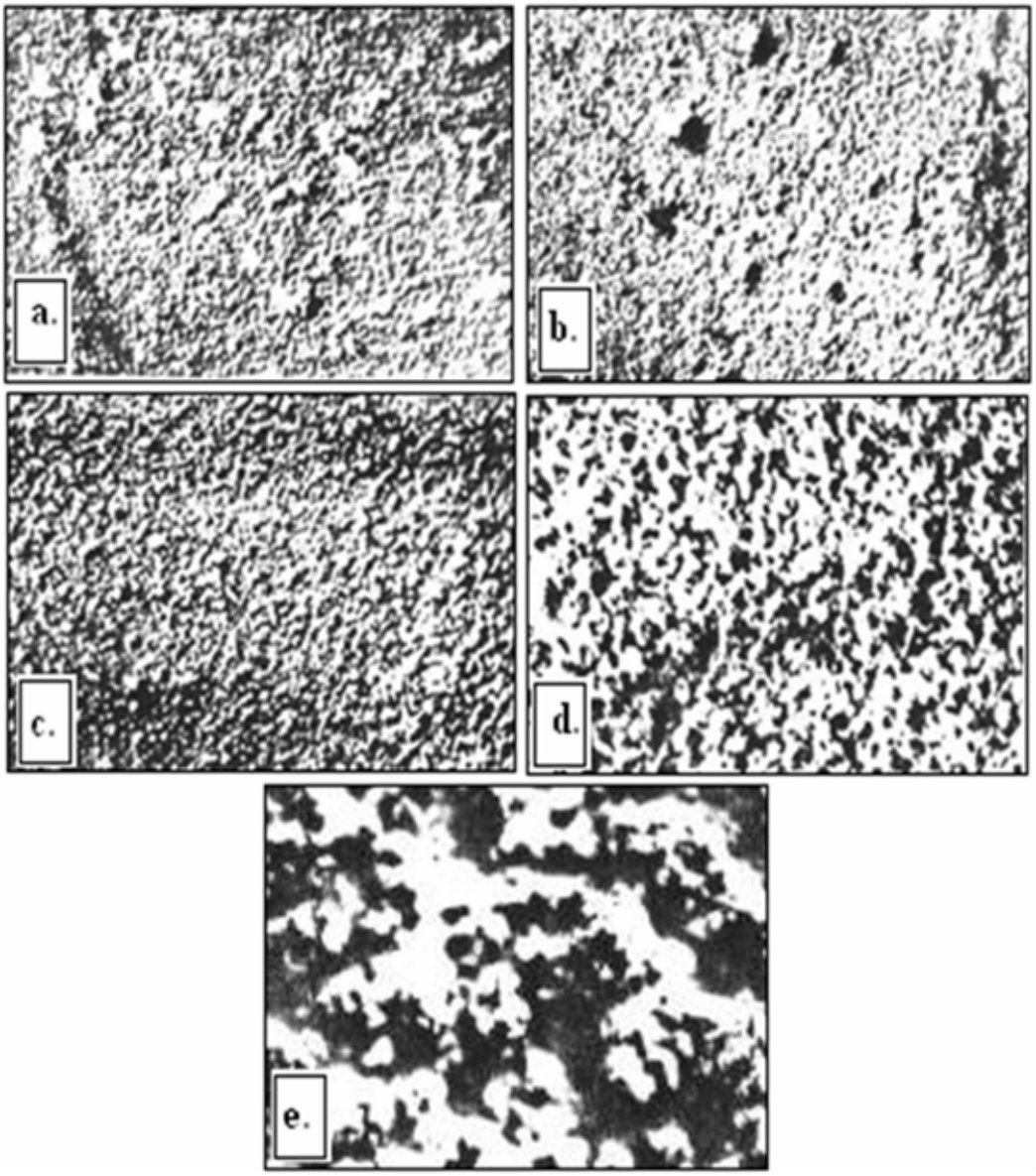

Fig.1. *Macrostructure of the peliculs electrodeposed (x 50):*
a - Ni deposition; b - Ni + Al_2O_3 composite deposition; c - Ni + CSi composite deposition;
d - Ni + ZrO_2 composite deposition e - Ni + B_4C composite deposition.

2.2 The micro structural analysis

The microstructures of the cross sections, in the analyzed samples (support + layer for adherence + composite film) have shown a very good adherence of the deposition at the metallic support (figure 2). The width and the deposition surface aspect have been highlighted, as well as the quantity and the disperse phase distribution in the width of composite deposition.

2.3 Thickness of composite deposition

Depending on the deposition period and the current density, composite films have been obtained with widths ranging from 10 to 80 μm (figure 3). Especially in the case of composite films Ni + B_4C, for widths higher than 30 μm, the aspect becomes coarse, dendritic, nonuniform.

Although the composite films Ni + ZrO_2 have a nice aspect, with a uniform deposition surface, with a fine granulation, a good adherence to the metallic frame, the microstructural analysis showed a strong unhomogenity in distribution of the Zyrconium oxyde particles in the Nickel matrix, under the shape of zonal agglomerating. This distribution can be explained by the tendency of ZrO_2 to form polymer species in water-like solutions, tendency that is growing as the environment acidity decreases.

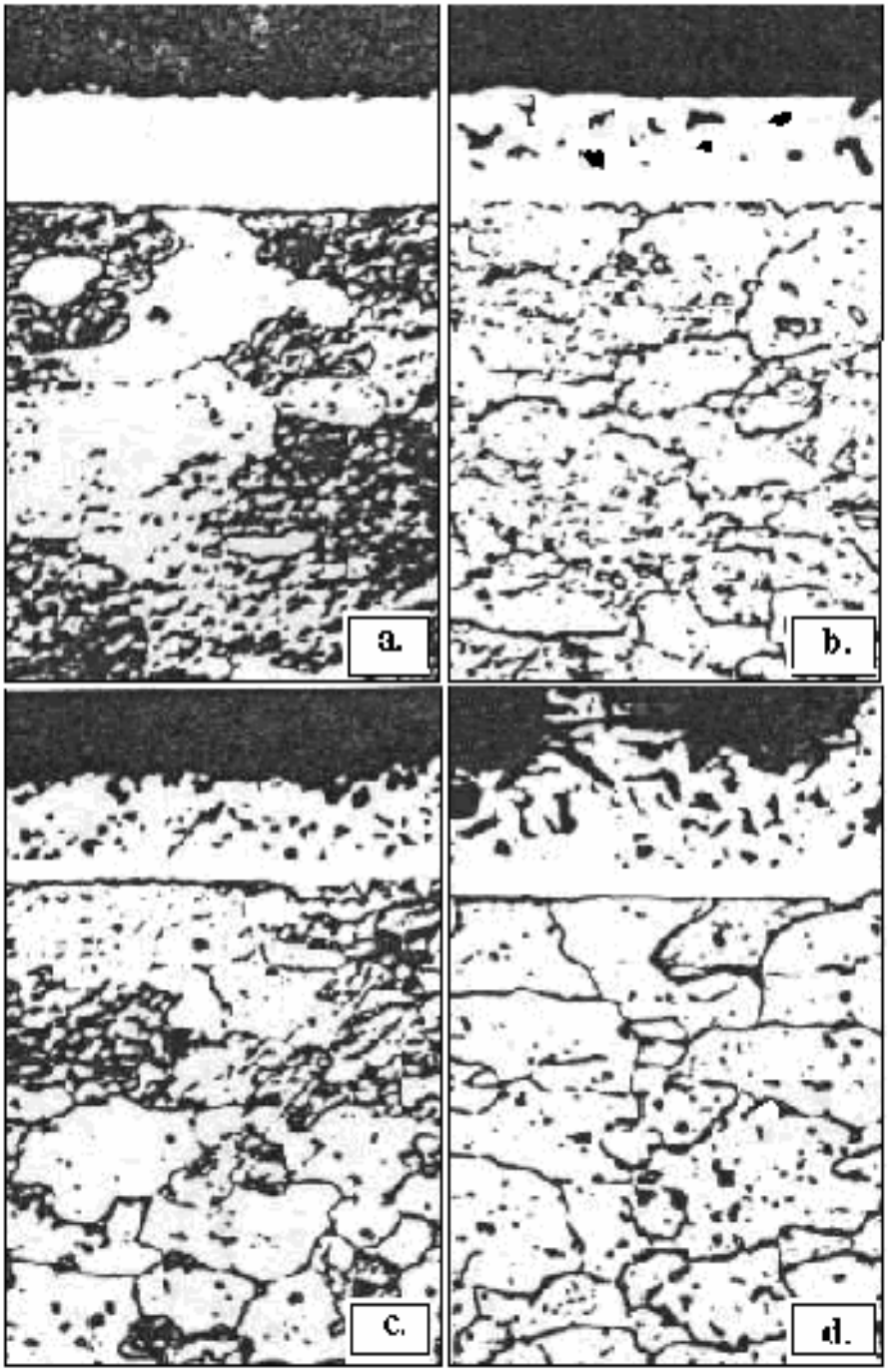

Fig.2. *The microstructure of the electrodeposited films (x 250) : a – Ni deposition; b – composite deposition Ni + Al_2O_3 ; c - composite deposition Ni + CSi; d - composite deposition Ni + B_4C.*

4. Conclusions

Depending on the deposition period and the current density, composite films have been obtained with widths ranging from 10 to 80 μm. Especially in the case of composite films Ni + B_4C, for widths higher than 30 μm, the aspect becomes coarse, dendritic, nonuniform.. The microstructures of the composite films Ni+Al_2O_3 and Ni + SiC, realized in cross and longitudinal sections, reveal a dispersion relatively uniform of the aluminum oxide particles and respectively, silicon carbure in the nickel matrix, a uniform deposition, lack of pores, a good compactity, a very good adherence at the metallic frame (fig. 2 b, 2c);

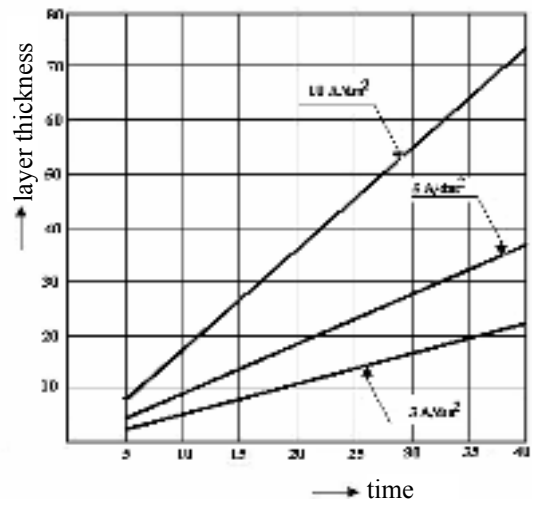

Fig. 3. *Influence of the electrodeposition parameters – current density, time on the thickness of the composite deposition Ni+ SiC*

The microstructures of the composite films Ni + B_4C, highlight when increasing the deposition period, a pore-material with non uniform indented aspect, but, with a relatively uniform distribution of the particles of boron carbide in the nickel matrix (fig. 2d).

Although the composite films Ni + ZrO_2 have a nice aspect, with a uniform deposition surface, with a fine granulation, a good adherence to the metallic frame, the micro structural analysis showed a strong unhomogenity in distribution of the zirconium oxide particles in the nickel matrix, under the shape of zonal agglomerating. This distribution can be explained by the tendency of ZrO_2 to form polymer species in water-like solutions, tendency that is growing as the environment acidity decreases.

References

[1] **G. Barkleit, A. Grahl, M. Maccagni, M. Olper, P. Scharf, R. Wagner, H. Warlimont**, 1999, *Electrodeposited, dispersion-hardened, lightweight grids for lead–acid Batteries* - Journal of Power Sources 78, p.73–78

[2] **S.R. Saifullin**, 1992, *Physical Chemistry of Inorganic Polymeric and Composite Materials*, Ellis Horwood Ltd. London, New York

[3] **J.R.Roos, J.P.Celis and M.De Dante,** 1991, *Electrodeposition of Materials and Alloys*, Materials Sciences and Technology, vol 15, p. 482

[4] **S.R.Saifullin,** 1983, Neorganiceshie Kompozitione Materiali, Izd Himia, Maskva, p 178

[5] **I.G.Haibibullin, R.A.Usmanov,** 1991, *Korrozionnaiastoicost metallov s disperno – upracinennimi pocratiami*, Moskva, Masinostrenie,

[6] **P.S.Sidky, M.G.Hocking,** 1999, *Review of inorganic coating and coating process for reducing wear and corrosion*, British Corrosion Journal, vol 34, nr 3, p 171-193

[7] **M.G.Hocking,** *In High Temperature materials chemistry*: The Charles Benjamin Alcock symposium, ed. B.C.H. Steele, 149-159; 1995, London, The Institute of Materials

[8] **D. Aslanidis, J. Fransaer and J.P.Celis,** 1997, *The Electrolytic Codeposition of Silica and Titania Modified Silica with Zinc*, Journ. Electrochem Soc. 144 (7), p. 2357

[9] **F. Potecasu**, **O. Potecasu, F. M. Braz Fernandes, V. Musat,** 2006, *Lead -Hardening by Oxide Dispersion*. Advanced Materials Forum III, 514-516 p718-722, ISSN 0255 – 5476

[10] **O. Mitoseriu, E.Drugescu, F.Potecasu, L.Benea, G.Carac,** 1998, *Composite Coatings Obtained by Sedimentation Codeposition During Copper, Cobalt and Iron Electroplating* - International Journal MATERIALS AND MANUFACTURING PROCESSES (USA), VOL XI, ISSN1042-6914, pag.417 – 422.

[11] **O. Mitoseriu, G. Filip, A. Preda, G. Carac, W. Schneider,** 2000, *The Corrosion Protection on the Composite Coatings in the Zinc Matrix with ZrO_2 and Al_2O_3* (n. 102) EMCR'2000 (CD)7th International Symposium on Electrochemical Methods in Corrosion Research, Budapest, Hungary, p.134.

THE ANNALS OF "DUNAREA DE JOS" UNIVERSITY OF GALATI.
FASCICLE IX. METALLURGY AND MATERIALS SCIENCE
N^0. 1 – 2008, ISSN 1453 – 083X

THE CONSERVABILITY OF OLD WOOD AT THE CONTACT WITH METALLIC STRUCTURAL COMPONENTS FROM ARTIFACTS

Ion SANDU[1], Viorica VASILACHE[2], Mikiko HAYASHI[3], Narcisa VRÂNCEANU[1], Adelina CIOCAN[1], Andrei-Victor SANDU[2]

[1] „Al.I.Cuza" University of Iasi, ARHEOINVEST Platform,
Laboratory of Scientific Investigation and Cultural Heritage Conservation
[2] Romanian Inventors Forum, RDI Department
[3] Ochanomizu University Tokyo
e-mail: ion.sandu@mail.dntis.ro

ABSTRACT

The paper presents the impact of metallic pieces being in contact with wood, as structural elements, used in obtaining artifacts. The paper studies, based on old samples, the reciprocal effect obtained at the wood-metal interface, the diffusion and segregation area of metallic cations in wood and the protective role of some wood volatile components on metal.

KEYWORDS: metallic cations, corrosion products; wood-metal interface, diffusion and segregation processes, protection layers.

1. Introduction

It is known that wood into an artifact is affected in time, together with the exogenous factors and a series of endogen agents and factors, related to the natural defects, quality of materials and the fabrication technology of the artifact.

Some known research work has distinguished the influence of metals on the reciprocal conservability [1]. For instance, the iron close to oak wood is conserved by the tannin from it and the wood on the other side by the Fe (II) and Fe(III) ions, even under conditions of the presence of the mushroom *Merullius Lacrymans*, which creates a tough regime for the wood degradation.

In this context, in our laboratory there are going on some studies about the influence upon some different essence of old wood bases, the preparation layer based on gyps and chalk powder and the iron nails utilized at the assembling or for hanging up.

The present work studies have been done with an electronic microscopy and a micro FT-IR for the effects of the nails and other structural elements made out of iron upon the bases of lime, poplar, fir and oak.

2. Experimental part

In these studies there were used some old wood samples from lime, poplar, fir and oak which have been influenced by the iron nails used in assamblation or for display.

The affected interfaces and zones have been analyzed by SEM-EDX and μ-FT-IR

The investigation was performed by means of a SEM VEGA II LSH scanning electronic microscope manufactured by TESCAN for the Czech Republic, coupled with an EDX QUANTAX QX2 detector manufactured by ROENTEC Germany. The microscope, entirely computer operated, contains an electron gun with tungsten filament that may achieve a 3nm resolution at 30KV, with a magnifying power between 13 and 1,000,000 X in the resolution mode, a gun potential between 200 V and 30 kV, a scanning speed between 200 ns and 10 ms per pixel. The working pressure is lower than 1x10-2 Pa. Quantax QX2 is an EDX detector used for qualitative and quantitative micro-analysis in industry, research and education, which performs quantitative measurements without using specific calibration standards. It has an active area of 10 mm^2, and it can analyze all items heavier than carbon, smooth or rough samples, thin coatings or particles, with a resolution below 1.33 eV (MnKα, 1000 cps). Quantax QX2 uses a 3rd generation Xflash detector, which does not require liquid nitrogen cooling and is about 10 times faster than the traditional Si(Li) detectors. IR absorption measurements have been performed with a FT-IR spectrometer, coupled with a Hyperion microscope, both from Bruker Optics, Germany. FT-IR spectrometer is a TENSOR 27, which is an advanced

flexible bentchtop instrument suitable for routine applications as well as laboratory research. TENSOR 27 is designed for measurements mainly in the mid – infrared region.

Fig.1. *Samples of old wood: a – oak (1820 A.D.); b – poplar (XVIII Century); c – fir (1860 A.D.); d – fir (1830 A.D.); e – poplar (XVII Century).*

The standard detector is a DLaTGS detector, which covers a spectral range from 12000 to 370cm^{-1} and operates at room temperature. The resolution is normally 4cm^{-1} but it can go up to more than 1cm^{-1} (apodized). The wave number accuracy is more than 0.01cm^{-1} at 2000cm^{-1}.TENSOR is equipped with a He-Ne laser which emits red light with a wavelength of 633nm, and an output power of 1mW. TENSOR has also a high stability ROCKSOLID alignment of the interferometer. The high throughput design ensures the highest possible signal – to – noise – ratio. TENSOR is completely software controlled, by OPUS software. The HYPERION microscope is an accessory that can be coupled to almost any Bruker FT-IR spectrometer. The software provided is an OPUS/VIDEO software for video interactive data acquisition. It can work both in transmission and reflectance modes. The detector is a MCT cooled with liquid nitrogen (-196^{0}C). The spectral range is 600-7500cm^{-1} and the measured area is optimized for a diameter of 250μm with a possibility of reaching a minimum diameter of 20μm. It is provided with a 15X objective.

3. Results and discussions

Fig. 2 presents the SEM microphotography with the two positions of the vector chosen by the analysis of the variation of the main components from the old oak wood (1820 A.D.) – metal interaction area.

From the EDX spectrum, one can point out the continuous and uniform variation of the penetration effect of the Fe oxidihydroxide (II, III) on the two directions in the preservation area of the old oak wood. Table 1 presents the average composition for the surface of the preserved area of the old oak wood by impregnation with the Fe oxidihydroxides.

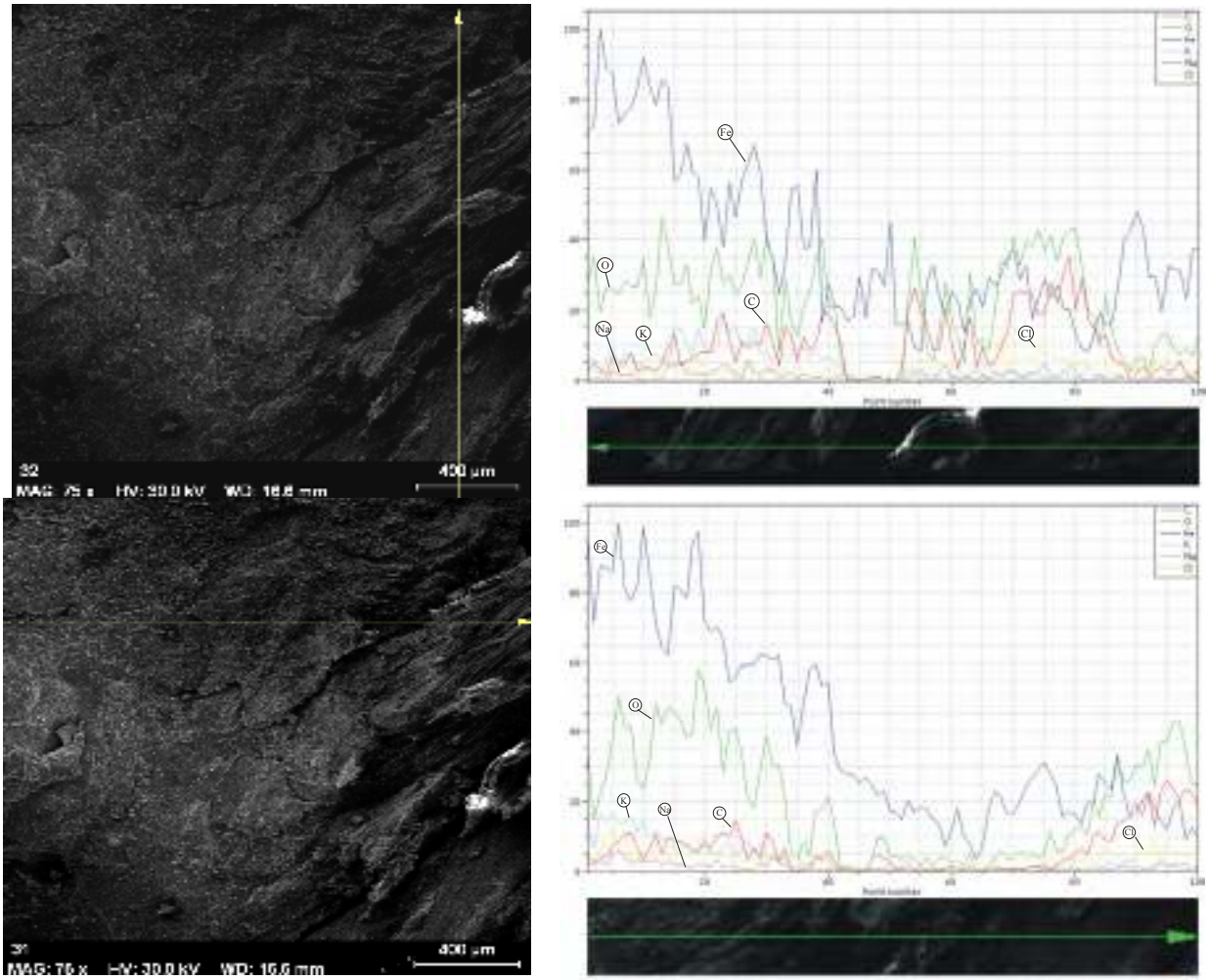

Fig. 2. *SEM Image with EDX spectra of distribution along a line on the sample from old oak wood with iron*

Table 1. *Composition on diffused structure surface: old oak wood-iron*

Element	Weight	Atomic	Error
	[%]		
Iron	48,50823	21,5885	1,315599
Carbon	3,876974	8,0227	1,491539
Potassium	2,508171	1,594433	0,121529
Chlorine	0,301288	0,211222	0,046833
Sodium	2,160776	2,33605	0,238743
Oxygen	42,64456	66,24709	5,868803
	100	100	

One can notice a very high concentration of the Fe ions (II, III). In spite of the fact that in the structure we can find the chloride anion (the main corrosion agent of iron and the most active one, a real catalyst) due to the inhibitor components from the oak wood, the iron nail has been pretty well preserved. Table 2 presents the composition of the alloy from which the nail has been manufactured (OL37). In figures 3, 4 and 5 there are shown SEM images and EDX spectra of the distribution along a line on the sample from other old wood samples with iron: fir (1860 A.D.), poplar (XVII and XVIII century).

Table 2. *Composition of the iron nail*

Element	Weight	Atomic	Error
	[%]		
Iron	95,849774	87,917083	2,664899
Carbon	0,353141	1,417842	0,558082
Silicon	0,247112	0,424298	0,059891
Phosphorus	0,186209	0,289913	0,051035
Sulfur	0,124372	0,187042	0,043107
Oxygen	3,239392	9,763822	0,884542
	100	100	

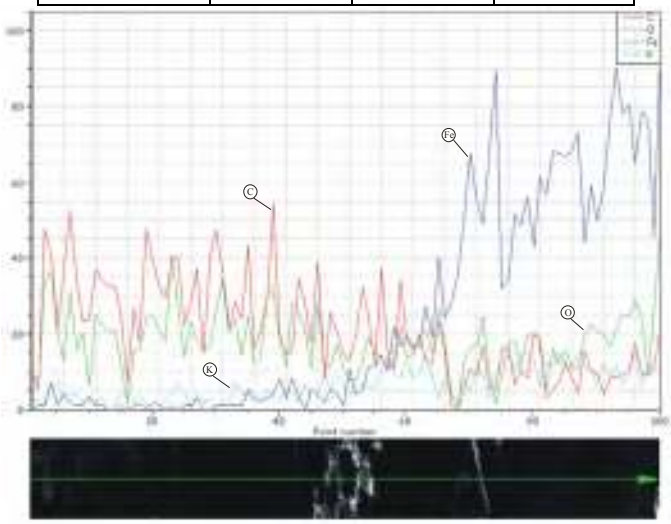

Fig.3. *SEM Images and EDX spectra of the distribution along a line on the sample from old fir wood (1860 A.D).*

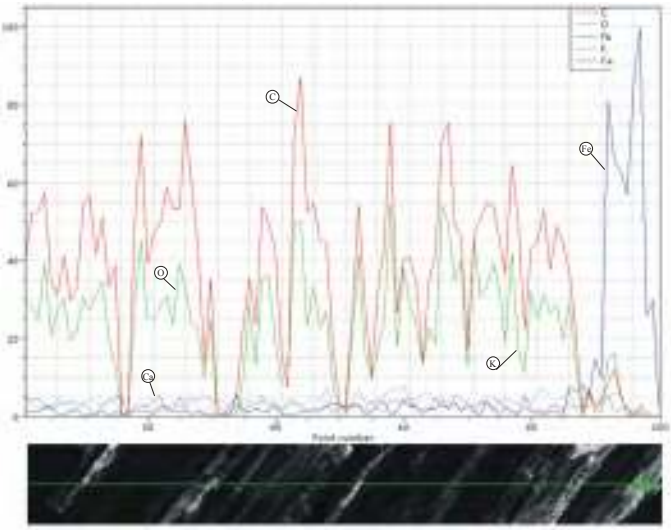

Fig.4*. SEM Images and EDX spectra of the distribution along a line on the sample from old poplar wood (XVII century).*

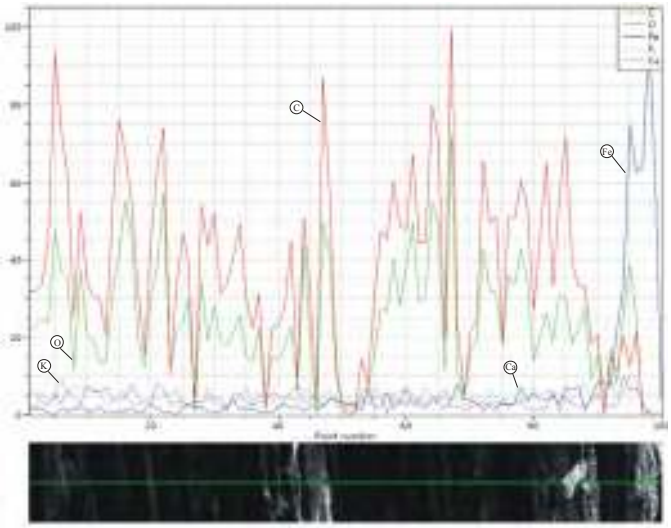

***Fig.5**. SEM Images and EDX spectra of the distribution along a line on the sample from old poplar wood (XVIII century).*

From these figures one can observe the capacity of penetration in time of the iron ions, which is different depending on the wood species, which interacts in a different way with the metal. If in the case of oak it is observed a reciprocal conservability wood-metal, due to the complex system of the coordination compound tanin - Fe (II, III) on the contrary in the case of fir and poplar it doesn't observe the same phenomenon due to the acidity of the wood increases with time.

In figures 6, 7 and 8 are shown the EDX spectra and the chemical composition.

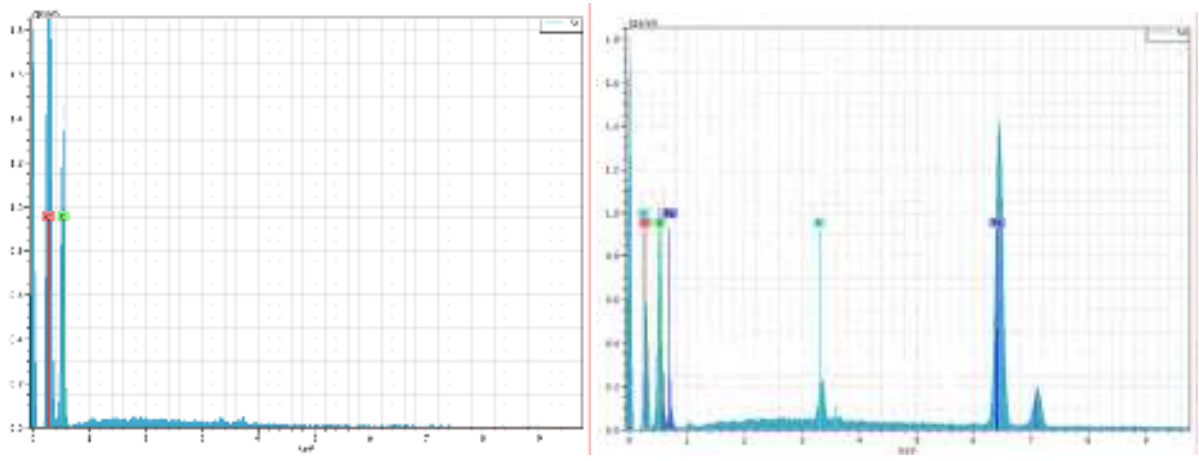

a **b**

Area of pure wood			
Element	**Weight**	**Atomic**	**Error**
	[%]		
Carbon	20,89	26,02	6,68
Oxygen	79,11	73,98	26,13
Total	100,00	100,00	

Area of the wood penetrated by iron ions			
Element	**Weight**	**Atomic**	**Error**
	[%]		
Carbon	10,22	17,80	1,92
Oxygen	51,80	67,67	6,91
Iron	35,94	13,44	0,85
Potassium	2,04	1,09	0,09
Total	100,00	100,00	

***Fig. 6**. EDX spectra and the chemical composition for the old fir wood (1860 A.D.): a – area of pure wood; b- area of the wood penetrated by iron ions.*

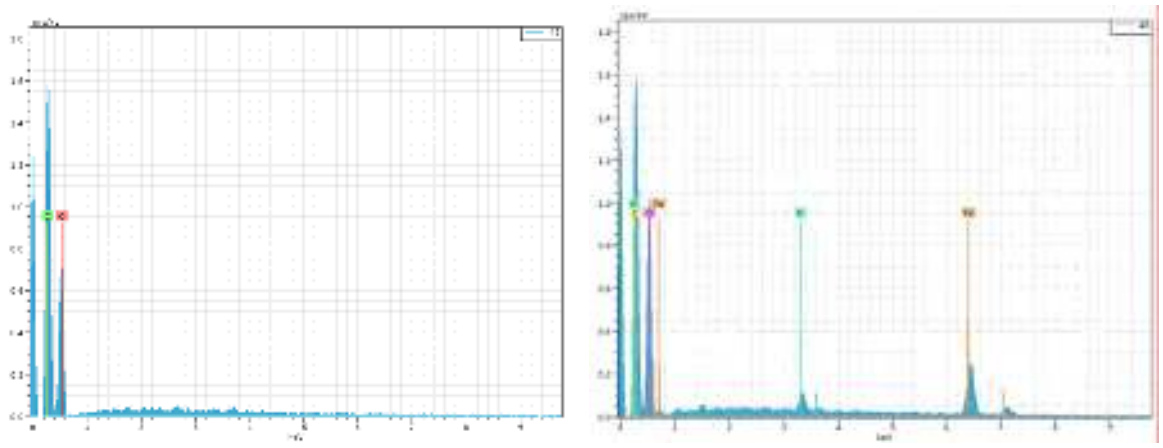

a **b**

Area of pure wood			
Element	**Weight %**	**Atomic %**	**Error %**
	[%]		
Carbon	20,47	25,53	6,60
Oxygen	79,53	74,47	26,52
Total	100,00	100,00	

Area of the wood penetrated by iron ions			
Element	**Weight %**	**Atomic %**	**Error %**
	[%]		
Carbon	17,60	23,18	7,29
Oxygen	75,67	74,80	25,05
Iron	5,81	1,65	0,21
Potassium	0,92	0,37	0,07
Total	100,00	100,00	

Fig. 7*. EDX spectra and the chemical composition for the old poplar wood (XVII century): a – area of pure wood; b- area of the wood penetrated by iron ions.*

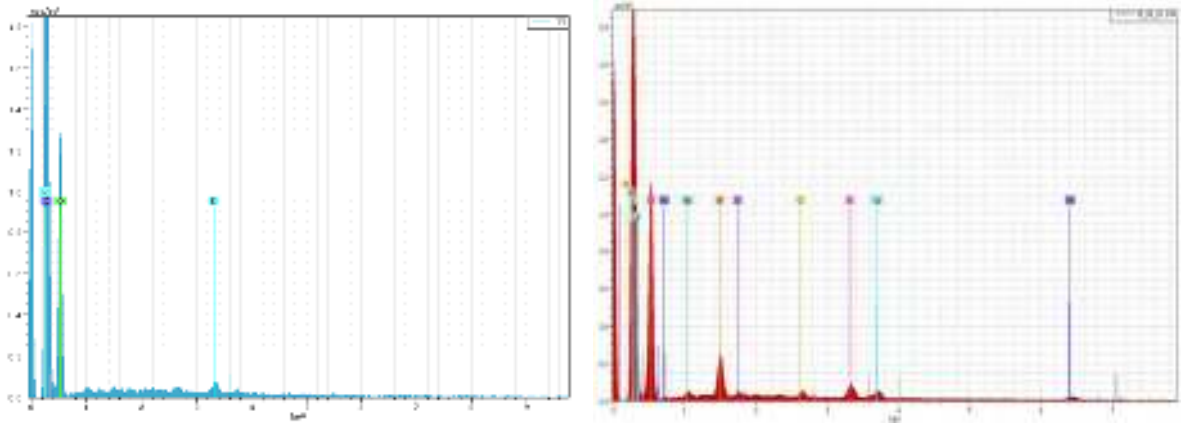

a **b**

Area of pure wood			
Element	**Weight**	**Atomic**	**Error**
	[%]		
Carbon	19,84	24,99	7,08
Oxygen	78,83	74,49	26,20
Potassium	1,33	0,52	0,10
Total	100,00	100,00	

Area of the wood penetrated by iron ions			
Element	**Weight**	**Atomic**	**Error**
	[%]		
Carbon	20,08	25,42	7,85
Oxygen	77,64	73,78	25,37
Iron	0,81	0,22	0,06
Potassium	1,26	0,49	0,07
Chlorine	0,21	0,09	0,04
Total	100,00	100,00	

Fig. 8*. EDX spectra and the chemical composition for the old poplar wood (XVIII century) a – area of pure wood; b- area of the wood penetrated by iron ions*

In the figure 9 there are presented μFT-IR spectra obtained with a poplar old wood sample which had an iron nail in it. The spectra were background corrected using a gold mirror which doesn't absorb IR radiation. The spectra were averaged over 64 scans for more precise results. It can be observed from the spectra of the four areas: not contaminated by iron ions; the area in contact with iron nail; the area in contaminated/decontaminated limit; the contaminated central area, that there are slight differences between the group vibrations from 2950 – 2900 cm^{-1}, 2150-2000cm^{-1}, 1750-1600cm^{-1} and bigger differences in the domain of 900-600cm^{-1} which represents the contribution of iron ions in the penetration area.

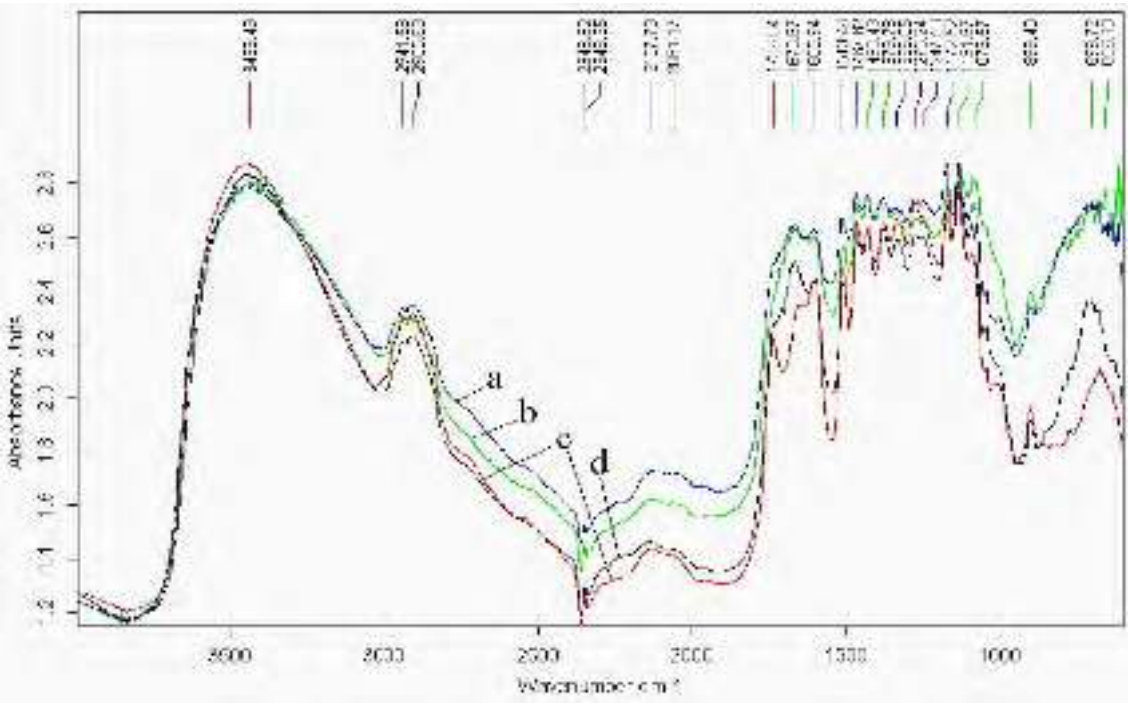

***Fig. 9**. μ-FT-IR spectrum for poplar old wood (XVIII Century):*
a – not contaminated by iron ions; b – the area in contact with iron nail;
c – the area in contaminated/necontaminated limit; d – the contaminated central area

4. Conclusions

In this paper the SEM-EDX and μ-FT-IR techniques have shown the way of interaction between iron and wood used in artefacts depending on time, with the impact upon the reciprocal conservability.

If the oak wood, due to tanin which forms with the iron ions coordination compounds, increases the capacity of dispersion and penetration and offers a reciprocal conservability, in the case of fir and poplar wood, the volatile compounds through degradation become compounds which decrease pH leading to the acceleration of the corrosion processes, and the compounds hard soluble from the wood-metal interface play the role of a membrane difficult to be penetrated by the iron ions in case of poplar wood and very porous for fir wood, Fe ions penetrating easily the wood along their fibers.

References

[1]. Sandu I., Hayashi M., Quaranta, M., Bejinariu C., Stanciu C., Sandu I.C.A., Vasilache V., 2007, *The study of metal – old wood interactions under the influence of pedological factors*, Advanced Technologies and Materials UGALMAT 2007, „Dunărea de Jos" University of Galaţi, p. 350-355

[2]. Sandu I., Hayashi M., Sandu I.C.A., Vasilache V., Stanciu C., Sandu A.V., 2007, „*Implication of the sem-edx technique in the study of old wood*", Advanced Technologies and Materials UGALMAT „Dunărea de Jos" University of Galaţi, p. 345-349

[3]. Sierra-Alvarez R., **Process Biochemistry, 42**, 5, 2007, p. 798-804

[4]. Rakotonirainy M.S., Caillat L., Heraud C., Memet J.B., Tran Q.K., 2005, Journal of Cultural Heritage, 8, 2, 2007, p. 160-169;

[5]. Li X.S., Englezos P., Journal of Colloid and Interface Science, 281, 2, p. 267-274;

[6]. Dominkovics Z., Danyadi L., Pukanszky B., 2007, Composites Part A: Applied Science and Manufacturing**, 38**, 8, 2007, p. 1893-1901;

[7]. Bjordal C.G., Nilsson T., Petterson R., Journal of Archaeological Science, 34, 7, p. 1169-1177;

[8]. Selwyn L.S., Rennie-Bisuillion D.A., 1993, Studies in Conservation, 38, p. 180-197.

THE ANNALS OF "DUNAREA DE JOS" UNIVERSITY OF GALATI.
FASCICLE IX. METALLURGY AND MATERIALS SCIENCE
N^0. 1 – 2008, ISSN 1453 – 083X

SURFACE HARDENING FOR LOW CARBON STEEL (A3k) BY YAG: Nd PULSE LASER THERMAL ACTIVATION

Nelu CAZACU[1], Liliana SAVA[2], Sorin DOBROVICI[1], Adolf BACLEA[3]
[1]Dept.of Metallurgy and Materials Science, Dunarea de Jos University of Galati, Romania,
[2]Unita VIG, Bucuresti, Romania,
[3]Socomar SRL, Sorento, Italy
e-mail: Nelu.Cazacu@ugal.ro, Sorin.Dobrovici@ugal.ro

ABSTRACT

The paper is based on experiments for surface hardening on A3k (low carbon steel) samples using YAG:Nd pulse laser. A small x-y moving system conducted by PC was made for sample scanning, relative to fixed focused laser beam. Laser energy, frequency and defocused, influences were studied. The results of laser/sample surface interactions were investigated by macrostructure and microstructure analyses. Hardness testing was used for evaluating the changes in surface properties.

KEYWORDS: surface hardening, steel, laser, YAG:Nd

1. Introduction

Surface treatment of metals (surface modification, surface engineering, and case hardening) is subdivided into two distinctive directions: deposition and diffusion techniques. Deposition techniques are characterized as transporting a substance from a source and depositing it onto the surface of metal (electroplating, thermal flame spray PVD, CVD, etc.) [8]. Diffusion techniques are usually named thermo chemical and thermal treatment. Thermo-chemical treatments (nitriding, carburizing, carbonitriding, nitrocarburizing, boronizing) are characterized as diffusing an element or many elements, into the surface of the steel by the application of the appropriate amount of heat, time, and the steel surface catalytic reaction, [8]. Thermal techniques are those that modify the surface phases of steel containing sufficient carbon to allow the transformation from austenite to martensite when the appropriate amount of heat is applied to the immediate surface. This is sometimes known as phase hardening and is applied to processes such as flame, laser, induction, and electron beam [8]. Surface hardening of steels is generally based on energy transfer and/or mass transfer (interactions) with material and exterior media. Because interactions are conducted only at surface, structure modifications are generated and properties modifications will be obtained.

This is thermal hardening of metals and alloys that is based on local heating of a surface under the influence of exterior heating system and subsequent fast cooling of this surface [1]. Surface hardening of steels by thermal interactions consists in formation of an austenite structure at a stage of heating and its subsequent transformation in martensite in a stage of cooling [1]. Temperature and time are more important factors and these appear for all surface treatments.

Temperature influence is localized at material surfaces for high values and time for short values. At surface hardening by induction treatments, electromagnetic field energy is localized at material surface (increasing local energy) and after heating, water spray is used for decreasing local energy. Cooling speed has a primary influence on structure and properties.

2. Experimental conditions

Lasers are complex systems which transform electric energy to radiation and have a very important property: higher control of characteristics. In these conditions, surface treatments using laser radiations have a high precision and are used for small surface operations.

For experiments, it was used a pulse laser system KVANT 17 (C.I.S.) based on two YAG:Nd ($Y_3Al_5O_{12}$) units [3].

Basic applications of this system are ceramic cutting and micro welding of different materials.

Some important technical characteristics are:

- active media: 6,3 mm diameter, 100 mm long;
- glass composition: $Y_3Al_5O_{12}$;
- wave length 1,06 μm (IR);
- pulse time 2…5ms;
- pulse frequency 1…20 Hz;
- objective focused 50 mm;
- trace diameter 0,3…1,3mm;
- pulse energy min. 8J.

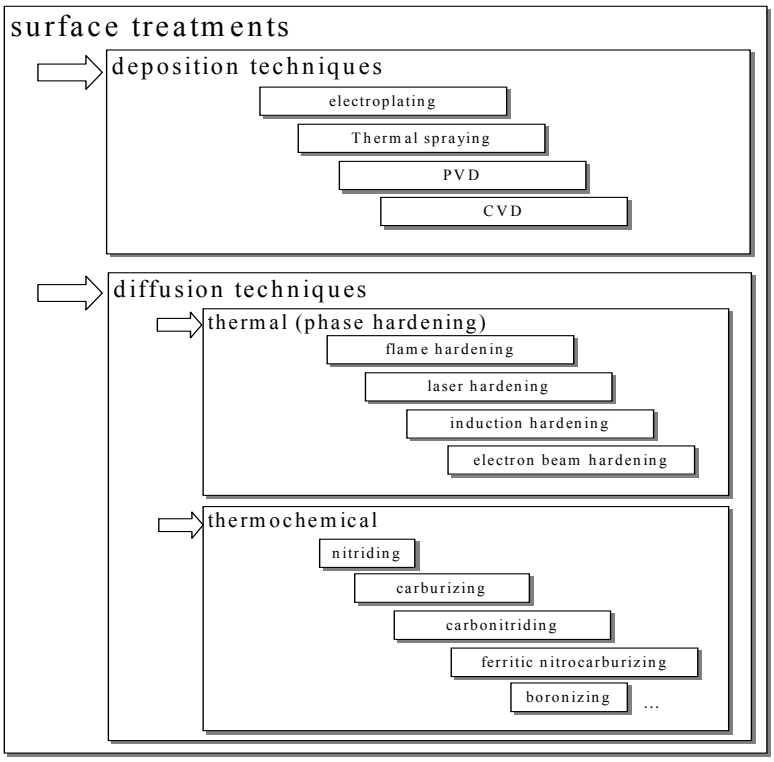

Fig.1. *Principal technique for surface treatments of metals.*

Table 1.*Experimental conditions and results*

No.	Working supply	Defocalisation	Hardness (HV_5)						
			d1	HV1	d2	HV2	d3	HV3	HVm
UM	V	mm	mm	daN/mm^2	mm	daN/mm^2	mm	daN/mm^2	
1	550	5,0	0,308	98	0,298	104	0,293	108	103
2	600	5,0	0,270	127	0,263	134	0,275	123	128
3	600	7,5	0,287	113	0,288	112	0,279	119	114
4	650	5,0	0,242	158	0,227	180	0,227	180	173
5	650	7,5	0,267	130	0,267	130	0,267	130	130
6	650	10,0	0,274	124	0,289	111	0,274	124	119
7	700	5,0	0,234	169	0,233	171	0,234	169	170
8	700	7,5	0,241	160	0,249	150	0,241	160	156
9	700	10,0	0,272	125	0,267	130	0,272	125	127
10	750	10,0	0,251	147	0,259	138	0,251	147	144

Fig.2. *Pulse laser system KVANT 17 (working module, supply and command module and technological module*

Fig.4. *Sample and technological xy system*

Fig.3. *Working module of KVANT 17 system*

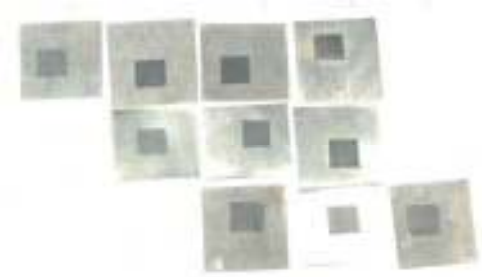

Fig.5. *Hardening surfaces on A3k samples arranged by laser energy and defocused*

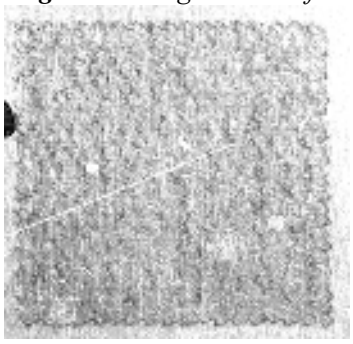

Fig.6. *Surface macrograph for sample no.5 600V/7,5mm/ 0,3Hz).Magnitude 5x.*

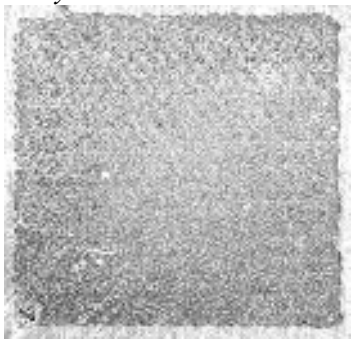

Fig.8. *Surface macrograph for sample no.9 (700V/10mm / 0,3Hz). Magnitude 5x.*

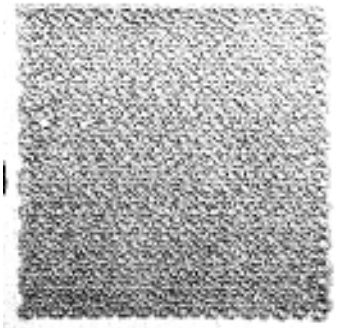

Fig.10. *Surface macrograph for sample no.3 (650V/5mm/ 0,3Hz). Magnitude 5x.*

Fig.7. *Surface macrograph for sample no.7 700V/ 7,5mm/ 0,3Hz). Magnitude 5x.*

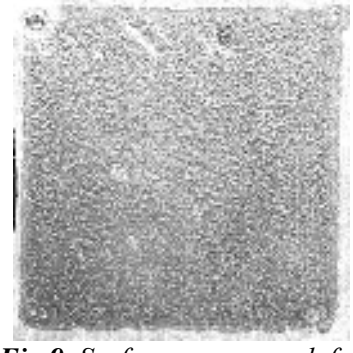

Fig.9. *Surface macrograph for sample no.10 750V/10mm/ 0,3Hz). Magnitude 5x.*

Fig. 11. *Surface macrograph for sample no.4 (700V/5mm/ 0,3Hz). Magnitude 5x.*

***Fig.12**. Surface micrograph (350x) for sample no.1 (550V/5mm/0,3Hz) Magnitude 150x*

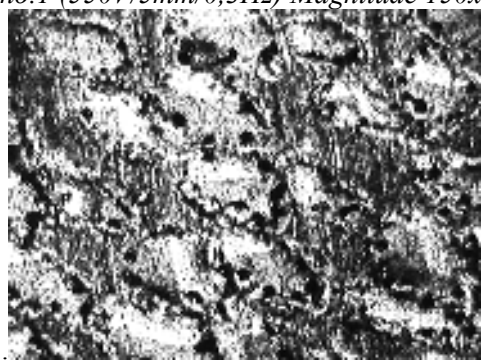

***Fig. 13.** Surface macrograph (350x) for sample no.2 (600V/5mm/0,3Hz). Magnitude 150x*

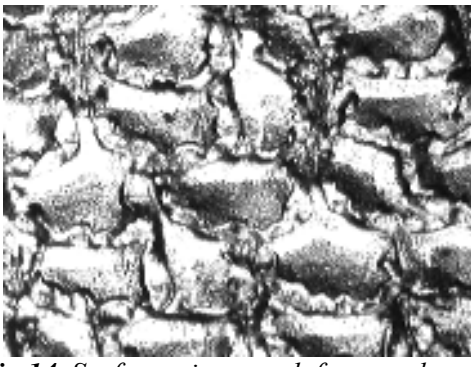

***Fig.14**. Surface micrograph for sample no.3 (650V/5mm/0,3Hz). Magnitude 150x*

***Fig.15**. Surface macrograph for sample no.4 (700V/5mm/0,3Hz Magnitude 150x*

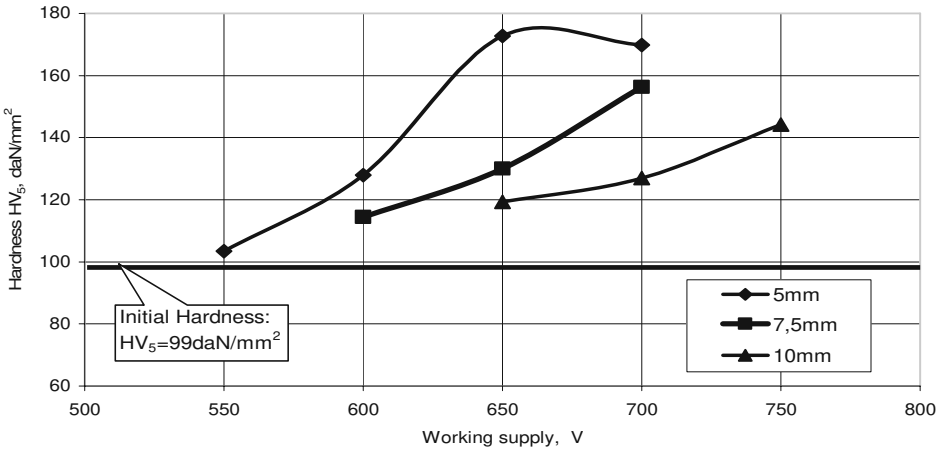

***Fig.16.** Hardness variation on the sample surface after pulse laser hardening.*

3. Results and discussion

The sample surfaces were relatively scanned by laser beam and *sample surface/laser pulses* interaction was present. In function of pulse energy, pulse frequency and defocused, surface interaction appears and has a specified macroscopic aspect (***Fig.6 …Fig.11***). Macroscopic analyses for A3k representative steel samples are showing in (***Fig.12 …Fig.15,** Magnitude 150x*).

Thermal zone influence is visible in ***Fig.12*** and the energy is insufficient for local quenching, [0]. By increasing the laser energy, the traces are larger and surface modifications is present (***Fig.13).*** If energy increasies a local melting is present that conduced to a major modifications on surfaces and to local quenching from melt steel (***Fig.14…Fig.15***). Hardness testing (HV_5) was used for evaluating surface properties modifications (***Table 1***).

4. Conclusions

By increasing defocused, specific energy on the interaction surface decreases and hardness is lower. If pulse laser energy increases, the hardness increases too, but the quenching process is limited by the melting phenomenon. For all regimes, a hardness increasing with 50%... 80% was measured in conditions when A3k steel has < 0.1%C in its chemical composition. The applications of YAG:Nd pulse laser are recommended to very small surfaces, because of the lower efficiency of laser (2…5%), [7].

References

[1]. Ganeev R. E., 2002, *Low power hardening of steels*, Journal of Materials Processing Technology 121 414-419
[2]. Popescu N., 1990, *Tratamente termice neconvenţionale*, Editura tehnică, Bucureşti pag.223…245
[3]. Samoila C., Ionescu M.S., Drugă L., 1986, Tehnologii şi utilaje moderne de încălzire, Editura Tehnică, Bucureşti, pag.291…360
[4]. Ursu I., Mihăilescu I.N., Prokhorov A.M., Konov V.I., 1986, *Interacţiunea radiaţiei laser cu materialele*, Editura Academiei, Bucureşti
[5]. Donţu O., 1985, *Tehnologii de prelucrare cu laser*, Editura Tehnică, Bucureşti
[6]. Savin Gh., 1981, *Laseri*, Editura Facla
[7]. De Kock J., 2001, *Lasers Offer Unique Heat Treating Capabilities*, Industrial Heating, oct. Laser Machining Inc., Somerset, Wis.

THE ANNALS OF "DUNAREA DE JOS" UNIVERSITY OF GALATI.
FASCICLE IX. METALLURGY AND MATERIALS SCIENCE
N^0. 1 – 2008, ISSN 1453 – 083X

ON THE CORROSION RESISTANCE OF Cu – Mo COMPOSITE MATERIALS OBTAINED BY PVD METHOD

V.G. GRECHANYUK[1], N.I. GRECHANYUK[2], L.ORAC[3],V.A. DENISENKO[1]
[1]Universitatea Nationala de Arhitectura si Constructii, Kiev
[2] Science National Academy of Ucraina
[3]"Dunărea de Jos" University Galaţi
e-mail: lucia_orac@yahoo.com

ABSTRACT

The Cu – Mo composite materials have been obtained by electron flow vaporizing followed by vapor –phase condensing. Researches have shown that corrosion resistance in wet environment varies with the content of molybdenum, working conditions and composition of the corrosion medium. The corrosion resistance of the composites has been studied by gravimetric method.

KEYWORDS: composite materials, PVD method, corrosion resistance, gravimetric method.

1. Introduction

One of the main causes of the limitation to the use of materials for electrical contacts free of Ag or other nobel matals, is the fast corrosive damage when operating in wet environment.

The composite materials of Cu-Mo have been obtained by simultaneous vaporising, from separate crucibles, of copper and molibden followed by the vapor flow condensing on a steel OL-37 sublayer, preheated up to 700 ±20 °C.

Copper and molibden ingots have been used as initial materials obtained by vaccuum electron flow remelting.

The condensate obtained as plates of 0,7 - 1,2 mm thickness have been used for the study of corrosion resistance [1].

The corrosion resistance is related to the formation and decay of the working surface films. Film formation is facilitated by the arc discharges when contacts are switched. The films formed on the contact working surface may be of organic or inorganic origin.

The main causes of film formation are the vapors and gases of organic and inorganic origin to be found in the environment, and the active chemical components of the contact material, which help the chemical reaction to take place with oxides and other combinations.

2. Experiment

The materials studied in this paper have been obtained at the Research and Production Center (CCP) „GEKONT", Vinitza, with the device UE-189 manufactured by the Electrical Welding Institute E.O. Paton of the Ukranian ASS.

For the purpose of establishing whether the contacts made from Cu-Mo composite materials obtained by electron flow vaporising and vaccuum condensing in closed air environment are suitable, researches have been focused on the study of corrosion resistance by gravimetric methods.

The gravimetric researches of Cu-Mo condensates have shown that the corrosion resistance depends on the chemical composition of the condensate materials. Introducing up to 5% molibden in the Cu -matrix has no influence on the corrosion resistance of the Cu-Mo composite material as compared with the pure copper.

With higher Mo concentrations (up to 12%) a decrease in the corrosion resistance can be noticed (approx 20%), which will limit the use of materials for Cu-Mo electrical contacts in oxidating environment [2]. T

The corrosion resistance has been studied by gravimetric method on samples immersed into tap water and distilled water. Measurements have been made on 10 samples simultaneously, every 20 h, for 100 h.

3. Results and discussions

The researches on the corrosion resistance in neutral media/environments show that, with higher concentrations of molibden in Cu-Mo condensates, there is a considerable decrease in the sample weight, which implies a lower corrosion resistance (table 1).

Table 1. *Weight loss in Cu-Mo samples containing a variable Mo content after 100 h corrosion tests.*

Content of Cu	**Content of Mo**	**Distilled water Dm**	**Tap water Dm**
[%]		mg/m^2	
100	-	0,04	0,09
98,9	1,1	0,08	0,1
97,7	2,3	0,1	0,11
95	5,0	0,13	0,14
89	11	0,64	0, 49

As shown in the Table above, the most significant changes of weight take place with Mo concentration higher than 5 %.

Such a phenomenon is accounted for by the structure of this composite material which determines the corrosion process progress/development according to an electrochemical mechanism. In accordance with the Cu-Mo equilibrium state diagram, within the concentration interval, these are not miscible in liquid nor in solid state, and their reciprocal solubility at 900 °C is very low. The disperse phase fails to interact with the matrix or to produce solid solutions or chemical combinations, i.e, Cu-Mo compositions are heterogenous systems having the matrix made from the main material – copper- into which a hard dispersed allowance (molibden) which does not dissolve into matrix at normal and high temperatures, is introduced. In contact with the neutral electroconductive environment, such as water, a multi-electron system is formed, consisting of a Cu cathod and a Mo anode. Since molibden is an active metal, it passes into the medium, which results in lower sample weights. This is also confirmed by the corrosive medium analysis performed after 100 h corrosion tests. The Mo concentration in corrosion medium increases with higher concentrations of molibden in composites (table 2). The increase in the copper ion concentration in the corrosion medium is accounted for by the balanced progress of the processes.[3]

Table 2. *The analysis of the corrosion medium after 100 h tests*

Composition		**Medium**							
Cu	Mo	**Tap water (initial state)**		**Tap water (after 100 h tests)**		**Distilled water (initial state)**		**Distilled water (after 100 h tests)**	
		Content Mo^{3+}	Content Cu^{2+}	Content Mo^{3+}	Content Cu^{2+}	Content Mo^{3+}	Content Cu^{2+}	Content Mo^{3+}	Content Cu^{2+}
		[mg/l]							
98,9	1,1	0,31	3,22	0,35	5,45	0,16	1,29	0,22	2,58
97,7	2,3	0,31	3,22	0,38	5,37	0,16	1,29	0,37	2,57
95	5,0	0,31	3,22	0,47	5,39	0,16	1,29	0,77	2,55
89	11	0,31	3,22	0,78	5,38	0,16	1,29	1,33	2,61

The values of the corrosion weight indices, calculated from the gravimetric researches, increase with tap water from 0,008 g/(m^2 · an) for a Mo concentration of 1 % to 0,048 g/(m^2 · an) for Mo concentration of 11 %, which is confirmed by lower corrosion resistance of the latter.

Mention must be made, that for molibden 5 % concentration the values of the corrosin weight index, 0,0082 g/(m^2 · an) are slightly different from its values for the pure copper 0,0079 g/(m^2 · an).

The depth of the surface corrosion damage increases with higher Mo concentration in the system, especially at concentrations higher than 5 % Mo (fig. 1). Considerable variations can also be noticed in the thermal stability of the Cu-Mo condensates when the Mo content increases. Thus, at Mo concentrations of 11 % the oxidation process velocity reaches up to 0,51 mg/min, as compared with the pure copper – 0,16 mg/min., while the sample weight increases from 0,45 % for pure copper , up to 4,88 % for the condensates featuring a Mo content of 11 %.[4,5].

The increase in the oxidation velocity and sample weight because of high Mo concentration in the system results in lower thermal stability of the condensate (table. 3).

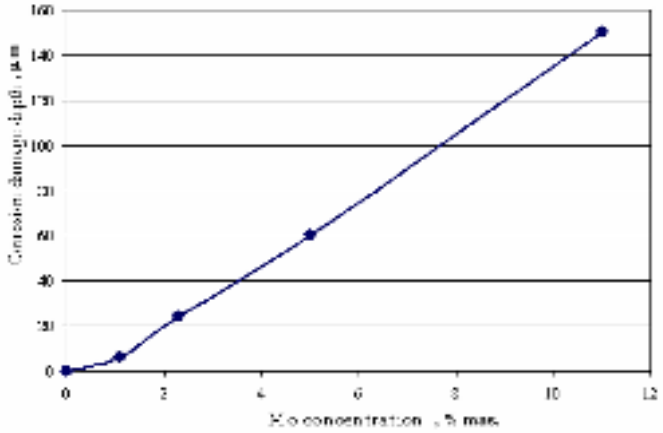

Fig. 1. *Influence of Mo concentration on corrosion damage depth.*

Table 3. *Thermal characteristics of the Cu-Mo condensate system*

Composition		**Temperature of initial oxidation, stage 1**	**Temperature of initial oxidation, stage 2**	**Oxidation velocity stage 1**	**Oxidation velocity stage 2**	**Weight variation at 600 °C**
Cu	Mo					
[%]		[°C]		[mg/min]		[%]
100	-	370	698	0,16	0,21	0,45
98,9	1,1	350	470	0,24	0,22	1,0
97,7	2,3	350	590	0,37	1,07	1,85
94,6	5,6	335	460	0,54	1,56	2,78
89,0	11	335	460	0,51	1,76	4,88

The researches carried out have shown that, after corrosion tests are perfomed in wet environment, on the surface of the Cu-Mo composite materials the line separating the sectors attacked by corrosion from perpendicular to the sublayer plan is a prevailing feature (fig. 2, *a*).

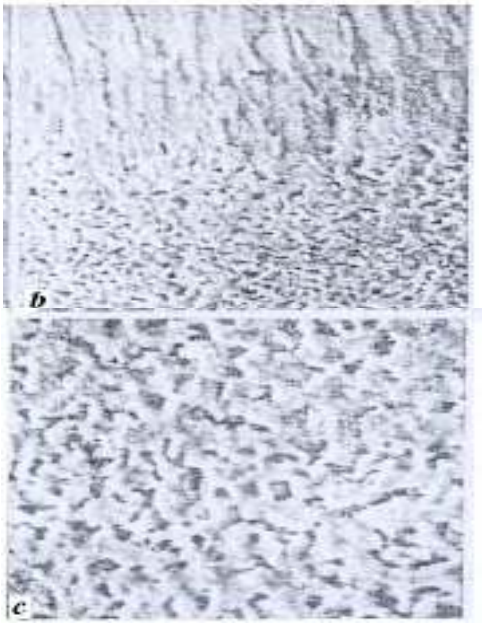

Fig. 2. *Structure of the composite materials Cu-Mo: a – initial condensate; b – after the corrosion tests; c – corrosive layer.*

After performing the corrosion tests (fig. 2, *b*, *c*), the limit separating the condensate layer attacked by those free of corrosion becomes obvious (fig.2). For the initial Cu-Mo condensate material, the crystal lamelar pattern corrosion from the corrosion-free area can be clearly seen.

The pitting formation is related to the fact that in the Cu-Mo condensates, upon contact with the wet environment, the electrochemical corrosion takes place along with the dissolving of the more active metal – molibden. The latter has much more affinity to oxygen and that is why in liquid/wet medium higher oxides of MoO_2 and MoO_3, are formed, their existence being confirmed by x-ray method. These oxides have protection effect and the Mo oxidation process develops because it is more likely for MoO_3 to form than the cathod limit of the Mo passive state to occur. The corrosive attacks penetrate deeper into the samples. Upon getting far from the solution-surface layer separating limit, the Mo valence in its combinations with oxygen decreases [6,7].
Within the surface layers pitting sectors can be seen, and when the amount of Mo increases, the corrosion attack depth increases, too.

4. Conclusions

The researches have shown that in Cu-Mo condensate materials in neutral medium, the corrosion processes take place according to the electrochemical mechanism.

Condensates where Mo concentration does not exceed 5 % feature better corrosion resistance.

The thermal stability decreases when Mo is introduced into the copper matrix, and large variations are noticed with Mo concentrations over 5 %.

In order to use Cu-Mo condensate as electrical contacts, taking into account the anticorrosion research results and the thermal variations, it is but reasonable to recommend compositions of approx. 5 % Mo concentrations.

References

[1]. B.A.Movcian, V.A.Osokin, L.V. Pusecinicova, N.I. Grechanyuk.,1991, *Electronno-lucevoe isparenie i condensatia medi cerez vannu-posrednic*, Probl. spet. electrometallurghii., Nr. 3, pp. 58-61.

[2]. N.I. Grechanyuk, V.A. Osochin, I.B. Afanasiev, 1998, *Electronno-lucevaia tehnologhia polucenia materialov dlia electriceskih contactov*, Electriceskie contacta i electrode, Sb. Tr. – Kiev: IMP NANU, pp. 51-66.

[3]. I.N. Grechanyuk, V.G. Grechanyuk, V.G. Roudenko, T.N.Sviridova, 1999, *Razrusenie compozitionnogo materiala Cu-Mo-Y-Zr v vodnah sredah, Electriceskie contacta i electroda*, Kiev, Nauk. Masli, pp. 125-134.

[4]. M.I. Grechanyuk, V.O. Osokin, I.B. Afanasiev (2002). Compozitionnai *material dlia elecriceskih contactov i sposob ih proizvodstva*, *Pat. 34875* Ukraina. MPK C23C/20 , Bul. Nr.12.

[5]. V.G.Grechanyuk (2004). *Sravnitelinaia otenca corrozionnoi stoikosti compozitionnah materialov na osnove medi v razlicinah usloviah* Electriceskie contacta i electroda, Kiev: Institut problem materialovedenia im. I.N. Frantevicia NAN Ukraina pp. 38-41.

[6]. S. Constantinescu, L. Orac, 2007, *Characterization of steels in terms of their phisical and mechanical properties,* Buletinul Institutului Politehnic Iasi, Tomul LIII (LVII), Fasc. 3, ISSN 1453 – 1690, pp.32 - 40.

[7]. S.Constantinescu, O. Mitoseriu, L. Orac, 2007, *Influence of manufacturing technology on chemical and structural homogeneity of X60 steel,* Tehnomus XIV Tehnologii si Produse Noi in Constructia de Masini, Suceava, ISSN 1224 – 029X, pp.267- 272.

THE ANNALS OF "DUNAREA DE JOS" UNIVERSITY OF GALATI.
FASCICLE IX. METALLURGY AND MATERIALS SCIENCE
N^0. 1 – 2008, ISSN 1453 – 083X

XRD ANALYSIS IN FRONT OF A CORROSION CRACK TIP

C. GHEORGHIEŞ, S. LEVCOVICI, V. PĂUNOIU, L. GHEORGHIEŞ, C. OANCEA, I. OSTACHE, P. ALEXANDRU
"Dunarea de Jos" University of Galati, Romania
email:cgheorg@ugal.ro

ABSTRACT

During exploitation of the heat exchangers some damages can appear in the contact region between the gaskets and the stainless steel walls. The studies upon the material were performed using SEM microscopy, X-ray diffractometry and the finite element method. The obtained data allow the explanation of the complex damage mechanism of the heat exchanger wall. Following our research, the manufacturing technology of the heat exchangers was changed and this way the rebuts were eliminated. The performed research is based upon physical methods and the damage mechanism of the heat exchanger plates is explained by means of the physical phenomena that appear and develop during working conditions.

KEYWORDS: stainless steel, structure, corrosion, crack, SEM, XRD.

1. Introduction

The aim of our research was to study the causes that led to the deterioration by cracking of the heat exchanger plates from some power stations. According to their technical documentation, the SCPW0.35 heat exchanger plates have a working temperature span between -10 degrees Celsius and + 150 degrees Celsius, at a maximum pressure of 1.6 MPa. The supplier of the product doesn't give any information concerning the material and its manufacturing technology. This is contrary to the data that other producers give concerning the material they used to make similar products, such as Alfa Laval Thermal (producing AISI 316, AISI 304, AISI 316L). The lifespan mentioned for their products in their documents is about 30 years. The beneficiary of the SCPW 0.35 products found out that the effective work regime of them agrees with the one specified by the producer, keeping into account that the primary agent didn't surpass 120^0 C and 4 bar pressure. Working into steps, the temperature difference between the primary and the secondary agent from the heat exchanger is sensitively smaller than working separately. The chemical composition of both the primary and the secondary agents was in normal limits. Cracks appeared without exception at the inlet of the primary agent (hot water) in the exchanger, in areas below the tightening gasket, there where no one expects to have any mechanical overstress.

This is why it was necessary to conduct a deep study of both the material and the technology used for the making of SCPW 0.35 heat exchanger plates. The steps of our study are: a computer simulation of the technological process of drawing of the plates, thus finding out the residual tensions following the plates' processing. It also studied on the computer the possible development and propagation of cracks due to purely mechanical causes, meaning the residual tension forces from processing. It is studied what happens to the plates when they are processed by cold plastic deformation, by taking into consideration the elastic turning back of the material (the so-called spring back). Then, we performed the chemical composition of the material, a metallographic analysis, a microhardness analysis and X-ray diffraction fine structure analysis [1], by comparing our results with some aspects concerning the corrosion under stress process. The investigated samples were taken from its proximity, but also from unaffected areas situated at the inlet of the secondary agent. The study will be continued by analyzing the behavior of the material of the heat exchangers made by other firms, maybe on samples taken from semi fabricated, before processing, in order to make comparisons and to give recommendations to the makers.

2. Computer simulation

The general simulation [2, 3] is called "the method of the finite element" and it is capable of a three-dimensional study of deformations.

It consists of more steps:

1) the geometrical profiles for both the die-block (the underlining plate), for the underlining punch and for the semi-fabricated plate used for deformation are generated.

2) all the generated elements are divided into a finite number of small parts.

3) the simulation parameters are introduced like the geometrical model and some specific parameters. 4) the simulation is performed and conclusions are drawn concerning the three-dimensional distribution of the values of several important physical parameters.

There are two deformation models for the analysis of the pressing process, a simplified one and a complex one. According to the simplified model, a small area of the sample is analyzed, such that the shape of the semi fabricated is a plane plate and the basic geometrical elements are a rib and a circular area corresponding to the corner where the breaking appears. The geometrical elements of the complex simulation model consist of 24 ribs placed symmetrically around the circular area where the tightening gaskets are placed. This is the area where the cracks appeared. The shape of the semi fabricated is now circular, with an inlet that is close to the shape of the corresponding area of the real semi fabricated used to make the heat exchangers.

Before starting the simulations we made measurements in order to determine the precise shapes and sizes of the profiles that form the piece, especially into those areas where the cracks appeared. According to these measurements we could establish the coordinates of the points of a characteristic profile, containing the ribs and the areas where the in-between plates gaskets are placed.

The specific parameters used for the simulation were:

1) 0.11 friction coefficients between the semi-fabricated and the active elements;

2) 5.5 mm punch run, according to the depth of the gasket's place;

3) We considered a hypothetical hardening curve of the material because we didn't have a sample of the initial semi-fabricated material from which we could get an experimental curve of this kind;

4) The other data referring to the material, such as the Poisson coefficient, the density and the modulus of elasticity where taken equal to the ones for steel.

We can see in figure 1 the complex geometrical model in the simulation position. After an 80 hours running program, we could get a complex simulation, starting with 2500 elements and finishing with 67852 elements because of the automatic remaking of the finite elements net.

This model offers a better approach to the real plastic deformation than the simplified one.

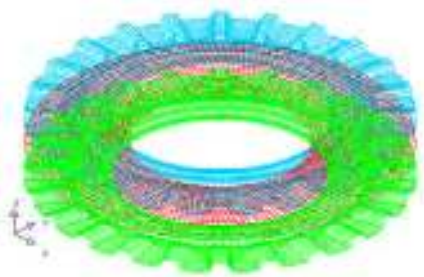

Fig.1 *The complex geometrical model in the simulation position*

Its results are shown in the following maps with specifically colored scales.

In figure 2 we can see the lack of uniformity of the thickness of our processed material. Even so, the thickness variations are rather small.

Fig. 2. *The thickness variation of the material*

The variation of the radial tension is presented in figure 3.

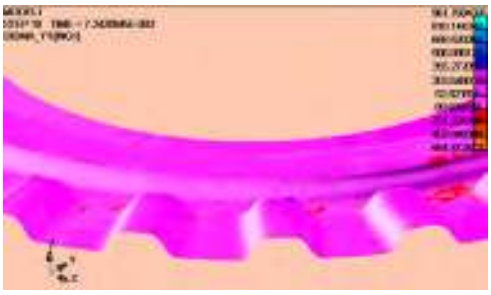

Fig.3*. The variation of the radial tension*

According to the values obtained for the radiate tensions, disposed perpendicular to the cracks, we could conclude that as it is normal, stretching tensions around 300 MPa appear at the edge of the gaskets' area, close to the outlet, in the middle of the material. In the lower part, the tensions are also of stretching type, with the same kind of values. In the upper part we have compression tensions, so that a bending effect emerges. The normal circumferential tensions are compression-type on the entire thickness and breadth of the fixing gaskets' area.

We came to the conclusion that the stress state for an individual element is close to a pure shearing state,

with a tangential tension close to the modulus of radiate and circumferential tensions. So, there is a possibility that cracks appear in a zigzag shape, such as we could really notice at a close exam of the affected areas.

The distribution of the Von Mises flow tensions is presented in figure 4, according to the Von Mises flow criterion, when the plastic state is attained if the value of the flow resistance surpasses the value given by the next formula:

$$\sqrt{2}\cdot\sigma_c = \sqrt{(\sigma_1-\sigma_2)^2+(\sigma_2-\sigma_3)^2+(\sigma_3-\sigma_1)^2} \qquad (1)$$

where σ_1, σ_2, σ_3 are the normal principal tensions and σ_c is the flow limit of the material [1].

Fig. 4. *The distribution of the Von Mises flow tensions*

From this last simulation it was concluded that the tensions that appear during the deformation process cannot represent a real cause for cracking of the heat exchanger plates [2, 4].

3. The experimental analysis of the cracked plates

The samples used for the metallographic and diffraction analysis were taken both from the cracked area, where the hot fluid enters and also from the uncracked areas, corresponding either to the exit of the hot fluid, either from the circulation of the heated fluid [5, 6].

Fig. 5. *Uncracked area of the heat exchanger*

It is interesting to notice that cracks appear every time at the inlet area of the hot thermal agent (the hottest area) and also on the plane portion of the rib that serves as the place for the tightening gaskets between the neighboring plates.

We can see clear corrosion traces of the piece's surface on the cracked area. These traces do not appear on the rest on the surface, which is also in contact with the same working fluid.

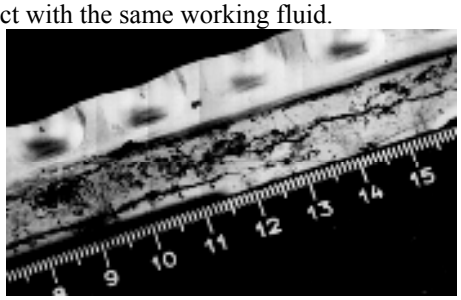

Fig. 6. *A cracked area of the heat exchanger*

The drawing of the samples was done by manual blade cutting such that the influence of the samples' detachment to be minimum. It was noticed that cutting the samples in the cracked area leads to the breaking of the surface in almost distinct pieces, even though cracks cannot be seen on the sample. This phenomenon was noticed even when drawing the samples from the very proximity of the cracked area, proving that the material was much more affected by cracks than it can be observed with the naked eye. A simple strain made by friction of the saw blade's cutting edges in these areas leads to the breaking into pieces of the surface. This aspect wasn't noticed when drawing samples from the uncracked (uncorroded) corners. We used the same drawing method of samples destined for metallographic and X-ray diffraction analysis. The results of our analysis are as it follows.

3.1 Chemical analysis

The determination of composition was performed by spectral method on the samples taken from the uncorroded part of the plate analyzed. The chemical composition of the investigated material is presented in table 1 according to the chemical analysis bulletin, emitted from the Mix Foundry Laboratory of MITTAL STEEL Company Galati, Romania. The niobium content was also checked by chemical analysis, according to the trial report, emitted from the Central Laboratory – MITTAL Steel Company Galati, Romania.

The thermal treatment recommended by STAS 3583-80 is hardening from 1050^0 C until 1100^0 C, followed by cooling in air, oil or water.

The chemical analysis points out that a stainless steel unstabilized with titanium or niobium being unstable in sulfur environments and having an oxidation temperature of 800 degrees Celsius of AISI 304 type (12NiCr180 STAS-ISO 3583-80 mark) for pieces used in corrosive media is recommended.

Table 1. *Chemical composition of samples*

	Analyzed material			
	Elements	Sample	AISI 304	
Chemical composition [%]	C			
	Mn			
	Si			
	P			
	S			
	Al			
	Cu			
	Cr			
	Ti			
	Ni			
	V			
	W			
	Nb			

3.2. Metallographic analysis

As it can be seen in figure 7, the samples were included in a teeth-type of acrylate in order to analyze them in cross-section. We prepared the samples for analyzis by buffing, polishing and electrolytically attacking them in a 50 % solution of nitric acid.

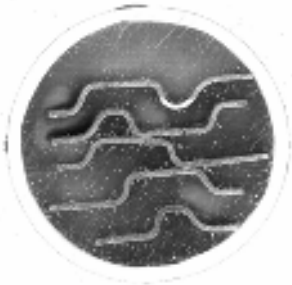

Fig. 7. *Sample preparation for metallographic analysis*

We performed the metallographic analysis at × 100 and ×500 increases, on the Neophot microscope, from the Material Science Laboratory of "Dunarea de Jos" University of Galati. This analysis on the polished samples proved the presence of more nonmetallic inclusions distributed into rows along the rolling line. We could also see in the samples some plastic formations of sulphures (see fig.8).

The electrolytically attacked samples have a microstructure made of thin austenitic grains with 8-point granularity, according to STAS 5490-80, with thin inter-grain precipitates of carbides (See fig. 9 and 10).

Fig. 8. *Nonmetallic inclusions*

Fig. 9. *Transcrystalline crack (attacked sample; 500 ×)*

Fig. 10. *A crack and nonmetallic inclusions (500 ×)*

3.3. Microhardness analysis

The microhardening analyses were performed in the cross-section of more cracked areas of two metallographic samples with different degrees of plastic deformation [7]. The samples were taken both from the crosscut direction and the planar faces of the rib where the gaskets are placed (see the sketch from below, in fig. 11). During the cold plastic deformation there is a high degree of deformation in the cross-rib, while in the plane-face of the rib the deformation is lower. We determined the $HV_{0.1}$ Vickers microhardness [daN/mm^2], at 100 grams load, according to STAS (ISO) 7657-78, at a PMT3-type of microhardness device from the Material Science Laboratory, as above. We found out at one of the samples the microhardness at 0.05 mm distance from the surface of the metal sheet, on its outline, in order to observe the hardening of the fibers that were stretched or compressed during the plastic deformation process. In figure 11 we present the values of the $HV_{0.1}$ Vickers microhardness in daN/mm^2 and the measuring points of the microhardness [8].

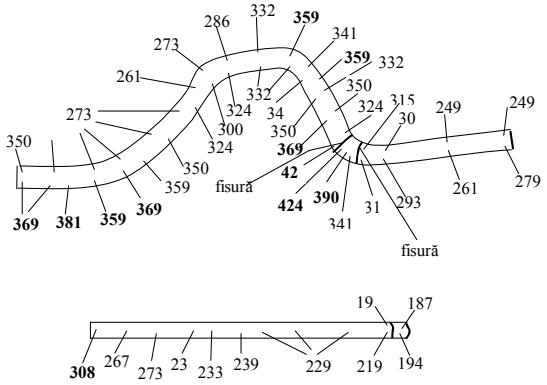

Fig. 11. *The experimental variation of the Vickers microhardness in diverse points.*

The characteristics of the sample with a complex profile and high degree of cold plastic deformation made for the relatively big pieces are as it follows:

1) The microhardness is relatively high compared with the one of the sample with a simpler profile.

2) The maximum hardness in the neighborhood of the cracks begun on the stretched fiber of the profile indicates the hardening is an encouraging factor for cracking.

3) During the cold plastic deformation of the plates' profile, the stretched fibers have a higher hardness than the compressed fibers. These stretched fibers are areas preferred for the cracks to begin.

4) The left edge area is hardened during the cutting of the initial metal sheet from which the heat exchanger plates were made.

5) The right edge area of the sample that breaks during use is softened because of the relaxation of the breaking tension forces.

The sample with a lower degree of plastic deformation during plates' making has a much lower microhardness. This fact proves both the relaxation of the stress state in the neighborhood of the cracks and the growth of the microhardness in the cold plastically deformed area.

The concerning literature[2] indicates that the global hardening results, during the cold plastic deformation (rolling and/or drawing) of the austenitic stainless steel, because of several special factors:

1) partial change of the austenite to martensite;

2) hardening of the formed martensite.

The elasticity limit of the steel is raised from 30 daN/mm^2 to 100 daN/mm^2 by a 50 % metal covering at ambient temperature of a stainless steel with 18 % Cr and 8 % Ni. Thus, the steel becomes less able to be processed by cold plastic deformation.

4. Theoretical aspects concerning the corrosion process

It was studied the electrochemical corrosion and the corrosion under mechanical stress of the heat exchangers' material.

4.1. Electrochemical corrosion and the influence of the microstructure upon it

The potential difference from a galvanic cell with electrochemical corrosion [9, 11] can be generated by a variety of causes that produce the heterogeneity of the metallic material or that of the electrolyte, such as:

1) differences between the chemical composition between the anode and the cathode;

2) differences in the state of residual or applied stress forces;

3) differences in the chemical composition of the electrolyte. According to these causes, the corresponding galvanic cells with electrochemical corrosion are classified into 3 classes: composition cells; elastic distortion cells and concentration cells, respectively.

At the heat exchanger plates, the chemical analysis shows an allied steel type AISI 304. External producers like Alfa Lava Thermal use for the heat exchanger plates both the 304 AISI steel for less aggressive media, and 1316 AISI steel with <0.08 % C; <2 % Mn; maximum 0.03 % S, maximum 0.045 % P, 16 – 18 % Cr; 10 – 14 % Ni and 2 – 3 % Mo. Meanwhile, ZILMET uses the 316L AISI steel, with carbon content less than 0.03 percent.

The 304 AISI steel doesn't contain molybdenum that has an increased role of corrosion resistance into wet media, into reducing agents and into chlorine media. Also, the low quantity of nickel from the steel of 8.24 % compared to minimum 10 % at 316 or 316L steel marks, decreases both the corrosion resistance into non oxidizing or weakly oxidizing media and the heat resistance of the steel.

The 304 AISI steel has higher carbon content than the 316L AISI steel. This favors, in the absence of enough Ti or Nb as stabilizing elements (Ti=5×C; Nb=10×C), a higher sensitivity to the apparition of carbides into the austenitic structure.

The microstructural analysis shows an inaccurate elaboration because of the observed big quantity of nonmetallic inclusions.

Because the exploitation temperature under 150^0 C doesn't lead to the precipitation of the carbides, we are probably talking about an unfit or absent thermal treatment of solving the carbides.

The presence of carbides and nonmetallic inclusions increases the chemical heterogeneity of the steel and its sensitivity to the apparition of the galvanic composition cells.

A worse condition for the corrosion is the local cover with corrosion products (rust or weak adherent oxides), because these products limit the access of oxygen. Thus, the covered metallic material becomes anodic and corrodes more and more. This is a pitting-type of corrosion and has the effect of a drastic cut-off of the lifetime of the metallic construction compared to the general corrosion that is characterized by the loss of weight.

In the case of the heat exchanger plates, the constructive solution of the exchanger activates a galvanic cell of differentiated aeration because of the aeration difference between the portion of the plate that is covered nonadherently with the gaskets, and the free surface that is in contact with the fluid. Thus, the visual and the microscopic analysis showed that the cracks began near the gaskets and then propagated into the area covered by the gaskets. There is also a potential difference due to the concentration difference between the primary and the secondary fluid on the two faces of the plate because of their different temperatures and pressures. The covering with cathodic products as rust of the face that is in contact with the hot fluid and also of the access area of the hot fluid in the exchanger is a consequence of the activity of a differentiated concentration cell of the electrolyte.

4.2. Corrosion under mechanical stress

Mechanical stresses that act over a metallic material from a corrosive medium can be: a) tension forces due to external forces implicated in the functioning conditions; b) residual tensions of mechanical, thermal or structural type that appear during the fabrication process (plastic deformation, thermal treatment, welding) or during exploitation (local plastic deformations, temperature variations in the materials with high anisotropy of the thermal dilatation coefficient).

The corrosion under stress takes place in weakly corrosive chemical media and under relatively small mechanical tensions. Thus, for a stainless steel type Cr-Ni-Mo, the risk of corrosion under stress is eliminated if the tensions are kept below 30 % from the flow limit.

The heat exchanger plates contain even from the making process an inhomogeneous state of internal tensions and they are in contact with fluids containing chlorine, which favors the corrosion under stress. We observed at the microscope that the heat exchanger plates present a pitting corrosion of initiation of the trans-crystalline cracks that are specific to corrosion under stress. The developed cracks also prove the evolution of the pitting corrosion and of the branching of the initial crack.

Most cracks begin near the gasket and then propagate into the planar area of the placing position of the gasket, with small tensions, which leads to the conclusion that this corrosion under stress was activated simultaneously with the action of the differentiated aerated cell. Also, the structural inhomogeneities (such as the presence of carbides and the nonmetallic inclusions) of the internal tension field and also the concentration inhomogeneities of the electrolyte (primary and secondary fluids with different temperatures and pressures) have favored the supplementary production of galvanic cells of composition, elastic distortion and of concentration-type, respectively [10].

Because of this complex stress, the 304 AISI steel isn't useful from the chemical composition and from the elaboration point of view, which led to a drastic decrease of the lifetime of our product (the heat exchanger plates).

The corrosion under stress appears at the austenitic stainless steels at the contact area between the steel and the chloride solutions, even at very low concentrations (> 5 ppm chlorine ions) and with very small tension forces. Thus, an austenitic steel type 18Cr – 10Ni suffers a high cracking corrosion in 50 ppm NaCl solutions, at 80^0 C, under tensions smaller than 1.5 daN/mm^2. This phenomenon is also fed by the continuous evaporation of the solution that increases the local chloride concentration and by the thermal shocks that locally destroy the passivating oxide film. The cracks and the corrosion that appear this way have a trans-granular character [8].

5. The experimental analysis of the fine structure and the residual tension state

We performed a detailed analysis of our samples at a microstructural level in order to point out some aspects concerning: a) the tensioned state of our material determined by the plastic deformation of the sample; b) eventual structural changes in the material following the stress suffered at the plastic deformation, that can favor the apparition of cracks [3]. We studied the fine structure at the level of the crystalline lattice and the state of residual tensions [12] at the DRON-3 diffractometer (X Cu K_α; U = 34 kV; I = 20 mA). The X-ray irradiation scheme is presented in fig. 12 (a – irradiation with a beam perpendicular on the direction of the crack; b – irradiation with a beam parallel with the direction of the crack.

The diffraction spectra of the material from the area unaffected by cracks are presented in figures 13 (according to the scheme from fig. 12a).

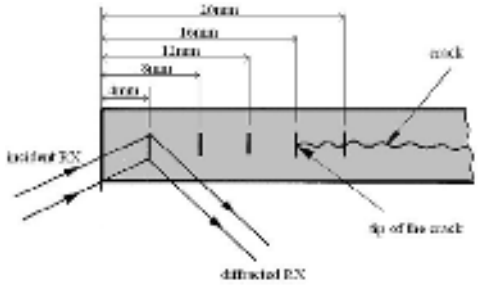

Fig. 12, a *- X-ray irradiation scheme with a beam perpendicular on the direction of the crack*

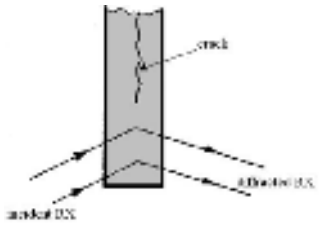

Fig. 12, b *- X-ray irradiation scheme with a beam parallel with the direction of the crack*

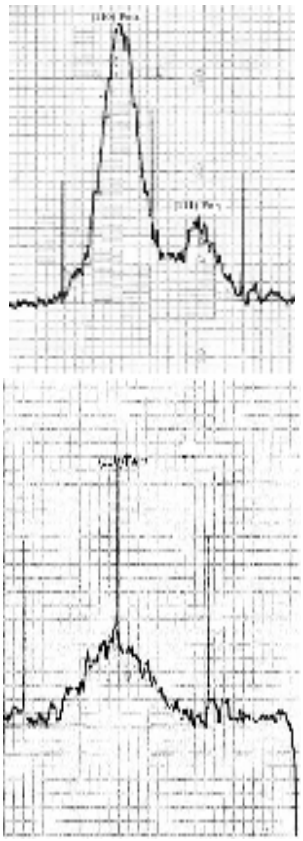

Fig. 13. *X-ray diffraction spectra fragment according to the scheme from fig. 12a*

These spectra fragments inform about the structural states and the tension states from the superficial layer, with a depth of approximately 80 μm

The irradiation schemes we used allowed us: 1) to establish the texturing degree of the material; 2) to get data concerning the 1st order internal tensions that appear at macroscopic level and that are oriented either to stretch, either to compress the material; 3) to get data concerning the 2nd order internal tensions that appear at the level of the mosaic blocks and that are unorientated tensions; 4) to establish the medium size of the mosaic blocks that dictate the breaking tension of the material; 5) to appreciate the density of dislocations from the crystalline lattice that determine the plasticity properties; 6) to make a phase analysis, meaning to determine the martensitic and the austenitic phases and the possible transformation type $Fe_\gamma \rightarrow Fe_\alpha$.

The presented diffraction spectra show the change of form of the diffraction lines for the martensitic and austenitic phases because of the action of the tensions from the areas near the tip of the crack. Their shape proves the existence of a $Fe_\gamma \rightarrow Fe_\alpha$ type of transformation because of the action of the internal tensions. Thus, we concluded that the material is unstable from the structural point of view and this is why the pitting-type of corrosion is favored in the stretched areas of the ply where the fittings are placed. Also, we deduced that the material is inhomogeneous from the texturing degree point of view, thus being favored the structural instabilities at the crystalline grain level, having negative consequences on the corrosion behavior of the heat exchanger plates.

By processing the data from the diffraction spectra we could get a series of important elements such as:

1) The B_{221} magnitude (see fig. 14) is directly proportional with the level of the 2-nd degree internal tensions. From the obtained data we could see that B_{211} increases towards the tip of the crack, thus showing the existence of a tensional inhomogeneity of the material at the level of the mosaic block. This aspect induces the beginning of the pitting corrosion (narrow spaces).

2) The $\Delta_{2\theta}$ magnitude (see fig. 15) is directly proportional with the level of the 1st degree internal tensions. Our results show that towards the tip of the crack there is a tendency that the internal tensions to grow, thus leading to a local stretching process of the material.

These tensions start the transformation of the austenite to martensite, thus influencing the stability of the material.

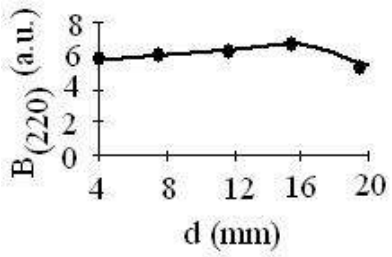

Fig. 14. *The distribution of B (220) size*

The structural stability decreases in time, fact that leads to the beginning and intensifying of the local corrosion process.

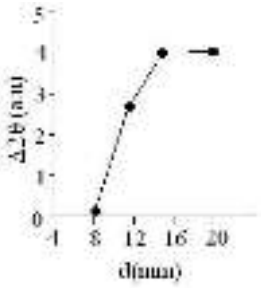

Fig. 15. *The distribution of the* $\Delta 2\theta$ *magnitude*

3) The B_{110} magnitude (see fig. 16) is directly proportional with the breaking tension of the martensitic phase. The data show that towards the tip of the crack the breaking tension decreases fact that favors the breaking of the martensitic phase from the steel.

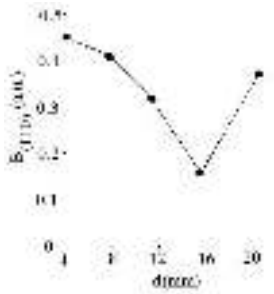

Fig. 16. *The distribution of* B_{110} *size*

4) The B_{111} magnitude (see fig. 17) is directly proportional with the breaking tension of the austenitic phase. From the data we concluded that towards the tip of the crack the breaking tension decreases, fact that also favors the beginning of the breaking of the material.

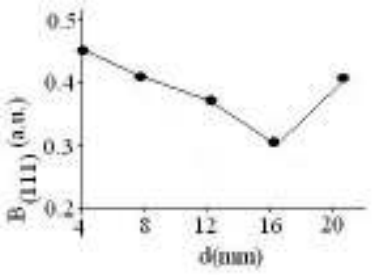

Fig. 17. *The distribution of* $B_{(111)}$ *size*

5) The I_{110} integral intensity magnitude (see fig. 18) is directly proportional with the quantity of the martensitic phase. This magnitude increases towards the tip of the crack as a consequence of the instability of the martensitic phase caused by the 1st and 2nd degree internal tensions. Thus, the martensitic phase appears, it is metastable and it creates supplementary tensions into the material.

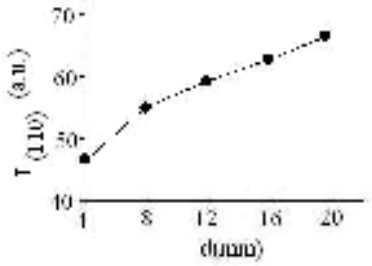

Fig. 18. *The distribution of the integral intensity* $I_{(110)}$

6) The I_{111} integral intensity magnitude (see fig. 19) is directly proportional with the quantity of the austenitic phase. The decrease of the quantity of austenitic phase is done because of its transformation to martensitic phase caused by the action of 1st and 2nd degree internal tensions. The steel looses its austenitic character, becomes martensitic and metastable from the structural point of view.

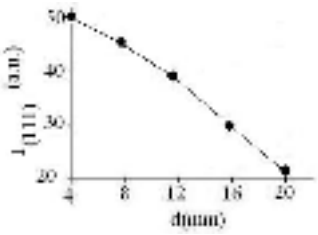

Fig. 19. *The distribution of the integral intensity* $I_{(111)}$

7) The $I_{211}^{min} / I_{211}^{max}$ ratio magnitude (see fig. 20) is proportional with the density of dislocations from the martensitic phase. The decrease of the density of dislocations leads to the decrease of the plasticity properties of the martensitic phase towards the tip of the crack, thus having negative effects over the answer of the material to mechanical stress (stretching or compressing).

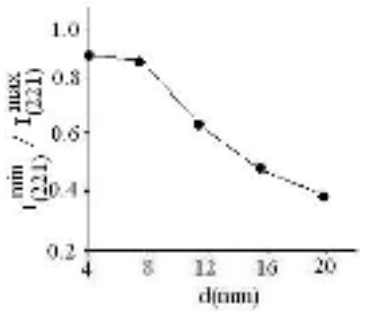

Fig. 20. *The distribution of the* $I_{211}^{min} / I_{211}^{max}$ *ratio*

6. Conclusions

The material used for the heat exchanger plates is an austenitic stainless steel with an unstabilized structure due to the presence of inadequate alloying chemical elements.

During the cold plastic deformation process the austenitic phase turned to martensitic phase. This fact determined the apparition of the state of supplementary tensions that overlapped with the residual tension state appeared during the processing of the material.

A lot of nonmetallic inclusions either dispersed or distributed in lines along the rolling direction were observed. We also observed that the material contained plastic formations of sulphures, thus indicating deficiencies concerning the steel making. There is also dispersed and unsolved cementite in the basis mass of the material. This indicates that the material wasn't thermally treated after the cold plastic deformation (hardening in order to be put in solution), which would have led to the diminishing or even to the elimination of the residual internal tensions. Such a treatment would have been indicated for the material used for the heat exchangers.

The first micro cracks accelerated the transformation of the austenite to martensite in front of the crack.

This change provoked a destabilization of the energetic equilibrium by worsening the behavior of the plates to the attack of the liquid medium over the crystalline grains. The elasticity properties of the plate's material decreased and the breaking tension lowered, favoring the propagation of cracks and the destruction of the plate. This process of developing of micro cracks and of their change to macro cracks, followed by their propagation is favored by the lack of material stabilization.

The cracks initiated at the surface of the material and having an obvious tendency of branching in depth and in plane are specific to the cracking corrosion under stress. This type of corrosion takes place even if the tensions from the material are relatively small compared to the limit of resistance of the steel, as the computer simulation showed us.

Because the plates of the heat exchangers have a complex shape, they have to be realized by cold plastic deformation. As a consequence, the microhardness increases, as we could notice at the analysis of microhardness we made.

The material is softer in the relaxed areas very close to the crack. The analysis made in cross-section showed a bigger hardening on the stretched part of the material then on the compressed part, which favored the propagation of cracks both in depth and on the plane part of the plates. The growth of hardness is favored by the partial transformation of the austenite to martensite caused by the instability of the structure of the material. One has to also keep into account that the martensite is harder than the austenite.

The analysis of the microhardness also showed that there is a hardening of the material at the edge of the plate due to the cutting of the semi fabricated as a metal sheet. This fact confirms that there wasn't done any thermal treatment during processing.

The absence of structural stability and the presence of residual tensions from the cold plastic deformation lead to the formations of deep craters of pitting-type in the material, even in low corrosive media. From these craters begin the transcrystalline cracking. We consider that this process is favored by the simultaneous action of more factors, such as:

- the presence of oxygen solved in the liquid medium;
- the higher temperature at the inlet of the primary thermal agent;
- the diminished circulation of the thermal agent in the area towards the exterior part of the heat exchanger plate;
- a possible aggressive action of the unlinked sulphur from the material of the fittings that, in time, can enter the metallic material, this process being favored by the higher temperature;
- the appearance of differentiated composition cells in the contact area between the gaskets and the plate, towards the exterior corner, opposite to the main flowing direction of the working fluid, thus favoring the corrosion process of the used steel.

Taking into account the processing and the functioning conditions of the material, we consider that it would have been better to use for the heat exchanger plates a stainless steel with stabilized structure, by adding molybdenum. Such steel is 316 AISI, which contains 2 – 3 % Mo (molybdenum).

References

[1]. Gheorghies, 1990, C. *Controlul structurii fine a materialelor cu radiatii X*, Ed. Tehnica, Bucuresti, p 272
[2]. He, S., Jiang, P.X., Xu, Y.J., Shi, R.F., Kim, W.S. and Jackson, J.D., Int. J. Therm. Sci., 2005, vol. 44(6), pp.521-530.
[3]. Satake, S., Kunugi, T., Shehata, A. M. and McEligot, D. M., 2000, Int. J. Heat Fluid Flow, 21, pp. 526-534.
[4]. Lours, P., Huchet, L., 2001, Analyse d'avaries de pieces metalliques, Ecole des Mines d'Albi-Carmaux, France.
[5]. Stephen, A. J., 2003, International Journal of Heat and Fluid Flow, vol. 24, Issue 6,
[6]. Kim, W. S., Jackson, J.D., He S. and Li, J., 2004, Journal of Mechanical Engineering Science, vol. 218, pp. 1361-1372.
[7]. STAS 3583-87
[8]. STAS 7657-78
[9]. Lucan, D., Pirvan, I., Radulescu, M., Fulger, M., Jinescu,G., 1998, Revista de chimie vol. 49, pp. 222 -226
[10]. STAS 7114/1991
[11]. Vukoslavcevic, P., and Wallace, J. M., 2001, 54th Annual Meeting, San Diego, USA, November. *Bull., Amer. Phys. Soc.*, 46 (No. 10), p. 89.
[12]. Gheorghies, C., 2003, The Ann. of Dunarea de Jos Univ. of Galati, Fasc. VIII, Tribology, vol.I, pp.302-312.

THE ANNALS OF "DUNAREA DE JOS" UNIVERSITY OF GALATI.
FASCICLE IX. METALLURGY AND MATERIALS SCIENCE
N^0. 1 – 2008, ISSN 1453 – 083X

RESEARCHES CONCERNING THE DEFORMATION BEHAVIOUR OF A LOW CARBON STEEL

Nicolae CANANAU, Petrica ALEXANDRU, Gheorghe GURAU, Ionel PETREA
"Dunărea de Jos" University of Galati
e-mail: nicolae.cananau@ugal.ro

ABSTRACT

The paper shows the results of the researches meant to establish the equation of deformation behavior of low carbon steel. The behavior law is established by the experimental way, using the torsion test method. The composed constitutive law had very good experimental verification.

KEYWORDS: thermo-plastic behavior, torsion test, stress intensity, strain intensity.

1. Introduction

The plastic deformation of a metallic material is described by the equation between the stress, strain, strain rate and temperature [1]:

$$\sigma = \sigma(\varepsilon, \dot{\varepsilon}, T) \qquad (1)$$

In this equation σ is the stress intensity in the real deformation conditions, ε - strain intensity, $\dot{\varepsilon}$ - strain rate intensity, T – temperature.

The equation of plastic deformation behavior is necessary for the evaluation, programming, modeling, simulation and optimization of the plastic deformation processes. This paper presents the results of researches effectuated for establishing the equation of plastic deformation behavior for low carbon steel for wires, destined to reinforce concrete.

2. Experimental conditions and results

The constitutive equation is established through experimental way using a torsion testing machine. The researched material has 0.18% carbon, 1.23% manganese, 0.21% chromium, 0.15% nickel. The testing sample is cylindrical and its active zone has the following dimensions $\phi 6 \pm 0.02$ mm in diameter and the length 36 ± 0.1 mm. The testing installation is equipped with: electro-hydraulic system for action of sample with the power of 5kW, the revolution is 1-2000 rpm, data acquisition system type Spider 8, heating system, maximum temperature of 1100^{0}C and precision ±5 ^{0}C [3,4].

The research program covers a temperature area, according to the researched material and a domain of the strain rate values. A test corresponds at a certain strain rate value and certain temperature according to the established research program. For testing we must regulate the revolution of hydraulic system, then this system mounts the sample in the action device and we turn on the function the heating system. Also it is also activated the data acquisition system. The research program consists in: research temperatures of 1023K, 1073K, 1123K, 1173K and the revolution of 25, 107, 400 rpm. As result of the torsion test we obtain the $M(\varepsilon)_{\dot{\varepsilon},T}$ torque diagram. The experimental torsion moment diagrams are rendered in the figure 1, 2, 3.

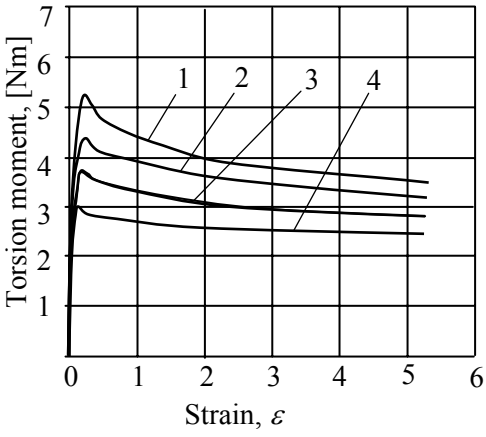

Fig. 1. *The torsion moment diagram – strain for the revolution of 25rpm: 1-1023K, 2-1073K, 3-1123K, 4-1173K*

The analysis of the diagram shows that at the increasing of the strain rate the deformation resistance of material increases and its deformability decreases.

At the increasing of the temperature the deformation resistance decreases and the deformability increases. At the temperature of 1073K it is manifest a trend of decreasing of the plasticity. The function of the torsion moment is depended of the deformation degree (ε), strain rate ($\dot{\varepsilon}$) and the temperature (T). The mathematical expression of the torque is the following:

$$dM = \frac{\partial M}{\partial \varepsilon} \cdot d\varepsilon + \frac{\partial M}{\partial \dot{\varepsilon}} \cdot d\dot{\varepsilon} + \frac{\partial M}{\partial T} \cdot dT \qquad (2)$$

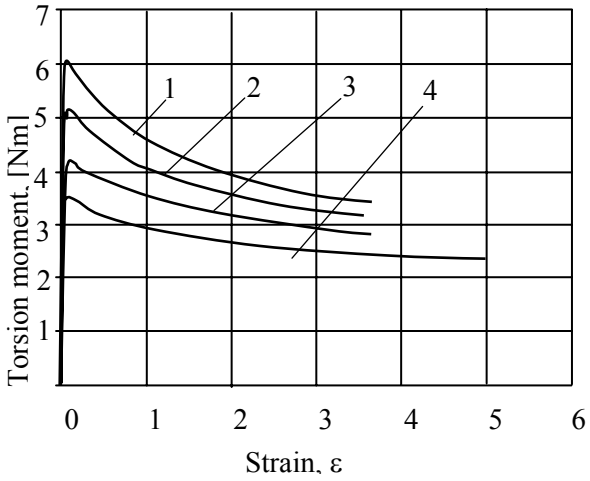

Fig. 2. *The torsion moment diagram – strain for the revolution of 107rpm: 1-1023K, 2-1073K, 3-1123K, 4-1173K*

The methodology of the solving of torsion testing diagrams and results are rendered in the [2].

For the maximum values of the torque the expression (4) becomes:

$$dM_{\max} = \frac{\partial M_{\max}}{\partial \dot{\varepsilon}} \cdot d\dot{\varepsilon} + \frac{\partial M_{\max}}{\partial T} \cdot dT \qquad (3)$$

The deformation strength of the metallic materials varies with the strain ε by a hardening law (power or exponential law), with the strain rate $\dot{\varepsilon}$ by a power law and in function of temperature through an exponential law.

The general mathematical expression of the torsion moment, frequently used for description of the function of the torsion moment has the following expression [2,4,5]:

$$M_{max} = A_1 \cdot \dot{\varepsilon}^m \cdot exp\left(\frac{m \cdot Q}{RT}\right) \qquad (4)$$

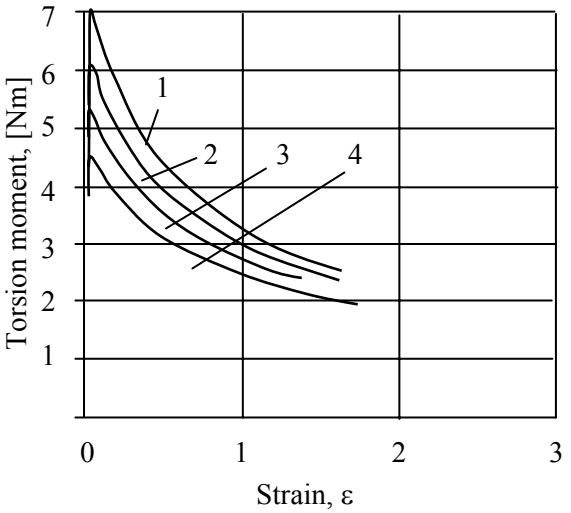

Fig. 3. *The torsion moment diagram – strain for the revolution of 400rpm: 1-1023K, 2-1073K, 3-1123K, 4-1173K*

In (3) *m* is the coefficient of the sensibility of deformation strength at the strain rate, Q is named the activation energy of deformation process, R – the ideal gas constant, T – temperature, in Kelvin, A_1 – experimental constant. We selected the maximum values of the torque, which correspond at the research tests, according to the strain rate and temperature values we obtain the adequate diagrams. We transformed the relation (3) in the linear form (we applied the logarithmic coordinates) and applied a regression calculus program with two independent variables and one dependent variable and we obtained the diagram rendered in figure 4 and the following results for experimental constants:

$A_1 = 0.081786$;
$m = 0.115973$;
$Q = 354.808$ kJ/mol

The value of the multiple correlation coefficient is 0.9827751. Thus the mathematical expression of the maximum torsion moment is the following:

$$M_{max} = 0{,}081786 \cdot \dot{\varepsilon}^{0{,}115973} \cdot \exp\left(\frac{4949{,}259}{T}\right) \qquad (5)$$

We admit a composed function for the hardening factor. The torsion moment may be defined by equation [2,5]:

$$M(\varepsilon, \dot{\varepsilon}, T) = \begin{cases} A_1 \cdot (1 - \exp(-n\varepsilon)) \cdot \left(\dot{\varepsilon}\right)^m \cdot \exp\left(\frac{mQ}{RT}\right) & for\ \varepsilon \le \varepsilon_0 \\ A_2 \cdot \exp\left(-p(\varepsilon - \varepsilon_0)\right) \left(\dot{\varepsilon}\right)^m \cdot \exp\left(\frac{mQ}{RT}\right) & for\ \varepsilon > \varepsilon_0 \end{cases} \qquad (6)$$

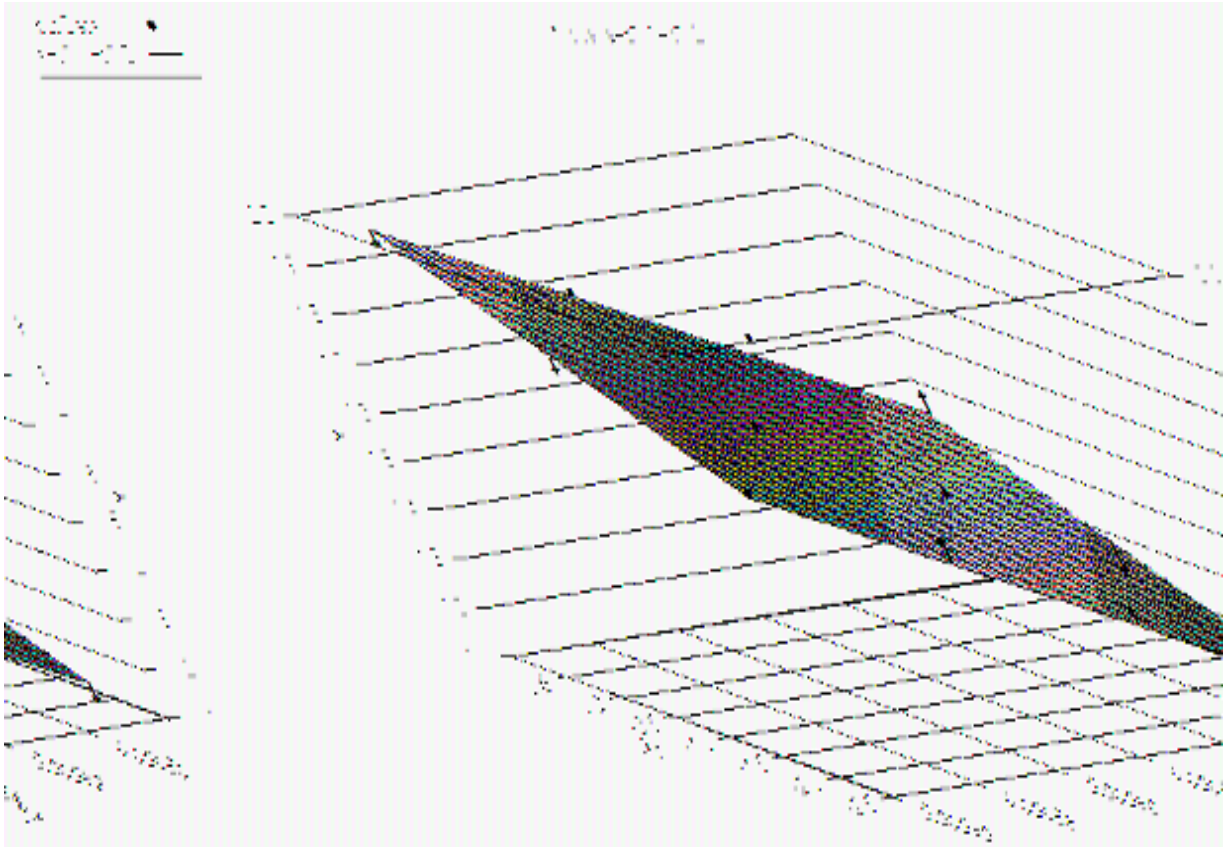

Fig.4. *Torsion moment diagram in logarithmic coordinates: 1-25rpm, 2-107rpm, 3-400rpm*

In this expression ε_0 is the value of the strain which corresponds at the maximum value of the torsion moment.

This factor is, also, a function of the strain rate and temperature. The experimental data for the strain ε_0 that corresponds at the maximum torque are rendered graphically in figure 5.

The function of the ε_0 has the expression:

$$\varepsilon_0 = a_\varepsilon \cdot b_\varepsilon^{\ T} \cdot \dot{\varepsilon}^{c_\varepsilon} \qquad (7)$$

The constants from this equation have the values:
a_ε =0.86267066
b_ε =0.99736158
c_ε =-0.549919768

Coefficient of Multiple Determination (R^2) = 0.9583618773.

This shows that the use of the expression (8) leads to the good values for the factor ε_0.

In the figure 5 the dependent variable *y* is defined by the strain ε_0 which corresponds at the maximum torsion moment.

The first independent variable x_1 is defined by the temperature *t*, in ^{0}C and the second independent variable x_2 is defined by the strain rate $\dot{\varepsilon}$. The values of the strain ε_0 are defined by the temperature through a exponential function and by the strain rate through a power function.

Using this expression we can apply the composed equation (7) at the calculation of the values of the deformation moment at the small deformations, relatively at the $\varepsilon \le \varepsilon_0$, with the first relation of the equation (7), and at the great deformation, using the second relation of the equation (7). For the practical calculus we must use a constitutive equation defined by a relation between the real stress intensity, strain, strain rate and temperature. The establishing of the constitutive equation, relation (1), is described in the next paper.

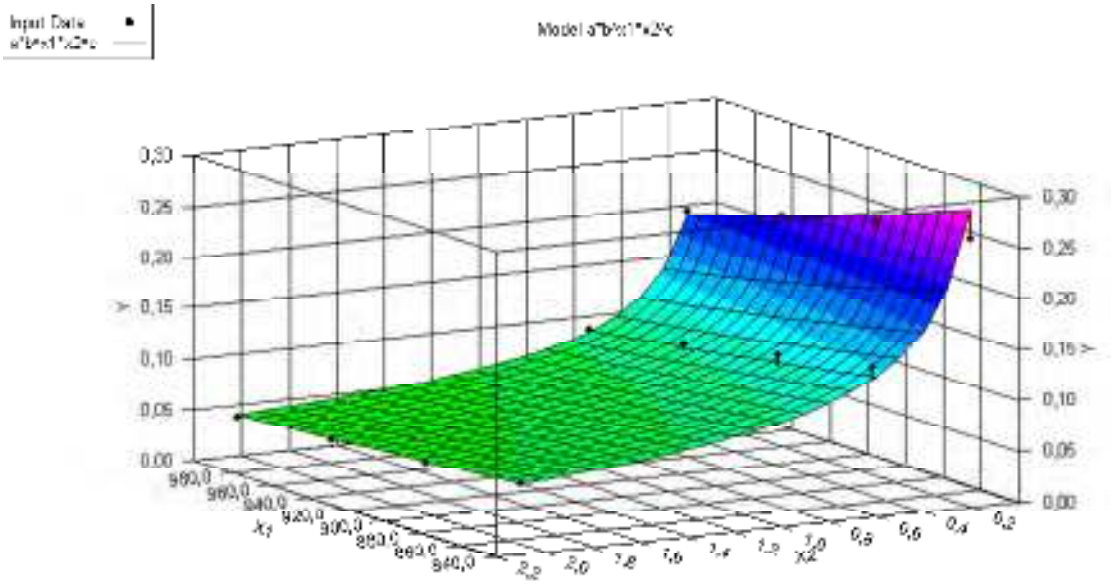

Fig.5. *The variation of the ε_0 with the strain rate and temperature*

4. Conclusions

The best method for establishing the thermo-plastic behavior is the torsion testing.

It was applied a research program at the torsion testing machine in the Plastic deformation laboratory at the Faculty of Metallurgy and Materials Science from *Dunarea de Jos* University of Galati on the samples of the low carbon steel low alloyed with manganese.

They were obtained the torsion moment diagrams necessary for establishing of constitutive equation of this steel.

References

[1]. Cănănău N., 1994, *Teoria deformării plastice,* Universitatea Dunarea de Jos din Galati

[2]. Dumitrescu A.T., 1986, *Contribuţii la modelarea laminarii in calibre*. Teza de doctorat, Institutul Politehnic Bucureşti

[3]. Corobete, G. 2006, *Contribuţii la cercetarea procesului de laminare a sârmelor din otel cu caracteristici mecanice superioare. Teza de doctorat,* Universitatea Dunărea de Jos din Galaţi

[4]. Moussy F., Franciosi P., 1990, *Physique et mecanique de la mise en forme des meteaux.* Presses du CNRS, Paris, ISBN 2-87682-023-4

[5]. Cananau N., Petrea I, Corobete G., 2005, *Modelling of the flow and deformation fields at the profiles rolling by field lines method* , The Annals of "Dunarea de Jos" University of Galati, Fascicle IX.

THE ANNALS OF "DUNAREA DE JOS" UNIVERSITY OF GALATI.
FASCICLE IX. METALLURGY AND MATERIALS SCIENCE
N^0. 1 – 2008, ISSN 1453 – 083X

MASS EROSION AND MATERIAL TRANSFER AT THE DEPOSITION OF LAYERS BY INVERSE ELECTROEROSION

Adrian ALEXANDRU, Marius HUŢANU,
Sorin IACOB STRUGARU
"Gh. Asachi" Technical University Iaşi
e-mail: axa72us@yahoo.com

ABSTRACT

The deposition and alloying of the superficial layers by inverse electroerosion or by electric spark given by a vibrating electrode permits to obtain a large scale of properties at the surface of metallic materials from tools, machines organs, electric contacts, etc. During the inverse electroerosion, the evaporated and ionizated material from electrode (+) under the influence of temperature and electric field, is transferred and deposed on the surface of the part (-). The intensity of material transfer depends on the parameters of the electrical discharge between electrodes, on the time of work and on the nature of the electrodes. This paper work wants to establish the type of evolution in time of the quantity of erodated material from electrode and deposed on the surface of the part. The experimental results are in accordance with the theory of the phenomena of erosion by temperature mixed with the phenomena of massic erosion. The results show that the deposed mass increases by the specific time of deposition until it reaches maxim value, then it decreases.

KEYWORDS: erosion, spark, discharge, electrode

1. Introduction

The electric erosion or processing by electric sparks based on the erosion of metals during the electric discharge by impulses.

When the electric current is pulsatory with direct polarity (the part = anode) and the interelectrodic space is a dielectric liquid (oil, kerosene) takes place the processing by electroerozion of the parts (on their surfaces appear cavities, profiles, etc).

If it is used an inverse polarity (part = cathode) and the interelectrodic space is a gas, it takes place a deposition of electrode material (anode) by the surface of the part.

In contrast with other superficial processings (superficial thermal treatments, thermo-chemical treatments, deposition with thermal spray, deposition by PVD and CVD, etc.) the deposition by electric spark given by a vibrating electrode ensures a very resistant union of the deposed layer with the basic material and permits the deposition with pure metals and with metallic alloys and the alloying of the sublayer with the electrode material.

Under the influence of the temperature from the electric spark (5 000 – 11 000^{0}C) and the electric field, take place on the electrodes some physical phenomena as: electrical discharges in impulse and electrothermical process which have as final result the electric erosion.

B.R. Lazarenko proposes the following succession of the phenomenon which takes place at the electric erosion in impulse. After the piercing of the space between electrodes, a fascicle of electrons emitted by the cathode (the part) interacts with the surface of the anode (the electrode) given their breaking energy and causes a micro explosion which makes a micro cavity on the surface. Because of the explosion, the evaporated material melted is plunged by the electrodynamic field, the hydrodynamic pressure and the gasocinetic pressure from the discharge on the surface of cathode (the part) and the result is the deposed (white) layer which is very hard and has other special properties.

The most important characteristic of the processing is the discharge energy of the electric spark in the interelectrodic space, which depends on the voltage and medium intensity of the electric current, the nature and the thickness of the deposed layer on the cathode, the nature and the thickness of the electrode (anode). At the medium values of the current (0.2 ÷ 80 A) and voltage 15 ÷ 220 V are obtained 8 ÷ 18 J energy. When the discharge energy

in impulse is lower, the quantity of material transferred between electrodes will be smaller.

The total energy W_i produced in the electrodic space during an electric impulse is:

$$W_i = \int_0^{\tau_i} U(t) \cdot I(t) \cdot dt \quad (1)$$

τ_i – total time of the impulse
U(t) – the voltage of the impulse
I(t) – the intensity of the impulse

The total energy (W_i) is given by electrodes (W_{el}) and by the channel of the discharge (W_k).

$$W_i = W_{el} + W_k \quad (2)$$

The energy who is transmitted to the electrodes which is turned into heat has as result the melting, the local vaporization and in the end the erosion of electrodes.

$$W_{el} = \int_0^{\tau_i} U(t) \cdot I(t) \cdot dt - S\int_0^{\tau_i} \varepsilon(t) \cdot I(t) \cdot dt \quad (3)$$

S – the distance between electrodes (3 ÷ 500 μm)

I(t) – the variation of electric potential by the channel of discharge.

2. Experimental method

In order to establish the time evolution of the mass erosion and the transfer of material from the electrode to the part, were made samples with thin strip form (55x10x1 mm) of two steels OLC 55 and 42 MoCr11.

The chemical composition of the two steels is given in table 1. On the samples which are in the initial stage normalized (N), quenched and tempered were successively deposed four layers with a wolfram carbide electrode (WCo8), with 2.2 mm ϕ.

The deposition was made on a single face with specific times of 1.25 minutes/cm^2. At every deposition was used a discharge energy in impulse of 0.3 J.

Table 1

Type of steel	Chemical composition, %									
	C	Mn	Si	P	S	Cr	Mo	Ni	Cu	
OLC55	0.52-0.60	0.50-0.80	0.17-0.37	0.04	0.045	-	-	-	-	STAS 880-88
	0.57	0.74	0.25	0.022	0.025	0.24	0.03	0.16	0.23	determinated
42MoCr11	0.38-0.45	0.6-0.9	0.17-0.37	0.035	0.035	0.9-1.2	0.15-0.3	-	-	STAS 791-88
	0.41	0.62	0.27	0.02	0.04	0.98	0.25	0.22	0.32	determinated

The deposed mass on the slide (cathode) or the massic erosion was determined by weighing the thin strip before and after each deposition.

The thermal treatment parameters applied before deposition by electric spark for the two steels, were:

- OLC 55 – normalizing from 850^{0}C/air
- quenching from 840^{0}C/oil
- tempering to 600^{0}C/air
- 42MoCr11 – normalizing from 870^{0}C/air
- quenching from 850^{0}C/oil
- tempering to 600^{0}C/air

3. Experimental dates

After deposition and alloying of four successive layers, when the specific time of the deposition was 1.25 ÷ 5 min/cm^2, were measured by weighing the masses before and after each deposition Mo, M1, M2, M3 and M4, and the masses for each deposed layer Δ M1, ΔM2, ΔM3, and ΔM4 and the total mass of the final layer $\sum_{i=1}^{4} \Delta M_i$. The values resulted by weighing at the analytical balance are given in table 2.

Table 2. *The deposed weight on the sample after DASE*

The part	**Initial state**	**Mo**	**M1**	**M2**	**M3**	**M4**	**Δ M1**	**ΔM2**	**ΔM3**	**ΔM4**	**ΣΔMi**
OLC55	N	4.1541	4.2804	4.2841	4.2848	4.2775	0.1252	0.0037	0.0007	-0.0073	0.1223
	C	4.3218	4.3319	4.3401	4.3409	4.3381	0.0101	0.0082	0.0008	-0.0028	0.0163
42MoCr11	N	4.2080	4.3405	4.3430	4.3439	4.3405	0.1325	0.0025	0.0009	-0.0034	0.1325
	C	4.3511	4.3654	4.3718	4.3791	4.3702	0.0143	0.0064	0.073	-0.0089	0.0189

Obs. Mo – initial weight; M1…M4 – weight of the samples after each; ΔM1 …ΔM4 – weight of each deposed layer; N – normalized; C – quenched.

By knowing the measured contribution (ΔMi) after each deposition, the density of WCo8 electrode (ρ) and the surface of deposition (L.l) it is possible to calculate the thickless of each deposed layer:

$$e_i = \frac{\Delta Mi}{\rho \cdot L \cdot l}, \text{ mm} \qquad (4)$$

The thickest layers are the same as those measured with the micrometric ocular of the device hardness measurement PMT 3.

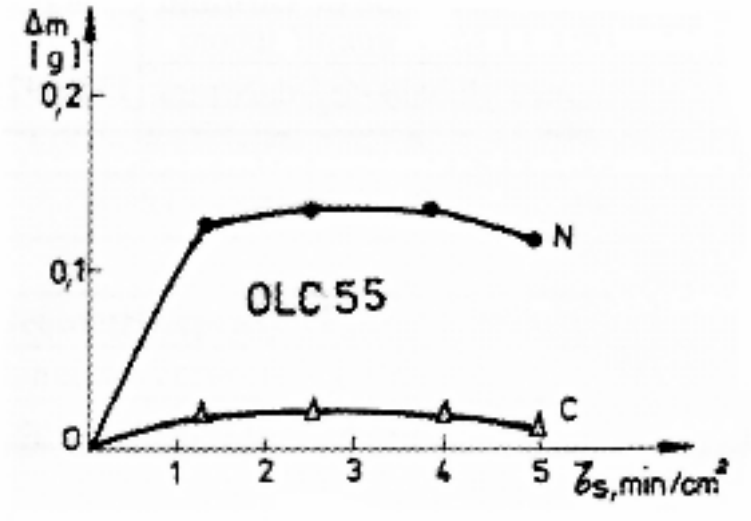

a.

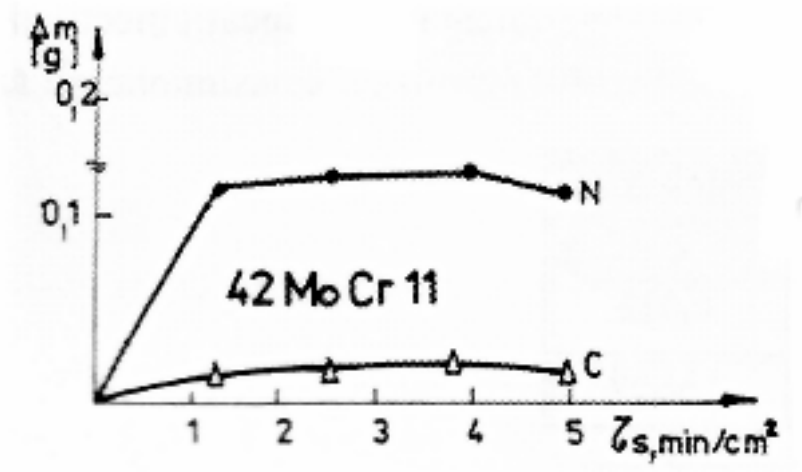

b.

Fig. 1. *The variation of the deposed mass with the specific time of the WCo8 electrode on the steel layers with the specific time of deposition. a) OLC55; b) 42MoCr11*

From table 2 and figure 1, it results that the biggest weight is obtained at the deposition of the first layer. The weight of the other layers is smaller, and after the fourth deposition, with the specific time of 5 min/cm^2, the massic contribution is even negative. From these data results that for deposed layers with a certain weight are necessary just 1÷3 successive depositions. Also, it has been pointed out that (τ_s = 1.25 min/cm^2) the deposed weight by the two steels, with the initial state normalizing is almost ten times larger after the first deposition as the weight deposed on the same steels in quenching and tempering state. After the second and third depositions (τ_s = 2.5 şi 3.75 min/cm^2) the massic contribution is very small; after the fourth deposion (τ_s = 5 min/cm^2) the weight increasey because the pulverization of the material deposed before. The pulverization of the deposed material after a large

specific time has as result the appearance in the layers of some stretch stress with higher values.

It has been shown that if after 1÷2 deposition, the layers are remove the stress by knocking with the vibrating electrode without voltage, the massic contribution will increase making possible the obtaining of layers with larger thickness.

4. Conclusions

* The quantity of eroded material from electrode (+) and deposed on the part surface (-) depends on the discharge energy in impulse; so this quantity also depends on the intensity of the work system and on the physical and geometrical constants of the electrodes.

* The deposed weight on the cathode (the part) is larger on the normalized steel than on the quenched and tempered steel.

* The deposed weight on the cathode increase swith the specific time of deposition to the 2 ÷ 3 min/cm^2 and after made it decreases because of the pulverization of the layers deposed before.

References

[1]. Alexandru A., 2002, *Contribuţii privind alierea şi depunerea superficială prin scânteie electrică şi influenţa tratamentelor termice asupra caracteristicilor straturilor obţinute ale materialelor metalice*. Teză de doctorat, Iasi

[2]. Pop, D., Pop, F. Alexandru, A., 1998, *Hardened Deposition with Tungsten Carbides on Carbon Steel Specimens*, Proceedings vol.II, EUROMAT, Lisabona,

[3]. Alexandru, A., Pop, F.. 1994, *Metalic materials with hardened deposit created by electric arc with vibrating electrode*. Proceedings EUROMAT JUNIOR, Lausane

[4]. Alexandru A., Carabet R.G., Carcea I., 2008, *Mathematical model for determining residual stresess from superficial layers at deposition and alloying by electrical spark*, Metalurgia International,nr 9.

[5]. Agop M.,Vizureanu P., Alexandru A., 2007, *Self-organisation phenomena in material structures. Applications in nanotechnologies. Material transfer between electrodes in the DASE process.* Metalurgia, nr 7.

THE ANNALS OF "DUNAREA DE JOS" UNIVERSITY OF GALATI.
FASCICLE IX. METALLURGY AND MATERIALS SCIENCE
N^0. 1 – 2008, ISSN 1453 – 083X

HARDENING OF THE GREY CAST IRON THROUGH THE VIBRATING ELECTRODE METHOD USING A WC ELECTRODE AND IN COMBINATION WITH TiC AND Ti ELECTRODE

Manuela Cristina PERJU, Carmen NEJNERU,
Tudor RAILEANU, Mihai AXINTE, Ioan HOPULELE
"Gh.Asachi" Technical University Iasi
email: cryss_ela@yahoo.com

ABSTRACT

There have been tested samples of grey cast iron, the hardening being made through WC coating through the vibrating electrode method with a layer, two layers and through double layers combined with Ti and TiC. Besides double layers combined there were also made triple combined layers. Afterwards there were taken photographs of macro-hardness and HV50 micro-hardness into the material in into the layer. There were also made rugosity measurements. Then in order to appreciate the internal stresses were made ring specimens type Naimov. On the exterior of these specimens were made coatings with the vibrating electrode.

KEYWORDS*:* vibrating electrode, hardness, coating, combined layer.

1. Introduction

The superficial heat treatments with material supply are domains which interest a lot. Some of these domains are: the surfaces processing with laser beam light, diffusion treatments in plasma, coatings through heat spraying, thin layers deposits through CVD and PVD proceedings.

The alternative methods of deposit on metallic surfaces can be divided according to the technological process:

- coatings through heat spraying which use arc flame, electric arc and plasma;
- PVD coatings (vapor physical deposition) that can be with ionic coating, electron bombing and laser alloying;
- Chemical deposition (CVD).

The vibrating electrode method belongs to the same class with the electric arc coatings. The principle of hardening through electric sparks of the metallic pieces consists in the fact that in case of sparking unloading under the pulsatory current takes place the polar transport of the electrode material, which represents the anode, on the surface of the piece, which is the cathode.

This material alloys the layer of the piece and by chemically combining with the atomic dissociated azotes from the air, the carbon and the material of the piece it forms a diffusion layer which is hardened and resistant to wear. In the superficial layer are formed complex chemical reactions: azotizes, carbonitriding, very stable nitridings and quenching layers.

2. Experimental results

It was used for the experiment the ferrite-pearlite grey cast iron to which the chemical composition is given in the table.

We have chosen the grey cast iron because the study depends on the implementation of the method within the technological processes of the piston rings which are made of cast iron and have a powerful wear on the exterior.

This made us think that we could prolong the life of the piston rings by making this micro alloying treatment. The tests were made on an apparatus type Elitron 22.

***Table 1**.The chemical composition of the cast iron specimens used in experiments*

C	Si	Mn	P	S	Cr	Ni	Cu	Mo
[%]								
3.97	2.87	0.25	0.06	0.07	0.28	0.126	0.17	0.03

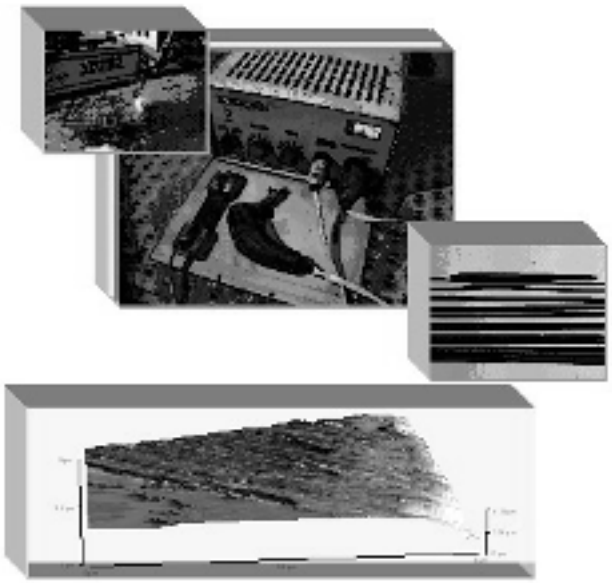

***Fig.1**.a) Elitron 22 –the installation for sputtering deposition with different kind of electrodes b) Deposition WC one layer(Atomic Force Microscopy).*

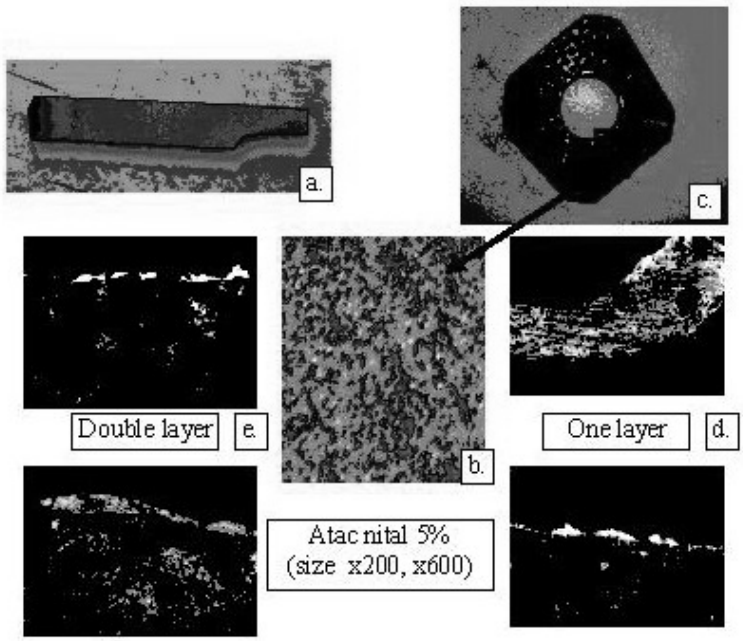

***Fig.2**. a. WC electrode; b. Macrostructure surface with WC deposition; c. Cast iron sample with WC deposition by vibrating electrode; d. Microstructure of WC deposition one layer; e. Microstructure of WC deposition double layer.*

There were made tests with layer deposition through sparking with W electrode, with a layer and two layers, but with double layer combined with Ti and TiC. Using W electrode we can observe that it is obtained a compact surface but with pronounced irregularities like in figure 2. The coating had some difficulty degree because the W electrode makes holes and jumps during the surface alloying.

We worked with high amplitude and average intensity (A_6, r_3). All the etchings were made with 5% Nital and the photos were made with a magnification power of x200 and x600. For the combined double layers I used as base Ti because it gave the layer a good compacting and anchor, the deposition was uniform and the WC was on the exterior because it gave hardness to the surface.

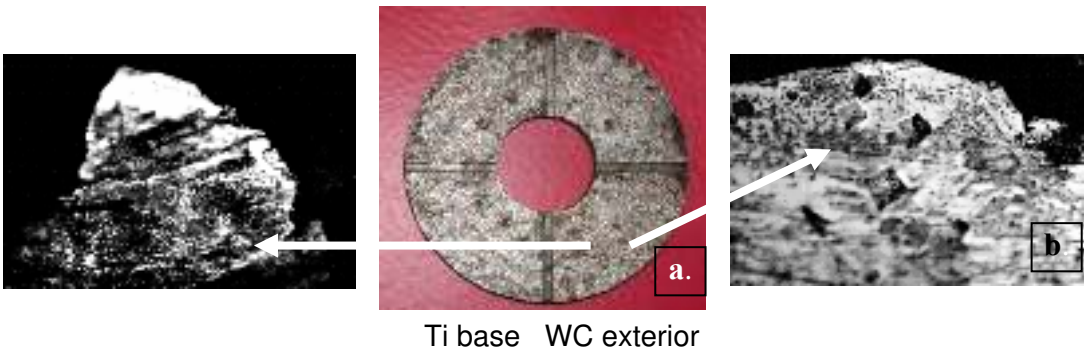

***Fig.3**. a. Cast iron sample with different kind of deposition-macrostructure; b. Microstructure double layer deposition, first layer Ti deposition and front layer.*

The deposition with Ti base takes to the disparity of the defects like holes and oxides.

We used for the triple combined layers W as base because it has a good adherence on cast iron, Ti as an intermediate layer because it gives the combination a good toughness and on the exterior it was used a WC because it has high hardness.

The second kind of sample was covered with triple combined layer having as base WC because it anchors on cast iron, TiC as an intermediate layer which leads to the extinction of the defects like holes and oxides and on the exterior it was used W which leads to the appearance of a uniform layer.

There was made the micro hardness after the depositions by using the apparatus PMT3. It was used a weight of 50 g in order to press the diamond penetrator.

Making an average to the realized tests, I noticed that we have the hardness much higher than the base material.

***Fig.4**. Cast iron sample with different kind of deposition-macrostructure; Microstructure triple layer deposition, first layer W, second layer Ti, WC exterior layer and WC first layer, TiC front layer, W exterior layer*

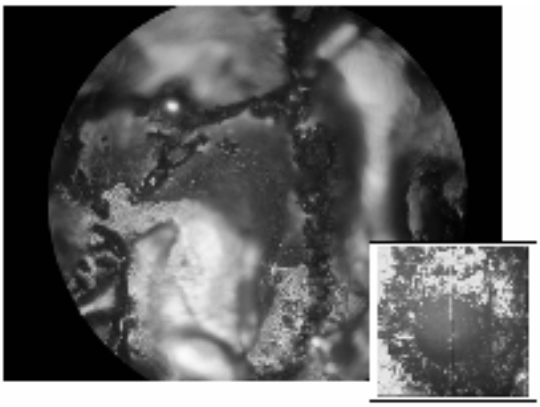

***Fig5**. Cast iron sample picture which shows the characteristics of the electrode WC deposition layers; cracks, oxides, surfaces uniformity ; in the corner is placed a drop of WC electrod deposition.*

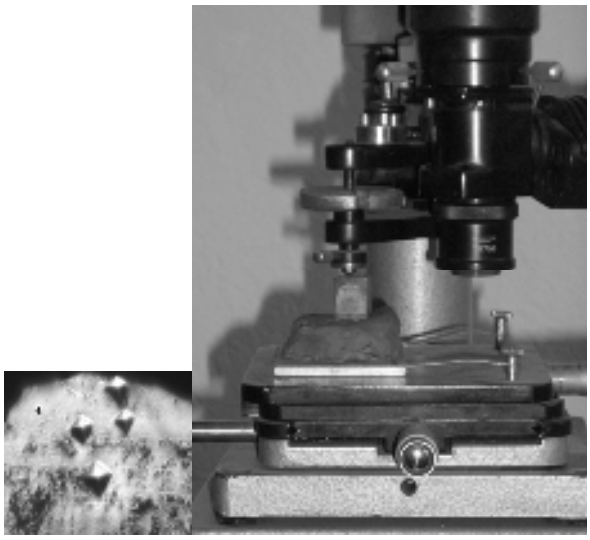

***Fig.6**. Apparatus PMT3 for micro hardness measurements.*

To determine the internal stresses there were used test bars type Naimov from grey cast iron.

$$\sigma_f = \Delta_e \frac{Eh^2}{36\pi R^3}\left(\frac{2h}{K(2R-h)} - 1\right) \qquad (1)$$

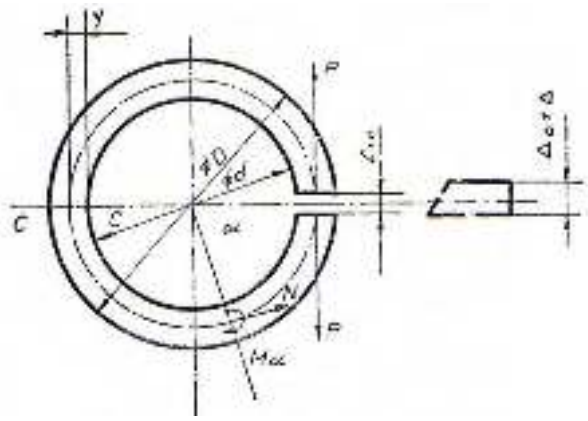

***Fig.7**. Test sample Naimov type*

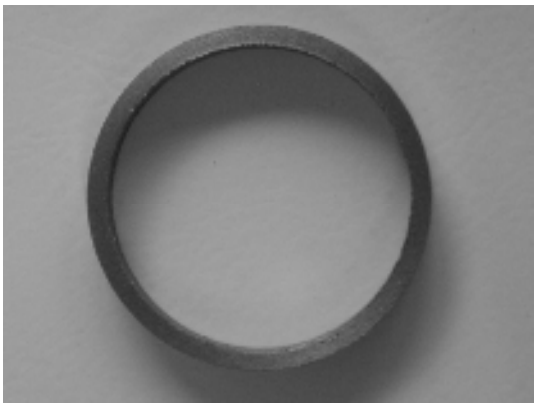

***Fig.8**. Test ring Naimov type*

The rings were stress relieving treated to the temperature of 550^{o}C for 3 hours and cooled with the furnace. On the rings there were traced two marks like a cross, the distance between them was measured before and after cutting. The cutting was made after deposition so that the obtained opening is proportional with the size of the introduced internal stresses. We used the calculus from curve girders for the calculus of the stresses.

The introduced stresses are mainly forging, drawing that adds on the value of the existent stresses from the piston rings prolonging their function period.

***Table 2**.Variation of hardness in deposition layer*

Base material	WC– one layer	WC – double layer	Ti first layer, WC front layer	W base, Ti second layer, WC front layer	WC base, TiC second layer, W front layer
400	976.56	818.325	566.89	979.42	867.29

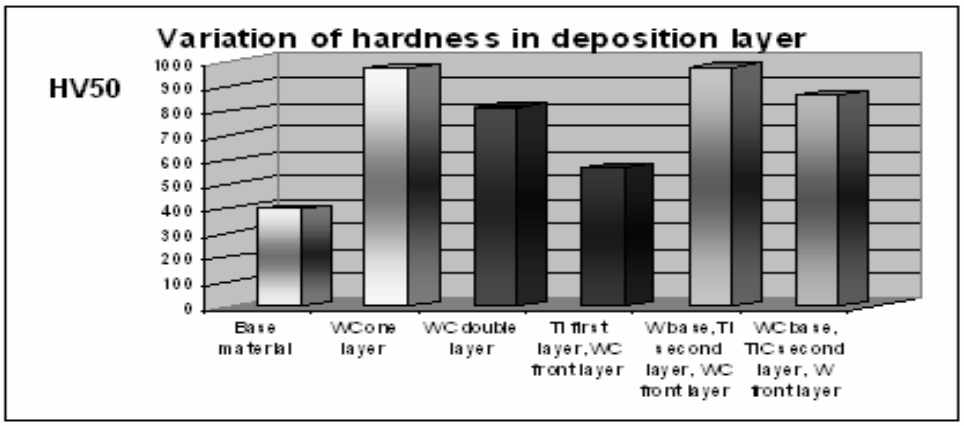

***Fig.9**. Graph of hardness in deposition layer*

***Table 3**. Variation of the internal stress*

No. rings	Deposition tipe	No. deposition layer	Δ_r [mm]	$\sigma_{rem.}$ [N/mm^2]
I	WC	1	+1.45	115.35
II	WC	2	+0.45	35. 8
III	Ti-b; WC-e	1+1	+0.24	19.09
IV	W-b1;Ti-b2;WC-e	1+1+1	+0.45	35.8
V	WC-b1;TiC-b2;W-e	1+1+1	+0.41	32.61

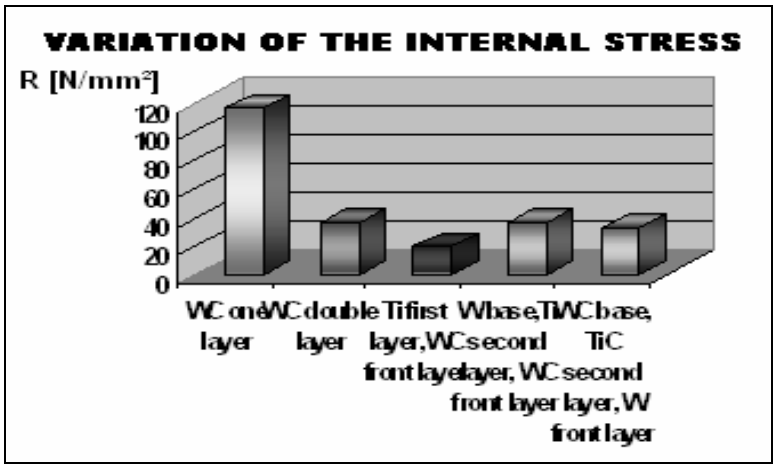

***Fig.10**. Graph of internal stress in different deposition layer*

3. Conclusions

1. The method has practical applicability not only for restoring but also for prolonging the function period of the cast iron pieces that work in intense regime like piston rings.

2. From technological point of view it works easier manually with electrodes of different dimensions: 3 - 6 mm diameter and the deposition are more uniform.

3. If we compare the results we can see from the graphs that the micro hardness in deposition layer is almost double the micro hardness of the base material.

4. From tensile graph we noticed that maximum value for tensile stress was obtained using WC electrode one layer and it has 115.35 N/mm^2, and the minimum value was obtained for combined layer Ti base and WC surface layer 19.09 N/mm^2.

References

[1]. Raileanu, T., 2000, *Teza de doctorat, Contributia privind influienta unor tratamente termice din faza lichida asupra calitatii suprafetelor si rezistenta la uzare a unor repere din fonta.*

[2]. Vermesan, G., Vermesan, E., Jichisan-Matiesan, D., Cretu, A., Negrea, G., Vermesan, H., Vlad, M., 1999, *Introducere in ingineria suprafetelor*, Editura Dacia, ISBN 973-35-0922-1

THE ANNALS OF "DUNAREA DE JOS" UNIVERSITY OF GALATI.
FASCICLE IX. METALLURGY AND MATERIALS SCIENCE
N^0. 1 – 2008, ISSN 1453 – 083X

MAGNETICAL PROPERTIES OF SILICON STEELS USED FOR ELECTROTECHNICAL INDUSTRIES

Ana DONIGA, Elisabeta VASILESCU, Miltiade ISTRATE
"Dunarea de Jos" University of Galati
e-mail: adoniga@ugal.ro

ABSTRACT

This paper-work shows the laboratory experiments achieved on more silicon steel plates, where the magnetic ranges were spot- lighted by particular technical requirements. On the same plates the texture analyses were made considering Goss characteristics, shape and orientation of the crystalline grains, too. Finally, a correlation between texture, structure and magnetic characteristics was gotten.

KEYWORDS: silicon steel plates, texture analyses, magnetic characteristics

1. Introduction

In silicon steels, the shape and grain-size have a particular importance, in great extent influencing the magnetically characteristics of the plates.

According to Weiss magnetic field hypothesis, [1] a ferro-magnetic material is made of great number of small regions characterized by a spontaneous parallel orientation of the electronical spins. In the absence of an external magnetic field, Ms magnetization vectors, of various zones, are so oriented that they cancel mutually and the body comes out as a nonmagnetized macroscopical one. These small regions are named spontaneous magnetization range or magnetic range [2].

In the absence of the magnetic field, Ms vector is oriented, in each range, alongside the gentle magnetization axis. It results that if we could see the magnetic range orientation, in a certain way, we should have an information of the crystallographic orientation of the respective plate.

For silicon steel the gentle magnetization axis is [100] and melts the rolling direction, and heavy magnetization axis [111] is at 55° to the axis [100] - fig. 1. This is Goss texture or "cube-on edge". A plate with such texture introduced in a magnetic field of which direction coincides to rolling direction (it means: to gentle magnetization direction) is easily magnetized getting very small magnetic losses ex: for B = 1.0 T, p< 0.6W/kg.

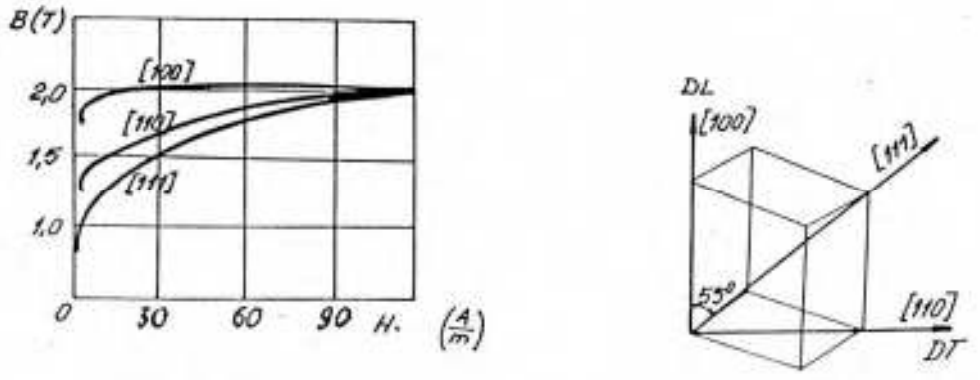

Fig.1. *Magnetic curves and directions of 3% Si steel – grades.*

2. Materials and experiments

In the paper framework, three silicon steel heats were studied and the chemical composition is written in table 1.

The samples were taken from the first cold rolled strips: rolling and black annealing.

Table 1 *Chemical composition of the tested steels*

Steel	C	Mn	Si	S	P	Al	Nb
	[%]						
1	0.004	0.08	3.04	0.015	0.009	0.002	0.09
2	0.004	0.07	3.02	0.020	0.013	0.070	-
3	0.003	0.07	3.04	0.022	0.009	0.010	-

The laboratory experiments were made on the two samples series [3]:

a) 1st series: different reduction ratio of the cold rolling, then secondary annealing for 6 hours at 1150°C. The influence of the reduction range on the texture and core losses in the finished strips was studied.

b) 2nd series: the samples were cold rolled to final thickness 0.35 mm, then secondary annealing at 900°C, 1000°C, 1150°C and hold in hydrogen atmosphere for 2, 4 and 6 hours. The parameters of the secondary annealing influence on the texture and core losses of the finished strips were studied.

The samples were taken from those three cold finished rolled heats with different reduction degree: 40%; 50%; 60%, 70%. Secondary annealing was used in the same range for all samples. On the finished strips the texture level (110)[100] and core losses were determined. The results are in figure 2 and 3.

From figure 2, it could be seen an increase of reduction from 40% to 60% determining a markable increase of Goss texture level for all three steel grades. The highest Goss texture was gotten for first heat samples (with Nb addition).

The different reduction degree influences the magnetic characteristics (core losses) – fig3.

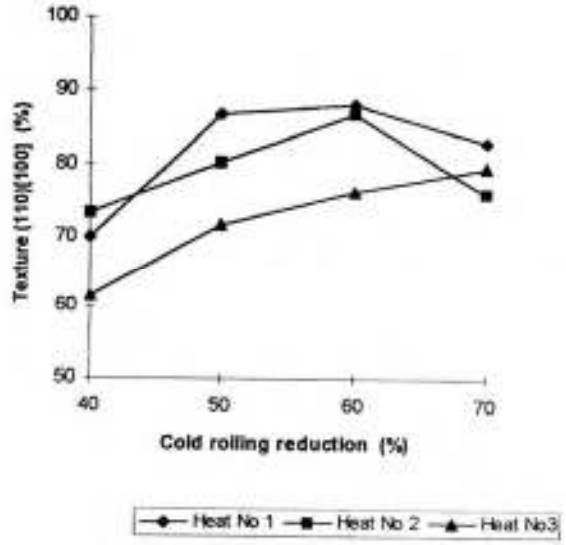

Fig. 2*. The influence of the cold rolling reduction ratio on texture (110)[100].*

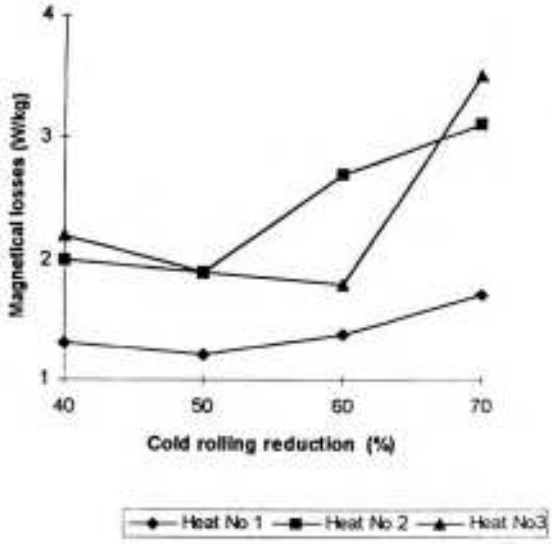

Fig.3*. Influence of the cold rolling reduction ratio on magnetically losses.*

For steel grade 1 and 2 the lowest value of the core losses is gotten at ε = 50%, i.e. there where Goss texture level was the highest. For steel grade 3 the lowest values of the core losses are recorded at ε = 60 %, but they are higher than for steel grades 1 and 2. The gotten results are conforming to the data of specialised literature [4] that explains Goss texture formation in the secondary recristallization strip by the orientation change of the main texture components during cold deformation and secondary recristallization. The (110)[100] component, developed during primary recristallization, undergoes rotations during final rolling in two opposed directions round axle [110]//DT.

The most approached slipping system (112)[111] and (112)[111] could be considered the most suitable for solving the tension condition of the initial orientation and, as result, the most movable.

The movability of these slipping systems brings about the marginal displacement that extends on the direction [110]//DT.

The rotation angle increases to deformation increase, attaining about 35° for one degree of 70 % deformation.

These rotations tend to form the two complementary texture components: (111)[112] and (111) [112] that, during the advanced rolling stage (ε > 70 %) could rotate round axle [111] ND. Taking

into account that (111)[112] type orientation is rotating with small angles (up to 30°) and it recrystallizes in (110)[100] component during secondary annealing, it is necessary that, during cold rolling, the optimum deformation degree should be established (i.e. original and final thickness of strip) to get the best combination of the crystalographical orientation that will generate the final Goss texture.

After the second rolling, the secondary annealing has in view the obtaining of some structure with large grains, characteristical this type of steel.

In the experiments, the grain size was determined after the secondary annealing at 1150°C, for 6 hours (fig.4).

For Nb steel (steel 1), a grain size with diameter for 6...8 mm resulted, for Al steel (2) the grain-size is of 2 ...4 mm and for MnS (inhibitor) steel 3 a grain size of 10…20mm was gotten, proving that an emphasized influence of the micro-alloying elements is on the finished plate structure.

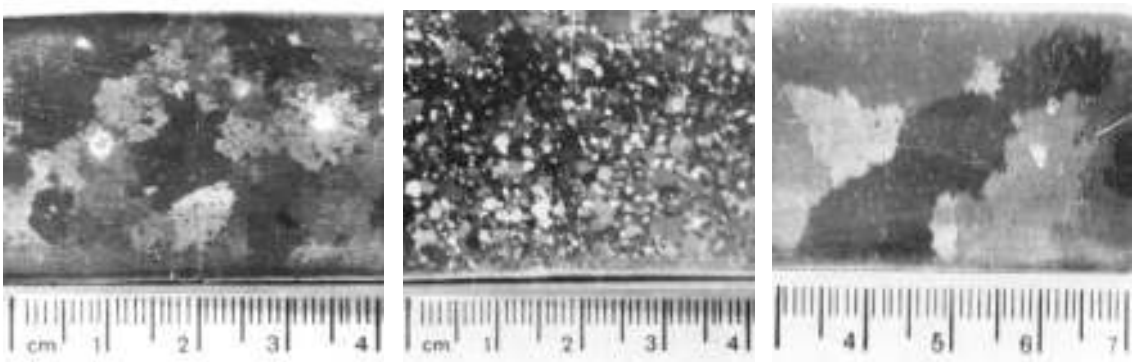

Fig.4. *The macrostructure of sheets after secondary annealing*
a- steel 1; b -steel 2; c –steel 3; t_{ann}*= 1150°C*

The component of the Goss texture increases together with the increase of temperature for all steels, the greatest value being recorded for the steel with Nb, at 1150°C. At the steel 3, although the grains are very large, the Goss texture is lower than at the steel 1 (fig.5). The magnetic losses here measured on some specimen on which Goss texture was analyzed, after the secondary annealing.

It was established that together with the increase of temperature and time of secondary annealing, the magnetic losses decrease [5] at temperature of 1150°C and 6h maintenance time.

The lowest values of magnetic losses were gotten for all steel grades (fig.6).

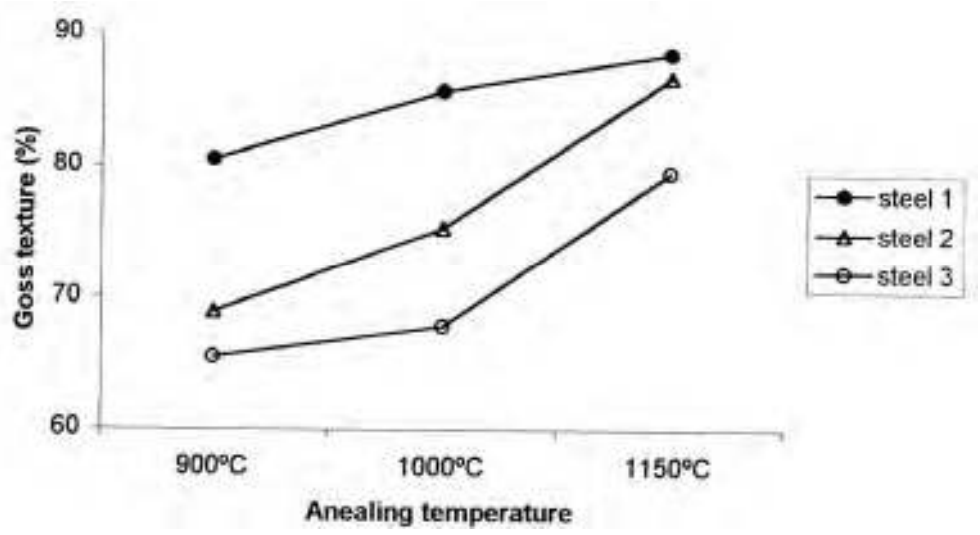

Fig.5*. Variation of the Goss texture to the annealing temperature*

At temperature of 1150°C and 6 h maintaining time the lower magnetic losses are noticed for Nb steel than for the other two steel grades (for B = 1,5 T). These results are very well correlated to grain size and to texture values. Steel grade no.1, with 6…8 mm grain size diameter, shows the highest Goss texture ratio and the lowest value of the magnetic loss.

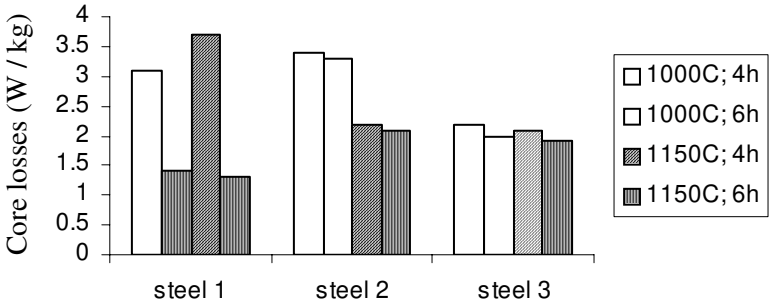

Fig.6. *Core losses of the experimental steels*

The core losses were comparatively estimated for three values of the magnetic induction: B1= 0.5 T; B2 = 1.0 T; B3 = 15 T and for all heat treatment ranges. The results are recorded in the tables and diagrams from figure 7. Core losses decrease once with increase of the temperature and holding time because an equiaxle or light elongated grain is formated increasing, in the same time, perfection degree of Goss texture.

For steel grade 1(with Nb), generally, lower losses are gotten than for other two steel grades in all heat treatment conditions.

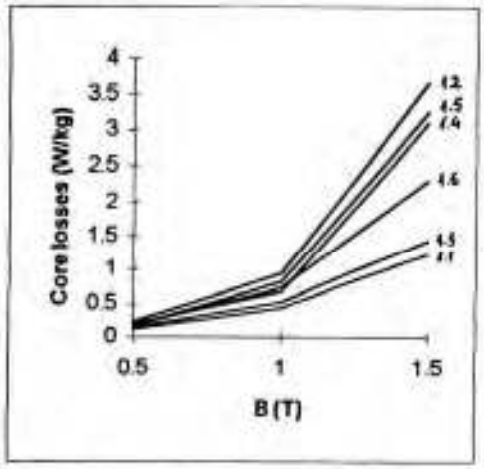

Sample	Recristallization parameters		Core losses (W/kg)		
	Temp (°C)	Time (h)	B_1 = 0.5 T	B_2 = 1.0 T	B_3 = 1.5 T
1.1	1150	6	0.103	0.430	1.217
1.2	1150	4	0.222	0.948	3.668
1.3	1000	6	0.139	0.523	1.427
1.4	1000	4	0.213	0.669	3.111
1.5	900	4	0.187	0.829	3.271
1.6	900	6	0.185	0.731	2.314

(a)

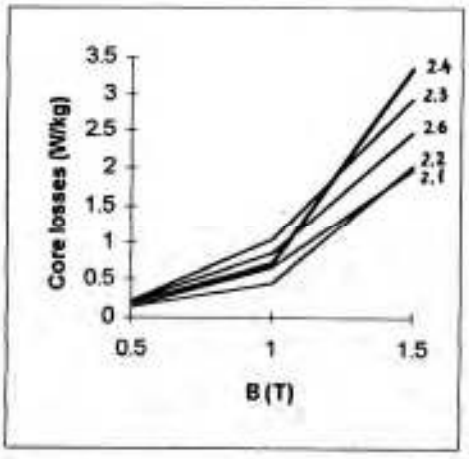

Sample	Recristallization parameters		Core losses (W/kg)		
	Temp (°C)	Time (h)	B_1 = 0.5 T	B_2 = 1.0 T	B_3 = 1.5 T
2.1	1150	6	0.143	0.664	1.974
2.2	1150	4	0.145	0.447	2.041
2.3	1000	6	0.181	0.705	3.338
2.4	1000	4	0.179	0.729	3.367
2.5	900	6	0.202	0.845	2.475
2.6	900	4	0.221	1.044	2.937

(b)

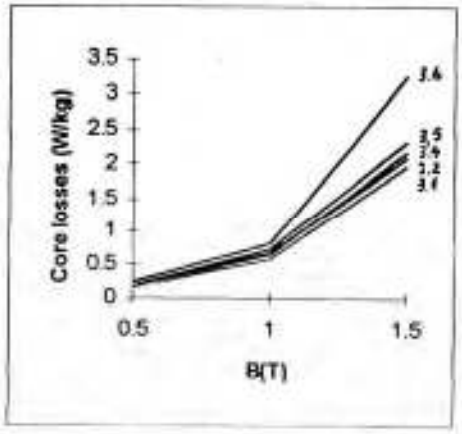

Sample	Recristallization parameters		Core losses (W/kg)		
	Temp (°C)	Time (h)	B_1 = 0.5 T	B_2 = 1.0 T	B_3 = 1.5 T
3.1	1150	6	0.140	0.547	1.952
3.2	1150	4	0.144	0.628	2.112
3.3	1000	6	0.182	0.673	2.105
3.4	1000	4	0.175	0.651	2.181
3.5	900	6	0.180	0.729	2.334
3.6	900	4	0.220	0.826	3.272

(c)

Fig.7. *Core losses for steel 1 (a), steel 2 (b), steel 3 (c).*

3. Conclusions

The gotten results led to the following conclusions:

- Second cold rolling reduction ratio influences the perfection degree of texture. An optimum reduction degree could be established to steel grade, for which the highest level of texture (110)[100] and lowest core losses could be gotten.

- Secondary recristallization is determining the forming of the equiaxed grain structures or light elongated grains, the size of which is influenced by the heat treatment: temperature and holding time.

- Grain size influences the perfection degree of Goss texture and, consequently, the value of the core losses.

-Nb microalloyed steel had the best behavior where the highest ratio of Goss texture and lowest values of the magnetic losses were gotten.

References

[1]. Cedigian, S., 1974, *Materiale magnetice*, Editura Tehnica, Bucuresti

[2]. Hug, E., Dumas, F., 1993, *Influences des deformation plastiques sur le component magnetique d'alliages fer-silicium, -* Revue de Metallurgie, dec., pag.1857.

[3]. Doniga A., 1998, *Researches regarding the silicon steels for transformers* – The doctor`s Paper – Galati - Romania

[4]. Nakashima, S., Takashima, K., 1991, *Effect of cold rolling reduction on secondary recristallization in grain-oriented Electrical steel*, - ISIJ International, vo1.31, pag.1013.

[5]. Ushigani, Y , Okazaki, Y., *Magnetic Properties of Thin Gauge 3% Si- Fe with {110} <001> orientation,-* Journal of Materials Engineering and Performance. vol.4, pag.435.

THE ANNALS OF "DUNAREA DE JOS" UNIVERSITY OF GALATI.
FASCICLE IX. METALLURGY AND MATERIALS SCIENCE
N^0. 1 – 2008, ISSN 1453 – 083X

STUDY OF SEVERE PLASTIC DEFORMATION BY TORSION TEST

Carmela GURAU, Gheorghe GURAU, Nicolae CANANAU
"Dunarea de Jos" University of Galati
email: carmela.gurau@ugal.ro, gheorghe.gurau@ugal.ro

ABSTARCT

High Torsion Pressure (HPT) is an advanced tool for inducing very significant grain refinement in a wide range of metals. In this research were studied parameters of severe plastic deformation using the torsion test. The material used in this research was a polycrystalline Cu-Al-Ni *alloy. For inducing in this material an ultrafine grain structure the thermo mechanical parameters were determined.*

KEYWORDS: Severe Plastic Deformation, HPT, torsion test.

1. Introduction

Nowadays ultrafine grained materials, especially nanocristaline materials (grain size smaller than 100 nm) [1, 2, 3, 4], attract scientific interest. For obtaining ultrafine structures two severe plastic deformation methods are very well known: High Pressure Torsion and Equal Channel Angular Extrusion [5, 6, 7, 8, 9, 10, 11, 12, 13, 14, 15]. In the present study torsion test was applied to define the specific severe plastic deformation parameters.

The researches provide specific information for HPT method in a special case of hard deformable bronzes which required hot plastic deformation.

2. Material and procedures

The program material is a copper alloy. The chemical analysis (optical spectroscopy) is presented in table 1.

The Cu-10wt. %Al-4 wt. %Ni bronze was elaborated in laboratories of *Dunarea de Jos* University of Galati. The cast ingots are conic shape. Cylindrical billets Φ30 x 30 mm have been cut away and plastic deformed by hot extrusion. Torsion test samples were machined from extruded Φ10 x 120 mm shapes.

The dimensions of calibrated zone of the torsion test sample are Φ6 x 36 mm.

Table 1

Al	Ni	Sn	Pb	Mn	Si	Cu
9.95	3.99	0.06	0.02	0.06	<0.01	Rest

The torsion test machine has direct hydraulic motor driven F112 10 PFC 20. For study of material behavior below 1000^{0}C a tubular furnace is attached. For cooling the samples after high temperature test also a cooling system with cold water is attached (fig.1).

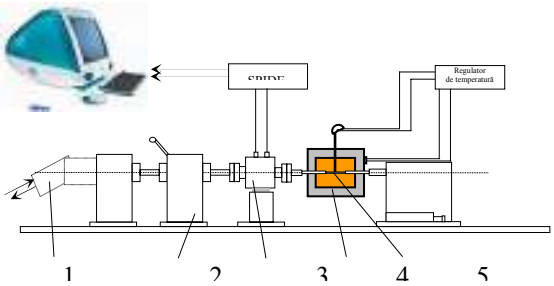

***Fig. 1** Torsion test machine*
1. Hydraulic engine, 2. Gear box,
3. Hottinger torsion measurement device,
4. Furnace, 5. Sample

Mechanical parameters were measured using a equipment type Hottinger Spider 8.

Before the torsion test the samples were heated at 200^{0}C, 400^{0}C, 600^{0}C, 800^{0}C and 900^{0}C for 15 minutes.

After breakage, the samples were rapidly cooled in cold water. One part of each sample was metallographic prepared. The metallographically study was performed using a Philips microscope.

For each sample the torsion moment – strain diagram was achieved. Upper 400^{0}C torsion test temperature, the end of samples were axially looked.

In this case additional axial stress is induced in the sample body.

4. Results and discussions

Torsion test shows an important decrease of the maximum torsion moment from 25 Nm for 20^{0}C to 0.4 Nm for 900^{0}C (figure 2). In the same time strain increases from 0.1 to 6.8

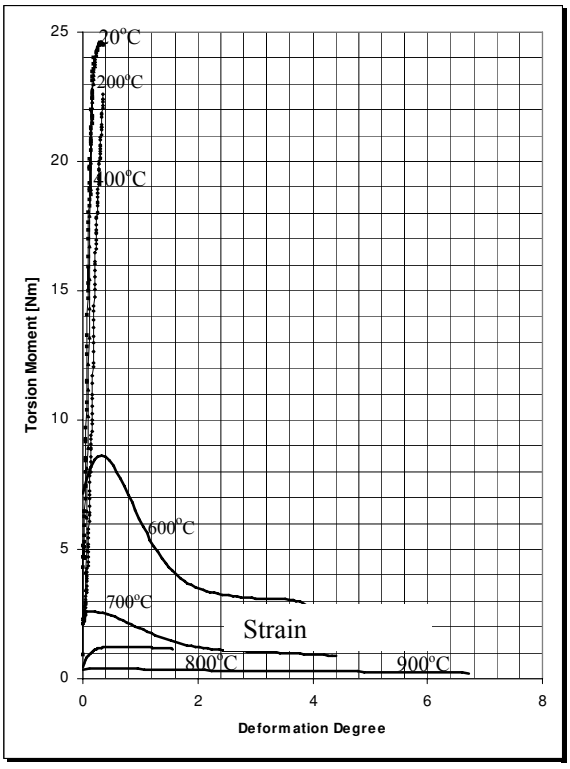

Fig. 2. *Variation of torsion moment with strain for different temperatures*

This behavior of CuAl10Ni4 is normal. The material is hard deformable at 20^{0}C but the plasticity runs up when the temperature increases.

In figure 2 is presented the optical micrograph for bronze CuAl10Ni4 in cast state. The microstructure presents solid solution α, eutectoid ($\alpha+\gamma_2$) and NiAl phase. The structure is dendritically specific for cast CuAlNi bronzes.

The microstructure is typical for this alloy. But after deformation we observe a refinement of structure (figures 3, 4, 5 and 6). The material is twisted and compressed in the same time because the axial stress. The axial stress becomes more important when the temperature increases. That because the plasticity increases maintaing the distance between the ends of the sample.

Fine structure is retained from deformation temperature to 20^{0}C because cooling. The cooling occurs when the test is finished and the sample breaks par way.

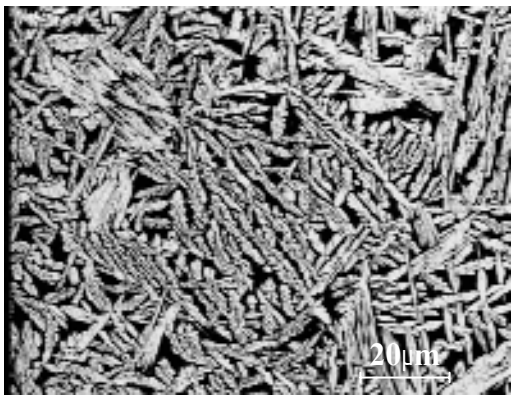

Fig. 3. *Optical micrograph cast CuAl10Ni4 alloy. Chemical composition: 9,95%Al, 3,99% Ni, Cu rest Attack: Fe Cl_3 10g, distilled water 120 cm^3, concentrate HCl 30 cm^3*

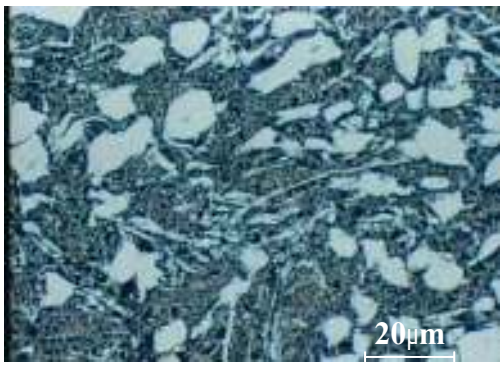

Fig. 4. *Optical Micrograph temperature 20^{0}C, strain rate 0.150 s^{-1}*

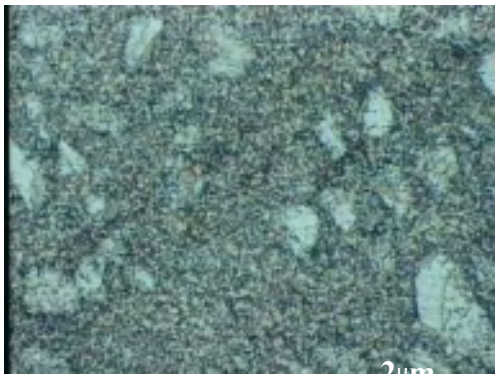

Fig. 5*. Optical Micrograph temperature 200^{0}C, strain rate 0.150 s^{-1}*

***Fig. 6**. Optical Micrograpf temperature 400^{0}C, strain rate 0.150 s^{-1}*

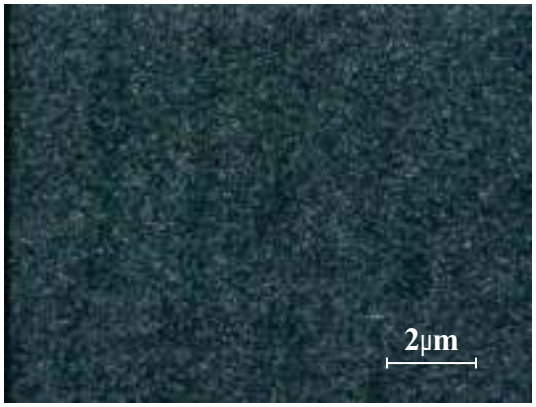

***Fig. 7.** Optical Micrograpf temperature 600^{0}C, strain rate 0.150 s^{-1}*

This observation is confirmed by the microstructures presented in figures 6 and 7.

The finest structures are obtained at 600^{0}C when the sample registers an important deformation degree.

4. Conclusions

The torsion test is a good method to determine the mechanical properties of materials due to certain advantages: constant strain rate, high deformation degree before breaking. Also in appropriate conditions this method allows to obtain fine and ultrafine structure.

This paper points out that, the torsion test made at different temperatures is a good method to determine SPD parameters for the hard deformable alloys which involve hot plastic deformation.

References

[1]. H. Morawiec, J. Lelatko, D, Stroz, Gila, 1999, *Structure and properties of melt-spun Cu-Al-Ni shape memory alloys,* Met Sci Eng, A273- 275

[2]. K.Otsuka and C.M. Wayman *"Shape memory materials"*

[3]. R.Gastien, C.E.Corbellani, M.Sade *Thermomechanical aspects of martensitic transformations in CuAlNi single crystals"*

[4]. Paula, J.P.H.G. Canejo, R.M.S. Martins, F.M. Braz Fernandes, 2004, *"Effect of thermal cycling on the transformation temperature ranges of Ni-Ti shape memory alloy"*- A.S., Mat.Sci. Eng., A378

[5]. Terence G. Langdon, 2006, *The principles of grain refinement in equal-channel angular pressing,* Materials Science and Engineering A

[6]. K. Mueller a, S. Mueller B, 2007, *Severe plastic deformation of the magnesium alloy AZ31* **Journal of Materials Processing Technology 187–188 775–779**

[7]. Mumin Sahin H. Erol Akata, Kaan Ozel, 2006, *An experimental study on joining of severe plastic deformed,* Materials and Design

[8]. S. Swaminathan,a T.L. Brown,b S. Chandrasekar,b T.R. McNelleya,* and W.D. Compton, 2007, *Severe plastic deformation of copper by machining:Microstructure refinement and nanostructure evolution with strain,* Scripta Materialia

[9]. Y. Huang, P.B. Prangnell, 2007, *Continuous frictional angular extrusion and its application in the production of ultrafine-grained sheet metals,* Scripta Materialia 56 333–336

[10]. S.C. Yoon, P. Quang, S.I. Hong, H.S. Kim, 2007, *Die design for homogeneous plastic deformation during equal channel angular pressing,* Journal of Materials Processing Technology 187–188 46–50

[11]. A.R. Eivani, A. Karimi Taheri, 2007, *An upper bound solution of ECAE process with outer curved corner*, Journal of Materials Processing Technology 182 555–563,

[12]. R. Lapovok, C. Loader, F.H. Dalla Torre, S.L. Semiatin, 2006, *Microstructure evolution and fatigue behavior of 2124 aluminum processed by ECAE with back pressure,* Materials Science and Engineering A 425 36–46

[13]. I.H. Sona, Y.G. Jin, Y.T. Imb, S.H. Chonc, J.K. Park, 2007, *Sensitivity of friction condition in finite element investigations of equal channel angular extrusion*, Materials Science and Engineering A 445–446 676–685

[14]. M. Hafoka, R. Pippana, 2007, *Role of strain gradient on the formation of nanocrystalline structure produced by severe plastic deformation*, Scripta Materialia 56 757–760

[15]. M. Delincea, Y. Brechet b, J.D. Emburyc, M.G.D. Geersd, P.J. Jacquesa, T. Pardoen, 2007, *Structure–property optimization of ultrafine-grained dual-phase steels using a microstructure-based strain hardening model*, Acta Materialia 55 2337–2350.

THE ANNALS OF "DUNAREA DE JOS" UNIVERSITY OF GALATI.
FASCICLE IX. METALLURGY AND MATERIALS SCIENCE
N^0. 1 – 2008, ISSN 1453 – 083X

TRIBOLOGICAL BEHAVIOUR OF NITROCARBURIZED STEELS AFTER THERMO-MAGNETIC TREATMENTS

Carmen Penelopi PAPADATU
"Dunarea de Jos" University of Galati
e-mail: PCARMEN-PENELOPI@email.ro

ABSTRACT

Two types of steels were subjected to a nitro-carburized thermo-chemical treatment after thermo-magnetic treatments. The structural aspects into the superficial layer of these steels are studied during the friction process using an Amsler machine, taking two sliding degrees, different contact pressures and testing time. It was determined the durability of these materials, the surface structure evolution at different tests after thermo-magnetic treatments.

The performed tests allowed to establish the influence of the thermal, magnetic and mechanical parameters on the behavior of these two steels taken for study during the friction process.

KEYWORDS: thermo-magnetic treatments, nitrocarburation, wear, difractometry

1. Introduction

Under the influence of the magnetic field, theoretically it is possible [1, 2] to modify the material state. The energy state of the ferrous-magnetic material is modified due to a certain magnetic moment, and the free energy is increased. This is possible to be a first cause which, under the effect of the magnetic filed, induces structure and physical-mechanical properties modifications in material (steel).

Martensite is decomposed upon tempering and the intensity of this process depends on both: temperature and time of the tempering. In addition to the martensite decomposition stages, other processes take place upon tempering: transformation of the residual austenite globulization of troostite,…

According to [1,3], with low tempering of the conventionally tempered steel, the magnetic field slows down the martensite decomposition process. If the steel has been tempered in magnetic field, the martensite decomposition is even slower, thus tending to increase the martensite stability. At the same time the magnetic field influences the cinetics of the residual austenite decomposition isothermally upon tempering, accelerating the transformation process.

The main cause of the above phenomena is the magnetostriction, which causes strains in the microvolumes of the solid solutions. These strains interact with the elastic strains field which corresponds to dislocations.

Magnetostriction is defined as a dimensional variation of ferrous-magnetic materials under the action of a magnetic field also called Joule effect, which depends on the size and direction of the external magnetic field, the material and the heat treatment previously applied to this material (temperature) [7,8,9]. The effect of the magnetostriction decreases with higher temperatures and disappears at the Curie temperature.

Magnetostriction is determined by the influence of the external magnetic field which generates the orientation of the elementary magnetic moments, modifying the balance conditions among the nodes of the crystalline mesh, inclusing variation of the ferrous-magnetic material sample lengths. Under these conditions, the magnetostriction curves can be a result of having measured the ferrous-magnetic sample lengths along the external magnetic field.

In addition to the linear magnetostriction, considered above for plotting the magnetostriction curves with ferrous magnetic materials, it can also be noted a volume magnetostriction which depends on the shape of the piece concerned as well.

The consequences of magnetostriction are:

- applying alternative magnetic fields causes mechanical oscillations [1,2,9] and in the diffusion processes, the strains which are generated by these mechanical oscillations along with the magnetostrictive volume modifications lead to a higher diffusion coefficient;

- of special importance are the local strains in the area of the ferrous-magnetic boundaries. Gradients of the magnetostriction strains occur which further cause higher diffusion coefficient inside the material. They come into contact with the internal strains redistributed by diffusion thus causing a new diffusion influencing factor to appear.

The mechanical oscillations produced by the alternative magnetic fields change the recrystallization conditions especially the germination velocity.

The strains generated by magnetostriction cause elastic deformations which in turn result in a magnetic texture, thus improving the magnetic and mechanical properties in the direction of the external field ($H_{ext.}$). From this viewpoint the effect of the thermal-magnetic treatment is maximum in the stages of the solid solution decomposition and, especially, upon cooling in magnetic alternative field from temperatures higher than Curie point (when orientation of ferrous-magnetic phase particles takes place) [4, 5, 7, 9].

Analysis of the iron-monocrystal magnetostriction [9, 7] shows that its size vary unevenly in different crystallographic directions. Relative elongations $\lambda=\Delta l/l$ have been found as follows: $\lambda_{[100]}= 1{,}9\ 10^{-5}$, $\lambda_{[110]}= -\ 10^{-5}$, $\lambda_{[111]}= -3{,}1\ 10^{-5}$, the cube getting deformed into a romboedru (Fig.1).

In spite of these deformations being very small, mentions must be made that the deformations of the martensite crystal upon magnetization in direction [111] cause its rotation inside plan [110] by an angle $\beta=6^{\circ}$. Magnetostriction may cause local plastic deformations thus determining ecruisation of the residual austenite. This further implies higher material durity/endurance.

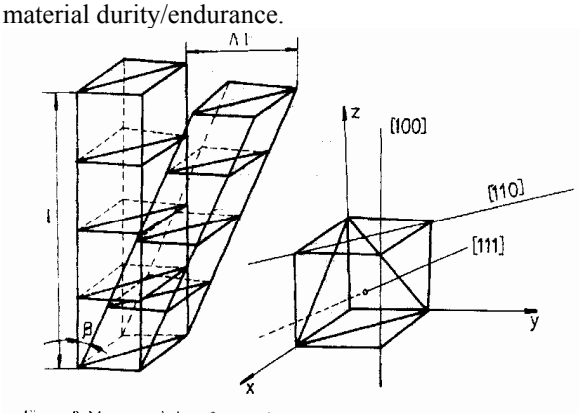

***Fig. 1**: The influence of magnetic field on the size of the iron monocrystal [7].*

2. Experimental researches

The steels analyzed in this paper are improved steels which should undergo high local variable strains: traction, compression, shearing and therefore certain properties are imperious:

- higher hardness and homogenity of the hardness values;
- elimination, if it is possible, of the residual austenite;
- a good tenacity;
- high elasticity point, so as to keep the plastic deformations within small limits.

The chemical compositions of the investigated samples, have been established by spectral analysis and are presented in Table 1.

***Table 1.** Chemical compositions of material samples*

Steel grade	C	Mn	Si	P	S	Cr	Cu	Mo	Al
	[%]								
42MoCr11	0.42	0.68	0.33	0.030	0.026	1.02	0.220	0.17	0.02
38MoCrAl09	0.38	0.50	0.25	0.026	0.020	1.38	0.058	0.17	1.18

The content of Ni of the steel 38MoCrAl09 samples is 0.26 %, and of the steel 42MoCrV11 samples is 0.32 %. It is stated that, according to the chemical composition, these steels are in compliance with the prescriptions STAS 329-83 and norms API – Spec11B-1982. The steels analyzed reach a max score 4.5 from inclusions and a fine grain (score 8-9).

The heat/magnetic treatments applied are:

- t1, t1'= quenching (850 ˚C) and high tempering (580 ˚C) applied to steel 42MoCr11 (code V) and quenching (hardening) (920 ˚C) and high tempering (620˚C) applied to steel 38MoCrAl09 (code R);
- t3, t3' = quenching (hardening) (850 ˚C) and high tempering (580 ˚C) applied to steel 42MoCr11 (code V), quenching (hardening) (920 ˚C) and high tempering (620˚C) applied to steel 38MoCrAl09 (cod R), cooling being performed in alternative current magnetic field (H=1300A/m);
- t4, t4'= quenching (850 ˚C) and high tempering (580 ˚C) applied to 42MoCr11 (code V), quenching (920 ˚C) and high tempering (620˚C) applied to 38MoCrAl09 (code R), cooling being performed in dc magnetic field (H=1300A/m);
- T9 = t1 (classic) + plasma nitrocarburation with 42MoCr11 (code V);
- T10 = t4 + plasma nitrocarburation with 42MoCr11 (code V);
- T11 = t3 + plasma nitrocarburation with 42MoCr11 (cod V);
- T12 = t1'(classic) + plasma nitrocarburation with 38MoCrAl09 (code R);

- T13 = t3' + plasma nitrocarburation with 38MoCrAl09 (code R);
- T14 = t4'+ plasma nitrocarburation, with 38MoCrAl09 (code R).

Plasma nitrocarburation was performed at treatment temperature of 530 ˚C.

The wear – tests (friction process) were carried out on an Amsler machine, using a wear roles cople which corresponds to a degree of sliding by 10% and the value of the strain are corresponding to Q=150 daN.

In the figures number: 2 ÷ 5 was presented the average mass loss and the worn layer depth, after three hours of wear process for these two steels with or without treatments in magnetic fields- alternative current or continuous current, treated with nitrocarburation treatment.

In both cases we can observe the lawest average mass loss -at T11and T13 treatments, using cooling being performed in alternative current magnetic field and the highest average mass loss -at T9, T12, using a classic treament of the steels.

The continuous magnetic field treatment applied before nitrocarburation treatment (T10. T14) determines intermediare values of average mass loss.

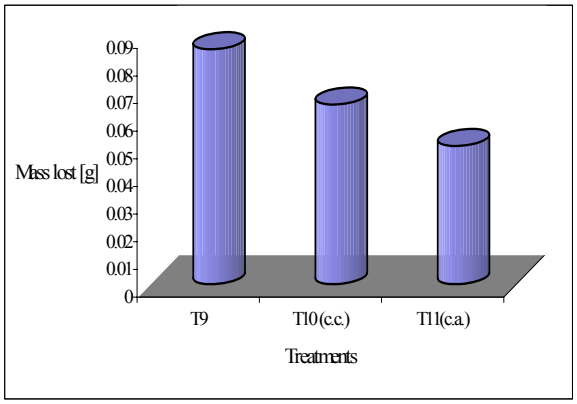

Fig. 2 . *The influence of the magnetic field on the average mass loss after 3 hours of wear friction process, strain corresponding to one degree of sliding by 10% and the value of the strain is corresponding to Q=150 daN, in case of 42MoCr11 (code V) steel grade after nitrocarburation treatment) [4]*

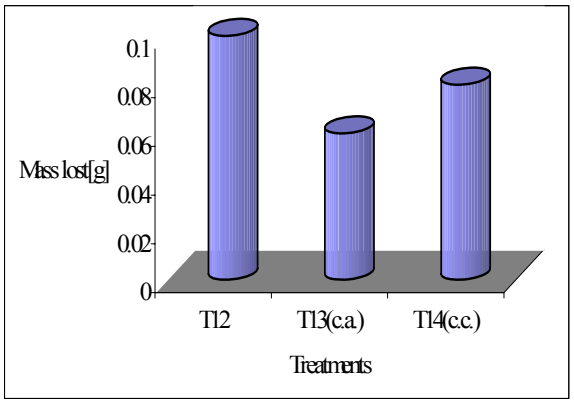

Fig. 3. *The influence of the magnetic field on the average mass loss after 3 hours of wear friction process, which corresponds to a degree of sliding by 10% and the value of the strain is corresponding to Q=150 daN, in case of 38MoCrAl09 (code R) steel grade (after nitrocarburation treatment) [4]*

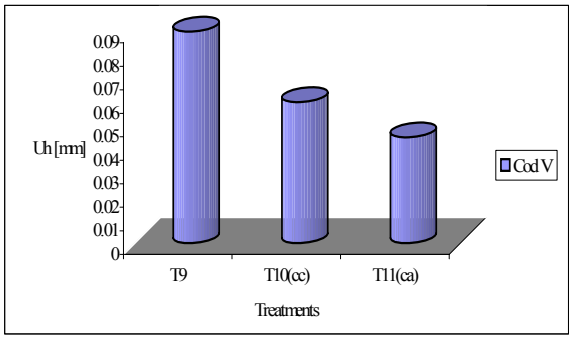

Fig. 4 . *The influence of the magnetic field on the worn layer depth, after 3 hours of wear friction process, which corresponds to a sliding degree by 10% and the value of the strain is corresponding to Q=150 daN, in case of 42MoCr11 (code V) steel grade (after nitrocarburation treatment) [4]*

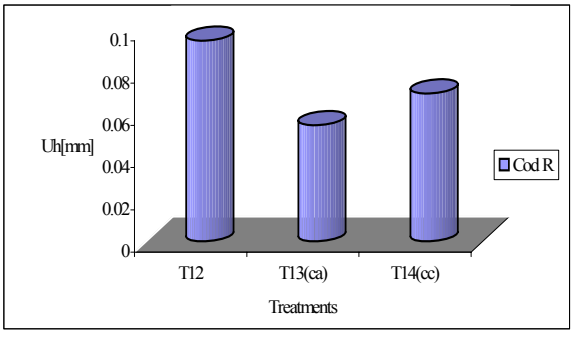

Fig. 5 . *The influence of the magnetic field on the worn layer depth, after 3 hours of wear friction process,which corresponds to a sliding degree by 10% and the value of the strain is corresponding to Q=150 daN, in case of 38MoCrAl09 (code R) steel grade (after nitrocarburation treatment) [4]*

Microstructures (Fig. 6, 7, 8) achieved on heat/ magnetic/chemical and plasma nitrocarburation treated samples show that the thickness of the heat/chemically treated surface layer is higher when applying the heat/magnetic treatment (for example, a.c. magnetic field) with steel 38MoCrAl09 (code R), vs. the conventional treatment case - magnetic field - free treatment [6]

Fig. 6. *Nitrocarburized layer on the sample R5 (code R), before wear process tests.*
Treatment: quenching (t=920˚C) and high tempering (t=620˚C) followed by water cooling in (dc)continuous current magnetic field and plasma nitrocarburation at 530 ºC (7 h)
(x100)
Nital attack 2%

Fig. 7. *Nitrocarburized layer on the sample R3 (code R), before of wear process tests.*
Treatment: quenching (t=920˚C) and high tempering (t=620˚C) followed by water cooling in (ac) alternative current magnetic field and plasma nitrocarburation at 530 ºC (7 h)
(x100)
Nital attack 2%

Fig. 8. *Nitrocarburized (surface) layer on the sample R2 (code R), before wear process tests.*
Treatment (classic):quenching(t=920˚C) and high tempering (t=620˚C) followed by water cooling -without magnetic field and plasma nitrocarburation at 530 ºC (7 h)
(x100)
Nital attack 2%

Diffractometric analyses were performed by means of a Dron 3. The curves of variation for phasis distribution and other characteristics in superficial layers because of the magnetic field applied before plasma nitrocarburized, function by wear – tests period, are presented in figures: 9 ÷ 26.

It was made a comparasion between classic treatment (blue lines) and unconventional (magnetic) treatment (red lines). We can observe that for T9 applied to 42MoCr11(cod V) steel (classic treatment), the martensite quantity (Fig 9-12), the nitro-carburs (Fig.13,14) and the internal tensions- II (B 211 ~σ_{II}) function by friction process length (Fig 15,16 from wear layer), are maintained constant during friction (wear) process. In the case of alternative or continuous magnetic field applied to the steels (T10, T11), we can observe a higher initial quantity of martensite and carbo-nitrurs, compared to the classic treatment. During the wear process, the martensite quantity increases and the carburs quantity decrease very rapidly. The internal tensions (II) increase easily according to the lenght of wear tests. This tendency is most important in the case of treatement T10. The martensite thetragonality grade evolution (c/a), function by wear-tests (Fig 17, 18) in the T10 case decreases more rapidly than the classic treatment (T9) and become constan at T11 case.

For 38MoCr Al09 steel, the tendency is the same (Fig 19-2.), but in this case, we can see a little martensite quantity after classic treatment and a higher nitro-carburs quantity, because of the magnetic field applied and because of the alloying elements.

It results a good behaviour of the steels treated with magnetic fields (alternatve current: T11 and T13), during wear tests, comparred to the classic situation (without manetic field treatment: T9, T12) because of the nitrocarburized layer, which has a high depth in magnetic teatment cases and because exists a higher alloyed martensite which determins a special hardness.

An important aspect in this case is that the superficial carbo-nitrurs quantity decreases during wear process.

In the case of magnetic field-continuous current (T10, T14), the nitrocarburized layer is reduced and appear a very important nitro-carburs layer decrease, during wear process. It results, in this case, a very strong wear.

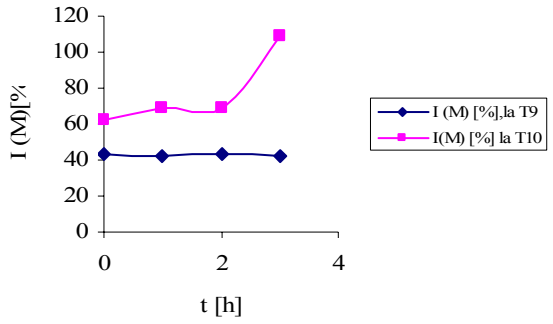

Fig. 9 . *The influence of magnetic field alternative current, on the Feα(M)-44,98˚phase distribution, function by wear-tests lenght (Q= 150 daN, ξ=10%)-code V*

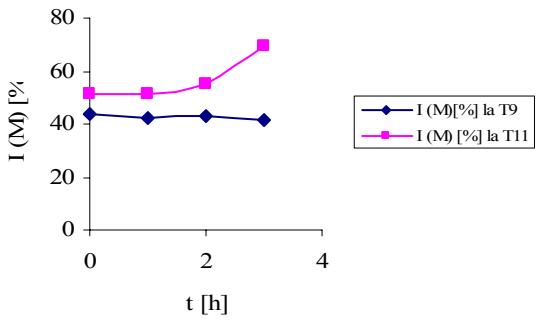

Fig. 10 . *The influence of magnetic field continuous current, on the Feα(M)-44,98˚phase distribution, function by wear-tests lenght (Q= 150 daN, ξ=10%)-code V*

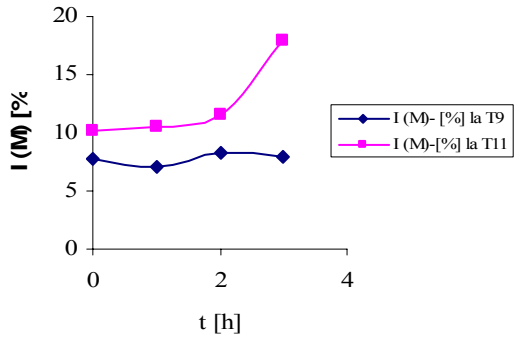

Fig. 11 . *The influence of magnetic field – alternative current (T11) on the Feα(M)-82,5˚ phase distribution, function by wear-tests length. (Q= 150 daN, ξ=10%)-code V*

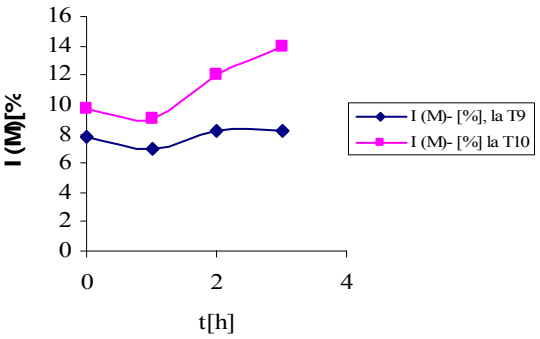

Fig. 12 . *The influence of magnetic field – continuous current (T10) on the Feα(M)-82,5˚ phase distribution, function by wear-tests length. (Q= 150 daN, ξ=10%)-code V*

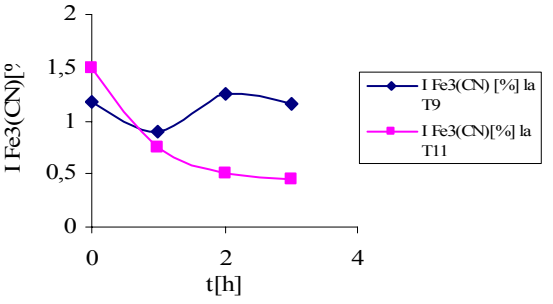

Fig. 13 . *The influence of magnetic field - current alternative-(T11) on the Fe_3CN) phase distribution, function by the wear-tests length (Q= 150 daN, ξ=10%)-code V*

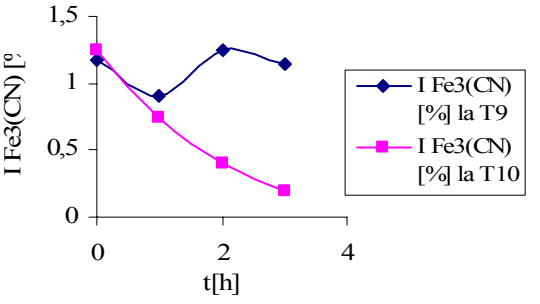

Fig. 14 . *The influence of magnetic field – continuous current -(T10) on the Fe_3CN)phase distribution, function by the wear-tests length (Q= 150 daN, ξ=10%)-code V*

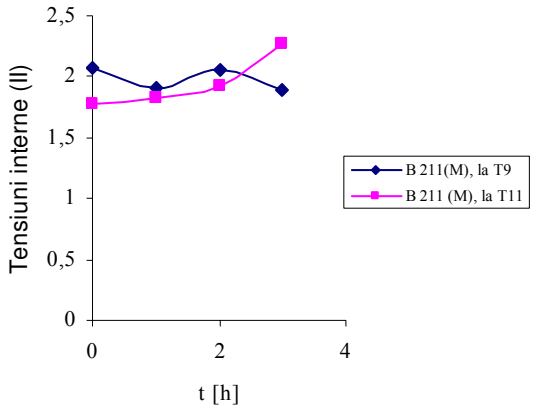

Fig. 15. *The influence of magnetic field (alternative c.)(T11) on the internal tensions- II (B 211 ~σ_{II}), function by friction process length (Q= 150 daN, ξ=10%)- code V*

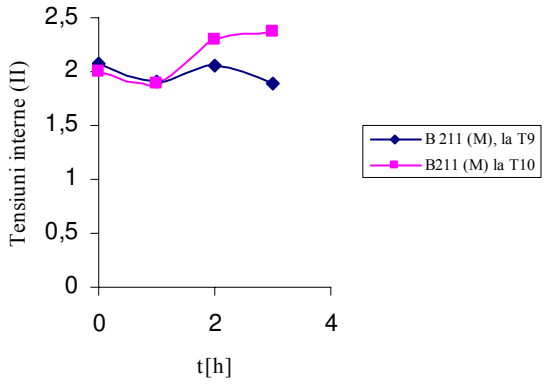

Fig. 16. *The influence of magnetic field (alternative c.)(T10) on the internal tensions- II (B 211 ~σ_{II}), function by friction process length (Q= 150 daN, ξ=10%)- code V*

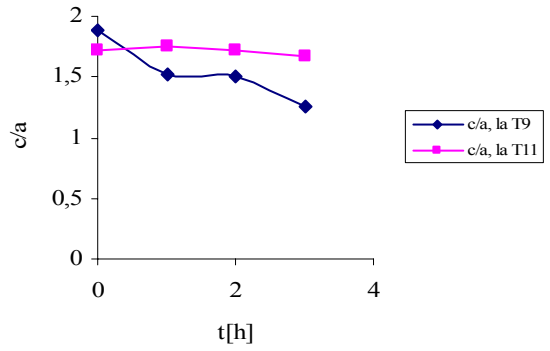

Fig. 17 . *The influence of magnetic field (alternative)-T11 on the martensite thetragonality grade evolution (c/a), function by wear-tests (friction process) duration. (Q= 150 daN, ξ=10%).- code V*

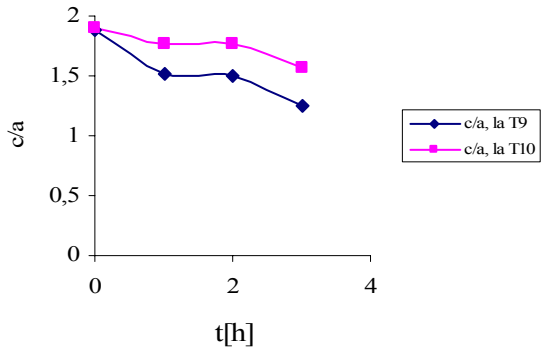

Fig.18. *The influence of magnetic field (continuous)-T10 on the martensite thetragonality grade evolution (c/a), function by wear-tests (friction process) duration. (Q= 150 daN, ξ=10%).- code V*

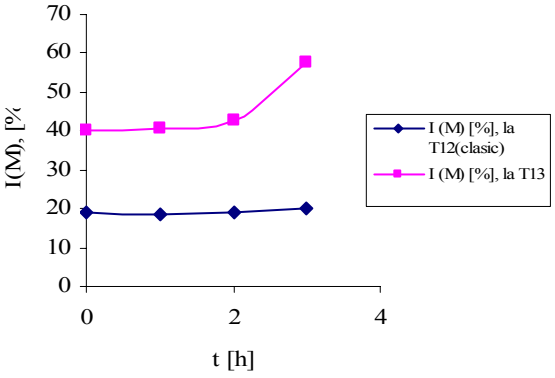

Fig. 19 *. The influence of magnetic field - current alternative (T13) on the Feα(M)-44,98˚ phase distribution, function by friction process length, (Q= 150 daN, ξ=10%).-code R*

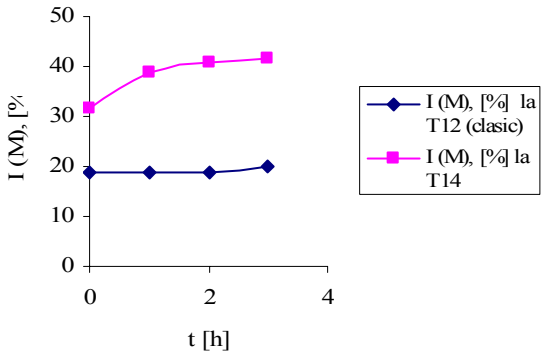

Fig. 20. *The influence of magnetic field - current continuous (T14) on the Feα(M)-44,98˚ phase distribution, function by friction process length, (Q= 150 daN, ξ=10%).-code R*

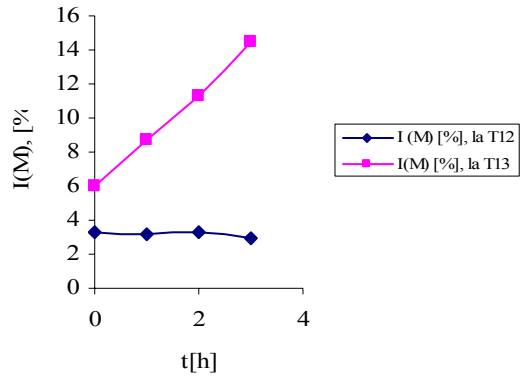

Fig. 21. *The influence of magnetic field -current alternative(T13) on the Feα(M)-82,5˚ phase distribution function by friction process length, (Q= 150 daN, ξ=10%).-code R*

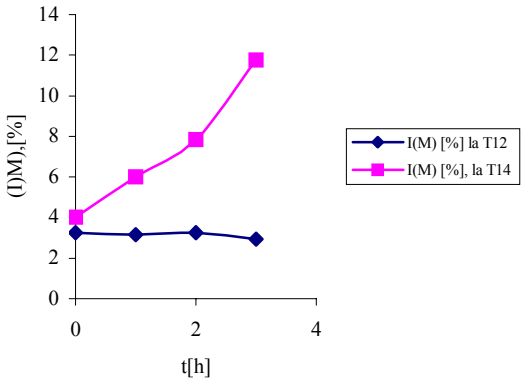

Fig. 22. *The influence of magnetic field -current continuous (T14) on the Feα(M)-82,5˚ phase distribution, function by friction process length, (Q= 150 daN, ξ=10%).-code R*

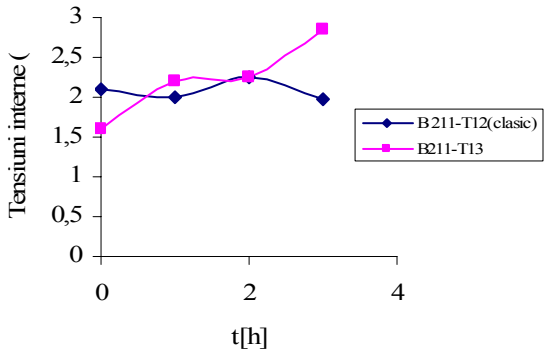

Fig. 23. *The influence of magnetic field (alternative c.)(T13) on the internal tensions- II (B 211 ~σ_{II}), function by friction process lenght (Q= 150 daN, ξ=10%)- code R*

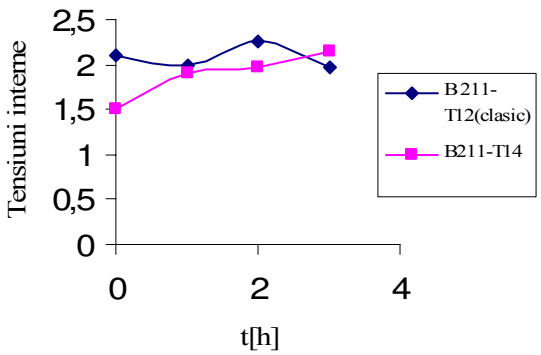

Fig. 24 . *The influence of magnetic field (continuous c.)(T14) on the internal tensions- II (B 211 ~σ_{II}), function by friction process lenght (Q= 150 daN, ξ=10%)- code R*

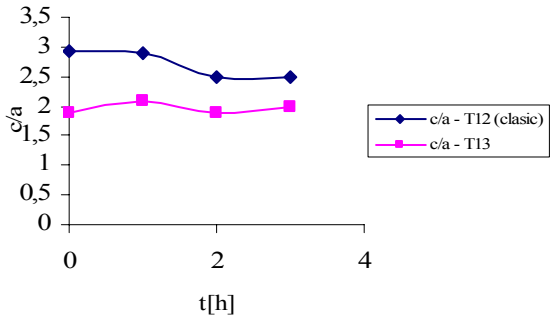

Fig. 25 . *The influence of magnetic field (alternative)-T13 on the martensite thetragonality grade evolution (c/a), function by wear-tests (friction process) duration. (Q= 150 daN, ξ=10%).- code R*

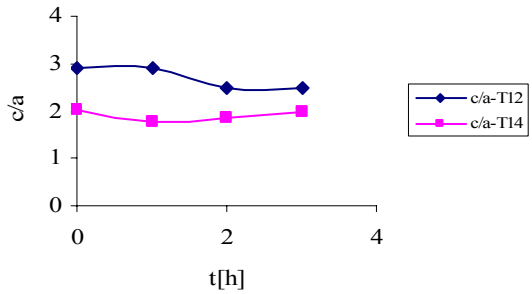

Fig. 26. *The influence of magnetic field (continuos)-T14 on the martensite thetragonality grade evolution (c/a), function by wear-tests (friction process) lenght. (Q= 150 daN, ξ=10%).- code R*

3. Conclusions

Applying the thermal-chemical treatament implies to make a hard layer into a heat treated (improved) core of a relatively low hardness as compared with the hardness obtained after the thermal-chemical treatment.

This research was focused on:

a). Improving the wear resistance characteristics of the thermo–magnetic treated surface layer by applying the thermo–magnetic *treatment to the piece core*. The modifications induced by the magnetic field to improve the core, have triggered the modifications of the mechanical and structure properties of the thermo-chemical treated layer. There is an obvious influence of the therm-magnetic treatment applied to the core on the structure of the thermo-chemical treated surface layer [4,6] (see the figures: 9 -26).

b). Continuity of the thermo-chemical treated layer tested to wear resistance and checking the results on three roller-type samples obtained under the same manufacturing and treatment conditions and tested in the same strain conditions for each thermo-chemical-magnetic treatment.

Another research direction was the study of the influence of the thermo-magnetic treatment applied before the thermo-chemical treated surface layer when applying plasma nitrocarburation. In a first stage, the samples of microstructures were analyzed after applying the thermo-magnetic treatment and, in the second stage, the microstructures after applying the thermo-chemical treatment of (plasma) nitro-carburization.

It has been shown that, when applying an alternative current magnetic field treatment (for example H=1300A/m), the thickness of the thermo-chemical treated layer increased up to 25% as compared to the conventional thermal, thermo-chimical treatment (H=0 A/m) without a magnetic field.

Microstructures achieved on heat/magnetic/chemical and plasma nitrocarburation treated samples show that the thickness of the heat/chemically treated surface layer is higher when applying the heat/magnetic treatment (for example, a.c. magnetic field) with steel 38MoCrAl09 (code R), vs. the conventional treatment case - magnetic field - free treatment [3].

The novelty of the present paper involves the application of the diffusion thermo-chemical treatment after the thermo-magnetic one, the temperature of the former being lower than that of the latter, except that the thermo-chemical treatment applied after the thermo-magnetic treatment should not modify – due to the high temperature - the improvements of the mechanical properties by the thermo-magnetic treatment The positive influence of the volume thermo-magnetic treatment on the surface layer treated thermo-chemically resulted in a higher hardness [4] and the wear resistance by the decreasing the depth of the used layer [4] by approx. 50% -in case of steel 38MoCrAl09 and by 40% - in case of the steel 42MoCr11, which has been proved by the wear tests and the evolution of the mass loss through wear and wet friction (see figures: 6,7,8).

References

[1]. Berkowitz, A.E., s.a., 1969 , « Magnetism and Metallurgy », Academic Press, New York and London,

[2]. Bozorth, R.M., 1951, "*Feromagnetism*", New York, Van Nastrand, Co.Inc.

[3]. Cedighian, S., 1974, "*Materiale magnetice*", Editura Tehnica, Bucuresti

[**4]. Papadatu, C.P.**, 2005, « *Cercetări privind ameliorarea proprietăţilor şi creşterea fiabilităţii unor oţeluri folosite în construcţia utilajelor metalurgice* » - Teza de doctorat, Galaţi

[5]. Popescu, N., s.a., 1990 , "*Tratamente termice neconvenţionale*", Editura Tehnice, Bucureşti, pag. :105-117

[6]. Papadatu, C.P., 2006, "*Posibilitati de imbunatatire a calitatii unor oteluri utilizate in industria metalurgica",* Editura Fundatiei Universitare Dunarea de Jos, Galati

[7]. Stefanescu, I., 1984,Teza de doctorat, Galaţi

[8]. Stefanescu, I., 1981, « *Contribuţii la studiul influenţei tratamentelor termomagnetice asupra unor caracteristici mecanice ale oţelurilor de rulmenţi RUL1* », Suceava

[9]. Vonsovschi, S.V., 1956, **«** *Teoria modernă a magnetismului* », Editura Tehnica, Bucureşti

[10]. Papadatu, C.P., 2008, "*Aspects regarding tribological behaviour of nitrocarburized superficial layer applied after thermo-magnetic treatments, using X-ray diffractometry",* Buletinul Institutului Politehnic din IASI, Tomul L,Fasc.6A/2008, ISSN 1011-2855;

[11]. Gheorghies, C., Papadatu, C.P., Stefanescu I., 2004, "*Study on the model of behaviour of some non-conventional treated steels, during friction process",* CENTIMFE, Marinha Grande, Portugal

[12]. Papadatu, C.P., Stefanescu, I., 2005, *"Experimental study on the behaviour of some non-conventional treated steels during friction process (I)"*, Tanger, spol.s.r.o., Ostrava

[13]. Papadatu, C.P., 2007, "*Some aspects regarding tribological behaviour of nitrocarburized superficial layer after thermo-magnetic treatments applied to steels, during friction process"*, Tanger, spol.s.r.o., Ostrava.

THE ANNALS OF "DUNAREA DE JOS" UNIVERSITY OF GALATI.
FASCICLE IX. METALLURGY AND MATERIALS SCIENCE
N^0. 1 – 2008, ISSN 1453 – 083X

MECHANICAL RESISTANCE ON COLD WELDING ACHIEVEMENT BETWEEN COGGED SURFACES

Bogdan GEORGESCU, Valeriu GEORGESCU
"Dunarea de Jos" University of Galati
e-mail: valeriu.georgescu@ugal.ro

ABSTRACT

Cold welding on cogged surfaces is a technology developed by researchers from Robotics and Welding Department, Dunarea de Jos University of Galati. Easily deformable samples, having plane surfaces, are pressed on cogged surfaces of harder samples. The paper presents several experimental results regarding mechanical resistance on cold welding achievement. Welded joints between aluminum and copper, brass, carbon steel, stainless steel have been obtained. The maximum mechanical strength is obtained at the deformation rates 20...30%, value obviously much lower that the one characterizing the usual cold welding (minimum 70%). While the tensile strength of the joint is low (around 10% of the tensile strength of the parent metal), the shearing strength is much relevant.

KEYWORDS: Mechanical Resistance, Cold Welding.

1. Introduction

Several theoretical aspects can justify our theory regarding the necessity of cogging the surface:

⇨ A welded sloped or tacking surface is greater than the plate's area (to be weld) normal section, as fig. 1a presents. That's why the strength total amount increases; even per square area strength is diminished due to the point like clinching of the materials or microscopic inclusions.

⇨ As other researchers confirm that the normal and tangential stresses existence makes the clinching and welding processes easier, improving joint strength and diminishing the material deformation rate for weld achievement.

⇨ It is known that in the joining area, reciprocal materials displacement with small velocity are produced, making possible the rapid slip-out of the oxide layer and the materials stick cold welding. Our theory regarding cold welding between cogged surfaces is based on the small material displacements when low pressure is applied, to the exterior cogged surfaces lengthwise [2].

Our intention was to cold weld an aluminum plate normally pressed with another one, with cogged surface, made from a different material with increased hardness.

Due to the normal pressing force applying, we expect the cold welding achievement at a lower material deformation degree, meaning that even the process necessary pressing force will be reduced.

Applying this method, small bimetallic objects, made from dissimilar metals can be obtained, at a single up-set of usually equipment [5].

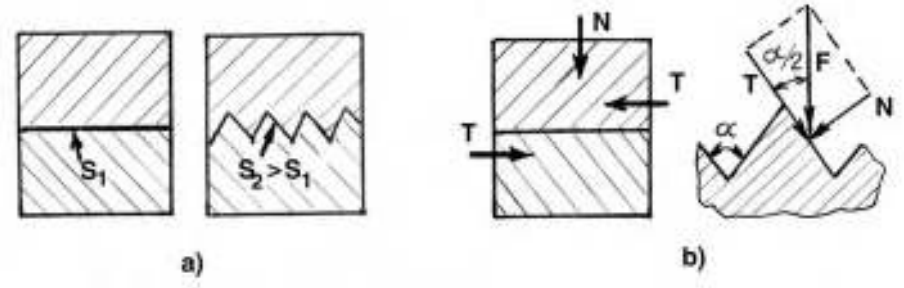

Fig. 1. *Cogging advantages: a – increasing welding surface; b – easy achievement of the normal and tangential stresses [2].*

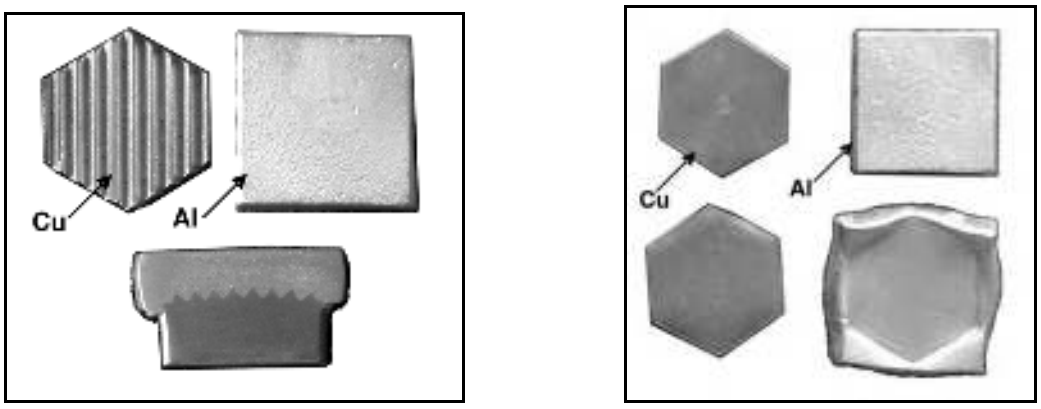

a) **b)**

***Fig. 2**. Al-Cu pressed samples at the same deformation rate: a) weld on cogged surface; b) un-weld samples on plane surfaces [7].*

2. Preliminary Tests

Tests on the above theoretical assumptions were performed on small samples made from aluminum and different metals as stainless steel, brass or copper. Triangular shape cogs, 3 mm metric module pitch, at a 60^0 angle, were machined on the hardest samples surface.

Plates joining areas were mechanically cleaned with a rotating wire-brush. After that, the plates were up-set without limiting the pressing machine stroke. A shearing resistant cold-welded joint was obtained. Although the coupled materials resultant deformation is smaller than usual, the joint was achieved due to the aluminum component. The plate's total deformation rates calculated as the ratio between the materials displacements and the initial thickness was about 20% [8]. The practical advantage of the cold welding on cogged surfaces is due to the fact that the joint is obtained only by deforming the easily deformable sample, at lower deformation rates than in the case of classical cold welding [7]. This aspect is illustrated in fig. 2. At the same deformation rate, the weld was achieved only in case of pressed samples on cogged surfaces; the pressed plane samples couldn't be joined.

From the welded plates cross section image it can be noticed that aluminum fills completely the space between the cogs.

3. Specimens for Mechanical Tests

The specimens were used to determine the minimum deformation rate of the materials when the cold welding process on cogged surfaces starts, respectively its influence on the joint tensile strength. To determine the moment when partial mechanical links between the two materials are initiating, the welded samples were used as tensile test specimens [1]. As fig. 3 shows, the cylindrical components have a M12 threaded hole to mount a double-ended bold before up-setting. After pressing, the cold welded joints were tensile tested, using two intermediary clamping nuts assembled on the bolts free ends. The direct clamping in the tensile testing machine's devices is avoided, because it may introduce supplementary stresses in the joint area.

The specimens' components were made from different materials as aluminum, brass, copper, steel and stainless steel. The aluminum parts had a smooth contact surface, while the others were cogged by cutting.

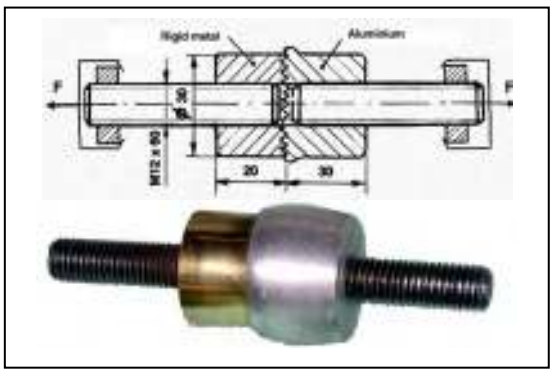

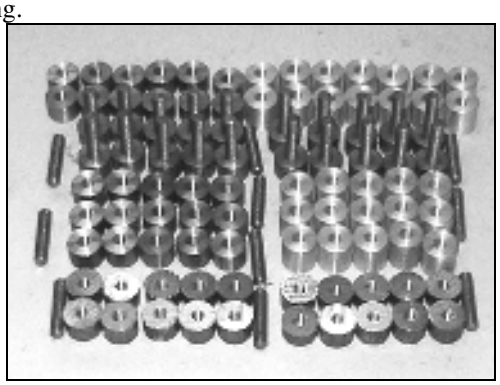

***Fig.3.** Specimens' components [3].*

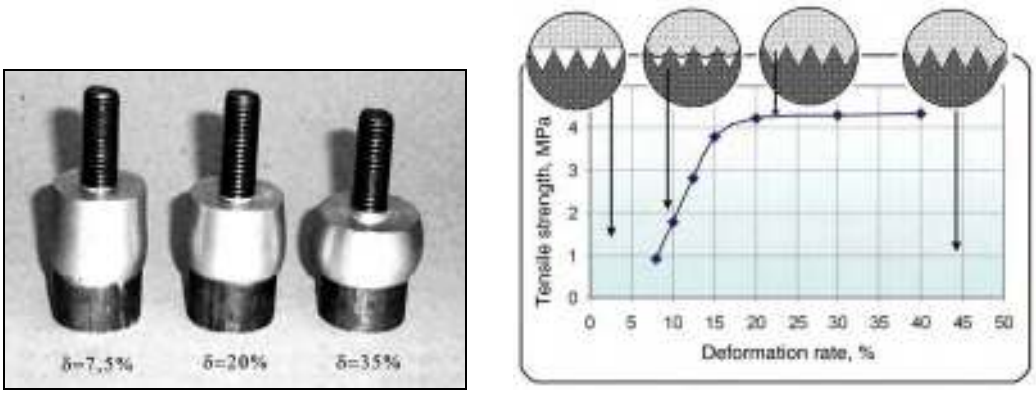

Fig.4. *Tensile strength versus material deformation rate for aluminum-brass couple [4].*

4. Stretching Resistance

We want to determine the minimum deformation degree, which makes possible cold welding achievement, and its influence on joint resistance.

To understand the starting moment of the materials atomic interaction was used as a tension test specimen a cold welded sample, presented in fig. 3. After cold welding achievement, the cylindrical sample with a threaded double-ended bolt was stretched.

The results obtained for aluminum-brass couple are presented in fig. 4. We notice that the cold welding process starts at small material deformation degrees (computed only for the deformation of the aluminum component). The maximum joint resistance is obtained for a material deformation rate $\delta = 15…20\%$ [4].

The reason for this small value can be the cold welding achievement only in isolated contact points of the coupled materials, due to aluminum small displacement and sticking on harder material cogs.

Figure 5 presents the tensile strength - deformation rate dependency in case of cold welding on cogged surfaces of the aluminum with different materials. Analyzing these curves plotted in case of pressing the aluminum component on copper, steel, respectively stainless steel, small differences regarding the joint resistance can be noticed, which allow grouping these materials in two categories [3]:

⇨ 1st group: copper and brass; the joint maximum resistance is obtained at 20% deformation rate (computed only for the aluminum component);

⇨ 2nd group: steel and stainless steel; the joint maximum resistance is lower than in copper and brass case and is registered at 30% deformation rate (computed only for the aluminum component).

In classical butt cold pressure welding case both materials are deformed. This joint's strength depends on the number of the cold welded points (of the contact surface) initiated as a result of the material flowing at deformation rates over 70%. In the case of the contact on cogged surface only the aluminum component is plastically deformed by up-setting.

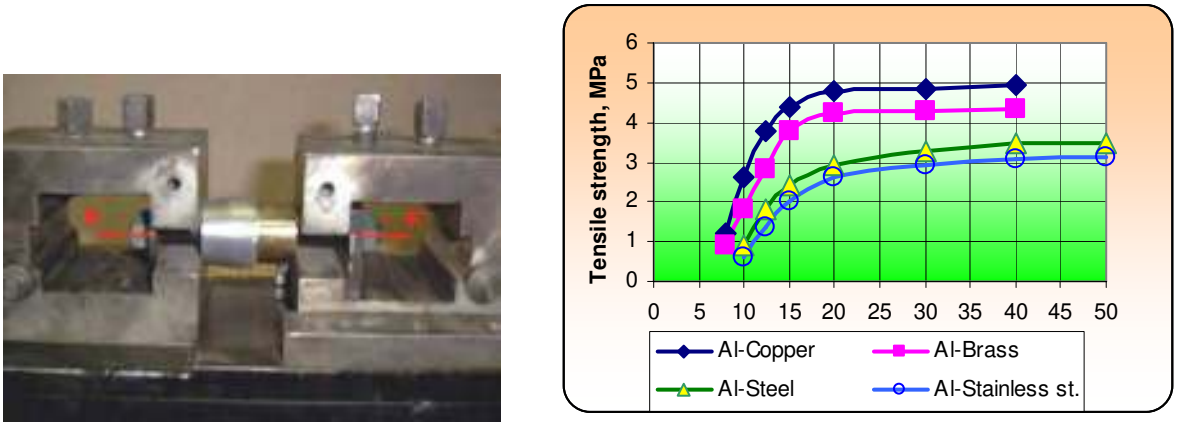

Fig.5. *The tensile strength-deformation rate dependency in case of cold welding on cogged surfaces of the aluminum with different materials [3].*

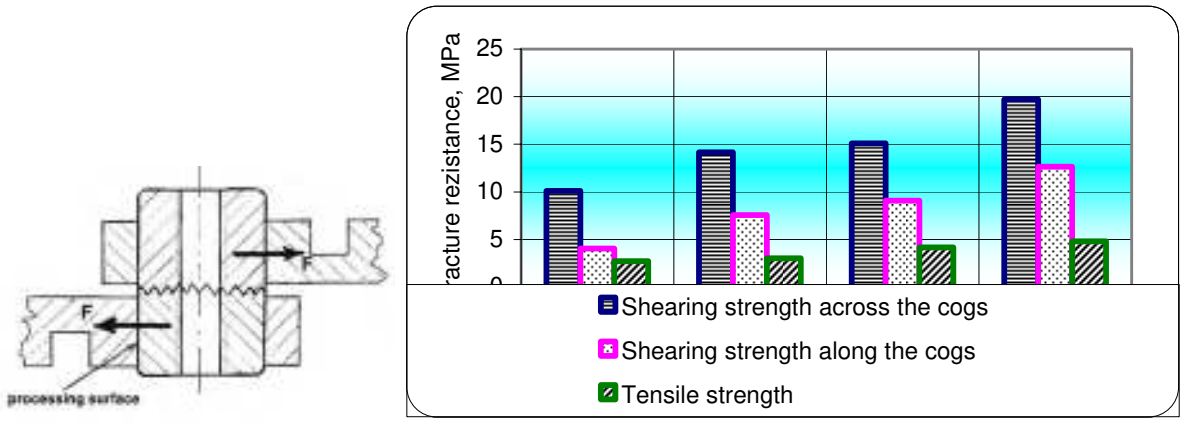

Fig.6. *The fracture resistance for different cold-welded samples on cogged surfaces [6].*

The increase of the aluminum deformation rate over 20-30% doesn't improve the joint strength. When pressing, the aluminum component slips and fills-in the gaps between the cogs. The harder component's cogs stop the aluminum flowing on the contact surface.

The increase of the deformation rate moves the material plastic deformation to a weaker, milder area, situated on the middle of the aluminum component, without any influence on improving the dissimilar joint's strength. This explanation was theoretically and practically confirmed by FEA, respectively by the metallographic analysis [4].

5. Shearing Resistance

Several tests on cold welding were performed. The values obtained for shearing stress are around 10…20 MPa, being greater than the values obtained for tensile strength (fig. 6).

On cogs normal direction, due to a supplementary anchoring of the pressed materials, the shearing stress values are bigger. This anisotropy can be reduced by double cogging (at 90^0) the harder material surface [6].

6. Conclusions

Due to its characteristics, we consider that, for this joining method, the term of cold welding is a little bit too much. In our opinion, appropriate terms would be bonding or adhesion.

The joint is achieved after cleaning and pressing the samples, due to atomic interaction in solid state, without forming common grains.

The stretched samples, pressed again in the same relative position are presenting the same resistance.

Cold welding achievement on cogged surfaces – with or without an intermediate layer – of dissimilar materials gives the possibility of obtaining small bi-metallic or multi-layer samples. The joint is the result of the aluminum 15…20% deformation rate. The joint tensile strength is 10% of aluminum resistance. The joint surface dimension at a single pressing stroke depends on the pressing equipment performance and can be extended, using multiple pressing, along the cogs. Resistance pieces can't be obtained using this method.

References

[1]. Georgescu, B., Iordachescu, M., Georgescu, V., 2005, *Characteristic of the cold welded joints on cogged surfaces*. Intern. Institute of Welding (IIW), Proc. Intern. Conf., Prague – Czech Republic, ISSN 0043-2288, pag. 435-442

[2]. Georgescu, B., Iordachescu, M., Georgescu, V., 2005, *Several aspects concerning cold welding of cogged parts*. The Annals of "Dunarea de Jos" University of Galati, Fascicle XII, Year XVI, ISSN 1221-4639, pag. 5-12

[3]. Georgescu, B., Constantin, E., Georgescu, V., 2005, *Gradul minim de deformare necesar sudarii la rece pe suprafete zimtate*. Revista Asociatiei de Sudura din Romania "SUDURA", ISSN 1453-0384, Nr 3, pag. 23-26

[4]. Georgescu, B., 2006, *Sudarea prin presiune la rece intre suprafete zimtate (Pressure cold welding on cogged surfaces)*, Teza de Doctorat, Universitatea Dunarea de Jos din Galati

[5]. Georgescu, B., 2006, *Sudarea prin presare la rece pe suprafete zimtate*, Cerere de brevet de inventie nr. 2006 00639 / 10.08.2006.

[6]. Georgescu, B., 2007, *Sudarea prin presiune la rece pe suprafete zimtate*, Editura EUROPLUS Galati, ISBN (10) 973-7845-49-8, ISBN (13) 978-973-7845-49-8.

[7]. Georgescu, B., Georgescu, V., 2007, *Study of stresses and strains during cold welding on cogged surfaces – Studiul tensiunilor si deformatiilor din timpul sudarii la rece pe suprafete zimtate,* Revista Asociatiei de Sudura din Romania "SUDURA", ISSN 1453-0384, Nr 2, pag 4-10.

[8]. Georgescu, V., Iordachescu, M., Georgescu, B., 2001, *Practica sudarii prin presiune la rece,* Editura Tehnica Bucuresti, ISBN 973-31-1558-4.

THE ANNALS OF "DUNAREA DE JOS" UNIVERSITY OF GALATI.
FASCICLE IX. METALLURGY AND MATERIALS SCIENCE
N^0. 1 – 2008, ISSN 1453 – 083X

EVOLUTION OF SOME STRUCTURAL FINE PARAMETER IN THE SUPERFICIAL LAYER DURING LOW CYCLE FATIGUE PROCESS

Silviu MACUTA
"Dunarea de Jos" University of Galati
email: smacuta@ugal.ro

ABSTRACT

Using laminate samples, investigations have been realized at variable solicitation of pure bending on a patented machine. The machine has two working places and it can be adjusted for different deformations, frequencies and number of cycles. The tests have developed in a symmetrical alternative regime at two frequencies. In this paper some results concerning the evolution of the crystalline lattice parameter, level of the texture were realized in steps of each two thousand cycles until a limit of 10^4 cycles. The X-ray diffraction method was used and information on the ferrite phase was obtained. The crystalline lattice parameter presents a decreasing tendency when the number of the fatigue cycles increase. This decreasing in jumps occurs. During fatigue tests at high testing frequencies, an increasing texture process is displayed, but at small fatigue testing frequencies, increasing and decreasing texture processes occur. Experimental data allows to estimate the history of the sample and its behavior in fatigue process.

KEYWORDS: steel, fatigue, low frequency, lattice parameter, texture, X-ray diffraction

1. General considerations

In order to perform a complete study of the behaviour of the superficial layer during fatigue test and to evince the main factors, which determine the damage process, the structural cybernetic model was introduced.

In fig.1 this model is presented and it allows to a systematic study of the input parameter changes under action of the commanding ones.

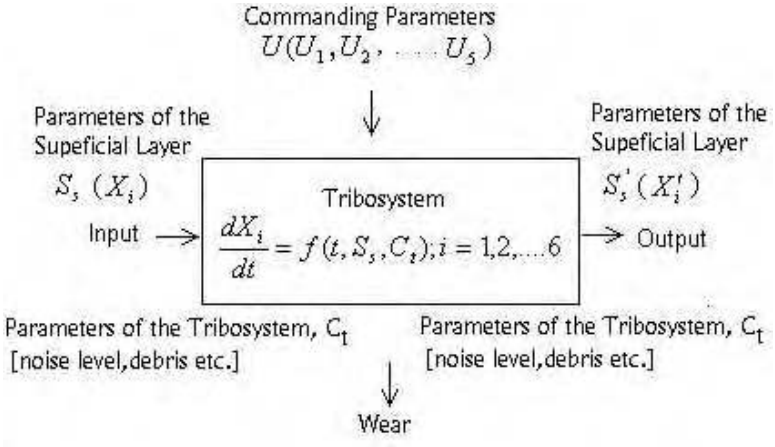

Fig.1. *Used cybernetic model*

The input/out parameters are: superficial layer parameters (S_s-S'_s) [X_1- macro and micro-geometry, X_2 - microhardness and hardness, X_3 – tension state, X_4 – chemical composition, X_5 – structure, X_6 – purity] and tribosystem parameters (C_s) [noise, debris]. Some of the mentioned parameters, as X_2, X_3, X_5, can be changed from exterior such the durability of the material to be in a certain interval.

The commanding parameters (U) [U_1 – nature of material, U_2 – shape of the sample, U_3 – dimension of the sample, U_4 – working medium, U_5 – kinematics, U_6 – energetics] called external factors, by their action can change some superficial layer parameters X_i, i=1 – 6. In our experimental program the evolution of the X_2, X_3 and X_5 was shown by changing U_1 (type of steel: OL 52) and U_5 (testing frequency: ν_1=20 cycles/min, ν_2=40 cycles/min., testing deformation: ε_1=2000 μm/m, ε_2=2500 μm/m, ε_3=3500 μm/).

2. Experiment

We have conducted the examination of material features in fatigue process for two steels used in pressure vessel engineering: OL 52 and 10TiNiCr180. Using laminate samples, the investigations have been performed at variable solicitations of pure bending on a patented machine [1].

The tests have been developed in a symmetrical alternative regime at two frequencies: f_1=20 Hz, f_2=40 Hz.

The deformation domain was established in an experimental program of tests using the resistive tensometry. The deformations of samples were imposed at the superior limit of elastic domain, evaluated from characteristic curves. The deformations imposed in case of OL52 were: ε_1=2000 μm/m, ε_2=2500 μm/m, ε_3=3500 μm/m and in case of 10TiNiCr180: ε_1=1500 μm/m, ε_2=2000 μm/m, ε_3=2500 μm/m, respectively.

In the present paper we presented the experimental results only for OL52 steel. The experiments were performed in steps of two thousand cycles until a limit of 10^4 cycles. In every step, we investigated the lattice parameter and texture level [2, 3]. For this investigation we used an X rays diffractometer, DRON-3.

3. Results and discussions

In figure 2 and 3 the evolution of the lattice parameter for OL 52 steel tested to fatigue process for three imposed strains, ε_1, ε_2 and ε_3 at two frequencies are respectively presented.

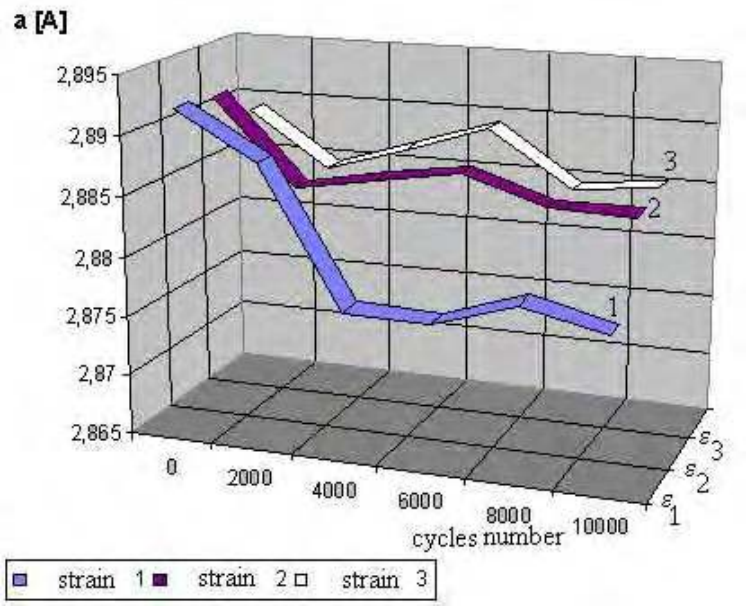

Fig.2. *Evolution of lattice parameter for f = 20 cycles/min*

Analyzing those two figures, a general tendency of decreasing of the ferrite phase lattice parameter, is evinced, when the number of the testing fatigue cycles increases. This occurs for the all imposed strains. A strong decreasing is revealed for small strains and frequencies, respectively for high strains and frequencies. The change of the lattice parameter can be explained by supposing that a migration process of some alloyed elements occurs during fatigue tests. This fact presents validity by a soft

increasing of the lattice parameter during the fatigue test for an established testing cycle number. This increase appears earlar when the strain is bigger. The migration process of atoms in and from elementary cell of the ferrite phase shows the existence of a high kinetic of atoms in the superficial layer during fatigue tests. This kinetic can have negative effects if the material is tested in corroding media.

The migration process is more slowly in case of the small strain and more intensive at high frequencies and big strains; at small strain the process is more intensive at small frequencies. The presented data show that there is the possibility to command from exterior the durability of the tested material by changes of the imposed strain and testing frequencies in a certain range.

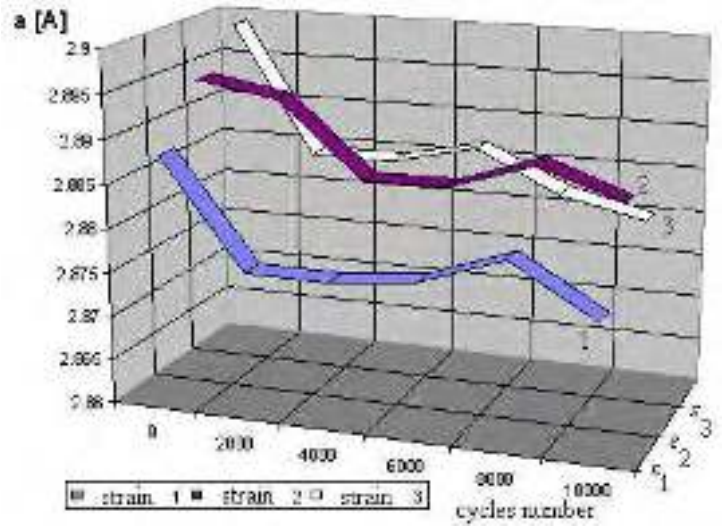

Fig. 3. *Evolution of the lattice parameter for f = 40 cycles/min*

In figure 4 and 5, for 20 cycles/min and 40 cycles/min, the evolution of the texture parameter, measured by ratio I_{max}/I_0, where I_{max} and I_0 are, respectively, the maximum intensities of the X-ray diffraction line (220) of the ferritic phase, for tested and non-tested samples, are presented. From figures, an inverse texture (IT) process of material is evinced. The higher degree of the IT occurs in the case of the bigger strain, ε_3.

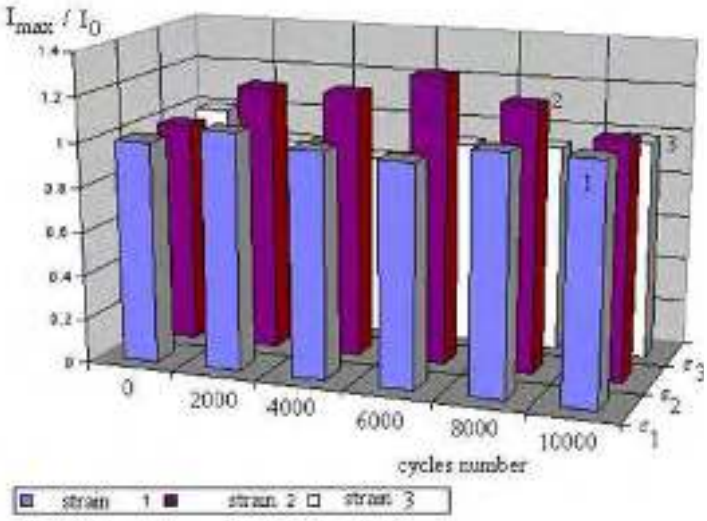

Fig.4. *Evolution of texture level for f = 20 cycles/min.*

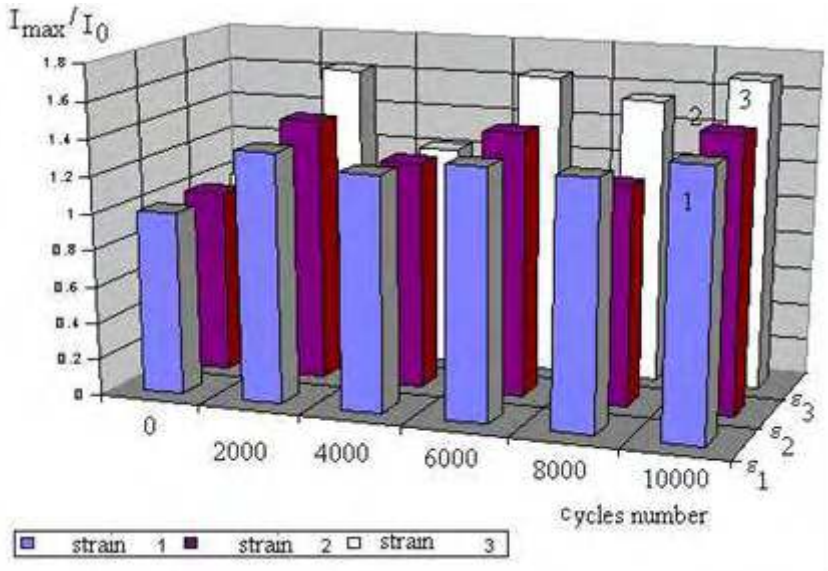

Fig.5. *Evolution of texture level for f = 40 cycles/min*

This IT can be associated to some mechanical micro-processes that lead to a preferential orientation of the crystalline planes in [220] direction in relation to laminated state of material, when $I_{max}/I_0 = 1$.

From the view of the presented histograms, can be analyzed the distribution of the texture degree of steel during fatigue tests and a relationship with plasticity properties can be established.

At small frequencies the material presents a normal hysteresis, but at high value the inertial properties of material are smaller.

Conclusions

1. During fatigue tests, the lattice parameter presents a general tendency of decreasing when the number of the cycles increases, for those three strains and those two frequencies. The decreasing occurs in jumps and can be associated to a migration of alloying elements from steel. The migration process is strongly influenced by number of fatigue cycles and level of strain.

2. During fatigue tests, a texture process of ferrite phase occurs and it is influenced by level of strain and frequencies. The texture process, evinced by X-ray diffraction method, shows data about inertial properties of fatigue tested material. The steel looses the elastic properties when it is tested at high frequencies, the influence of strain not being very important.

References

[1]. I. Crudu, S. Macuta, L. Palaghian, L. Fazekas, 1991, *Patent brevet,* nr.102714, Romania
[2]. C. Gheorghies, 1990, *Control of fine structure of metal by X-rays*, Ed. Tehnica, Bucuresti p.128.
[**3]. Buzdugan, Gh., Blumenfeld, I.,** 1979, *Calculul de rezistenţă al organelor de maşini*, Ed. Tehnică Bucureşti.
[4]. Bogatet, K. Budaci, T., *Sovremennie sredstva dlia ispîtanii na maloticlovaia ustalosti*, Laboratoria nr. 7/1980 pp. 654-658.
[5]. Crudu, I., Măcuţă, S., 1991, *Maşină universală de încercat materiale*, Brevet de invenţie nr. 102714/1991.
[6]. Fouquet, I., *Dislocations et deformation plasique,* Ecole d' été d'Yravals, Paris 1979.
[7]. Karpenko, G., Katov, K.B., Kokotailo, I.V., Rudenko, V.P., 1977, *Maloticlovaia ustalosti stali v rabocih sredah,* Kiev
[8]. Lieurade, M.P., 1987, *La rupture par fatigue des aciers,* Collection IRSID OTUA- Propriétés d'emploui des aciers- études de base, Paris,
[9]. Mocanu, D.S., 1982, *Incercarea materialelor*, vol I-II, k, Ed. Tehnică Bucureşti.
[**10]. Puskar, A.,** 1989, *Microplasticity and failure of metalic materials* Bratislava.
[11]. Strijala, V. A., 1987, *Malotiklovaia ustalosti pri nizkih temperaturah*, Kiev
[12]. Troscenoko, V. T., 1985, *Ticliceschie deformatii I ustalosti metalov*, vol I, Kiev.
[13]. C. Gheorghies, 1990, *Control of fine structure of metal by X-rays*, Ed. Tehnica, Bucuresti 128.
[14]. S. Macuta and C. Gheorghies, 1998, Proc. 15-th Symposium "Danubia-Adria," Sept. 30-Oct. 3, Bertinoro, Italy, 59
[15]. S. Macuta and I. Crudu, 2000, *The Annual Symposium of The Institute of Solid Mechanics*, SISOM 2000, Bucharest, October 26-27 19.
[16]. S. D. Macuta, C. I. Gheorghies and I. Crudu, Proc.2-nd ESAFORM Conf. on Mat. Forming , Guimaraes, Portugal (1999) 199.

THE ANNALS OF "DUNAREA DE JOS" UNIVERSITY OF GALATI.
FASCICLE IX. METALLURGY AND MATERIALS SCIENCE
N^0. 1 – 2008, ISSN 1453 – 083X

ON THE PREDICTION OF THE STRIP SHAPE IN A COLD ROLLING MILL (1700 mm)

Stefan DRAGOMIR, Georgeta DRAGOMIR, Marian BORDEI
"Dunărea de Jos" University of Galati
e-mail: doromir@yahoo.com

ABSTRACT

In this paper is shown a new way for predicting the precision of laminated strip in a cold rolling mill (1700 mm). The increasing demands on the quality of rolled strip; need new technology for monitoring the strip shape, by using complex system control for technological parameter of the rolling mill process. It is very important to reduce the dynamic load, to choose the optimal functionary parameters and modern systems to control the stress, tensions, lamination force and speed in cold rolling mill machine.

KEYWORDS: shape, prediction, dynamic load, monitoring, roll bending

1. Introduction

The shape control determines the deviation of the measured strip tension stress distribution from the selected set point curve. It uses a special procedure to convert the control deviation into a polynomial whose coefficients can be individually assigned to the available execution elements.

These can be: tilt; roll bending; variable crown roll shifting; roll force; strip speed.

Each execution element takes over a component of the control difference according to its "execution element efficiency". The analysis is based on the control deviations, a least square analysis and on the self-adapted execution element efficiencies. In order to coordinate the operation of execution elements which have similar effects, the control system uses a priority principle.

This ensures that the faster execution elements react for the first, the slower execution elements being brought in later so as to achieve the best possible operating point for the faster execution elements. The flatness control procedure then combines the execution element setting so as to ensure, even during the alteration, a coordinated interaction between the execution elements. In this way undesirable tension distribution during the execution element setting is avoided.

The variable combination of the execution element movements, together with the self-learning function for the estimation of the execution element efficiencies allow the application of the control principle for any execution element or stand type.

The control system adapts itself automatically to achieve the best performance for any combination of the available execution elements.

2. Experiments and results

The efficiencies of the mechanical execution elements which are required for the set point calculation and shape control are determined by an "on-line self-learning process" (patent learning).

An accurate knowledge of the execution element efficiencies is a prerequisite for the calculation of the execution element set points and a successful compensation of shape errors. The execution element efficiencies are automatically determined on-line during rolling, using measured data from the rolling mill. The self-adaptive estimation of the plant behavior is based on the execution element control actual values and the associated changes in shape values. The self-learning of the execution element efficiencies takes place in two stages. In the first stage the efficiencies are determined based on the strip width. In the second stage, the efficiencies are determined by functionary of the strip width, the roll force and roll diameters by means of neural networks.

This two stage operation has the advantage that, even after a short time, that is after the first stage, relatively accurate execution element efficiencies are available to the shape control and that no separate.

These accurate execution element efficiencies are also made available to the computer process (setup) for the improvement of the calculated preset execution element position (fig.1).

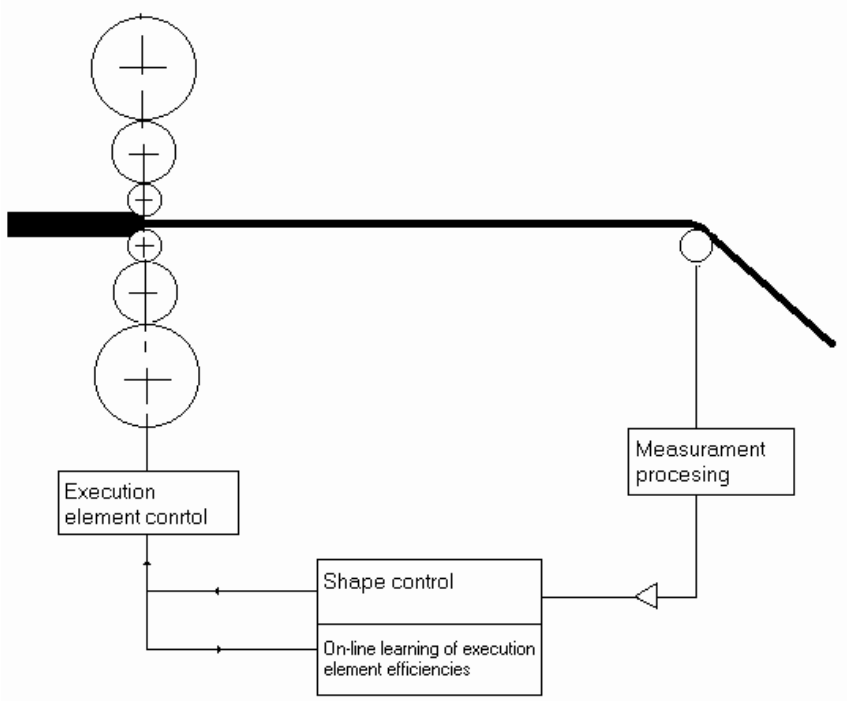

Fig.1. *On – line monitoring system.*

The execution element efficiencies are extremely difficult to determine mathematically being heavily dependent on various operating point parameters, such as for example strip width, roll load, roll diameter and roll shape.

The strip thickness is not only one of the most important quality factors of rolled strip, it is also of vital importance to the rolling process since shape errors lead to non-uniform distribution of tension stresses across the strip width. As this can cause the breaks of the strip in many cases, a reliable measurement of the strip tension distribution or shape is necessary. A measure of the shape of a cold-rolled strip is the strip tension stress distribution, recorded across the strip during rolling.

Unflatness or waviness for a strip is caused by length differences between neighboring segments across the strip. Provided that the material remains completely stressed and within its elastic range, these length differences are converted proportionally into strip tension stresses.

The tension stress distribution across the strip is recorded by the shape measurement roll consisting of a solid body which is divided into individual measuring zone. Each measuring zone contains a sensor which records the pressure resulting from the strip tension. The sensors are inserted in such a way to prevent the transmission of any forces from the roll body, thus torque and force errors caused by roll bending are not transferred to the sensors.

The sensors operate according to the piezzo-electric principle and the recorded signals are processed in charge-coupled amplifiers built into the shape roll. The output of each charge-coupled amplifier is digitized and transmitted over an optical decoupler to the processing electronics.

The processing electronics allocate the signals to the measuring zones, evaluate them and pass them to the monitor for display. Measurement errors are avoided by monitoring the channels continuously and calibrating them automatically. An optimum signal level is ensured by means of automatic amplification switching in the charge-coupled amplifier (Fig. 2.).

The research effectuated on the strip shape concerning the thickness, the length, the width, have the purpose to increase a new quality for laminated sheet. It must control and monitor all the rolling mill parameters (force, tension, mill speed, rolls bending) and also the drive parameters which can be the attribute of a good work for mill. On the monitoring display of the mill stand it can be seen the gauge of strip shape, determined by work roll bending.

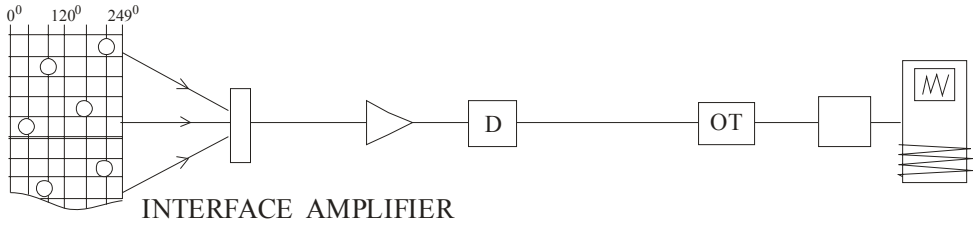

Fig.2. *Shape Measurement, Transmission and Processing*

This tension distribution is recorded and displayed by the shape measurement system (Fig.3.). The shape control has the task of setting the required strip tension stress distribution whereby the roll gap is matched to the strip shape as far as possible. Various execution elements are available to the shape control for this purpose. Any roll force change causes a corresponding alteration of the roll gap profile leading to shape errors which must be corrected by the shape control. This delayed correction is avoided by the implementation of a feed forward control which simultaneously alters the other roll gap execution elements (roll bending) is such a way as to compensate the expected effect of a roll gap change.

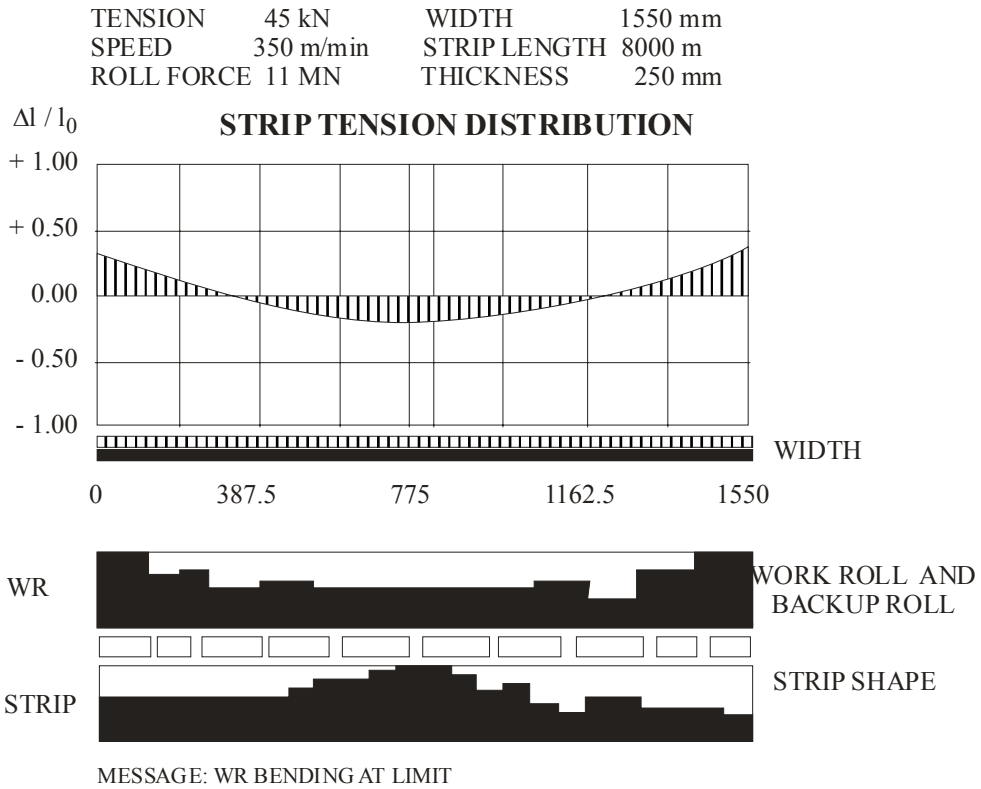

Fig.3. *Shape Display Screen.*

The relationship between roll force changes and changes of the other execution element positions is given by a factor, which is determined by the on-line self-learning function.

A feed forward correction is only executed if it supports the shape control in reducing the shape errors.

3. Conclusions

The strip is subject to additional influences which either cannot be measured or can distort the measurement.

These are mainly:

-temperature variations over the strip width, so far that they cannot be compensated:

-errors resulting from the geometric changes of the measuring path.

-plastic deformation during the winding of the strip on the rewired.

These effects mean that the wound strip will display, after cooling, a different shape characteristic the one measured. These factors can be taken into account by adjusting the shape of the set point curve over the following parameters: edge drop; set point curve from and amplitude; coil shape curve from and amplitude. In addition the operator can undertake an on-line set point curve correction during rolling which has an immediate effect on the tilt, bending or edge drop of components of the shape curve.

References

[1]. Tamiga,T.Furui K., 1990, *Analysis of Complex Phenomenon in Cold Rooling* "Proccedings of International Conference on Steel Rolling, Vol.2, Tokyo,

[2]. Forsyth P.I.E., 1991, The physical basis of Metal Deformation Blockie and Sou, London,

[3]. The Shock and Vibration Digest **,**1992., Published by Shock and Vibration Information Center, Washington D.C.,

[4]. Sungzoon Cho,Yongjung Cho, Sungchul Yoon, 1977, *Reliable Roll Force Prediction in Cold Mill Using Multiple Neural Network*, IEE Transactions On Neural Network, Vol 8, Nr 4.

[5]. Bishop C., 1995, *Neural Networks for Pattern Recognition*. Oxford,U.K:Oxford Univ. Press

[6]. Cohn D., Atlas L., Ladner R., 1994, *Improving generalization with active learning*, Machine Learning, vol.15 no.2, pp.201-221.

[7]. Pohang Iron and Steel Company Tech.Rep., 1989, 2nd Cold Mill Contr. Equipment (PCM part), POSCO, Korea.

[8]. Lee W., 1994, *Improvement of set-up model for tandem cold rolling mill*, Tech. Rep. POSCO Res.Inst.Sci.Technol.

[9]. Pican N, Alexandre F. and Bresson P., 1996, *Artificial neural networks for the presetting of a steel temper mill*, IEEE Expert,vol.11, no1. 22-27.

[10]. Portman N., 1995, *Application of neural nerworks in rolling mill automation*, Iron and Steel Eng., vol.72, no.2, pp.33-36.

[11]. Rosen B., 1996, *Ensemble learning using decorrelated neural networks*, Connections Sci.,vol.8,pp.373-384

THE ANNALS OF "DUNAREA DE JOS" UNIVERSITY OF GALATI.
FASCICLE IX. METALLURGY AND MATERIALS SCIENCE
N^0. 1 – 2008, ISSN 1453 – 083X

AUTOMATIC SETTLEMENT SYSTEM OF LIQUID STEEL LEVEL INTO THE TUNDISH FOR CONTINUOUS CASTING MACHINE

Viorel Munteanu
„Dunarea de Jos" University from Galati
e-mail: viorel.munteanu@ugal.ro

ABSTRACT

The increasing quality of steel and a reliability indices of the afferent installations need an automation system for continuous steel casting machines. This paper presents an original solution of automatic settlement of liquid steel debit and level in tundish as well as an analysis of the dynamic behaviour of automatic installation.

The results of continuous casting timing satisfy quite all the quality conditions of technological operations: the level variation stands in admissible limits while the records of the level allow the control of installation functions. During all the experiments, the automatic settlement was stable and reliable.

The realization of automatic settlement system of liquid steel level in tundish is important for the continuous casting slab quality (under the purity aspect of non-metalic inclusions) as well as the surface defects avoidance, with efects over productivity of continuous casting machines and cost reduction.

KEYWORDS: continuous casting machine, tundish, liquid steel level, dynamic behavior

1. Introduction

The increasing quality of steel and a reliability index of the afferent installations need an automation system for continuous steel casting machines.

The spatial mechanism of closing gate represents an element of automatic settlement system of level in tundish [2]. In the following paper there is an original solution of automatic settlement of level in tundish and an analysis of the dynamic behaviour of automatic installation.

2. The automatic settlement algorithm of liquid steel level in tundish

The automatic settlement system adoption needs a reliable mechanism, taking into account that the mechanism is running in heavy conditions. The use of a settlement system with continuing action should lead to a permanent running of the spatial mechanism, resulting in its pronounced wear. The basic idea of the proposed system consists in running a mechanism, that works in heavy conditions (mechanic and thermic variations), with an adequate electric system command that works in parsing. The idea is the adoption of a settlement system with sampling. Sampling period, T, is adopted equal to 10 s.

At a some discrete value of time kT, (k = 0, 1, 2, ….), it runs the next processes that compare the reaction purveyed by the signal of transducer, with the reference signal; if the resulted error in absolute value surpasses an imposed limit then, a short displacement commands the adequate assignment quantity. If the error is smaller than the imposed limit, the mechanism is not activated. Between the sampling periods, the mechanism stands.

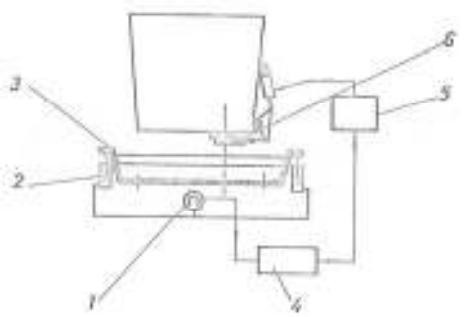

***Fig. 1**. Draft of settlement system of liquid steel level in tundish.*

The tenet draft of the settlement system of liquid steel level in tundish is given in figure 1, in which: 1 is pressure traductor, 2 – hydraulic drum, 3 – tundish, 4 – command element by impulses (with sampling), 5 – execution element, 6 – mechanism with sliding gate.

The move and the vertical position of the tundish is adjusted by a hydraulic installation with a behaved electric pump and four hydraulic cylinders with lifter rods and pistons, placed on the sustenance support of the tundish-car. Assigned uniform task on the sustenance pistons of tundish creates in the hydraulic cylinder a pressure which can be metered. [1]

The level variation in the machines tundish of continuous casting translates in the pressure variation from the hydraulic cylinder of tundish sustenance, which it transmited to transducers in unified system or pressure-gauges with electric contacts.

The reaction signal, given by transducers is transmitted by impulses to the command element, which is a tripozitional controller with sampling. Delicate purveyed command by the controller applies hydraulic execution element, which acts the rectifying mechanism of passage reach.

The running tenet of automatic settlement system of level in tundish is ilustrated by the given diagram in figure 2, in which enters the indicial reply of h(t) system, to an applied variation of reference, the execution size action x_m (the settlement organ opening), and also the delicate purveyed command controller.

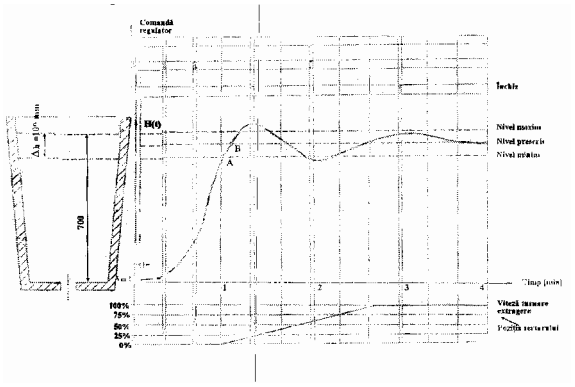

***Fig. 2**. The running tenet of automatic settlement system of liquid steel level in tundish*

3. Automatic dynamics installation study

The representation by input-output sizes of the formed installation is given in figure 3, in which: h is the level (the output size), x_m – case opening (execution size), x_{p1} – liquid steel level in the casting container, x_{p2} and x_{p3} – settlement organs position to the exhaust from tundish, x_{p4} – metal temperature, x_{p5} – steel quality etc. (x_{pk}, k = 1, 2, …, are disturbed sizes).

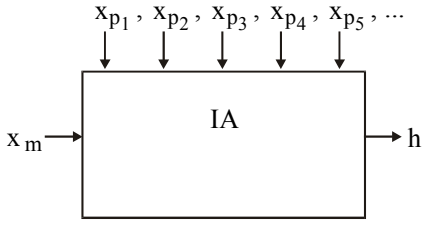

***Fig. 3**. The formed installation representation by input-output sizes.*

The mathematical pattern of automatic installation is formed from state equation, representing the material balance-sheet in tundish and from the relations which explain the intermediate variables which appear in the state equation.

The material balance-sheet equation is:

$$\frac{d(V\rho)}{dt} = Q_1 - Q_2 \qquad (1)$$

in which:

V is the liquid steel volume;

ρ – steel consistency

Q_1 and Q_2 – input debits and, respectively, the output debits.

It does the next hypotheses, according to the physical process:

- The liquid steel temperature variation is negligible, therefore, ρ = constant;
- The interest variation of free surface liquid, in the stabilization behaviour of level is negligible.

For a given quality of steel, the disturbed sizes which intervene are: x_{p1}, x_{p2} and x_{p3}.

From the relation (1), with the exposed hypotheses, results:

$$A \cdot \rho \frac{dh}{dt} = Q_1 - Q_2 \qquad (2)$$

where, A is the free surface area of liquid.

The input debit in tundish is:

$$Q_1 = S(x_m) \cdot \rho \cdot 60 \sqrt{\frac{2gh_1}{2 + \lambda \frac{L}{D}}} \qquad (3)$$

in which:

$S(x_m)$ is constructive characteristic of settlement organ to the steel exhaust from the casting container;

h_1 – liquid level from the casting container;

D – rated diameter of outflow orifice;

λ - endurance ratio (constant);

L – by-pass span.

The relation (3) be written also can under form:

$$Q_1 = k_1 \cdot S(x_m) \cdot \sqrt{h_1} = k_1 \cdot S(x_m) \cdot \sqrt{x_{p_1}} \qquad (4)$$

where, k_1 is a ratio depending the static running point parameters on settlement organ characteristic.

Alike, it is inferred the debit relation to the exit from tundish:

$$Q_2 = k_2 \cdot \sqrt{h}\left[S_1\left(x_{p_2}\right) + S_1\left(x_{p_3}\right)\right] \quad (5)$$

in which $S_1\left(x_{p_2}\right)$ and $S_1\left(x_{p_3}\right)$ are the constructive characteristics of settlement organs to the steel exhaust from tundish, while k_2 is a suchlike ratio k_1.

The non-linear pattern of automatic installation is:

$$A\rho\frac{dh}{dt} = k_1 S(x_m)\sqrt{x_{p_1}} + k_2\sqrt{h}\left[S_1\left(x_{p_2}\right) + S_1\left(x_{p_3}\right)\right] \quad (6)$$

As the installation functions in stabilization behaviour of level, the mathematical pattern can be lineared around rated running point. Considering that all the physical sizes from system hold a constant component (the par) and a variable component, relatively small tcompared to the par, namely:

$$h = \bar{h} + \Delta h and x_m = \bar{x}_m + \Delta x_m and x_{p_k} = \bar{x}_{p_k + \Delta x_{pk}}, k = 1,2,... \quad (7)$$

where the pars are barred, linearization supposes the relations subrogation (7) in equation (6) and hold the first two terms from the serial development Taylor of non-linear terms

$Q_1 = Q_1\left(x_m, x_{p_k}\right)$ and $Q_2 = Q_2\left(h, x_{p_2}, x_{p_3}\right)$.

It results as that:

$$Q_1\left(x_m, x_{p_1}\right) \cong \bar{Q}_1 + \frac{\partial \bar{Q}_1}{\partial x_m}dx_m + \frac{\partial \bar{Q}_1}{\partial x_{p_1}}dx_{p_1} \quad (8)$$

$$Q_2\left(h, x_{p_2}, x_{p_3}\right) \cong \bar{Q}_2 + \frac{\partial \bar{Q}_2}{\partial h}dh + \frac{\partial \bar{Q}_2}{\partial x_{p_2}}dx_{p_2} + \frac{\partial \bar{Q}_2}{\partial x_{p_3}}dx_{p_3} \quad (9)$$

in which:

$\bar{Q}_1 = Q_1\left(\bar{x}_m, \bar{x}_{p_1}\right)$, $\bar{Q}_2 = Q_2\left(\bar{h}, \bar{x}_{p_2}, \bar{x}_{p_3}\right)$,

while barred derivatives entail the rated running behaviour.

Taking account of the expressions (4) and (5), it results:

$$Q_1 = \bar{Q}_1 + \frac{\partial \bar{S}}{\partial x_m}\bar{k}_1\sqrt{\bar{x}_{p_1}\Delta x_m} + \frac{1}{2}\frac{\bar{k}_1}{\sqrt{\bar{x}_{p_1}}}S\left(\bar{x}_m\right)\Delta x_{p_1} \quad (10)$$

$$Q_2 = \bar{Q}_2 + \frac{1}{2}\frac{\bar{k}_2}{\sqrt{\bar{h}}}\left[S_1\left(\bar{x}_{p_2}\right) + S_1\left(\bar{x}_{p_3}\right)\right]\Delta h + \bar{k}_2\sqrt{\bar{h}}\left[\frac{\partial \bar{S}_1}{\partial x_{p_2}}\Delta x_{p_2} + \frac{\partial \bar{S}_1}{\partial x_{p_3}}\Delta x_{p_3}\right] \quad (11)$$

In fixed behaviour there are the valid relations:

$$\bar{Q}_1 = \bar{Q}_2 = \bar{Q} \quad (12)$$

$$\frac{dh}{dt} = \frac{d\Delta h}{dt};\ \bar{k}_1 = \frac{\bar{Q}_1}{S\left(\bar{x}_m\right)\sqrt{\bar{x}_{p_1}}};$$

$$\bar{k}_2 = \frac{\bar{Q}_2}{\sqrt{\bar{h}}\left[S_1\left(\bar{x}_{p_2}\right) + S_1\left(\bar{x}_{p_3}\right)\right]} \quad (13, 14, 15)$$

and from the relations (10) and (11) it is calculated grafo-analytically, utilizing the constructive characteristic plots of settlement organs.

$$\frac{\partial \bar{S}}{\partial x_m} = \frac{\Delta S}{\Delta x_m}\bigg|_{\bar{x}_m} = S_1 \text{ and}$$

$$\frac{\partial S_1}{\partial x_{p_{2,3}}} = \frac{\Delta S_1}{\Delta x_{p_{2,3}}}\bigg|_{\bar{x}_{p_{2,3}}} = S_{2,3} \quad (16, 17)$$

Replacing the relations (13) and (17) in equations (10) and (11), it results:

$$Q_1 = \bar{Q} + \frac{\bar{Q}}{\bar{S}}s_1\Delta x_m + \frac{1}{2}\frac{\bar{Q}}{\bar{x}_{p_1}}\Delta x_{p_1} \text{ and}$$

$$Q_2 = \bar{Q} + \frac{1}{2}\frac{\bar{Q}}{\bar{h}}\Delta h + \frac{\bar{Q}}{\bar{S}_{1,2} + \bar{S}_{1,3}}\left(s_2\Delta x_{p_2} + s_3\Delta x_{p_3}\right) \quad (18,19)$$

where are utilized the notations:

$\bar{S} = S\left(\bar{x}_m\right)$, $\bar{S}_{1,2} = S_1\left(x_{p_2}\right)$ and $\bar{S}_{1,3} = S_1\left(x_{p_3}\right)$.

Pursuant to the relations (13), (18) and (19), the state equation of automatic installation becomes:

$$A\cdot\rho\cdot\frac{d\Delta h}{dt} = \frac{\bar{Q}}{\bar{S}}s_1\Delta x_m + \frac{1}{2}\frac{\bar{Q}}{\bar{x}_{p_1}}\Delta x_{p_1} - \frac{1}{2}\frac{\bar{Q}}{\bar{h}}\Delta h - \frac{\bar{Q}}{\bar{S}_{1,2} + \bar{S}_{1,3}}\left(s_2\Delta x_{p_2} + s_3\Delta x_{p_3}\right) \quad (20)$$

It can be observed that all the ratios from the lineared pattern equation (20) express contingent on the constructive characteristics or the parameters of installation, as well as contingent on the pars of physical sizes ($\bar{Q}, \bar{h}$ etc.), to the numeric values computation of those ratio is a highly simple problem.

Using the notations:

$$T = \frac{2\cdot A\cdot\rho}{\bar{Q}}\cdot\bar{h};\qquad k_1 = \frac{2\cdot\bar{h}}{\bar{S}}\cdot s_1;\qquad k_2 = \frac{\bar{h}}{\bar{x}_{p_1}} \text{ and}$$

$$k_{3,4} = \frac{2\cdot s_{2,3}}{\bar{S}_{1,2} + \bar{S}_{1,3}}\cdot\bar{h} \quad (21, 22, 23 \text{ and } 24)$$

the linear pattern of automatic installation becomes:

$$T\frac{d\Delta h}{dt}+\Delta h = k_1\Delta x_m + k_2\Delta x_{p_1} - k_3\Delta x_{p_2} - k_4\Delta x_{p_3} \quad (25)$$

whereupon it correponds the flow-process chart from figure 4.

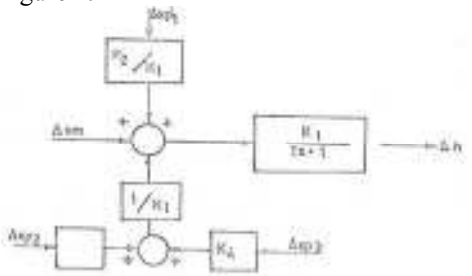

Fig. 4. *Flow-process chart of lineared pattern of automatic installation*

The lineared pattern ratios computation did in hypothesis as the sizes from system have small variances around pars. This hypothesis is valid for all the sizes from the analysed process, except for size $x_{p_1} \equiv h_1$. The use of the analytic relation (23) manages to an incertitude taking into account the value adoption $\overline{x}_{p1}$. In order to care with of this problem, we have the curve families which give the debit Q_1, contingent on h_1 and of equivalent diameter D of outflow reach. In the equation (18), the variable ratio x_{p1} entails average slope of curves which give the debits. Thus, the relation (18) becomes:

$$Q_1 = \overline{Q} + \frac{\overline{Q}}{S} s_1 \Delta x_m + \alpha \Delta x_{p_1} \quad (26)$$

where α entails chart: $\alpha = \frac{\Delta Q_1}{\Delta h_1}\cdot\overline{D}$ (27)

In the final equation, the ratio k_2 will entail the relation:

$$k_2 = \frac{2\alpha\overline{h}}{\overline{Q}} \quad (28)$$

The mathematical pattern of pressure transducer is formally presented:

$$T_T\frac{dx_r}{dt} + x_r = K_T\Delta h \quad (29)$$

where T_T and K_T are the roll parameters of the apparatus.

The mathematical modelling of hydraulic execution element wa pursuant to the acquainted methodology establishment of dynamics equations for a tundish system – hydraulic drum. Considering the cynetic energy filling in the elements found in movement and taking account of noted delay [1] with T_m, in the command transmission electro-hydraulic, the execution element equation is:

$$T'\frac{d^2\Delta x_m(t)}{dt^2} + \frac{d\Delta x_m(t)}{dt} = k\cdot x_C(t - T_m) \quad (30)$$

where x_C is the given command data of the controller.

Flow-process chart of settlement system of level in tundish, with details of mathematical pattern of managed process, is given in figure 5.

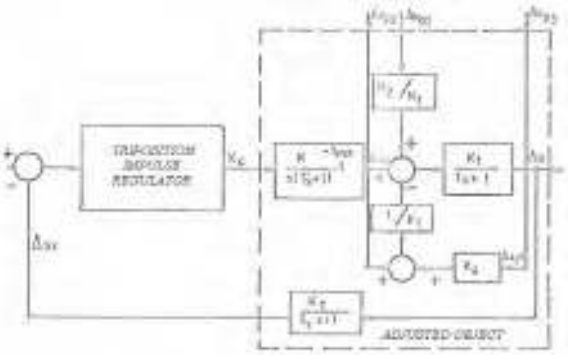

Fig. 5. *Flow-process chart of settlement system of level in tundish*

4. The settlement level system realization in tundish and tests data

The proposed settlement system performances study did by numeric simulation and by experiments on the physical system realized.

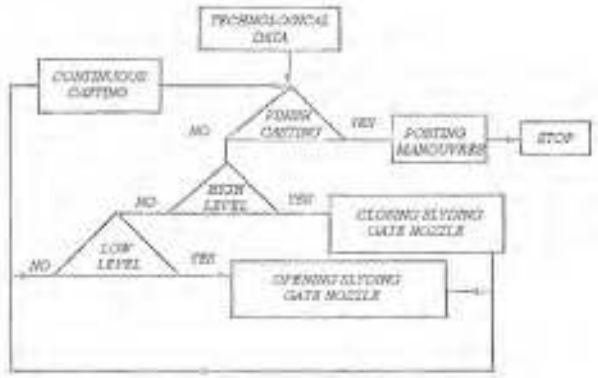

Fig. 6. *Logical draft of command system on the normal function.*

Logical draft of command system on normal function is given in figure 6, while logical draft command of controller by impulses is given in figure 7, in which PA_{max} is the maximum acting pressure, PA_{min} – the minimum acting pressure, DSS – distance between centers, P_{min} and P_{max} – pressure chosen limits.

[1] The delay period determination T_m was realized by experimental way, and qualitative analytic evaluations.

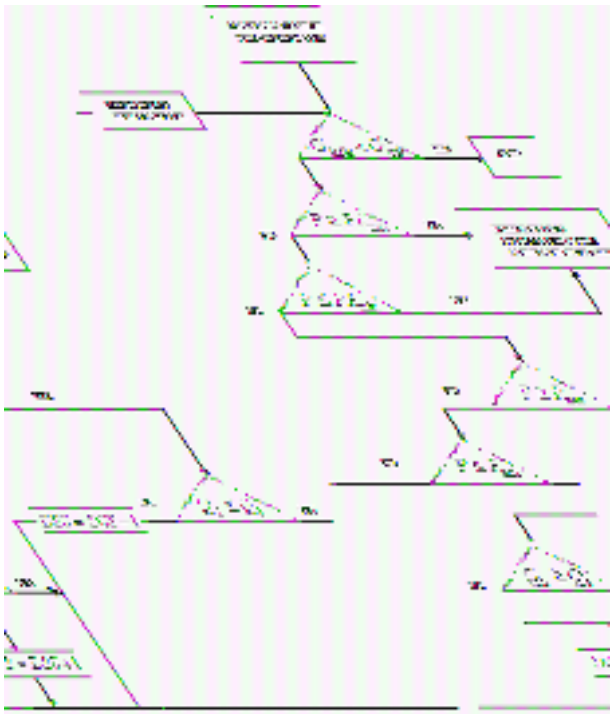

***Fig. 7**. Logical draft of controller by impulses*

Conclusions

The obtained results by continuous casting timing satisfy quite all the quality conditions and technological operations: the level variation stands in admissible limits, the level record allows the control of installation function. In figure 8, are given records of level variation, in manual settlement behaviour and in automatic settlement behaviour.

The records of level variation in manual settlement behaviour and in automatic settlement behaviour as well as the performance indices became decisive in favour of the automatic settlement.
During all the experiments, the automatic settlement was stable and reliable.

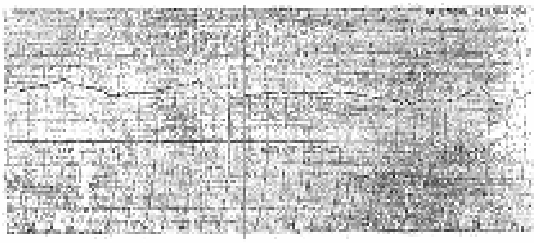

***Fig. 8**. The liquid steel level in tundish in manual and automatic settlement behaviour*

References

[1]. Munteanu V. – *Instalaţie de autoreglare a nivelului oţelului lichid în distribuitorul maşinilor de turnare continuă*, Brevet de invenţie nr. 78734 - România;
[2]. Orănescu A., Munteanu V., Bocioacă R., 1982, *Structural Optimizing of the Sliding Gate Nozzle Devices for Casting Ladles*. Buletinul Universităţii din Galaţi, pag. 49-55;
[3]. Munteanu V., Orănescu A., 2004, *Posibilităţi de optimizare a procesului tehnologic de turnare a oţelului.* Simpozion cu tema „Reducerea consumului de materii prime, combustibili şi energie" Galaţi 8-9 aprilie, pag. 237-243.
[4]. Thomas G., Zhang L., 2001, *Mathematical Modeling of Fluid Flow in Continuous Casting*. ISIJ International, Vol. 41 No.10, 1181-1193
[5]. Thomas G.B., 2004, *Recent Advances in Computational Modeling of Continuous Casting of Steel*. Scanmet II Conference, MEFOS, Lulea, Sweden, 6-8 June 2004
[6]. Munteanu,V., 1984, *Teza de doctorat*, Universitatea ''Dunarea de Jos'' Galati.

THE ANNALS OF "DUNAREA DE JOS" UNIVERSITY OF GALATI.
FASCICLE IX. METALLURGY AND MATERIALS SCIENCE
N^0. 1 – 2008, ISSN 1453 – 083X

INFLUENCE OF THE CHEMICAL COMPOSITION ON THE BEHAVIOR OF AUSTENITIC STAINLESS STEEL IN FLUID LAYER NITRIDING PROCESS

Ovidiu DIMA
"Dunarea de Jos" University of Galati
e-mail: ovidiu.dima@ugal.ro

ABSTRACT

The main factors that influence the stainless steel behavior to the nitriding process are: chemical composition, nitriding temperature, treatment time. Researches have revealed that, with low temperature nitriding, the chemical composition expressed directly by the alloying elements or indirectly by the austenite or ratio E_{Cr}/E_{Ni} stability index decisively influences the characteristics of the nitride layer. The high alloyed steels having over 50% alloying element and high stability index S=30, produce a diffusion layer of a low nitrogen concentration, below the saturation limit, and hardness less than 500 HV_{005}. The usual stainless steels CrNi, CrNiMo of low stability index S=17.5-24 at 500^{o}C, within the sensitive temperature range form high hardness combinations (1200-1400 HV_{005}) and at temperatures of 450^{o}C under the sensitive range, diffusion layers of high nitrogen concentrations close to the saturation limit, featuring high hardness 1100-1200 HV_{005} and slightly lower depths, tens of microns.

KEYWORDS: nitriding process, stainless steel, austenite

1. Introduction

Due to the large variety of austenitic stainless steels subject to nitriding process it is compulsory to investigate their behavior under the specific technological conditions of the nitriding treatment and fluid layer process.

Under similar nitriding conditions, i.e. nitriding atmosphere consisting of nitrogen and 30% ammoniac, gas pressure able to provide smooth fluidization, the enclosure characteristics, it was found that the major factors nitriding behavior depends upon are: the steel chemical composition, nitriding temperature and time.

The chemical composition of the austenitic stainless steels is an extremely important factor which is characterized directly from the concentrations of the chemical elements or indirectly from the austenite stability index S or E_{Ni}/E_{Cr} ratio. Table 1 gives the chemical compositions, the values of the stability index S and E_{Ni}/E_{Cr} ratio for six austenitic stainless steel grades which undergo the nitriding treatment.

Table 1.

Steel code	Steel SR: EN 10283-98	C	Cu	Cr	Ni	Mo	Ti	V	S	E_{Cr}/E_{Ni}
		[%]								
1	X2CrNi18.8	0.12	0.06	23.2	9.8	0.11	0.01	0.02	24	1.78
2	X6CrNi18.10	0.06	0.08	17.1	9.3	0.05	0.60		19	1.26
3	X2CrNi18.9	0.03	0.19	18.9	8.95	0.15	0.01	0.02	17.5	1.95
4	X2CrNiMo17.11.2	0.02	0.27	20.0	8.8	2.7	0.03	0.03	21.6	2.23
5	X6CrNiMoTi17.12.2	0.045	0.16	18.1	11.6	2.04	0.32		22.6	1.48
6	X1CrNiMoCu20.18.7	0.02	0.70	20.1	18.1	6.1		0.2	29.8	1.40

2. Results and discussion

Nitriding process was carried out at 450^{o}C and 500^{o}C for 3 hours. With the steel code 6-X1CrNiMoCu20.18.7 having a concentration of the alloying elements of 50% and a very high austenite stability index S=29.8, the behavior to nitriding was different from that of the other steels, irrespective of temperature or exposure times.

At low temperatures, 450^{o}C and 500^{o}C, the layer hardness was about 500HV$_{005}$ or even lower and the layer depth of tens of microns.

Even lower values of the layer hardness and depth were reported with temperatures below 450^{o}C. This result is accounted for by the low velocity of nitrogen diffusion into the high-alloyed steel and high concentration of Ni and Cu which increase the Ni austenitezed effect.

The high stability index of the austenite prevents the formation of combination layers at all treatment temperatures applied. The diffraction diagram analysis made on DRON confirms the presence of the diffusion layer of austenitic structure for the steel code 6-X1CrNiMoCu20.18.7. The aspect of the diffraction diagram in case of steel code 6 is similar to that of the initial austenitic stainless steel with some modifications determined by the occurrence of phase γ_N. Figure 1 illustrates the presence of drops according to the diffraction angles as determined by the gamma phase γ_{Fe}. With the austenitic stainless steel, the gamma phase is a solid carbon solution in the Feγ which is highly alloyed with Cr Ni Mo etc. It can also be seen the drops of the phase γ_N diffraction angles, which is nitrogen enriched austenite by its diffusion into the inter-atom spaces which cause a slight expansion of the crystalline mesh.

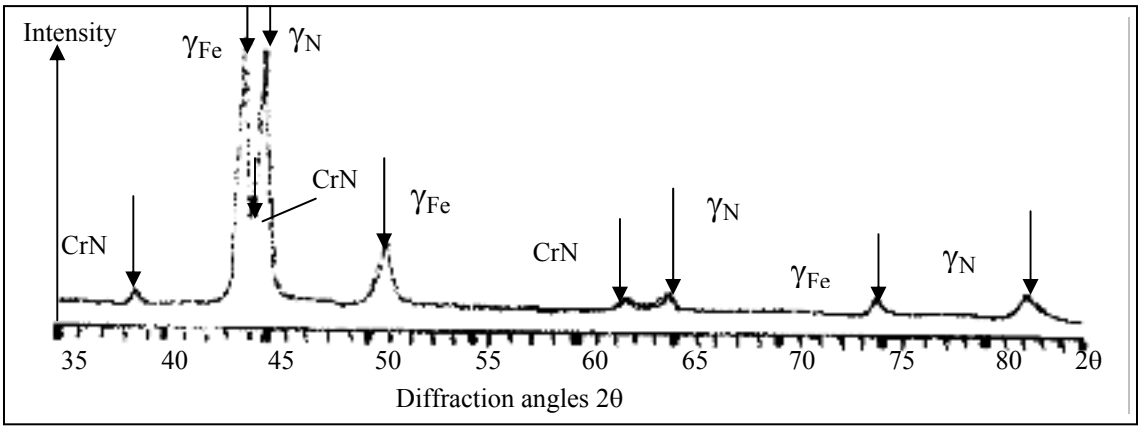

Fig 1. *Diffraction diagram, nitrated sample steel code 6-X1CrNiMoCu20.18.7.*

The austenite nitrogen enrichment results in increased hardness, to a large extent this is also due to the small amount of nitrogen. The max value of hardness reported was 500 HV$_{005}$.

To a lesser degree is visible the phase CrN, the chrome nitrides looking like scarce points in the vicinity of the surface. As mentioned before the steel code 6-X1CrNiMoCu20.18.7 features over 50% alloying elements, a high austenite stability index S=29.8 consequently , the nitrogen gets dissolved into austenite without causing nitride separations but in very small, negligible amounts.

The structure, however, is still austenitic due to the small concentration of dissolved nitrogen. The metallographic analysis carried out on nitrated samples of this steel, figure 2, does not seem to show a distinct layer structure; the layer proved to be a diffusion austenitic layer made up of phases such as γ_{Fe} -austenite and γ_N -nitrogen enriched austenite, whose mesh has a slightly high parameter because the mesh expansion is determined by the penetration of interstitial nitrogen atoms.

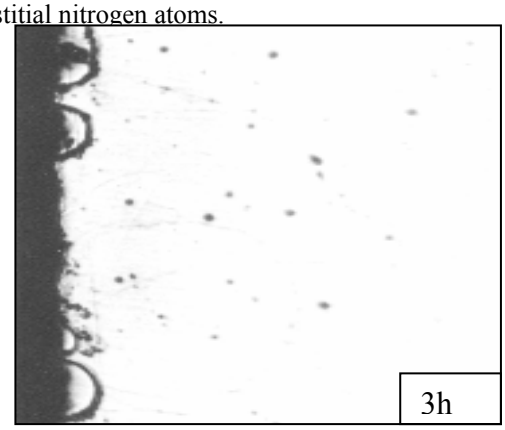

Fig 2. *Microstructure of the nitrated layer at 500^{o}C steel code 6-X1CrNiMoCu20.18.7 x400*

The other steels code 1 –X10CrNi18.8, code 2 – X6CrNiTi18.10, code 3 –X2CrNi18.9, code 4 – X2CrNiMo17.11.2, code 5 – X6CrNiMoTi17.12.2 features a totally different behavior as compared with steel code 6 - X1CrNiMoCu20.18.7 but somehow similar among them. With nitriding at 500^{o}C they formed an external hard layer, hardness varying between 1200-1400 HV_{005}, consisting of nitrogen-enriched austenite and strong nitrides separations CrN, Fe_4N, etc. of high hardness.

The nitride layer could be seen by metallographic analysis figure 3 and figure 4 featuring a distinct structure due to the existing combinations of tens of micron depths.

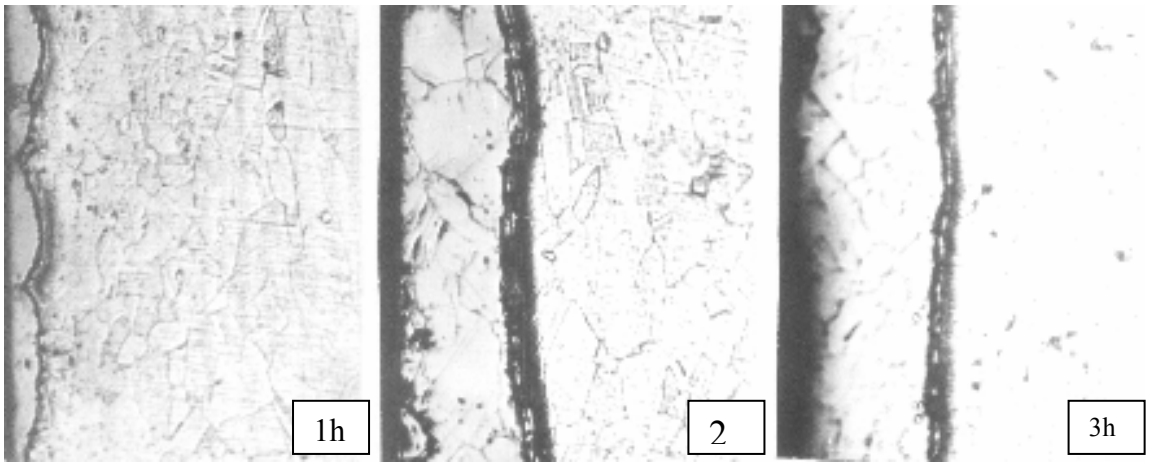

Fig 3. *Microstructure of the nitrated sample of steel code 2–X6CrNiTi18.10*

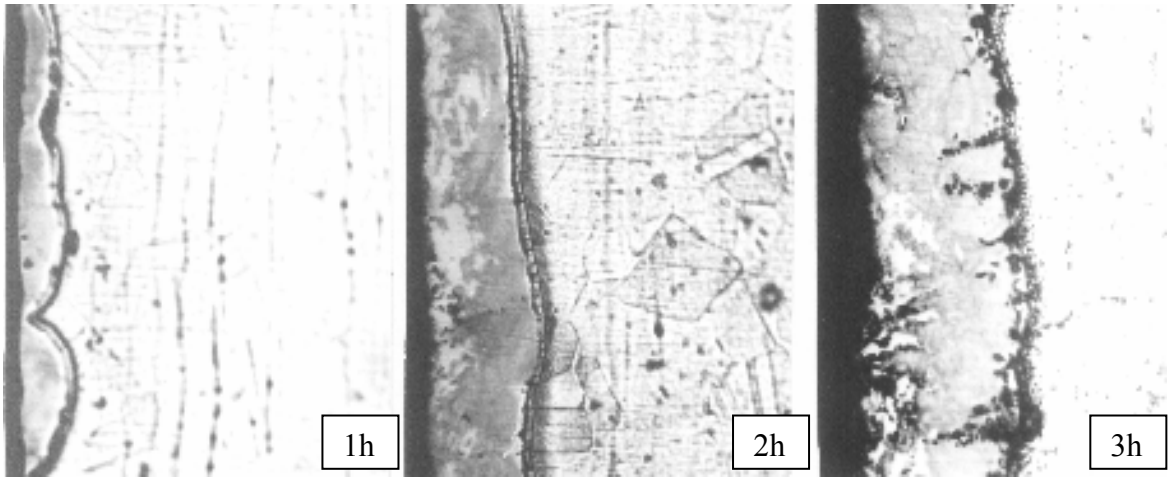

Fig 4. *Microstructure of the nitrated sample of steel code 4–X2CrNiMo17.11.2 x400*

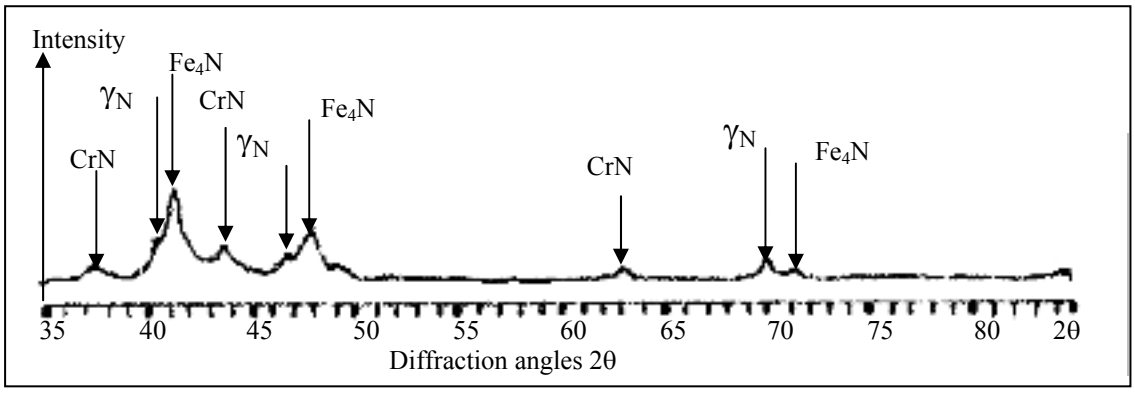

Fig 5. *Diffraction diagram for sample steel code 2–X6CrNiTi18.10*

Depth is different from one steel to another; the depth of steel code 2–X6CrNiTi18.10 and steel code 3–X2CrNi18.9 is higher by almost 40 microns as these steels have austenite stability indexes smaller of about S_2=19, S_3=17.5.

With steel, nitrogen diffusion takes place under more favorable conditions.

The analysis of the diffraction diagram for steel code 2–X6CrNiTi18.10 figure 5 indicates the presence of drops corresponding to Fe_4N, CrN and to a smaller extent the presence of gamma phase γ_N. Both nitrides and solid phases in nitride based austenite determine considerable increase of hardness above $1200HV_{005}$.

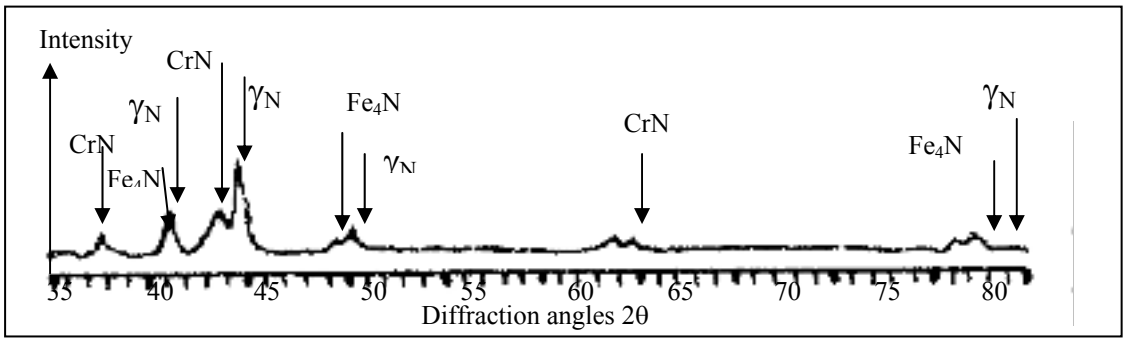

Fig 6. *Diffraction diagram sample steel code 4–X2CrNiMo17.11.2.*

The aspect of the diffraction diagrams is similar for the first five steels except that drop intensity corresponding to phase γ_N takes a larger or smaller value depending on its stability. Figure 6 presents the diffraction diagrams for steel code 4–X2CrNiMo17.11.2 with an austenite stability index higher than steel code 2. It can be noted that the relative drop intensity of phase γ_N is higher as well. The decrease in the nitriding temperature of these steels results in a spectacular change. The metallographic analysis fails to reveal the presence of a surface layer of distinct structure figure 7. The structure is of diffusion type consisting of nitrogen enriched austenite with nitride punctilious segregations. The hardness reported in the nitrated layer takes values over $1100HV_{005}$ which indicates a higher concentration of nitrogen, almost close to the saturation limit. Figure 8 makes a comparison between the diffraction diagrams for the samples of steel code 4–X2CrNiMo17.11.2.in initial state and under nitriding process at 450^{o}C.

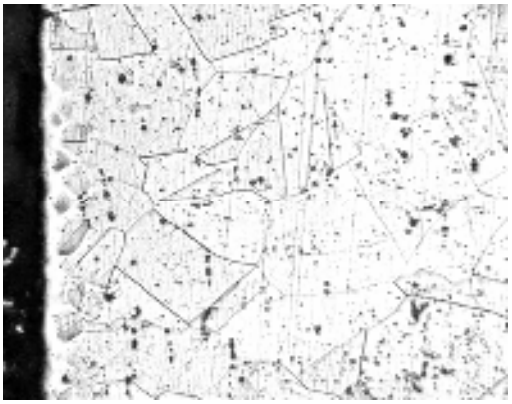

Fig 7. *Microstructure of steel code 4–X2CrNiMo17.11.2.nitrated at 450^{o}C*

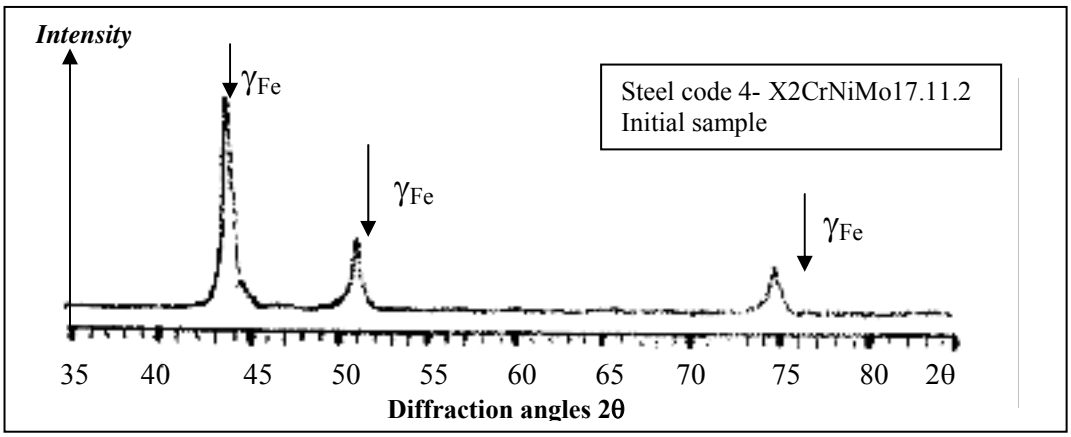

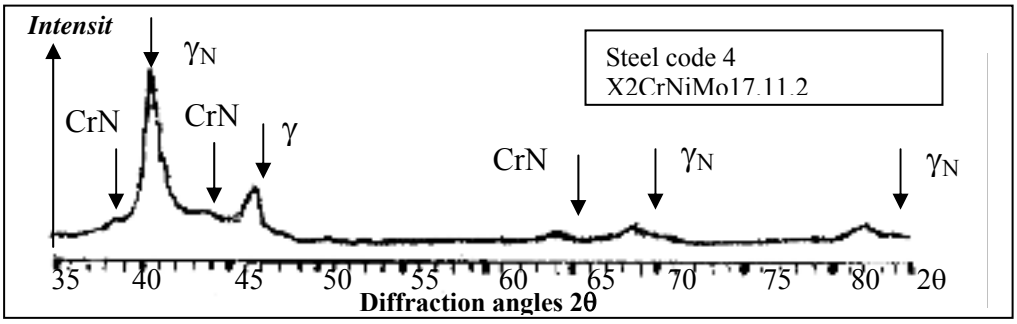

Fig 8. *Diffraction diagrams of the samples of steel code 4–X2CrNiMo17.11.2.in initial state and under nitriding process at 450^{o}C.*

On the diffraction diagram of the initial sample drops corresponding to phase angles γ_{Fe} can be seen, featuring an austenitic structure as well. On the diffraction diagram of the sample nitrated at 450^{o}C it can be seen large amplitude drops corresponding to the diffraction angles of phase γ_N, nitrogen enriched austenite and smaller amplitude drops for the diffraction angles corresponding to the CrN phase. This indicates that the structure contains small amounts of CrN nitrides along with nitrogen enriched high alloyed gama solid solution. The presence of the two phases accounts for the increase in the pregnant hardness to be found with the nitriding layer at 450^{o}C.

3. Conclusions

Low temperature nitriding of high alloy austenitic stainless steels fails to result in harder layers since austenite stability does not allow for nitrides separation. At the same time the high concentration over 50% of the alloying elements limits nitrogen diffusion and keeps it well below the saturation limit. The highest influence is that of the Ni concentration over 18% and copper of about 1% which increase the Ni austenitezed effect. With usual austenitic stainless steels nitriding at 500^{o}C results in layers of separate nitride combinations inside the nitrogen enriched austenitic volume as a consequence of the low stability index, the deepest depths being reported with low index steels. Decreasing the nitriding temperature to 450^{o}C under the austenitic stainless steel sensitivity limit leads to diffusion layers made up of nitrogen enriched austenite of high nitrogen concentration which is close to the saturation limit.

References

[1]. Berns H., 2002, *"Case hardening of stainless steel using nitrogen"*. Ruhr University, Bochum, Germany
[2]. Bard A.J., Faulkner L.R., 2000, *"Electrochemical methods, Fundamentals and aplications"* Wiley Science Publication
[3]. Dima O. Cazacu N., 2006, *"Surface hardening by nitration for some stainless austenite steel types."* Simpozionul international "Turnatoria de la rigoarea tehnica la arta" Ed. ACADEMICA Galati
[4]. Dima O. Levcovici S. Georghies C., 2006, *"Aspects of nitrated layer structure for some types of austenite stainless steel"* Simpozionul international "Turnatoria de la rigoarea tehnica la arta" Ed. ACADEMICA Galati
[5]. Dima O. Mitoseriu O., 2006, *"Behavior of some stainless nitrated austenite steel types to corrosion and abrasion"*. Simpozionul internation "Turnatoria de la rigoarea tehnica la arta" Ed. ACADEMICA Galati
[6]. Fossati A, Borgioli F, Galvanetto E, Bacci T. 2006, *"Corrosion resistance properties of glow-discharge nitrided AISI316L austenitic stainless steel in NaCl solution"* Corrosion Science, Vol.48, Issues 6, June 2006, pag. 1513-1527.
[7]. Gheorghies C. s.a., 1994, *"Incercarea materialelor Vol.III"* Ed. Tehnica Buc.
[8]. Levcovici S.M. s.a., 2003, *"Ingineria suprafeţelor"* EDP, RA Bucureşti
[9]. Mirkin L.I., 1979, "Controlul cu raze X a structurii materialelor" Moscova
[10]. STAS 9229 -1995 *"Incercarea rezistenţei la coroziune in ceata salina"*
[11]. STAS 9639-1981 "*Incercarea la uzura prin abraziune*"

THE ANNALS OF "DUNAREA DE JOS" UNIVERSITY OF GALATI.
FASCICLE IX. METALLURGY AND MATERIALS SCIENCE
N^0. 1 – 2008, ISSN 1453 – 083X

SURFACE HARDENING FOR 38MoCrAl09 STEEL USING FLUIDIZED BED NITRIDING

Adolf BACLEA[1], Sorin DOBROVICI[2], Nelu CAZACU[2]
[1]Socomar SRL, Sorento, Italy ,
[2]Dept.of Metallurgy and Materials Science, Dunarea de Jos University of Galati, Romania
e-mail: Nelu.Cazacu@ugal.ro, Sorin.Dobrovici@ugal.ro

ABSTRACT

The paper is based an nitriding experiments made in a fluidized bed laboratory furnace. Fluidization was obtained in a steel refractory retort by solid granular (burned fire clay) and fluid (mixture of ammonia and nitrogen). Heating system is based on indirect electrical method. Heating transfer from furnace to retort is high and is determinate by high value of heat transfer coefficient for fluidized bed. Nitriding processes were driven by a classic experimental matrix (ammonia proportion is constant, nitriding time and nitriding temperature are variable). Results were investigated by: hardness HV_5, micro-hardness $HV_{0,05}$, microstructure and XRD. The results confirm nitriding process, media capacity for heat and mass transfer and a good behavior of 38MoCrAl09 steel.

KEYWORDS*:* fluidized bed, nitriding, nitraaloy steel, short time

1. Introduction

After nitriding treatment, superficial layer with special properties (high hardness) simultaneously with a reliable core will offer to part exploiting exceptional properties (fatigue and wear resistance, tenacity). For increasing quality for treated machine parts, different techniques have a rapid developing, diversification and adaptability to product processes. Fluidized bed technology (FBT) offer an active media to thermochemical treatments at low investment costs, [0], [0]. For FBT applications with open furnace, technological costs for gases increase, [0].

Some limitations for shape parts are important too. Simple surfaces in vertical/axial positions are recommended for uniformity of treatments. Important mechanical gas solid processes (fluidized bed gasdynamics) having high influences over mass transfer and heat transfer processes are shown in Fig.. High surfaces for solid/gas interfaces are an important characteristic for fluidized bed.

2. Experimental conditions

For nitriding in fluidized bed experiments we used a pilot furnace (Fig.2).

Some important characteristics were:

- fluidized bed furnace (140mm diameter, H/D=1,2)
- heating technique: indirect electrical heater
- solid granular: burned fire clay with granulation 0,010…0.016mm
- fluidization gas: mixture from ammonia (33%) and nitrogen (rest)
- samples: 38MoCrAl09 steel (Table 1)
- experimental procedure: classical "full factorial" array with two factors and three level for each factor.

Many factors have influence over nitriding process but nitriding temperature and nitriding time are present for all nitriding technologies. Some fluidization factors were fixed by preliminary experiments at constant values. Fluidization was conduced driven by diagram pressure drop/velocity [5] but process repeatability is important. Gas mixture debit was constant for all nitriding regimes and visual observation was important for quality of fluidization. One of the most important factors influencing the quality of fluidization is the uniformity of gas flow across a constant pressure drop [3]. A drop pressure in fluidized bed was measured by "U" manometer. Samples had a disc shape and were immersed vertically in fluidized bed.

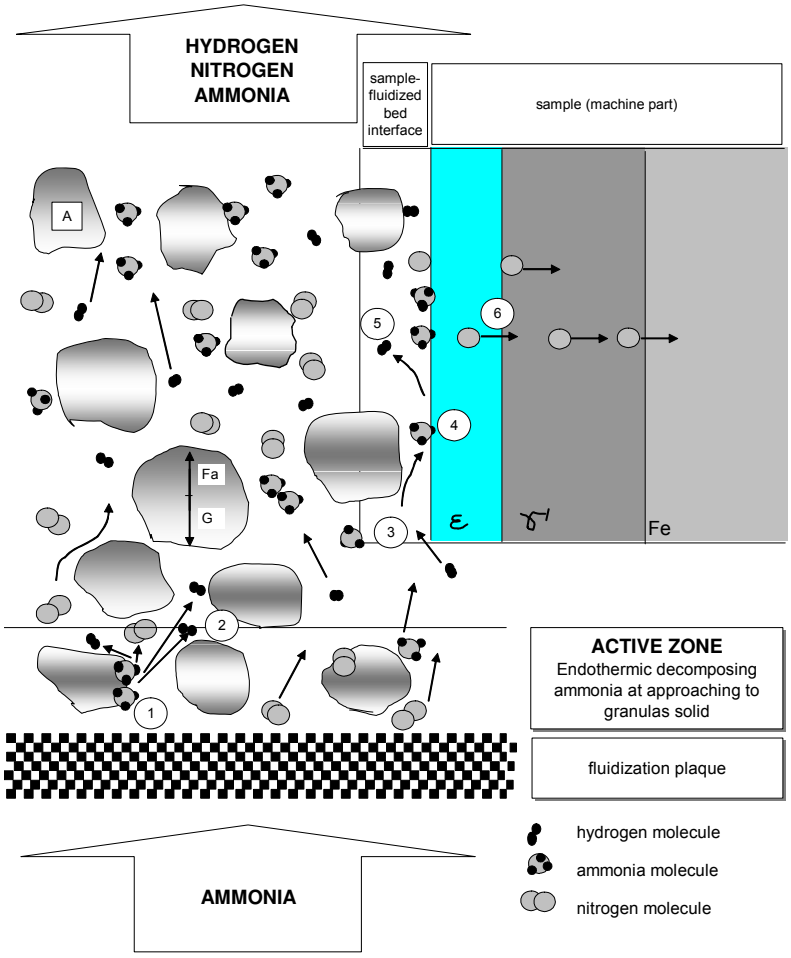

***Fig.1**. Representation of processes on fluidized bed nitriding: A-solid, G-weight, Fa- ascension force, 1- endothermic decomposing ammonia, 2-hidrogen molecule formation from atoms (similarity to nitrogen), 3-ammonia molecules approaching the surface, 4-endothermic decomposing ammonia, 5- hydrogen molecule formation from atoms, 6-nitrogen atoms diffuse into metal surface*

***Table 1.** Chemical composition for 38MoCrAl09 steel (nitraaloy steel, mass %)*

steel	C	Mn	P	S	Si	Mo	Cr	Ni	Al
38MoCrAl09	0,41	0,53	0,22	0,011	0,33	0,18	1,35	0,11	0,86

***Fig.2**. Image with nitriding furnace.*

Table 2. *Experimental regimes for 38MoCrAl09 nitrided in fluidized bed*

Exp. no.	Chemical composition of gas mixture	nitriding temperature	nitriding time
m.u.	%	°C	h
1	33%NH_3+67%N_2	520	1
2			2
3			3
4		550	1
5			2
6			3
7		580	1
8			2
9			3

3. Results and discussion

Results were investigated by: hardness HV_5, micro-hardness $HV_{0,05}$, microstructure and XRD. Microstructures of all samples (Fig.3, 38MoCrAl09 steel), shown nitrided layers. By increasing nitriding temperature and nitriding time, a combination layer formation is present. HV_5 measurements over nitrided surfaces for all regimes showed an appreciable hardness increasing.

For 550°C and three hours hardness is over 1200 daN/mm^2 (Fig.4).

Total nitriding layer depth for all nitriding regimes by micrographic measurements is shown in Fig.5.

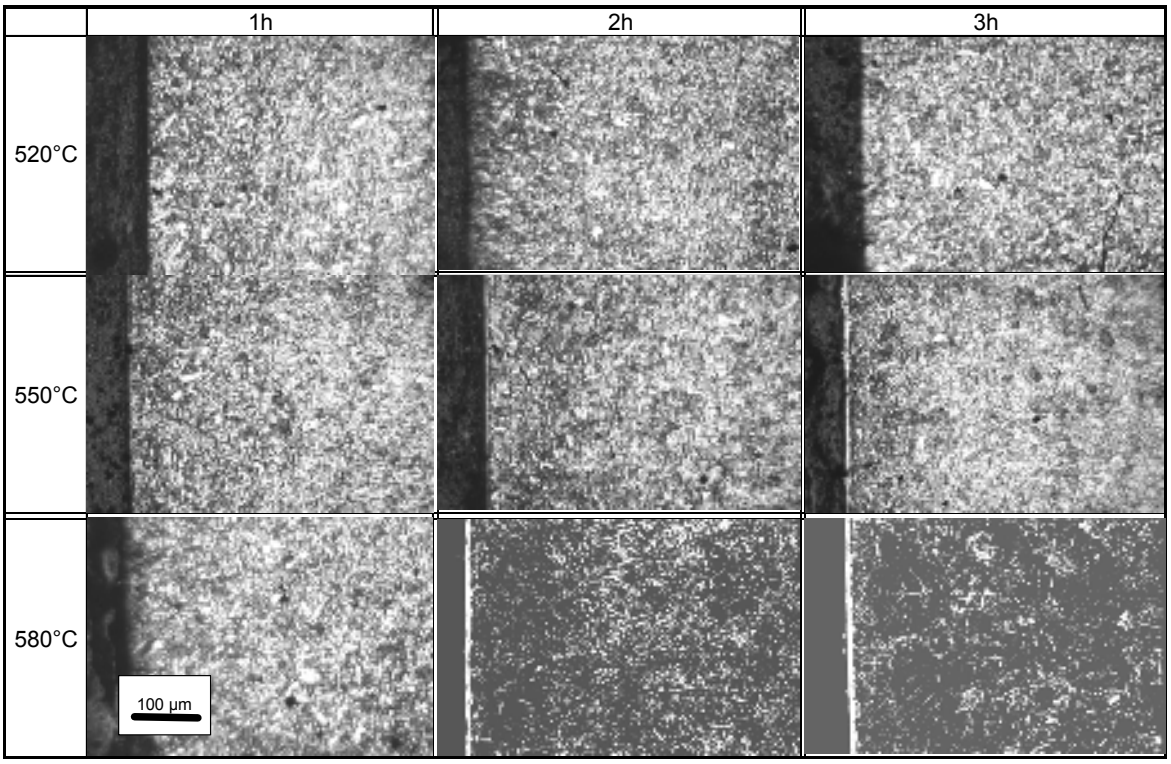

Fig.3*. Micrographs of nitrided 38MoCrAl09 steel samples after experimental regimes [1].*

All 38MoCrAl09 steel samples shown nitriding layers. A combination layer is present. By increasing nitriding temperature and nitriding time a combination layer is present and that increasing by nitriding time. Diffusion layer has for three hours Hardness HV_5 measurements on the nitriding surfaces shown an appreciable increasing for all regimes.

The presence of specific nitiding phases was investigated by XRD (DRON 3) and for 550°C nitriding temperature and one hour nitriding time, the diagram is shown in Fig.7.

The XRD investigation gives only the phases presence, [6].

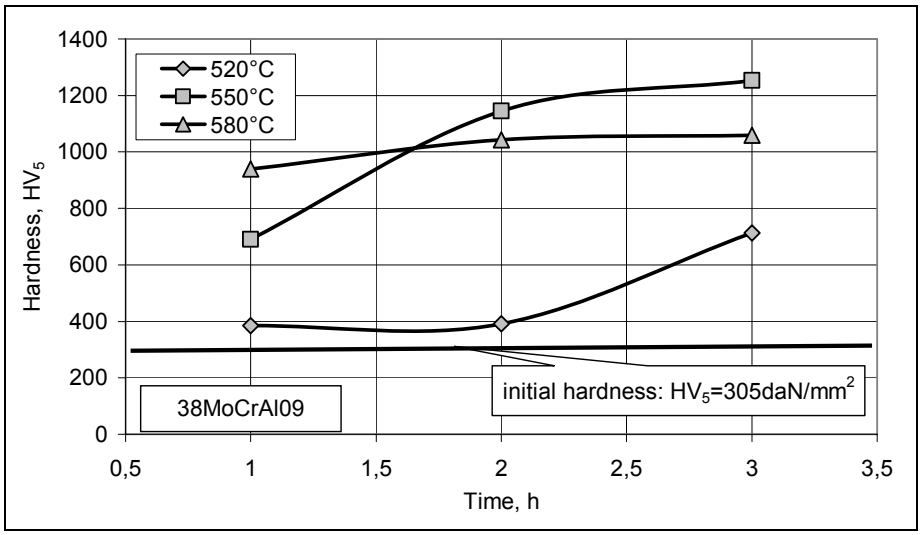

***Fig.4**. Hardness HV_5 on the nitriding surface for 38MoCrAl09 steel samples after nitriding in fluidized, [1].*

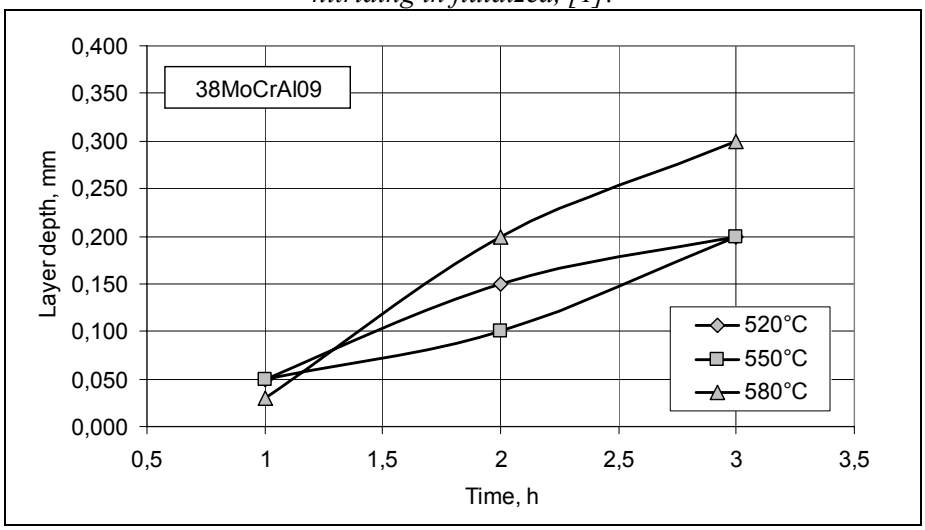

***Fig.5.** Total nitriding depth layer for 38MoCrAl 09 sample nitriding in fluidized bed for different temperature and time, [1].*

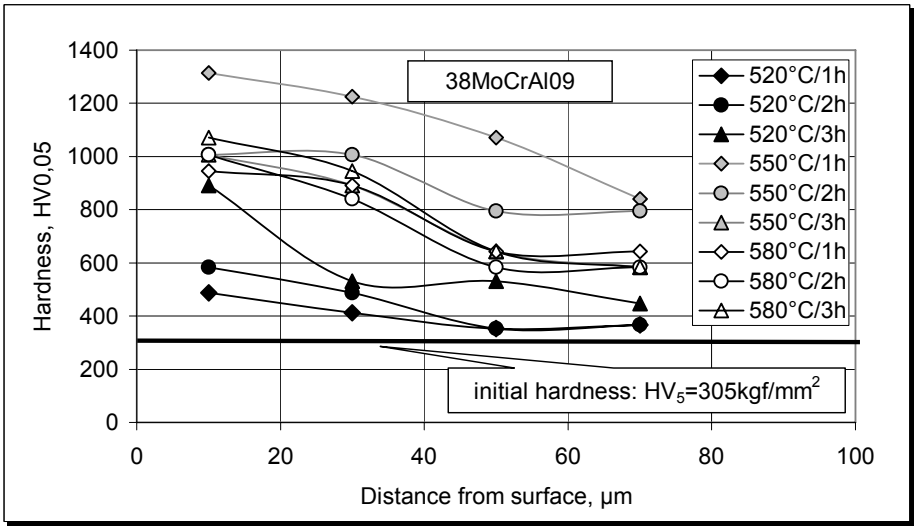

***Fig.6**. Micro hardness $HV_{0,05}$ for 38MoCrAl09 steel sample, [1].*

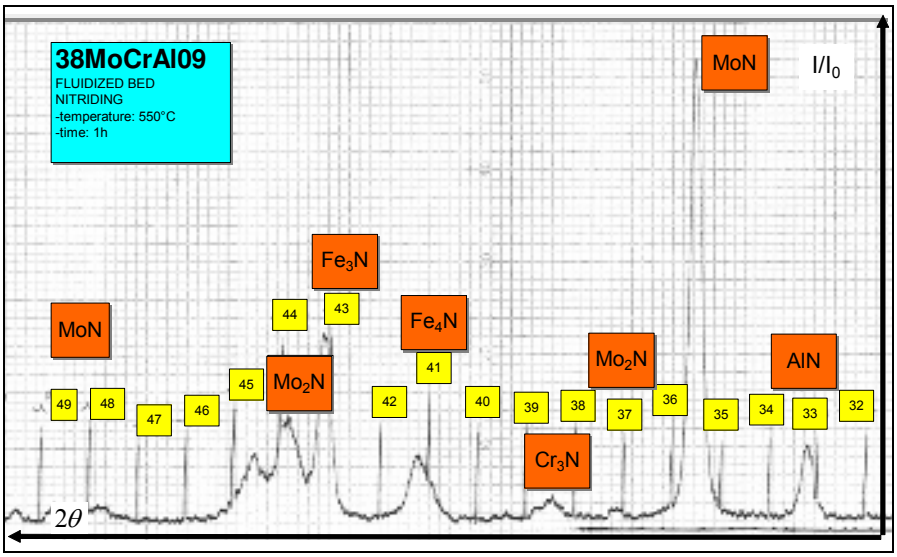

***Fig.7**. XRD investigations by DRON 3*

The steel has in chemical compositions Mo, Cr and Al that conduced to hard phases at nitrogen presence and temperature. Because fluidized bed has a high thermal and mass transfer coefficient the specific nitriding phases were formed for one hour nitriding time and 550°C nitriding temperature.

Conclusions

The results investigated confirm nitriding process in fluidized bed, media capacity for heat and mass transfer and a good behavior of 38MoCrAl09 steel. Nitriding in fluidized bed process is characterized by a short time cycle (1…3h) because in experimental conditions we used an open furnace. The cooling process is shorter when comparing nitriding processes with other nitriding technologies; that increasing efficiency, [3]. The gas mixture after nitriding reactions containing hydrogen and rests of ammonia; that was burned in atmosphere at nonpolluting gasses (carbon dioxide and steam). For low alloyed steel with Cr, Mo and Al the hardness on surface (HV_5) had 700… 1250 daN/mm^2 for 550… 580°C and 1…3 hour nitriding time. By adequate selection of steel [7] and fluidization factors, nitriding in fluidized bed is characterized by a short total time of treatment that increases efficiency of process. Some limitation of part shapes and positions in fluidized bed are available for industrial applications.

References

[1]. Bâclea, A., 2004, *Studii şi cercetări privind implementarea nitrurării în strat fluidizat la ameliorarea proprietăţilor unor repere utilizate în construcţii navale*, Teză de doctorat, Galaţi

[2]. Iacob, C., Vigier, P, 1995, *Transfert d'azote em lit fluidise: influence des parametres dynamiques du lit sur la nitruration d'un acier non allie*, ATTT 95 Internationaux de France du traitement thermique, Paris 21-23 juin 1995

[3]. **Sagon-King, F**., ASM Handbook, Vol. 4, *Heat Treating, Fluidized-Bed Equipment*, ASM International, Materials Park, OH 44073-0002, pages 484-491;

[4]. Ivanuş Gh, etc., 1996, *Ingineria fluidizării*, Editura Tehnică, Bucureşti

[5]. Kunii D., Levenspiel O, 1969, *Fluidization engineering*, John Wiley & Sons, Inc., New York

[6]. Convert F, 2004, *Analyse des couches de combination par diffraction X*, Traitements thermique, no. 352, pg.27

[7]. **Murry Guy**, 2002, *Une nouvelle norme europeenne "Acier pour nitruration*, Traitement Thermique, nr.339, mai 2002, pag.30.

THE ANNALS OF "DUNAREA DE JOS" UNIVERSITY OF GALATI.
FASCICLE IX. METALLURGY AND MATERIALS SCIENCE
N^0. 1 – 2008, ISSN 1453 – 083X

THE INFLUENCE OF COLD ROLLING ON THE MECHANICAL CHARACTERISTICS FOR DRAWING STEELS

Octavian POTECAŞU, Florentina POTECAŞU, Petrică ALEXANDRU, Tamara RADU
„Dunarea de Jos" University from Galati
email: fpotec@ugal.ro

ABSTRACT

The paper presents the changes of the mechanical and technological characteristics of steel for deep drawing, cold rolled and recrystallization heat treated. The research was conducted on samples taken from cold rolled strip, treated and rerolled after the ARCELOR MITTAL technology and, for comparison samples sampled from the steel strip before cold deforming (hot rolled) were used as blank tests. The thermal processing of the cold deformed samples, having different degrees of deformation "ε" (2.2% ; 6.5% ; 15.2%; 32.5% ; 50.0% ; 65.0%) and of the blank tests (ε = 0%) were carried out under industrial conditions in a bell furnace.

KEYWORDS: drawing steel, mechanical characteristics, deformation degree, recrystallization

1. Introduction

The research was made on samples sampled from the rolled strap, treated and rerolled after the present technology. For comparison blank samples were taken from the hot rolled strap. For the samples with different degrees of deformation taken from rolling and industrial thermal treated in bell furnace subsets of samples were made from the directions of 0^o, 45° and 90° against the rolling direction.

The chemical composition of the analysed steel is presented in table 1.

Table 1. *The chemical composition of the steel specimens used in experiments.*

C	Mn	Si	S_{max}	P_{max}	Al
[%]					
0.04	0.25	0.1	0.009	0.012	0.05

In order to establish the influence of the cold deformation degree on the steel straps' properties, samples were sampled from a coil deformed on the continuous milling machine TANDEM with five four-high stands with the working cylinders' diameter of 550 mm. To obtain samples with different degrees of deformation the rolling process was started and when the normal running regime was reached, the mill was stopped and cut off parts of the strap between the stands. To achieve deformation degrees lower than 20%, the rolling process was continued only with the first stand.

2. Experimental Research

Samples with different deformation degrees were taken – 2.2% ; 6.5% ; 15.2%; 32.5% ; 50.0% ; 65.0% and in fig.1 is presented the variation of the mechanical characteristics relative to these cold deformation degrees.

The samples with the specified deformation degrees were treated under industrial conditions in bell furnace according to the diagram in fig.2.

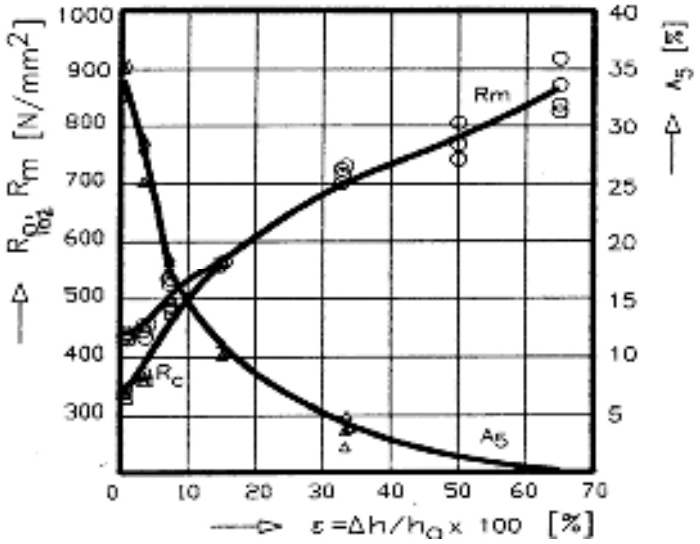

***Fig. 1**. Variation of the mechanical characteristics (ultimate strength, yield strength and breaking elongation) for the cold deformed samples with different degrees.*

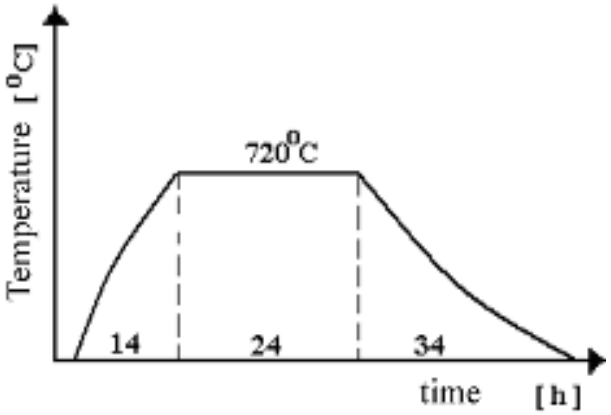

***Fig. 2.** Diagram of thermal treatment conducted in industrial conditions, for the cold deformed samples with different deformation degrees.*

The results referring to the mechanical characteristics for different degrees of deformation and after the chosen thermal treatment according to the diagram in figure 2 under industrial conditions in bell furnace are presented graphically in figures 3 and 4. Fig. 3 shows the influence of the deformation degree on the mechanical characteristics R_m, $Rp_{0.2}$ and A_5 for the rolled samples with different deformation degrees "ε" ($\varepsilon = \Delta h/h_o x100$) on samples taken after the rolling direction. In fig. 4 are presented the variations of the mechanical characteristics depending on the deformation degree for the samples treated under industrial conditions in bell furnace, according to the diagram in fig. 2 for samples sampled from the three directions of 0°, 45° and 90° relative to the rolling direction. The sample characterizing the drawing (the drawing behaviour) was determined by calculating the anisotropy factors on the three directions with the formula:

$$r = \frac{\log \frac{b}{b_0}}{\log \frac{g}{g_0}}$$

where: r – anisotropy factor (r_o, r_{45}, r_{90});

b_o, b – width of sample before and after deformation at the tensile test;

g_o, g – thickness of sample before and after deformation at the tensile test.

The average anisotropy factor was calculated with the formula:

$$r_m = \frac{r_0 + 2r_{45} + r_{90}}{4}$$

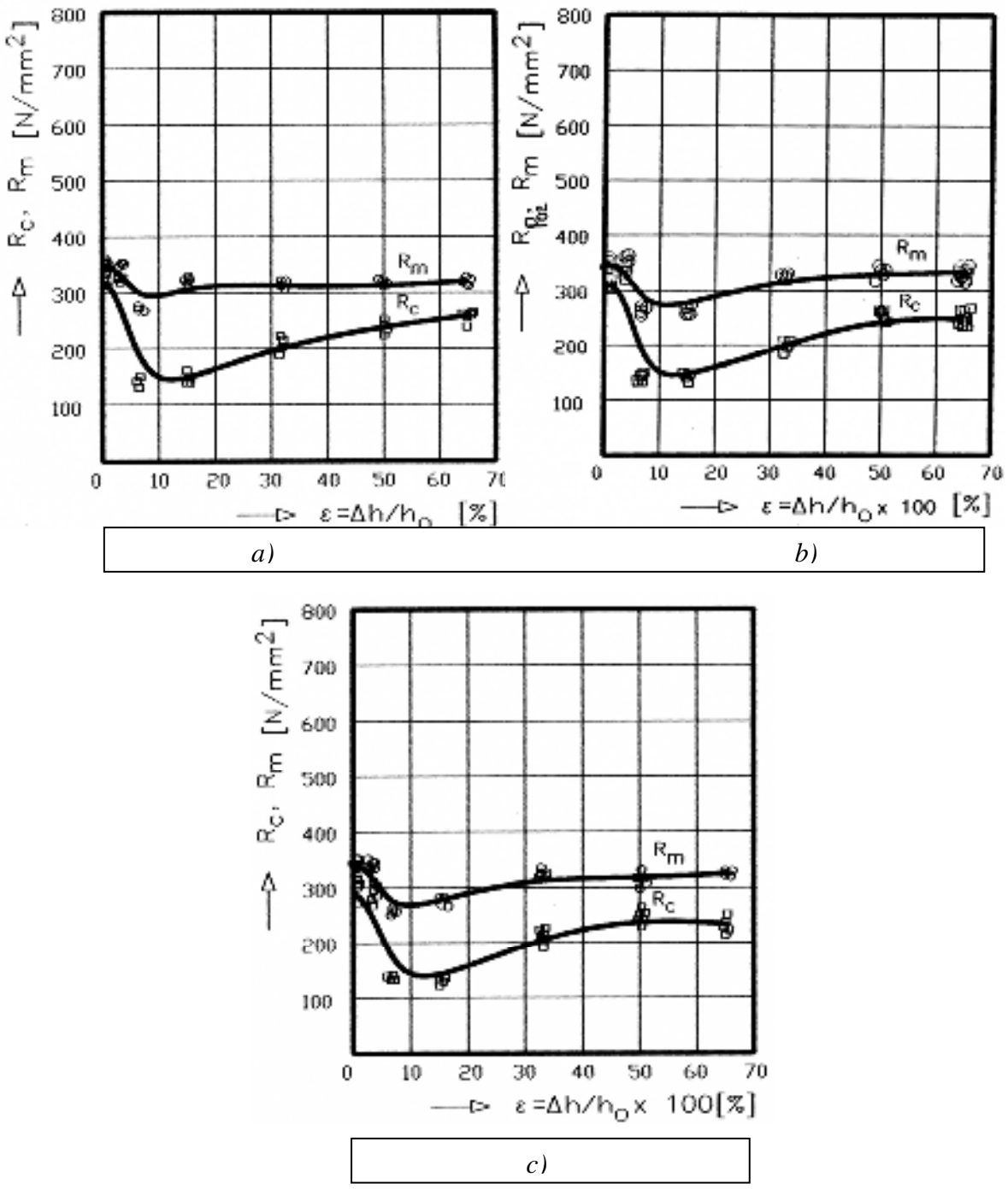

Fig. 3 *Variation of the breaking strenght and yield strength for cold rolled samples having different defformation degrees and thermally treated under industrial conditions:*

a – longitudinal direction;
b – transversal direction;
c –direction of 45° from the rolling direction.

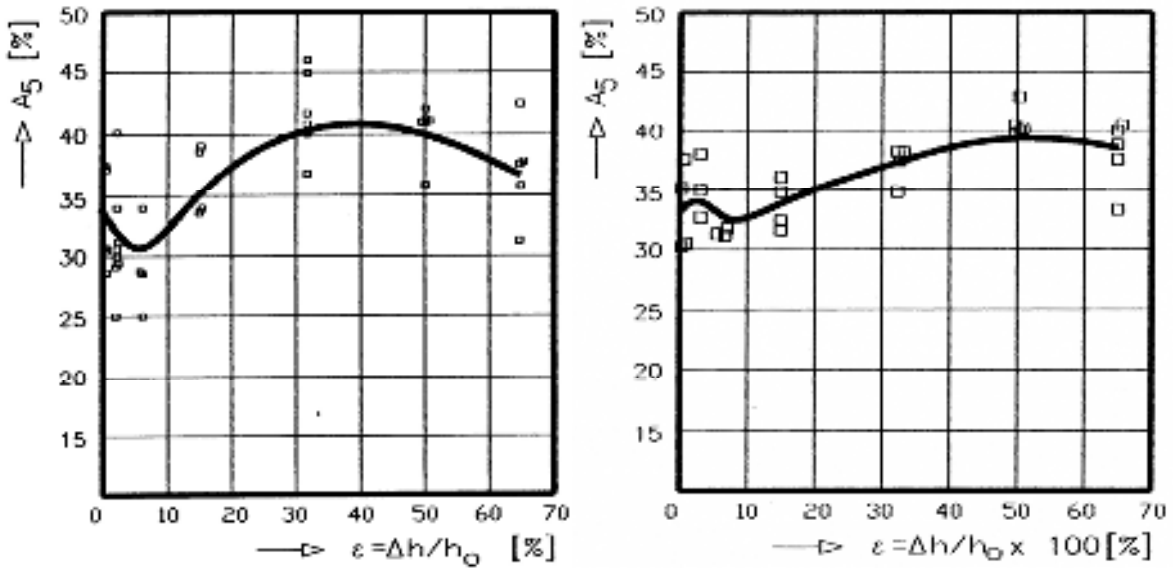

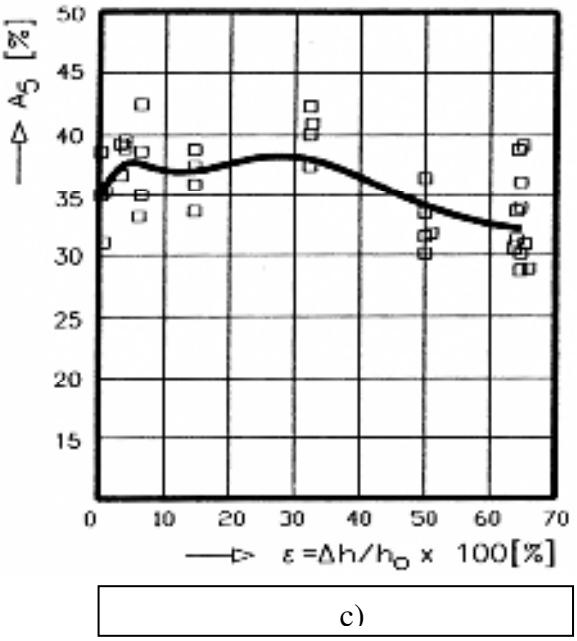

Fig. 4 *The variation of the breaking elongation for the cold rolled assays with different deformation degrees and thermally treated under industrial conditions:*
a – longitudinal direction;
b – transversal direction;
c – direction of 45° from the rolling direction.

where: r – anisotropy factor (r_o, r_{45}, r_{90});
b_o, b – the width of the sample before and after the deformation through the tensile test;
g_o, g – the thickness of the sample before and after the deformation through the tensile test.

The average anisotropy factor was calculated with the formula:

$$r_m = \frac{r_0 + 2r_{45} + r_{90}}{4}$$

Fig. 5 shows the variation of the anisotropy factors depending on the deformation degree for the experimented treatment.

3. The analysis of the results

The influence of the deformation degree on the mechanical characteristics for the analysed steel is highly pronounced in the case of the cold rolled samples, reaching high values for the tensile test, over 800 N/mm^2, for deformation degrees higher than 50%, followed by a drastic shortening of the elongation (in correlation to the occurrence of the fibrous structure at deformation degrees over 50%, a highly noticeable aspect in the longitudinal sections).

Maximum elongations can be obtained for deformation degrees between 30% and 50%, as the elongation is more influenced by the deformation degree than the resistances R_m and Rp_{02}. The anisotropy factors grow with the deformation degree, presenting specific evolutions for the three directions of sampling the samples (fig. 12). One can notice that when reducing with 30%, the factors have values corresponding to deep drawing (1.4-1.6), with the smallest differences between the values calculated for the three directions.

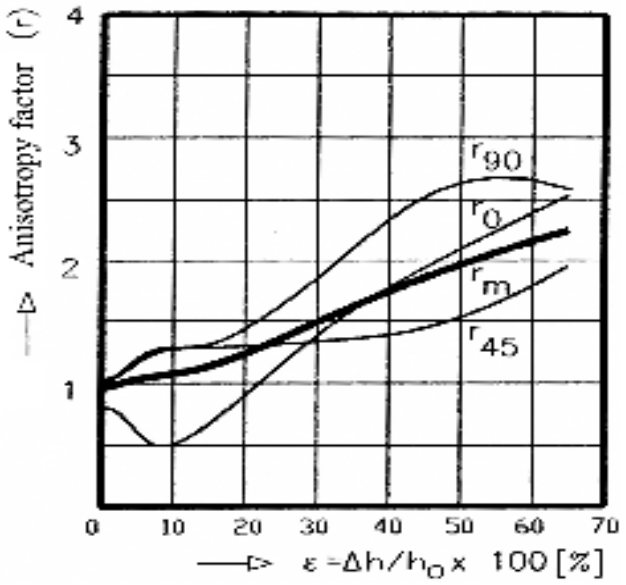

Fig. 5 *Variation of the anisotropy factors depending on the deformation degree for the cold rolled and heat treated assays, under industrial conditions:*
a – longitudinal direction;
b – transversal direction;
c – direction of 45° from the rolling direction.

The direction for sampling the samples for the tensile test, as compared to the rolling direction (0^o, 45° and 90°), is important as it highlights the distribution of the mechanical characteristics and of the anisotropy factors in strap's plan, allowing for a better assessment of its behaviour to drawing. It is known that in this case a higher uniformity in the properties' distribution is necessary. It was noticed that usually the elongation has maximum values on the longitudinal direction (0^o) and minimum values on the 45^o directions, with differences between 10% and 20%. The samples deformed with the degree of 32.5 % had the longest elongations, with minimum differences among the values from the three directions. The flow resistance and the tensile test vary along the three directions within the limits 3%-10% and 3%-6%, obtaining the smallest differences for the deformed samples with 32.5 %.

The anisotropy factors vary a lot along the three directions within the limits of 20%-50%, depending on the deformation degree.

The cold deformation degree has a high influence on the mechanical and technological properties of the chosen deep drawing steel straps, as well as on their distribution on the characteristic directions as compared to the rolling direction (0, 45° and 90°);

Applying some deformation degrees higher than 50% in TANDEM, leads to obtaining ultimate strength of over 800 N/mm^2 and elongations under 2%, for the cold-hardened strap.

The studied mechanical characteristics are especially influenced by cold rolling with small reductions, while rolling with higher reductions only the elongation is strongly influenced.

The deformation degree of 32.5 % and the heat treatment under industrial conditions made in bell

furnace, gave the best results on the values of the characteristics and their distribution in the strap's plan. The values of the mechanical characteristics and of the anisotropy factors (which characterizes the behaviour at drawing the straps) are different along the three directions as compared to the rolling direction.

4. Conclusions

Using some of the cold deformation degrees higher than those strictly necessarily in obtaining the characteristics for deep drawing has the disadvantage that the mechanical resistance increases for the cold-hardened strap at values higher than 800 N/mm^2, which determines higher energy consumption, higher consumption of the plate rolls and difficulties in achieving the thickness tolerances and in smoothness of the strap due to using stronger rolling forces.

The research shows that lower degrees of deformation can also be used to obtain some good characteristics for drawing, when using steels of high purity (S_{max} = 0.009 %, P_{max} = 0.012%), aspect that in the present industrial conditions no longer creates problems.

References

[1] **Engl, B., Potte – Schmidt, K**., 1994, *Korneigenschaften und ihr Einfluse auf dasunterbesonderer Berucksichtingung von kaltgewaltzten Feinblechstahles:* Stahl und Eisen nr.7.

[2] **Randle, V., Engler, O**. 2003, *Introduction to texture analysis; macrotexture, microtexture and orientation mapping*. Taylor & Francis, London.

[3] **E.J. Drewes and B. Engl** - Stahl und Eisen 108 (1988), p. 987

[4] **C.G.H. Brun and M.J.M. Munier,** 1986, *HSLA steels metallurgy and applications*, ASM International, p. 941

[5] **K. Olsson,** 1988, *Processing microstructure and properties of HSLA steels*, TMS, Warrendale (PA), p. 331

[6] **Wilson, Aw., Spanos, G**., 2001, *Application of orientation imaging microscopy to study phase transformation in steels*. Materials characterization, volume 46, page 407.

[7] ASM Handbook, Volume 1, Properties and Selection: Irons, Steels, and High Performance Alloys - Carbon and Low-Alloy Steels - Processing of Solid Steel – Annealing - Continuous Annealing

[8] ASM Handbook, Volume 4, Heat Treating - Heat Treating of Steel - Continuous Annealing of Steel

[9] **F. Potecasu, O. Potecasu, P. Alexandru,** 2005, *Influence of the deformation degree on the structure and mechanical characteristics of steel sheets intended for producing car bodies* - The 12th International Metallurgy & Materials Congress and Fair 28-30 sept 2005 Istanbul, Turkey, e-book, ISBN 9944-89-073-1, p.89-95.

THE ANNALS OF "DUNAREA DE JOS" UNIVERSITY OF GALATI.
FASCICLE IX. METALLURGY AND MATERIALS SCIENCE
N^0. 1 – 2008, ISSN 1453 – 083X

MATHEMATICAL MODEL OF THE LD STEEL DEOXIDATION KINETICS WITH MANGANESE AND ALUMINIUM

Alexandru IVANESCU, Lilica IVANESCU, Elisabeta VASILESCU
"Dunărea de Jos" University of Galati
e-mail: ivanescu1944@yahoo.ca

ABSTRACT

The paper presents the mathematical model of the kinetics of the electric arc furnace steel deoxidation with Mn and Al. Based on the solving of the kinetics model differential equations, the variation of the deoxidants solubility during the deoxidation process can be determined, as well as the kinetic constants of the reactions and the maximum durations which are necessary for the complete assimilation of the deoxidants.

KEYWORDS: mathematical model, steel deoxidation kinetics

1. Introduction

The steel elaboration in electric arc furnace is a very complex process as a result of the fact that many technological parameters which interact among them and influence its progress are involved. The steels used for automobile industry are characterized by high grades of cupping and can be obtained only by an advanced deoxidation of the ferrous metallic bath using manganese and aluminum [1-3]. The efficiency of the deoxidation with manganese and aluminum depends to a great extent on the speed of the dissolving and assimilation processes of the two deoxidants, Mn and Al [4-7]. During the deoxidation process into the casting tank successive processes of Mn and Al pieces dissolving in iron are taking place, forming a liquid solution Fe-Mn-Al according to the scheme:

$$\underset{100-z}{Fe} \xrightarrow{k_1} \underset{y}{Mn} \xrightarrow{k_2} \underset{x}{Al}$$

Where k_1 and k_2 are the speed constants of the reactions. At the initial moment *t=0*, when the entire refined slag is removed, the iron concentration is 100% and those of the Mn and Al are zero. After a time *t*, the iron concentration becomes *100-z* and those of the Mn and Al are *y* and *x*, respectively. It results that:

$$x + y = z \tag{1}$$

With the aid of the relation (1) it can be determined the concentration of a certain element if the concentrations of the two others are known.

If we derived the relation (1) with the deoxidation time, we obtain the following kinetic relation of the deoxidation and alloying with Mn and Al:

$$\frac{dx}{dt} + \frac{dy}{dt} = \frac{dz}{dt} \tag{2}$$

The relation (2) expresses the fact that the speed of the iron content diminution is equal to the sum of the two deoxidants assimilation speeds.

2. Mathematical model of the kinetics of the steel deoxidation with Mn and Al

The kinetic equations of the deoxidation reactions are:

$$\frac{dz}{dt} = k_1\,(100 - z) \tag{3}$$

$$\frac{dy}{dt} = k_1\,(100 - z) - k_2\,y \tag{4}$$

$$\frac{dx}{dt} = k_2\,y \tag{5}$$

By integrating the relation (3) we obtain the solution:

$$100 - z = 100\,\exp(-k_1 t) \tag{6}$$

from which it results:

$$z = 100\ [1-\exp(-k_1 t)] \quad (7)$$

Replacing the relation (6) in (4) we obtain:

$$\frac{dy}{dt} + k_2 y = k_1\ \{100 - 100\ [1-\exp(-k_1 t)]\} \quad (8)$$

or:

$$\frac{dy}{dt} + k_2 y = 100\, k_1 \exp(-k_1 t) \quad (8')$$

Solving this inhomogeneous differential equation, we obtain the solution having the form:

$$y = C_1 \exp(-k_1 t) + C_2 \exp(-k_2 t) \quad (9)$$

The constants C_1 and C_2 are calculated by deriving the equation (9) and replacing the obtained expression together with relation (9) in (8'):

$$\frac{dy}{dt} = -k_1 C_1 \exp(-k_1 t) - k_2 C_2 \exp(-k_2 t) \quad (10)$$

$$-k_1 C_1 \exp(-k_1 t) - k_2 C_2 \exp(-k_2 t) + k_2 C_1 \exp(-k_1 t)$$
$$+ k_2 C_2 \exp(-k_2 t) = 100\, k_1 \exp(-k_1 t) \quad (11)$$

It results:

$$C_1 = \frac{100\, k_1}{k_2 - k_1} \quad (12)$$

Replacing (12) in (9) we obtain:

$$y_{Mn} = \frac{100\, k_1}{k_2 - k_1} \exp(-k_1 t) + C_2 \exp(-k_2 t) \quad (13)$$

At the beginning of the deoxidation ($t=0$) y=0 and it results:

$$C_2 = \frac{100\, k_1}{k_1 - k_2} \quad (14)$$

Replacing C_1 and C_2 in expression (9) we obtain the manganese concentration as a function of the speed constants k_1 and k_2 and of the deoxidation duration:

$$y_{Mn} = \frac{100\, k_1}{k_2 - k_1} \exp(-k_1 t) + \frac{100\, k_1}{k_1 - k_2} \exp(-k_2 t) \quad (15)$$

The aluminum concentration is obtained from the relations (1) and (15):

$$x_{Al} = z - y_{Mn} = 100[1-\exp(-k_1 t)] -$$
$$-\frac{100\, k_1}{k_2 - k_1}[\exp(-k_1 t) - \exp(-k_2 t)] \quad (16)$$

or

$$x_{Al} = 100\left[1 - \frac{k_2}{k_2 - k_1}\exp(-k_1 t) + \right.$$
$$\left. + \frac{k_1}{k_2 - k_1}\exp(-k_2 t)\right] \quad (16')$$

In figure 1 are represented the variations of the concentrations *100-z*, *y* and *x* respectively, as functions of the elapsed time from the moment of adding of the deoxidants Mn and Al in the iron metallic bath.

The maximum value of manganese concentration, y_{max}, depends on the speed constants k_1 and k_2, which in turn, depend on the temperature, according to Arrhenius law.

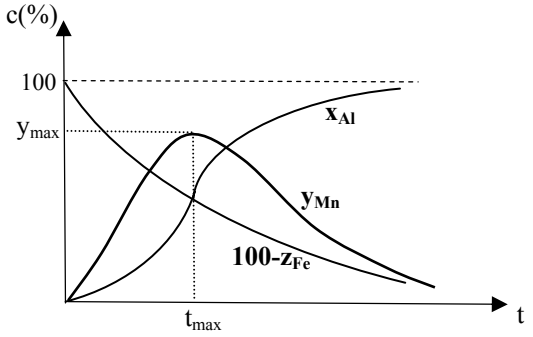

Fig. 1. *The variations of the Mn and Al concentrations (c) as functions of the deoxidation time (t)*

In order to obtain the maximum duration necessary to achieve the maximum concentration of manganese, we put the derivate $\frac{dy}{dt}$ from relation (15) equal to zero for $t = t_{\max}$:

$$\frac{dy}{dt} - \frac{100\, k_1}{k_2 - k_1}[k_1 \exp(-k_1 t) - k_2 \exp(-k_2 t)] = 0 \quad (17)$$

resulting

$$k_1 \exp(-k_1 t_{\max}) = k_2 \exp(-k_2 t_{\max}) \quad (18)$$

from which we obtain:

$$t_{\max} = \frac{\ln k_2 - \ln k_1}{k_2 - k_1} \quad (19)$$

If we put the ratio $\frac{k_2}{k_1} = p$, we obtain:

$$t_{\max} = \frac{\ln p}{(p-1)\ k_1} \quad (20)$$

From the relation (20) we can conclude that the necessary time for manganese to reach the maximum concentration depends only on the speed constants of the deoxidation reactions i. e. on the nature of the reactants Mn and Al, and not on their concentrations. Replacing the relation (20) in (15) we obtain the maximum manganese concentration from the liquid solution Fe-Mn-Al:

$$y_{\max Mn} = \frac{100}{1-p}\left[\exp\left(-\frac{p\ \ln p}{p-1}\right) - \exp\left(-\frac{\ln p}{p-1}\right)\right] \quad (21)$$

It can be observed that the value of the manganese maximum concentration does not depend on the absolute values of the speed constants of the two reactions, but only on their ratio.

The greater k_1 and smaller k_2, the greater the manganese concentration at $t = t_{max}$.

The aluminum concentration variation curve presents an inflexion point which coincides with the duration of the maximum manganese assimilation. If we put the derivate of the relation (16') with the deoxidation time equal to zero, we obtain the minimum duration of aluminum deoxidation, t_{inf}:

$$\frac{d^2x}{dt^2} = k_2 \frac{d}{dt}\left(\frac{100\,k_1}{k_2 - k_1}[\exp(-k_1 t) - \exp(-k_2 t)]\right) = 0 \quad (22)$$

or

$$-k_1 \exp(-k_1 t_{inf}) + k_2 \exp(-k_2 t_{inf}) = 0 \quad (23)$$

By logarithmation of the last expression it results:

$$t_{inf} = \frac{\ln k_1 - \ln k_2}{k_1 - k_2} = \frac{\ln p}{(p-1)\,k_1} = t_{max\,Mn} \quad (24)$$

Analyzing the overall kinetic equation of the aluminium concentration variation during the deoxidation period, $x = f(t)$, we can observe two limit cases:

a) $k_1 >> k_2$ and $x = 100[1 - \exp(-k_2 t)]$ (25)

b) $k_1 << k_2$ and $x = 100[1 - \exp(-k_1 t)]$ (26)

The overall kinetics in successive deoxidation processes is determined by the slowest stage which is, in the case of steel manufacture in electric arc furnace and deoxidation in the casting tank, the manganese dissolution, so that $k_1 << k_2$ and the kinetic equation has the form (26). On the curve of manganese concentration variation it can be observed that at the maximum reaching, the speed of passing into solution is zero:

$$\frac{dy}{dt} = 0 \Rightarrow k_1(100 - z) = k_2\, y \quad (27)$$

It results that:

$$y_{max} = \frac{k_1}{k_2}(100 - z)_{max} = p\,(100 - z)_{max} \quad (28)$$

If the dependence of the temperature of the speed constants is taken into consideration, according to Arrhenius law, the equation (28) becomes:

$$y_{max} = \frac{A_1\, exp(-E_1/RT)}{A_2\, exp(-E2/RT)}(100 - z)_{max} \quad (29)$$

where E_1 is the activation energy of the deoxidation process with manganese and E_2 is the activation energy of the deoxidation process with aluminum.

Because the reactions of the manganese and aluminum dissolving into iron are of the first order, it can be admitted that the pre-exponential factors are approximately equal, $A_1 = A_2$.

It results that:

$$y_{max} = \exp\left(-\frac{E_1 - E_2}{RT}\right)(100 - z)_{max} \quad (30)$$

Because aluminum is a stronger deoxidant than manganese, $E_2 > E_1$ and the maximum manganese solubility increases exponentially with $E_2 - E_1$.

3. Experimental results

The aim of this experiment was the deoxidation of a alloyed steel with Mn (1.4/1.6%Mn) and minimum 0.025%Al.

On the bases of the relations (25), the constant k_1 was determined after logarithmation:

$\ln x = \ln 100 - k_1 t$

$$k_1 = \frac{1}{t} ln \frac{100}{x} = \frac{1}{2} ln \frac{100}{0{,}025} = 2.645\, min^{-1} \quad (31)$$

where: t- represents the duration resulted for an Al concentration, x=0,025, in the variation graph of Mn and Al deoxidation.

The k_2 constant is graphically determined at the intersection of the two curves $f(k_2)$ and $g(k_2)$

$f(k_2) = Y_{Mn} \cdot k_2 - k_1 Y_{Mn}$

$g(k_2) = 100k_1 e^{-k_1 t} - 100k_2 e^{-k_2 t}$

$f(k_2) = g(k_2) \rightarrow k_2 = 2{,}61\ min^{-1}$

The maximum duration of Mn dissolution in steel is determined with the relation:

$$t_{max\ \ Mn} = \frac{ln\,k_1 - ln\,k_2}{k_1 - k_2} = 3.55\, min \quad (32)$$

Considering the values of k_1 and k_2 we can calculate:

$Y_{max} = 1.6\%$ Mn

$X_{max} = 0.07\%$ Al

4. Conclusions

The speed of the making process of the Mn and Al tempered steel depends on the speed of the two deoxidants assimilation. During the manganese and aluminium deoxidation process the iron content decreasing speed is equal to the sum of the deoxidants dissolving speeds.

The necessary time for manganese to reach the maximum concentration depends only on the speed constants of the deoxidation reactions i.e. the nature of the reactants and not on their concentrations. The maximum value of the manganese concentration does

not depend on the absolute values of the speed constants of the two reactions, but only on their ratio.

The variation curve of the aluminium concentration presents an inflexion point which coincides with the duration of the maximum assimilation of manganese.

The characteristics of the profound cupping steels in electric arc furnace co depend in a great extent on the assimilation grade of the deoxidants Mn and Al, at the steel temperature during the deoxidation process.

Based on the curves in Fig.1 it can be determined the concentrations of manganese and aluminum at different times and at known temperatures, and with their aid we can determine the speed constants k_1 and k_2 of the two reactions.

On their basis we can establish the maximum durations necessary for the complete dissolution of the two deoxidants.

References

[1]. Richardson, C.B., 1974, Physical Chemistry of Melts in Metallurgy, Academic Press, London, 56-80.
[2]. Janke, D., , 1986, Proceedings of the International Symposium of Metallurgy, University of Galati.
[3]. Hooper, V.C., and Hart, W.H., 1978, Corrossion - NACE, **34**, 320,
[4]. Yoshimura, H., and Shimizu, T., 1981, Tetsu-to-Hagane, 67, 102
[5]. Schmatz, D.J., 1969, Transactions AIME, 215, 66,
[6]. Schmatz, D.J., 1960, Transactions ASM, 52, 898,
[7]. Oprea, F., Ivanescu, Al., et al, 1984, Metallurgic Processes Theory, Editura Didactica si Pedagogica, Bucharest, 80-106.

THE ANNALS OF "DUNAREA DE JOS" UNIVERSITY OF GALATI.
FASCICLE IX. METALLURGY AND MATERIALS SCIENCE
N^0. 1 – 2008, ISSN 1453 – 083X

HYDRODYNAMIC ASPECTS ON EAF's SMELT METALLIC MIRROR

Ruxandra Ioana MUSTAŢĂ[1], Costică T. MUSTAŢĂ[2]
[1]Universitatea "Politehnica" Bucuresti, [2]UZINSIDER Bucureşti
e-mail: c.mustata@yahoo.com

ABSTRACT

Using the Physical and Mathematical knowledge, a new approach to EAF bath's hydrodynamic aspects is proposed to be developed in this paper. Experimental results and a mathematical equation package have been concluded that the metallic bath mirror has a ondulatory surface during steelmaking process. The shape of slag-metal interface depends on resultant of wave interaction. A higher contact surface between slag and metal correlated with a good velocity of the melted material, lead to a better exploitation of EAF.

KEYWORDS: EAF, wave, mathematical model, potential line, flow line, velocity

1. Introduction

Into EAF, after scrap's melting and the formation of the metallic bath, the interface slag-metal has a variation in time as well as shape and as surface. Around the three electrodes of the EAF, the bath mirror is rippling, forming waves that propagate to the furnace walls. The simultaneous effect of the waves started from the three electrodes is a complex movement, giving to the separation interface slag – molten bath a specific aspect, called hydro-dynamic spectrum.

2. Physical Modeling

The study on a physical model indicates that the 120^0 phase difference of the momentary electric potential applied to the three electrodes does not lead to a cancellation of these waves, due to their interference. The physical model on which the experiments were done was a vessel with the internal diameter of 88 mm and the electrodes circle diameter of 34 mm.

The metallic bath was represented by liquid mercury and the slag by a molar solution of natrium chloride. In paper [1] are fully presented aspects concerning the physical phenomenon of rippling the metallic bath around the three electrodes.

Bellow is presented a physical and a mathematical model of the hydro-dynamic spectrum for the molten metal mirror.

It will be first an analysis of the phenomenon that takes place at one electrode, in order to determine the banc movement by extrapolating and combining of the individual movements (the phenomenon is similar at all three electrodes).

The main parameters of the metallic bath hydro-dynamic spectrum are related to potential lines, stream lines, propagation velocity and flow.

The potential lines represent concentric circles (waves), with the origin in the centre of the source and the stream lines, lines that pass through the source and indicate the direction of the wave propagation.

If the current lines have the direction from the source to exterior, the source is called spring, and contrary is called fountain. In the contact zone of the electrode with the metallic bath are taking place complex phenomena of mechanic, electric, magnetic kind.

Practically, in the contact point between electrode and bath, an electrical discharge occurs and a part of this is transforming into mechanical energy. In this point, the metallic bath mirror is rippling and the waves are propagated towards the furnace wall. As the wave is moving away from the formation zone that we call source or spring, its energy decreases and together with this the height of the wave also decreases (fig.1).

At the contact with the furnace wall, the wave is broken and loses most of its energy.

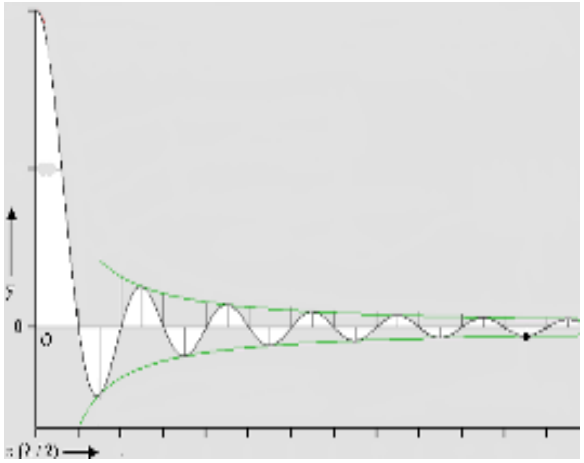

Fig. 1. *Wave's energy variation*

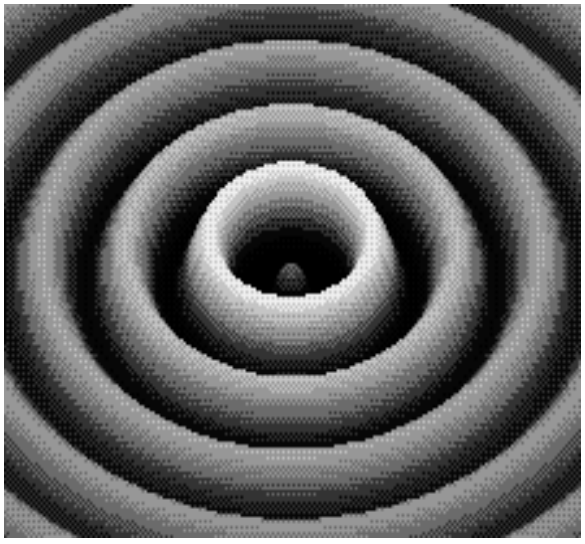

Fig. 2. *3-D wave simulation, one source*

A wave's origin and its propagation is simulated in fig. 2 [2]. If instead of one there are two sources, then the created waves will be interpenetrated and will influence each other. Interpenetration of the waves is named interference [2] and is graphicallz represented in fig.3a and 3b.

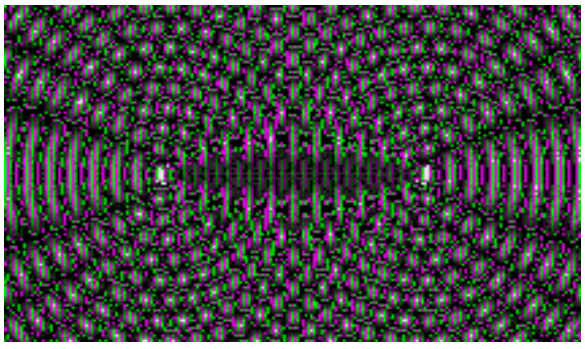

a)

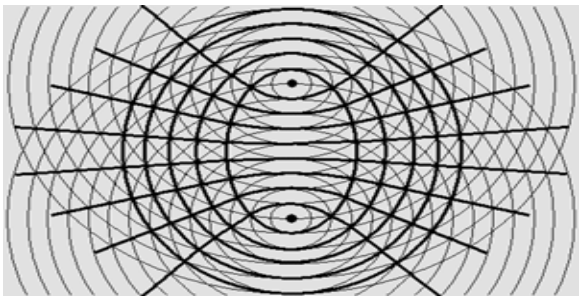

b)

Fig. 3. *Wave interference, two sources*

The interference effect leads to different results, namely the amplifying, decreasing or even annihilating of the wave. The compound of the waves is graphically shown in fig. 4.

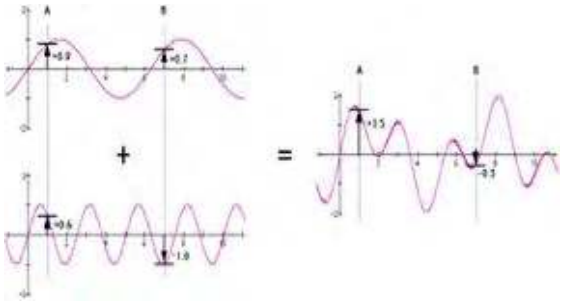

Fig. 4. *Wave's compound resultant*

In the case of three sources, the situation is greaterly complicated, the interference being a complex function of wavelength, electrode circle diameter and furnace internal diameter.

3. Mathematical Modeling

Considering the electrode zone a point source from which the waves are propagated concentrically to the furnace wall, the movement is described by the continuity equation (1) and Euler equations (2) and (3), [3, 7].

$$\frac{\partial u}{\partial x}+\frac{\partial v}{\partial y}=0 \qquad (1)$$

$$\frac{\partial u}{\partial t}+u\cdot\frac{\partial u}{\partial x}+v\cdot\frac{\partial u}{\partial y}=X-\frac{1}{\rho}\cdot\frac{\partial p}{\partial x} \qquad (2)$$

$$\frac{\partial v}{\partial t}+u\cdot\frac{\partial v}{\partial x}+v\cdot\frac{\partial v}{\partial y}=Y-\frac{1}{\rho}\cdot\frac{\partial p}{\partial y} \qquad (3)$$

where: $u = u\,(x,y,t)$, $v = v(x,y,t)$ are the variations in time of a liquid particle speed; $\frac{\partial u}{\partial t}, \frac{\partial v}{\partial t}$ - local unit inertia force; $u\cdot\frac{\partial u}{\partial x}+v\cdot\frac{\partial u}{\partial y}$, $u\cdot\frac{\partial v}{\partial x}+v\cdot\frac{\partial v}{\partial y}$ -

convective unit inertia force; x, *y* - mass unit force; $\frac{1}{\rho}\cdot\frac{\partial p}{\partial x}, \frac{1}{\rho}\cdot\frac{\partial p}{\partial x}$ - pressure unit force.

To consider the function $\varphi = \varphi(x, y)$, a harmonic function for which:

$$u = \frac{\partial \varphi}{\partial x} \text{ and } v = \frac{\partial \varphi}{\partial y} \quad (4)$$

are solutions of the system (1), (2), and (3). The function $\varphi = \varphi(x, y)$ is called velocity potential.

In this case the stream lines equation for a plane movement is:

$$\frac{dx}{u} = \frac{dy}{v} \text{ or } -vdx + udy = 0 \quad (5)$$

The continuity equation (1) written in the form

$$\frac{\partial u}{\partial x} = \frac{\partial(-v)}{\partial y} \quad (6)$$

represents the condition for equation (5) to be the exactly total differential of a tuning function $\psi(x,y)$, and namely:

$$d\psi = \frac{\partial \psi}{\partial x}dx + \frac{\partial \psi}{\partial y}dy = -vdx + udy \quad (7)$$

therefore

$$u = \frac{\partial \psi}{\partial y} \quad \text{and} \quad v = \frac{\partial \psi}{\partial x} \quad (8)$$

Function ψ is called stream function. It can be easily verified that the expressions (8) are also solutions of the equations systems (1), (2) and (3).

From the equations (4) and (8) it may be noticed that:

$$\frac{\partial \varphi}{\partial x} = \frac{\partial \psi}{\partial y} \text{ and } \frac{\partial \varphi}{\partial y} = \frac{\partial \psi}{\partial x} \quad (9)$$

The functions ψ and φ are conjugation harmonic functions and both of them verify the Cauchy-Rieman conditions.

In this case the functions $\varphi = \varphi(x, y)$ and $\psi = \psi(x, y)$ represent the real and respective the imaginary part of a function, *f(z)* of a complex variable with this form:

$f(z) = \varphi(x,y) + i\,\Psi(x,y)$ *with* $z = x+iy$ (10)

named complex potential of movement.

Therefore, to a plan potential movement it can associate a monogyny function of a complex variable.

The complex potential analysis of the movement, function *f(z)* respectively, points out the following aspects:

- the real part of the complex potential *f(z),* (the harmonic function $\varphi = \varphi(x,y)$) represents the velocity potential, and the curves family $\varphi(x,y)$ = constant, the potential lines family (fig. 5);

- the imaginary part of the complex potential *f(z),* (the harmonic function $\psi = \psi(x,y)$) represents the stream function, and the curves family $\varphi(x,y)$ = constant, the stream lines family (fig. 5).

The graphic representation of the potential lines family and of the stream lines family is called the hydro-dynamic spectrum of the movement (fig. 5).

In case of a movement produced by a punctual source, the complex potential has the form:

$$f(z) = C\cdot\ln z, z \neq 0, \quad C \in R\{C > 0\} \quad (11)$$

which written in polar coordinates, r,θ and $z = r\,e^{i\theta}$ becomes:

$$f(z) = \varphi + i\cdot\psi = C\cdot\ln(re^{i\theta}) = C\cdot\ln r + i\cdot C\cdot\theta \quad (12)$$

Through identification, these two functions are:

$$\varphi = C \ln r \;;\; \Psi = C\,\theta \quad (13)$$

These elements established, the main features of the movement can be determined, namely:

- the potential lines:

$$\varphi = C\cdot\ln r = \beta \quad \text{or} \quad r = e^{\frac{\beta}{C}} = \beta_1 \quad (14)$$

representing concentric circles, with the origin in the centre of the source;

- the stream lines:

$$\psi = C\cdot\theta = \lambda \text{ or } \theta = \frac{\lambda}{C} = \lambda_1 \quad (15)$$

representing straight lines that pass through the origin having the direction from the source to the outside;

- the velocity components;

$$V_r = \frac{\partial \varphi}{\partial r} = \frac{C}{r} \text{ and } V_\theta = \frac{1}{r}\cdot\frac{\partial \varphi}{\partial \theta} = 0, \quad C > 0 \quad (16)$$

- the flow rate for any wave (circle):

$$Q = \int V_r dS = \int_0^{2\pi}\frac{C}{r}d\theta = 2\pi C \quad (17)$$

the constant value *C* being $C = \frac{Q}{2\pi}$

In these conditions the complex potential may be written like this:

$$f(z) = \frac{Q}{2\pi}\cdot\ln z \quad (18)$$

or in the case when the punctiform source is placed in a certain point of the complex plane $z_0 - x_0 + iy_0$:

$$f(z) = \frac{Q}{2\pi}\cdot\ln(z - z_0) \quad (19)$$

The phenomena that occur at the other two electrodes are identical with those presented above. Therefore, in the interior of the electric arc furnace used for steel manufacture are three sources (each electrode, E_1, E_2, E_3, represents an independent source – fig. 5) from which concentric waves are propagated toward outside (the furnace wall). These waves are interfering and influencing each other, forming a complex waving surface of the metal bath. Knowing the complex potential of the movement of the three punctiform sources the compound movement can be analyzed.

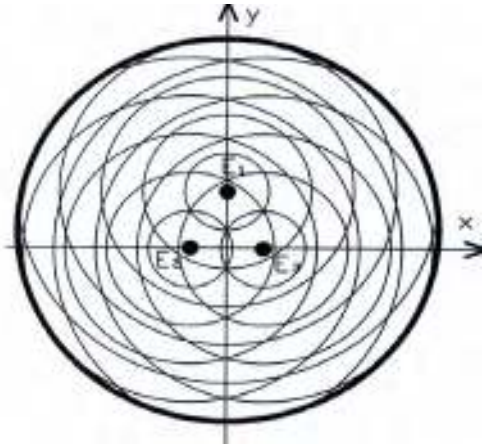

Fig. 5. *Potential and flow lines into EAF.*

The compound of the movements is made taking into account the sources position (electrodes) in the complex plane, pertain to a suitable chosen axis system.

The complex potential of the three punctual sources has the form (11) and is given by the relations:

$$f_1(z) = C \cdot \ln(z + a) \text{ for } E_1 \text{ source} \quad (20)$$

$$f_2(z) = C \cdot \ln(z - a) \text{ for } E_2 \text{ source} \quad (21)$$

$$f_3(z) = C \cdot \ln(z + ib) \text{ for } E_3 \text{ source} \quad (22)$$

The equation of the compound movement is: $f(z) = \sum_{k=1}^{3} f_k(z)$

or

$$f(z) = C \cdot [\ln(z + a) + \ln(z - a) + \ln(z + ib)] \quad (23)$$

Equation (23) represents the compound movement equation, on the basis of which the hydrodynamic spectrum of the metallic bath mirror from the electric arc furnace can be analyzed from a mathematical point of view. The paper could be detailed by an advanced study of an interference complex function in the form of [5], [6]:

$$\Omega = f(\lambda_i, \omega, \delta_{el}, \delta_{ce}) \quad (24)$$

where: λ is the wavelength of the wave's series for the electrodes; ω-a factor that takes into account the electric parameters of the furnace; δ_{el} – electrode circle diameter; δ_{ce} – furnace's internal diameter

4. Metallurgical Effects and Conclusion

From the metallurgical point of view it is important that the metal bath surface swows wave of so that the oxygen transfer from the slag to the bath should be greater. On the other hand it is pursuing that the settling of the products resulting after the different chemical reactions that are taking place in the bath should be more advanced.

The electric driving of the furnace and the putting in phase or phase difference of the electricity at the three electrodes may constitute an important element in obtaining an optimal charge time, a higher quality by realizing a lower nonmetallic inclusion level and a good life of refractory liners. It is known that a plane smelt mirror has a negative effect on vault. So, the EAF steelmaking workers should know the right procedure to be followed, to reach the proposed goal.

References

[1]. Tripşa Iosif, 1969, *Etude d'un phenomene physique sur la surface interphasique acier-latier dans les fours electric a arc,*Centre National de Investigationes Metalurgicas-CENIM, Espania.

[2]. Frenier La, Gabriel, *Matter is made of Waves*, 2007, Cycle Research Institute.

[3]. Duncn, J.W., s.a, 1981, *Mecanics of Fluids*, Edward Arnold, London.

[5]. Mustaţa, T. Costică, 2000, *Cercetări de optimizare şi posibilităţi de conducere automată a proceselor siderurgice folosind modelarea*, Teza de doctorat, Universtiatea Politehnica Bucuresti.

[6]. Iacob, Caius, 1959, *Introduction Mathematique a la Mecanique des Fluides,* Editura Academiei Romane, Bucuresti.

[7]. Carafoli, Elie, Oroveanu, Teodor, 1952, *Mecanica fluidelor*, Editura Academiei Romane, Bucureşti.

THE ANNALS OF "DUNAREA DE JOS" UNIVERSITY OF GALATI.
FASCICLE IX. METALLURGY AND MATERIALS SCIENCE
N^0. 1 – 2008, ISSN 1453 – 083X

INFLUENCE PRESSURE AND SIZE PARTICLE TO EXTRACTION BY CO_2

Vladan MICIC[1], Zika LEPOJEVIC[2], Milovan JOTANOVIC[1], Goran TADIC[1], Boris MANDIC[3]

[1] Faculty of Technology, University of Eastern Sarajevo, Karakaj bb, Zvornik, Bosnia and Herzegovina
[2] Faculty of Technology, University of Novi Sad, Bulevar Cara Lazara 1, Novi Sad, Serbia
[3] Faculty of Chemistry, University of Belgrade
e-mail adress: Vlado21micic@ptt.yu

ABSTRACT

Supercritical fluid extraction (SFE) is an efficient extraction technique for the separation of various organic compounds from herbs, or more generally, from plant materials. These proporties of SFE make the products more advantageous in the field of foods, pharmaceuticals, and cosmetics. The aim of this study was to investigate the effect of pressure and particle size on the extraction yield and the quality of the extracts.

KEYWORDS: supercritical extraction, carbon-dioxide, sage, solvent, size particle, extracts

1. Introduction

With increasing public interest in herbal medicine and natural products, the conventional methods such as hydro-distillation and solvent extraction were found unsatisfactory. To improve efficiency and selectivity of the extraction, alternative extraction techniques such as supercritical extraction started to be developed.

Supercritical extraction is not widely used yet, but as new technologies are coming there are more and more viewpoints that could justify it, as high purity, residual solvent content and environment protection [1, 2, 3]. Some of the advantages and disadvantages of extraction by supercritical fluids compared to extraction by conventional liquid solvents for separations are:

Advantages

- Dissolving power of the SCF (supercritical fluid) is controlled by pressure and/or temperature
- SCF is easily recoverable from the extract due to its volatility:
- Non-toxic solvents leave no harmful residue
- High boiling components are extracted at relatively low temperatures
- Separations not possible by more traditional processes can sometimes be effected
- Thermally labile compounds can be extracted with minimal damage as low temperatures can be employed during the extraction

Disadvantages

- Elevated pressure required
- Compression of solvent requires elaborate recycling measures to reduce energy costs
- High capital investment for equipment

The choice of the SFE (supercritical fluid extraction) solvent is similar to the regular extraction.

Principle considerations are the followings:

- Good solving property
- Inert to the product
- Easy separation from the product
- Cheap

Carbon dioxide is the most commonly used SCF, due primarily to its low critical parameters (31.1°C, 73.8 bar), low cost and non-toxicity.

Dependence pressure and density by temperature are shown in Fig. 1 and Fig. 2 [2].

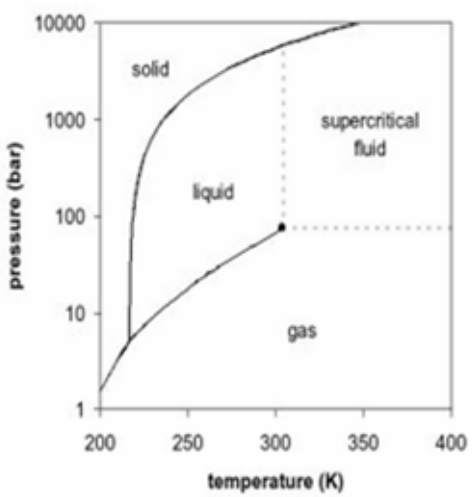

Fig. 1. *Carbon -dioxide pressure - temperature phase diagram*

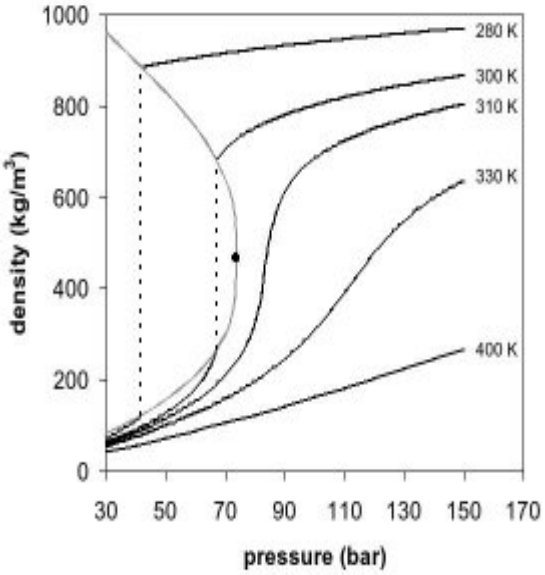

Fig. 2. *Carbon dioxide density-pressure phase diagram*

The special properties of supercritical fluids bring certain advantages to chemical separation processes. Several applications have been fully developed and commercialized.

SFE is applied in food and flavoring industry as the residual solvent could be easily removed from the product no matter whether it is the extract or the extracted matrix. The biggest application is the decoffeinization of tea and coffee. A process for removal of caffeine from coffee using supercritical carbon dioxide was patented in the United States in 1974, and a commercial plant went on stream in the FRG in 1978. Other important areas are the extraction of essential oils and aroma materials from spices. Brewery industry uses SFE for the extraction of hop. The method is used in extracting some edible oils and producing cholesterine-free egg powder. Consequence, supercritical CO2 extraction as an environmentally friendly and efficient extraction technique was studied and numerous research paper concerning extraction of different natural products have been published [4-9]. In this papers, the influence of particular size and pressure to SFE of Salvia officinalis L. was investigated.

2. Experiment

Plant Material

For this experiments *Salvia officinalis L.* from Berkovici, near Trebinje gathered in 2006 was used.

Chemicals

Commercial carbon dioxide (99% purity, Tehno–gas, Novi Sad, Serbia) as the extracting agent was used. All other chemicals were of analytical reagent grade.

Chromatographic procedures:

MS, Finnigan – MAT 8230 BE geometry, resolution 1000, EI – CIU source at 200º. EI 70 eV, 0.5 mA; CI, 1 mtorr of isobutane 150 eV 0.2 mA.

GC/MS, Varian 3400 GC equipped with Split/Splitless injector (1:99) operated at 244°. Column J&W Scientific DB-5ms-ITD 30m, 0.25mm id, *0.25*μm film. Carrier gas hydrogen, 1 ml/min measured at 210°. Column temperature was linearly programmed from 40° to 285° at 4.3°/min. Transfer line at 270°, coupled to Finnigan-MAT 8230 BE mass spectrometer. Ion source temperature 170^O, EI, 70eV 0.1 mA. Scan range 33-333 / 1 sec.

GC, HP5890 series II 3400 GC equipped with Split/Splitless injector (1:99) operated at 244°. Column J&W Scientific DB-5ms-ITD 30m, 0.25mm id, *0.25*μm film. Carrier gas hydrogen, 1 ml/min measured at 210°. Column temperature was linearly programmed from 40° to 285° at 4.3°/min.

Supercritical Fluid Extraction

SFE by CO_2 was carried out with a laboratory – scale high – pressure extraction plant (NOVA – Swiss, Effretikon, Switzerland). The main parts and characteristics (manufacturer specification) of the plant were as follows: a diaphragm – type compressor (up to 1000 bar), extractor with an internal volume of 200 mL (P_{max} = 250bar), and maximum CO_2 mass flow rate of approximately 5.7 kg/h.

The mass of Salvia sample in extractor was 60g at the investigated value of pressure and at 40ºC, and the CO_2 flow rate was 97.72 dm^3/h. Separator conditions were 15 bar and 25ºC.

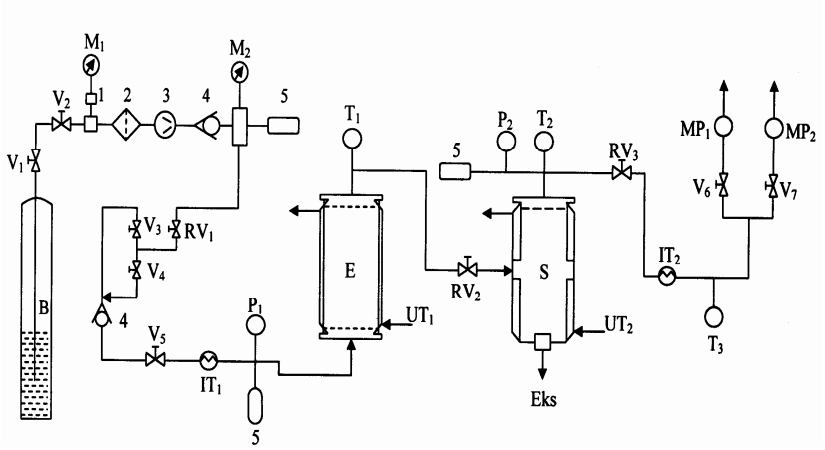

Fig. 3. *Laboratory scale high pressure SFE plant*

3. Results and Discussion

The supercritical fluid extraction (SFE) of *Salvia officinalis* L. by carbon dioxide (CO_2) was investigated. Firstly, supercritical extraction of *Salvia officinalis* L was performed at different particles size, all other extraction conditions were the same (Table 1).

Table 1. *Conditions for supercritical extraction by different particles size*

Sample	Particle diameter size (mm)	Extraction time (h)	Flow rate of carbon dioxide (kg/min)	Temperature (°C)	Pressure (bar)
F_1	0.21	4	$3.225 \cdot 10^{-3}$	40	100
F_2	0.43	4	$3.225 \cdot 10^{-3}$	40	100
F_3	1.13	4	$3.225 \cdot 10^{-3}$	40	100

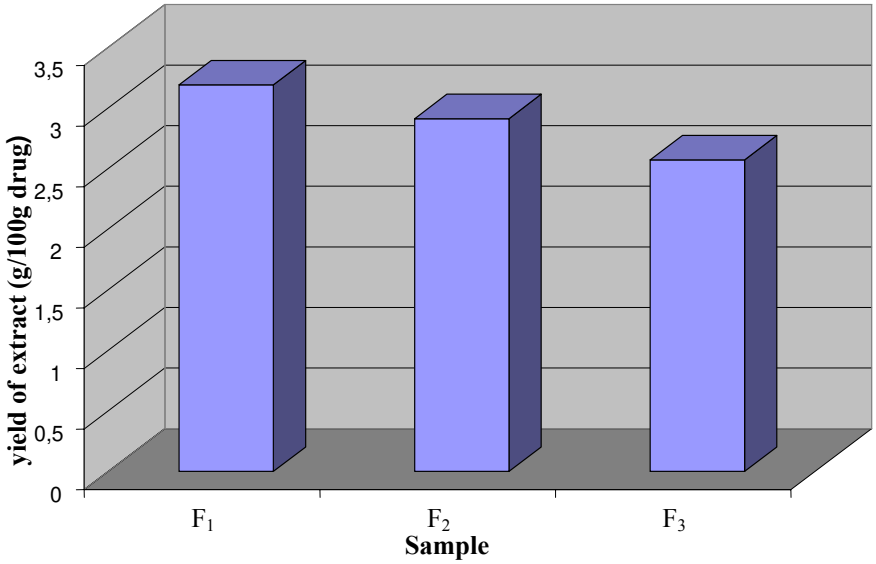

Fig. 4. *Yield of extract for different particles diameter size*

It was found that yield of extracts increases as particle diameter size decreases.

The relative contents identified compounds of SC-CO_2 extracts are given in table 2.

***Table 2**. Composition of Salvia extract for different particle size*

Number	R_t (min)	Compound	Sample			I_k
			F_1	F_2	F_3	
1	10.902	α – thujone (cis)	2.7013	0.5419	0.2741	1102.7
2	12.188	camphor	10.7024	-	-	1138.4
3	12.998	Isoborneol	9.6996	9.1258	6.2918	1162.8
4	13.274	Terpineol L-4	1.7389	1.2051	0.6254	1169.7
5	16.771	Bornyl acetate	4.3975	4.9818	2.0299	1268.1
6	16.828	Sabinyl acetate	2.7628	0.5966	-	1274.4
7	20.983	Isocaryophyllene	1.5904	1.7771	1.0393	1389.1
8	21.554	α - gurjunene	0.5673	0.5612	0.4568	1406.8
9	22.088	γ - elemene	11.3822	15.6045	9.8248	1424.9
10	26.156	Selina–3,7(11) diene	13.6412	20.4167	18.9666	1559.9
11	26.575	1,11-epoxyhumulene	3.9439	6.2998	5.7718	1573.1
12	27.221	Caryophyllene oxide	2.3676	3.2769	2.9539	1595.4
13	37.777	phyllocladene	21.6559	28.5225	38.8671	1995.1
total			87.2	92.9	87.1	

R_t = chromatographic retention time

In supercritical extract obtained for different particle size, 13 compounds were identified, with major compounds being: isoborneol, γ – elemene, Selina–3,7(11) diene and phyllocladene.

The higest persentage phyllocladene is in sample F_3 (38.87%), Selina–3,7(11) diene and β - elemene in sample F_2 (20.42%; 15.60%).

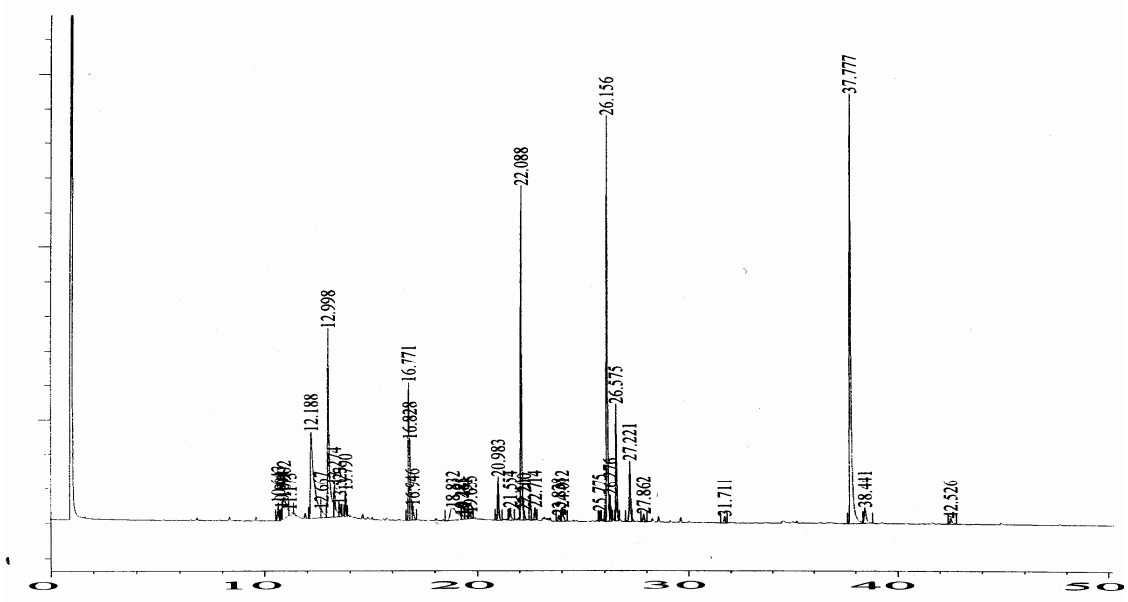

***Fig. 5.** GC chromatogram of Salvia extract (sample F_1)*

Figure 6 ilustrates the effects extraction time to yield of Salvia extract for different particle size.

Extraction rate rapidly increased in first 90 minute, and for farther extraction slowly increased.

Effect particle size to yield of extract is small. Now, SFE was performed at different pressure (80, 100, 150, 200 and 300 bar), all other extraction conditions were the same(Tabele 3).

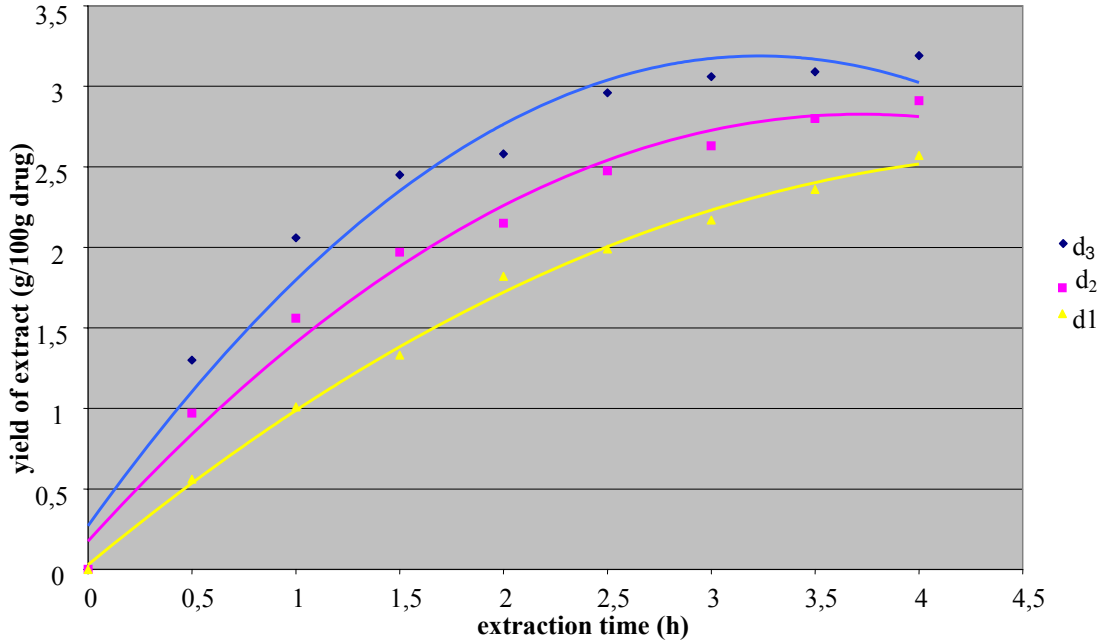

Fig. 6. *Yield of extract vs. extraction time for different particle size*

Table 3. *Conditions for supercritical extraction by different pressure*

Sample	Mean particle diameter (mm)	Extraction time (h)	CO_2 flow rate (kg/min)	Temperature (ºC)	Pressure (bar)
F_4	0.3157	4	$3.225 \cdot 10^{-3}$	40	80
F_5	0.3157	4	$3.225 \cdot 10^{-3}$	40	100
F_6	0.3157	4	$3.225 \cdot 10^{-3}$	40	150
F_7	0.3157	4	$3.225 \cdot 10^{-3}$	40	200
F_8	0.3157	4	$3.225 \cdot 10^{-3}$	40	300

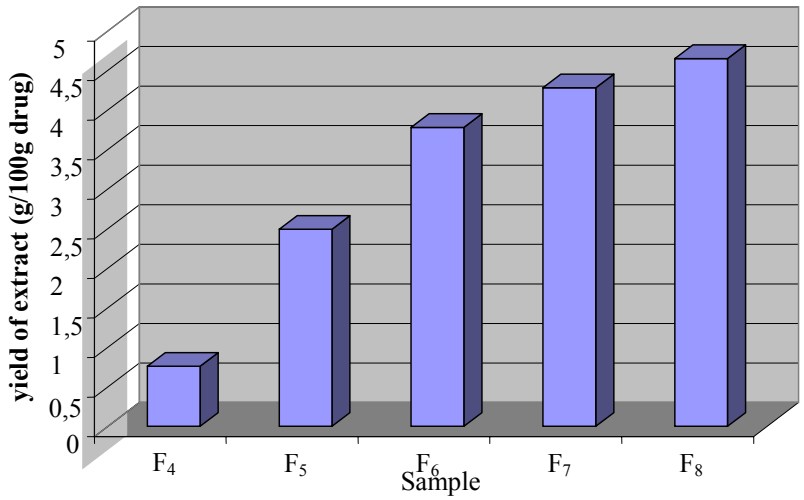

Fig. 7. *Yield of extract for different pressure values*

Table 4. *Composition of Salvia extract for different pressure*

Num.	R_t (min)	Compound	Sample				
			F_4	F_5	F_6	F_7	F_8
1	10.870	α – thujone	0.663	4.445	4.183	3.769	5.153
2	11.901	ß – thujone	-	-	0.1952	0.7016	-
3	12.175	Camphor	1.433	11.929	11.372	14.877	15.239
4	13.001	Isoborneol	11.287	7.389	6.804	9.523	8.167
5	13.214	Terpineol L-4	2.081	0.321	0.248	0.332	0.298
6	16.769	Bornyl acetate	5.905	3.586	2.015	4.621	3.959
7	16.946	Sabinyl acetate	1.053	0.534	0.406	0.643	0.421
8	20.979	Isocaryophyllene	2.745	1.179	0.839	1.300	1.168
9	21.549	α – gurjunene	1.448	0.544	0.439	0.621	0.549
10	22.085	γ – elemene	24.982	9.309	7.018	9.731	9.001
11	26.155	Selina-3,7 (11) diene	11.253	12.168	13.827	12.507	12.141
12	26.574	1,11-epoxyhumulene	8.989	4.557	5.869	4.958	4.921
13	27.220	caryophyllene oxide	2.755	2.662	2.640	2.390	2.456
14	37.783	Phyllocladene	10.420	26.056	30.645	21.990	24.603
Total			85.0	84.7	86.5	88.0	88.1

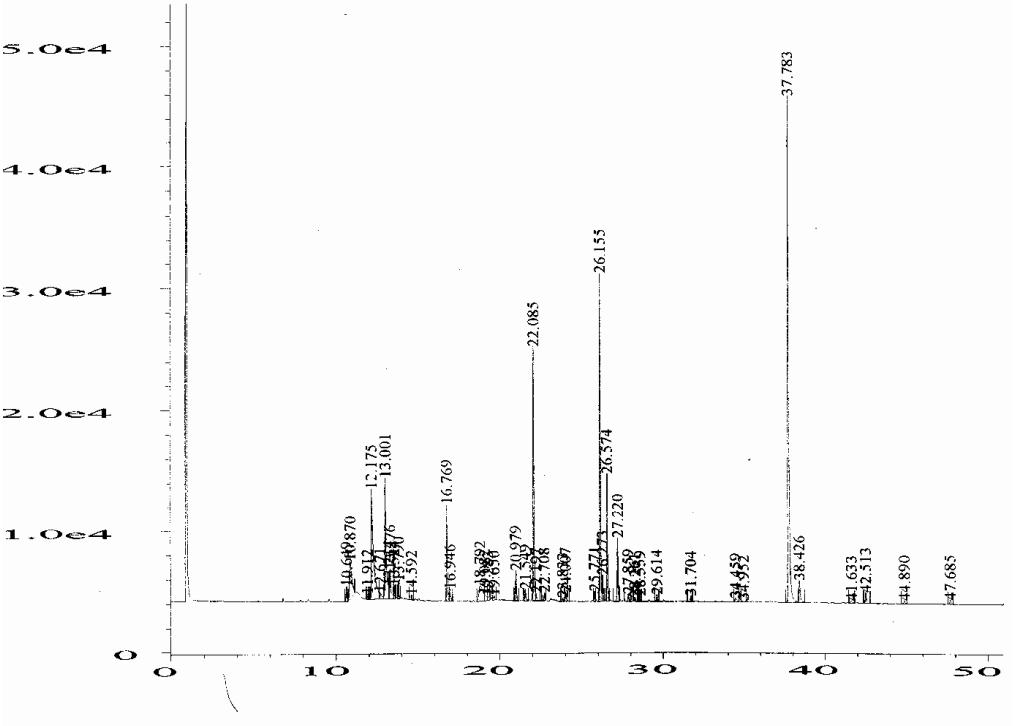

Fig. 8. GC chromatogram of Salvia extract (sample F_5)

Fig. 9 ilustrates the effects extraction time to yield of Salvia extract for different pressure. Extraction rate rapidly increased in the first 90 minutes, and for farther extraction slowly increased. Effect to yield of extract is more different for pressure p = 80bar from other pressure. In supercritical extract obtained for different pressure, 14 compounds were identified, with major compounds being: isoborneol, γ–elemene, Selina–3,7(11) diene and phyllocladene.The higest persentage phyllocladene (30.6%), and Selina–3,7(11) diene (13.8%) is in sample F_6 and γ - elemene in sample F_4 (24.98%).

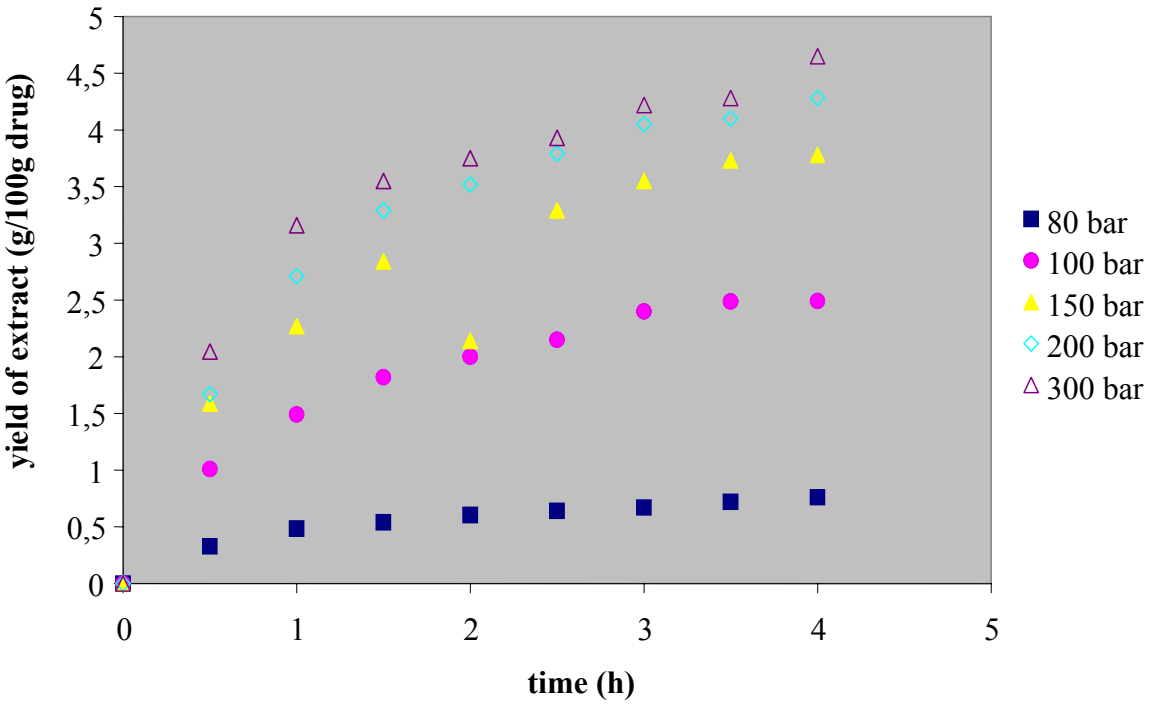

Fig. 9. *Yield of extract vs. extraction time for different pressure*

4. Conclusions

As expected from the studies on Salvia officinalis, the main compounds in extract are camphor, isoborneol, γ – elemene, selina – 3,7 (11) – diene and phyllocladene.The composition of main compounds in supercritical extract is not largely influenced by extraction pressure, exception pressure p=80bar. Indeed, chemical analysis of sage extract at different pressures evidenced composition variations along the extraction process but it they are not too large. The composition of main compounds in extract at pressure p=80 bar is largely different from composition at other pressures.

In the first 90 minutes of extraction, yield of extract rapidly increased, and for father extraction yield of extract slowly increased.

The five most abundant compounds (camphor, isoborneol, γ – elemene, selina – 3,7 (11) – diene, phyllocladene) represent 66.851 % of the extract (sample F_5).

References

[1]. Stahl, E. , Quirin, K. –W., Gerard, D. Verdichtete, 1987, *Case zur Extraktion und Raffination*; Springer Verlag; Berlin

[2]. Reverchon, E., Schiraldi, A., Fantozzi, P., 1993, *Fluidi Supercritici,* Applicazioni AgroAlimentari; CNR RAISA; Rome,.

[3]. Reverchon, E., Senatore, F. J.; *Agric. Food Chem.* 1994, 42, 154

[4]. Zeković, Z.; Lepojević, Ž.; Vujić Đ., 2000, *Supercritical Extraction of Thyme (Thymus vulgaris L.)* Chromatographia, 51 (3/4), 175

[5]. Zeković, Z., Lepojević, Ž, Milošević, S. , Tolić A., 2001, *Thyme (Thymus vulgaris L.) compounds in SFE.* Proceedings 6th Conference on Supercritical Fluids and Their Applications, Maiori, Italy, September, 9/110, 209

[6]. Zeković Z, Lepojević, Ž., Tolić, A., 2001, *Modelling of the Thyme – Supercritical Carbon Dioxide. Extraction System; Ithe influence of Carbon Dioxide Flow Rate and grinding degree of Thyme.* Sep. Sci. Technol. 36 (15), 3459

[7]. Aleksovski, S., Sovova, H., Poposka, F., 1998, Curapova, B. *Supercritical fluid extraction of essential oils from peppermint and wild thyme and its comparison with hydrodistillation.* XIII CHISA '98 (13 th International Congress of Chemical and Process Engineering), Praha, Aug 23 – 28, Summaries 4, 118

[8]. Reverchon, E., 1997, *Supercritical fluid extraction and fractionation of essential oils and related products*, Journal of Supercritical Fluids, 10, 1 – 37

[9]. Reverchon, E., Senatore, F., *Isolation of rosemary oil: Comparision between hydrodistillation and supercritical CO_2 extraction.* Flavour and Fragrance Journal, 7, 227-230.

MANUSCRISELE, CĂRŢILE ŞI REVISTELE PENTRU SCHIMB, PRECUM ŞI ORICE CORESPONDENŢE SE VOR TRIMITE PE ADRESA:

MANUSCRIPTS, REVIEWS AND BOOKS FOR EXCHANGE COOPERATION, AS WELL AS ANY CORRESPONDANCE WILL BE MAILED TO:

LES MANUSCRIPTS, LES REVUES ET LES LIVRES POUR L'ECHANGE, TOUT AUSSI QUE LA CORRESPONDANCE SERONT ENVOYES A L'ADRESSE:

MANUSCKRIPTEN, ZIETSCHRITFTEN UND BUCHER FUR AUSTAUCH SOWIE DIE KORRESPONDENZ SID AN FOLGENDE ANSCHRIFT ZU SEDEN:

UNIVERSITATEA "DUNĂREA DE JOS" DIN GALAŢI
REDACŢIA ANALELOR
Str. Domnească nr. 47 – 800036 Galaţi, ROMÂNIA
E-mail: mbordei@ugal.ro

After the latest evaluation of the journals achieved by National Center for the Science and Scientometry Politics (**CENAPOSS**), as recognition of its quality and impact at national level, the journal is included in B category, 215 code (http://www.cncsis.ro/2006_evaluare_rev.php).

The journal is indexed in Cambridge Scientific Abstract (http://www.csa.com/ids70/serials_source_list.php?db=materials-set-c).

The papers published in this journal can be visualized on the "Dunarea de Jos" University of Galati site, the Faculty of Metallurgy and Material Science page: www.fmsm.ugal.ro.

AFFILIATED WITH:

- *ROMANIAN SOCIETY FOR METALLURGY*
- *ROMANIAN SOCIETY FOR CHEMISTRY*
- *ROMANIAN SOCIETY FOR BIOMATERIALS*
- *ROMANIAN TECHNICAL FOUNDRY SOCIETY*
- *THE MATERIALS INFORMATION SOCIETY (ASM INTERNATIONAL)*

Annual subscription (2 issues per year)

Edited under the care of
Faculty of
METALLURGY, MATERIALS SCIENCE AND ENVIRONMENT
and Research Center
QUALITY OF MATERIALS AND ENVIRONMENT

Edited date: 15.05.2008
Issues number: 200
Printed by
Galati University Press
accredited CNCSIS
47 Domneasca Street, 800036 Galati,
Romania